Atomic structure of thin films and heterostructure of Bi_2Te_3 and Bi_2Se_3 topological insulators

Arsham Ghasemi

Doctor of Philosophy

University of York

Physics

September 2017

Abstract

The atomic structure of transition metals doped three dimensional (3D) topological insulators (TIs) and the bonding nature of Bi_2Te_3 with FeSe layers and Ge(111) substrate were studied. Motivation behind transition metal doping of 3D TIs is driven by achieving long range ferromagnetism of Bi_2Se_3 and Bi_2Te_3, which is expected to give rise to different spintronic effects that can be utilise in device applications. The nature of this magnetisation depends on the location of the dopants in the Bi chalcogenide matrix. Dopants in Bi based TIs can substitute for Bi, Te, or incorporate between the quintuple layers in the van der Waals gap. Long range ferromagnetism is observed in both Cr doped Bi_2Se_3 and Mn doped Bi_2Te_3; however, the main goal of achieving room-temperature ferromagnetism in homogeneously doped TIs has proven to be difficult. In this thesis it is shown that 4.6 at-% of Cr is incorporated substitutionally on Bi sites with no phase segregation. The presences of grain boundaries can cause Cr segregation; hence by controlling the defect density a homogeneous Cr distribution could in principle be achieved even at higher concentrations. In case of Mn as a dopant, we show that the local environment of Mn in Bi_2Te_3 is heterogeneous. The first principal calculations revealed that the Mn dopants ferromagnetically couple in Bi_2Te_3 lattice. In addition, we have shown that doping of Bi_2Te_3 with Mn should be limited to low concentrations (< 6 at-%), higher dopants concentrations results in the formation of secondary phases.

Next we have demonstrated that epitaxial growth of $Fe_xCu_{1-x}Se$ on Bi_2Te_3 is possible regardless of their different lattice symmetries and large lattice mismatch of 19%. First-principles energy calculations revealed that this is realised through van der Waals-like bonding between the Se and Te atomic planes at the interface.

Finally, we have shown that the weak van der Waals bonding between the Bi_2Te_3 and Ge(111) substrate can be strengthen by formation of a Te monolayer at the interface. The electronic band structure calculations revealed that this is due to the stronger atomic p-type orbital hybridization at the interface.

List of Contents

List of Contents

List of Tables

List of Figures

List of Figures

List of Figures

List of Figures

Acknowledgements

First of all, I am very thankful to my supervisor Dr Vlado Lazarov for giving me the opportunity to work on this research, as well as for his continuous and excellent supervision.

I would like to thank Prof. Thorsten Hesjedal from Oxford University, UK, for his collaboration; the provided specimens were very important for this research. I am thankful to Dr Demie Kepaptsoglou and Prof. Quentin Ramasse from the SuperSTEM Laboratory in Daresbury, UK, for their collaboration on electron microscopy. Many thanks also to Dr Leonardo Lari for the training and support regarding the electron microscope in York.

I would also like to thank all my fellow PhD students from the group of Dr Vlado Lazarov for their training and support on the density functional theory calculations using the CASTEP code.

Finally, I would like to dedicate this thesis to my family. I have been extremely fortunate in my life to have a family who have shown me unconditional love and support.

Declaration

I declare that the work presented in this thesis is based purely on my own research, unless otherwise stated, and has not been submitted for a degree in either this or any other university.

List of publications resulted from this thesis work:

[1] **A. Ghasemi**, D. Kepaptsoglou, L. J. Collins-McIntyre, Q. Ramasse, T. Hesjedal and V. K. Lazarov, Atomic-level structural and chemical analysis of Cr-doped Bi_2Se_3 thin films, *Scientific Reports*, 6, 26549 (2016).

[2] **A. Ghasemi**, D. Kepaptsoglou, A. I. Figueroa, G. A. Naydenov, P. J. Hasnip, M. I. J. Probert, Q. Ramasse, G. van der Laan, T. Hesjedal, and V. K. Lazarov, Experimental and density functional study of Mn doped Bi_2Te_3 topological insulator, *Applied Physics Letters Materials*, 4, 126103 (2016).

[3] **A. Ghasemi**, D. Kepaptsoglou, P. L. Galindo, Q. Ramasse, T. Hesjedal and V. K. Lazarov, Van der Waals epitaxy between the highly lattice mismatched Cu-doped FeSe and Bi_2Te_3, *Nature Asia Materials*, 9, e402 (2017).

[4] **A. Ghasemi**, D. Kepaptsoglou, K. Nawa, Q. Ramasse, K. Nakamura, T. Hesjedal and V. K. Lazarov, Modification of the van der Waals interaction between Bi_2Te_3 and Ge(111), Submitted to *Applied Physics Letters*, (2017).

List of other publications:

[5] B. Kuerbanjiang, Z. Nedelkoski, D. Kepaptsoglou, **A. Ghasemi**, S. E. Glover, S. Yamada, T. Saerbeck, Q. M. Ramasse, P. J. Hasnip, T. P. A. Hase, G. R. Bell, K. Hamaya, A. Hirohata, and V. K. Lazarov, The role of chemical structure on the magnetic and electronic properties of $Co_2FeAl_{0.5}Si_{0.5}$/Si(111) interface, *Applied Physics Letters*, 108, 172412 (2016).

[6] Z. Nedelkoski, D. Kepaptsoglou, **A. Ghasemi**, B. Kuerbanjiang, P. J Hasnip, S. Yamada, K. Hamaya, Q. M. Ramasse, A. Hirohata and V. K Lazarov, Controlling the half-metallicity of Heusler/Si(111) interfaces by a monolayer of Si–Co–Si, *Journal of Physics: Condensed Matter*, 28, 395003 (2016).

 [7] Z. Nedelkoski, B. Kuerbanjiang, S. E. Glover, A. Sanchez, D. Kepaptsoglou, **A. Ghasemi**, C. W. Burrows, S. Yamada, K. Hamaya, Q. Ramasse, P. Hasnip, T. Hase, G. bell, A. Hirohata, and V. Lazarov, Realisation of magnetically and atomically abrupt half-metal/semiconductor interface: $Co_2FeSi_{0.5}Al_{0.5}$/Ge(111), *Scientific Reports*, 6, 37282 (2016).

[8] Z. Nedelkoski, A. M. Sanchez, **A. Ghasemi**, K. Hamaya, R. F. L. Evans, G. R. Bell, A. Hirohata and V. K. Lazarov, The antiphase boundary in half-metallic Heusler alloy $Co_2Fe(Al,Si)$: atomic structure, spin polarization reversal, and domain wall effects, *Applied Physics Letters*, 109, 222405 (2016).

[9] B. Kuerbanjiang, C. Love, D. Kepaptsoglou, Z. Nedelkoski, S. Tear, **A. Ghasemi**, Q. Ramasse, K. Hamaya, S. Cavill, and V. Lazarov, Effect of annealing on the structure and magnetic properties of $Co_2FeAl_{0.5}Si_{0.5}$ thin films on Ge(111), *Journal of Alloys and Compounds* under review (2017).

[10] B. Kuerbanjiang, Y. Fujita, M. Yamada, S. Yamada, **A. Ghasemi**, P. J. Hasnip, A. M. Sanchez, D. Kepaptsoglou, G. Bell, K. Sawano, K. Hamaya and V. K. Lazarov, Correlation between spin transport signal and ferromagnet/semiconductor interface quality in lateral spin-valve devices, Submitted to *Applied Physics Letters*, (2017).

[11] Y. Yan, X. Lu, W. Liu, X. Zhang, J. Wang, **A. Ghasemi**, K. Zhang, D. Sarnjeet, I. Will, V. Lazarov, J. Du, J. Wu, R. Zhang, and Y. Xu, The origin of the uniaxial magnetic anisotropy in Fe-GaAs(100) system, Submitted to *Applied Physics Letters*, (2017).

1   Motivation and thesis overview

1.1   Motivation of the thesis

The field of condensed matter physics attracted significant research interest after the discovery of topological insulators (TIs). TIs are new states of quantum matter in which the surface states are protected by time-reversal symmetry. The study of surface states in TIs was originally inspired by the robustness of these materials to scattering in quantum Hall systems. In recent years, the interplay between topological order and ferromagnetism inspired the scientific community to realize exotic quantum phenomena, such as the quantum anomalous Hall effect. TIs also attracted attention in the field of spintronics, due to the intrinsic spin polarization in these materials.

One of the commonly studied family of TIs is the Bi based chalcogenides. The unit cell of Bi_2Se_3 and Bi_2Te_3 consist of three quintuple layers (QLs) bonded to each other via a weak van der Waals (vdW) bonding while the atoms inside the QL are bonded with a much stronger covalent bonding. The presence of this weak vdW bonding is one of the reasons that TIs are not being used in monolithic devices.

Doping TIs with transition metals is one of the commonly used ways of achieving ferromagnetism in these materials. Dopant positions in the Bi based TIs can be both substitutional and interstitial. They can substitute for Bi and Te, or can sit between the QLs in the vdW gap or between the atoms inside the QL. The goals of achieving room-temperature ferromagnetism in homogeneously doped topological insulators and also using TIs in monolithic devices for spintronic applications have proven to be difficult.

Many magnetisation and device manufacturing studies have been performed in the past few years on the Bi based TIs. However, observing long range ferromagnetism at room temperature has been proven highly dependent on the type of the dopants as well as the location of the dopants in the Bi chalcogenide matrix. In order to improve the

transition temperature of doped TIs and to shed a light on the position of dopants, an atomic and spectroscopic study of these materials is needed.

The motivation of this thesis is to atomically study the position of Cr and Mn dopants in the Bi_2Se_3 and Bi_2Te_3 TIs using both theoretical and experimental techniques. Furthermore, we are motivated to improve the applicability of these weakly bonded materials. In order to do so, an atomic study of the vdW epitaxy between TIs and other commonly used materials (e.g. FeSe and Ge) in the fields of superconductors and semiconductors was needed.

1.2   Overview of thesis

The thesis contains eight chapters. **Chapter 1** and **Chapter 2** give the motivation and a brief introduction into the subject of study. Brief explanation on the properties of TIs will be given. Furthermore, the atomic structure of the studied TIs will be discussed in detail. Furthermore, it will be discussed why these materials are important for spintronic applications. Finally, the current and possible future applications of these materials will be discussed.

In **Chapter 3**, the methodology used during the thesis will be discussed. This includes mostly the experimental techniques with some explanation of the theoretical method. The experimental part is mainly related to electron microscopy, starting from detailed description of the procedure for specimen preparation using both conventional and focused ion beam (FIB), then discussing conventional transmission electron microscopy (TEM), and finishing with the basics of the frequently used state-of-the-art high angle annular dark field (HAADF) scanning transmission electron microscopy (STEM) and electron energy loss spectroscopy (EELS). The second part discussed the computational methodology using the density functional theory (DFT).

In **Chapter 4**, first, the overall crystallinity of Cr doped Bi_2Se_3 will be shown. Then, the exact atomic position of the Cr dopants will be demonstrated using STEM-EELS. The HAADF-STEM and EELS results will show that the Cr dopants in Bi_2Se_3 substitute Bi atomic columns and in the presence of dislocation they will accumulate at the dislocation or

boundaries. Furthermore, small discussion on the use of principal component analysis (PCA) is also given.

Chapter 5 is focussed on doping of Bi_2Te_3 TI with Mn atoms. It will be shown that the local environment of Mn atoms inside the Bi_2Te_3 lattice is heterogeneous. In the second part of this chapter, using DFT calculation, it will be shown that the most favorable positions for Mn occupation is in the vdW gap. Furthermore, it will be shown that the closest Bi sites in different planes and furthest Te sites in nearby planes are the most favorable configurations for Mn occupying Bi and Te sites, respectively. Moreover, HAADF-STEM imaging on a sample with higher Mn concentration (~ 6 at-%) is also be shown.

In the second half of the thesis the epitaxy between the TIs and other materials will be demonstrated. In **Chapter 6,** it will be demonstrated that fully epitaxial single-crystalline $Fe_xCu_{1-x}Se$ inclusions embedded in a Bi_2Te_3 film can be grown despite the different lattice symmetries and the high lattice mismatch of 19%. Using DFT calculations, it will be shown that epitaxial heterostructures of materials with significant differences in lattice symmetry with corresponding large lattice mismatch can be realised through vdW - like bonding across the interface.

In **Chapter 7** it will be shown that single crystalline Bi_2Te_3 can be grown on Ge(111) substrate. It will be demonstrated that the presence of an extra Te monolayer at the interface drastically changes the electronic structure and bonding nature at the interface. Moreover, it will be shown that the stronger atomic *p*-type orbital hybridization at the interface overcomes the inherent weak bonding between Bi_2Te_3 and Ge.

In **Chapter 8** a brief summary of the results obtained in the thesis will be given and an outline of future related work will be discussed.

2   Introduction

Recently a new class of materials called 'topological insulators' have emerged, which are insulating in the bulk, but have conductive surface states. These exotic materials properties were predicted [2-7] and later experimentally confirmed in HgTe/CdTe quantum wells as well as at the surfaces of tetradymites materials such as Bi_2Se_3, Bi_2Te_3, and Sb_2Te_3 [8-12]. One of the most interesting properties of the TIs is the robustness of their surface states from backscattering which originates from the special topological nature of surface electronic bands [13-15].

2.1   Hall effect

Hall effect, discovered by Edwin H. Hall (1879), plays an important part towards discovery of topologically phases of matter. Hall experimented with the effect of magnetic field on the electric current in metallic sheets. [16]. His measurements showed that when magnetic field is perpendicular to the charge current (**Figure 2.1**) an electric voltage perpendicular to the charge current arises at the specimens' edges, as a result of the Lorentz force, as illustrated in **Figure 2.1**.
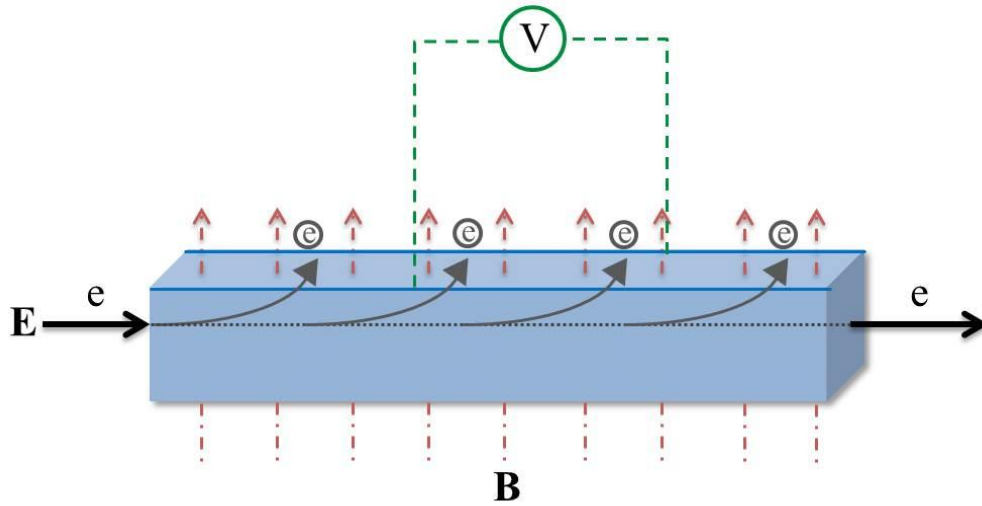
Figure 2.1: Hall setup showing measured voltage that arises from deflected motion of charged particles in solids under external electric (E) and magnetic fields (B).

The basic physics of the Hall effect can be understood as following. Let's consider a sample with width of W in an external magnetic field B. When charged particles go through the sample, due to the Lorenz force they will change their path and accumulate near the edge. These accumulated charges will produce an electric field, E, perpendicular to the charge current direction. In equilibrium, the Lorenz force on a moving charged particle becomes zero:

$$F = q(E + v \times B) = 0 \qquad (2.1)$$

where v and q are the velocity and the charge of the particles, respectively. The voltage difference between the two boundaries is $V_H = EW$ and the electric current through the sample is $I = q\rho_e vW$ where ρ_e is the density of the charged carriers. In order to find the Hall resistivity, we simply need to divide the voltage to the electric current:

$$R_H = \frac{V_H}{I} = \frac{B}{q\rho_e} \qquad (2.2)$$

The Hall resistivity is linearly depending on the magnetic field of B. The Hall effect can be used to determine the sign of the charged carriers, that is, the particle-like or the hole-like.

2.2   The 2D electron gas

In 1970s, one of the most important developments was to achieve structures in which the electronic behaviour is essentially two dimensional, forming the so called two dimensional electron gases (2DEG). In a 2DEG we have a confining potential along the z direction and the electrons are free to move in the xy-plane. If we assume that we have only one electron the eigenfunction for the Schrodinger equation can be separated as:

$$\Psi(x,y,z) = e^{ik_x x}e^{ik_y x}u_n(z) \tag{2.3}$$

and the energy eigenvalues are

$$E_n(k_x, k_y) = \frac{\hbar^2 k_x^2}{2m_{xx}} + \frac{\hbar^2 k_y^2}{2m_{yy}} + \epsilon_{n,z} = \frac{\hbar^2 k^2}{2m_{x,y}} + \epsilon_{n.z} \tag{2.4}$$

where $\boldsymbol{k} = (k_x, k_y)$ is a two dimensional wave vector, n is the quantum number of the confinement potential, and m is the effective mass.

Now we consider the effect of a magnetic field on our 2DEG. We put the magnetic field parallel to the confinement direction z. We introduce the electric potential, ϕ, and magnetic vector potential, $\boldsymbol{A}$, to generate electric field ($\boldsymbol{E}$) and magnetic field ($\boldsymbol{B}$), respectively.

$$\boldsymbol{E} = -\frac{\partial}{\partial r}\phi \tag{2.5}$$

$$\boldsymbol{B} = \frac{\partial}{\partial r} \times \boldsymbol{A} \tag{2.6}$$

$\boldsymbol{A}$ and ϕ both enter the Schrodinger equation in the same way, by substituting energy ($\boldsymbol{E}$) with $(i\hbar\,\partial/\partial t + e\phi)$ and momentum with $(-i\hbar\,\partial/\partial r + e\boldsymbol{A})$. If we choose the Landau gauge for the vector potential to be $\boldsymbol{A} = (0, Bx, 0)$ the Hamiltonian becomes:

$$H = \frac{\hbar^2}{2m}k_x^2 + \frac{\hbar^2}{2m}(k_y + eBx)^2 + \frac{\hbar^2}{2m}k_z^2 + V(z) \tag{2.7}$$

from which we can find the discrete eigenvalue $\in_n$ separating the z part. As the Hamiltonian is independent of y, the eigenfunction is a product of a plane wave e^{iky} and a wave function $u(x)$. After rearranging the terms we can finally find that the x-part of the Hamiltonian is the same as a harmonic oscillator whose Schrodinger equation is:

$$\left[\frac{\hbar^2}{2m}\frac{\partial^2}{\partial x^2} + \frac{1}{2}m\omega_c^2\left(x - \frac{\hbar k}{eB}\right)^2\right]u(x) = Eu(x) \tag{2.8}$$

where the angular frequency is $\omega_c = \frac{eB}{m}$ and called the cyclotron frequency. Hence the magnetic field acts as a parabolic confinement potential in the x direction. We can write the discrete eigenvalues as:

$$E_i = \hbar\omega_c\left(v + \frac{1}{2}\right), v = 0, 1, 2, \dots \tag{2.9}$$

known as Landau levels.

2.3   The quantum Hall effect

Less than one year after in August of 1980, von Klitzing was studying the Hall effect in a 2DEG under a strong magnetic field and at a temperature ~ 1.5 K he discovered that in contrary to the classical Hall effect, in which the Hall resistance is proportional to the applied magnetic field, in a 2DEG under low temperature and strong magnetic field, the longitudinal conductance becomes zero and quantum plateau of the Hall conductance appears at ve^2/h (where h is the Planck's constant)(**Figure 2.2**) [17]. The prefactor is an integer ($v = 1, 2, \dots$), known as filling factor. This effect is known as integer quantum Hall effect (IQHE) or simply the quantum Hall effect (QHE). The discovery of QHE was fascinating in the sense that such a macroscopic measurement only depends on basic physical constants of h and e.
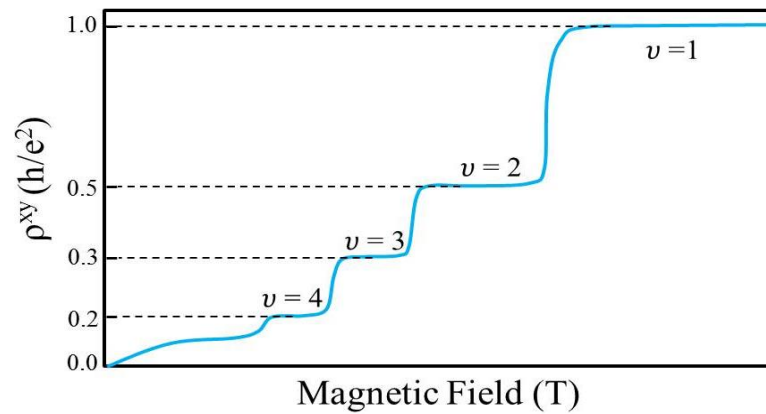
Figure 2.2: Illustration of the Hall resistivity plotted as a function of applied field. ρ^{xy} plateaus at $h/\upsilon e^2$ in a quantum Hall phase.

Few months later, Tsui *et.al.* discovered that in extremely low temperature (~0.42 K) $Al_xGa_{1-x}As$ you can get a fraction of e^2/h for the Hall conductance which is known as fractional quantum Hall effect (FQHE) [18].

To further understand the QHE, we use a semiclassical picture. A charged particle in a uniform magnetic field will cycle fast around the magnetic flux with radius of $R_n = \sqrt{(2n+1)\frac{\hbar}{eB}}$ due to the Lorentz force. When the particle is close to the boundary as it cannot go further, will bounce back from the rigid boundary and skips forward along the boundary. As a result, it will make a conductive channel along the boundary which is called edge state (**Figure 2.3**).
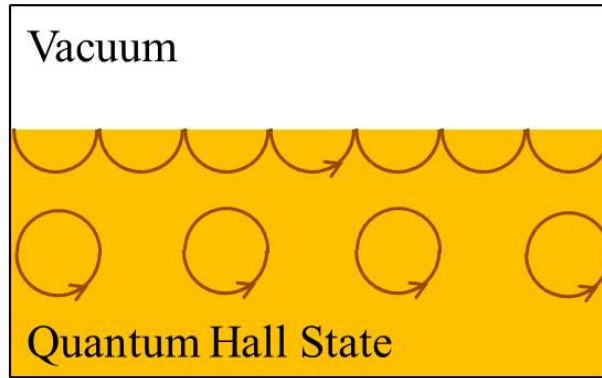
Figure 2.3: Conductive edge state in QHE.

In the low temperature range, the cyclotron velocity of the particles is bigger than the group velocity in the bulk, so the particles away from the edges are pinned or localised by the impurities or disorder. However, the rapid-moving particles along the edge channel are not affected by the impurities and form one dimensional conductive edge state with quantum conductance of e^2/h. If we consider that the Landau levels are discrete, each Landau level will make one edge channel and the number of filled Landau levels or filling factor will determine the quantised Hall conductance. Thus the most important feature of the QHE is that the electrons in the bulk are localised and electrons near the edge will form series of conductive edge channels which is a characteristic of a topological phase [19].

While the above picture is simple, it fails to explain why the QHE quantisation is unaffected by the impurities and material geometry. It was through the works of Thouless *et.al.* [20] along with Simon *et.al.* [21] and Berry [22], the link between the Hall conductivity and topology of Bloch wavefunctions was established [7, 19, 23-30]. They showed Hall conductivity is invariant under adiabatic changes to the system. This means that the v is topological invariant and is insensitive to the geometry of the system.

In a crystal which has periodic potential, the single-electron wavefunctions will satisfy the Schrodinger equation:

$$H\psi_{\boldsymbol{k}}^{\mu}(r) = E_{\boldsymbol{k}}^{\mu}\psi_{\boldsymbol{k}}^{\mu}(r)$$

(2.10)

the wavefunctions can be written as product of a plane wave and a periodic function:

$$\psi_{\boldsymbol{k}}^{\mu}(r) = e^{(i\boldsymbol{k}.r)}u_{\boldsymbol{k}}^{\mu}(r) \tag{2.11}$$

where μ is the band index, and the k is the wave vector. The energies $E_{\boldsymbol{k}}^{\mu}$ and the Bloch function $u_{\boldsymbol{k}}^{\mu}(r)$ will determine the bandstructure of the crystal. The discrete translational symmetry of the lattice makes the wave vector to be confined in a specific Brillouin zone (BZ). We note that the periodicity of the BZ makes it topologically a torus (**Figure 2.4**).
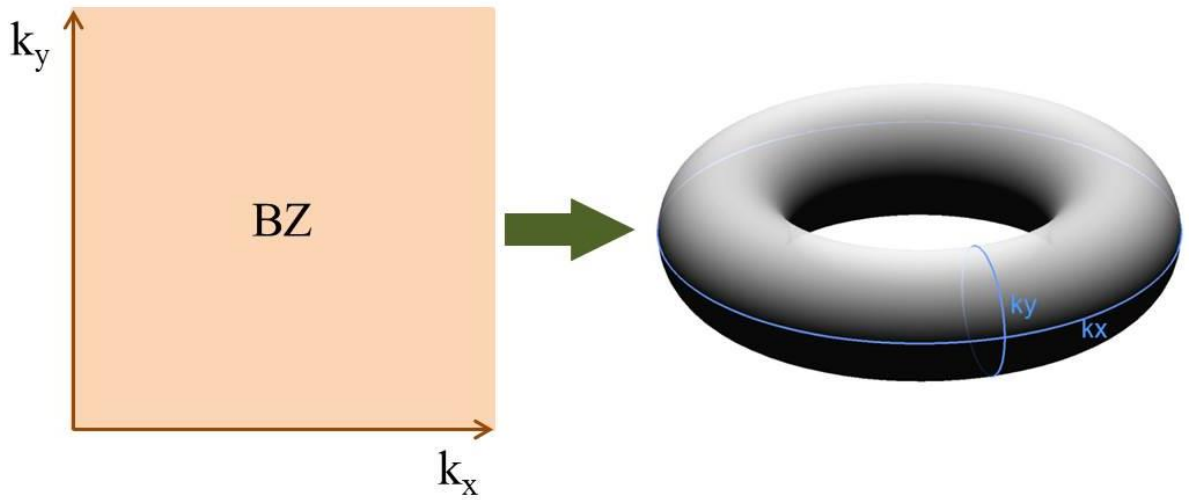
Figure 2.4: BZ in 2 dimensions upon periodicity will become a torus in 3 dimensions.

The Hall conductivity in a 2D system in terms of Bloch functions can be written as:

$$\upsilon = \frac{h}{e^2}\sigma^{xy} = \sum \oint_{BZ} \frac{i}{2\pi}\left(\left\langle \partial_{k_x}u_{\boldsymbol{k}}^{\mu}\middle|\partial_{k_y}u_{\boldsymbol{k}}^{\mu}\right\rangle - \left\langle \partial_{k_y}u_{\boldsymbol{k}}^{\mu}\middle|\partial_{k_x}u_{\boldsymbol{k}}^{\mu}\right\rangle\right)dk_x dk_y \tag{2.12}$$

where the summation is over all the occupied bands, and the integration is performed over the entire BZ. The expression is complicated but we can see that it only depends on Bloch function and not the energies. This shows that the only role of the energies is to distinguish between the occupied and unoccupied bands. Furthermore, one may derive and conclude that the integral over the BZ always will end up being an integer value. This

means that the ν must be integer as long as we don't have partially filled bands [31]. Moreover, as long as we have the same number of the occupied bands, because ν is an integer value, it must be constant under continuous changes to the system.

In order to give an explanation why the filling factor must be an integer number, we define the concept of Berry phase [22] and discuss how the Berry phase arises during the adiabatic evolution of a quantum state.

2.4   Cyclic adiabatic evolution and Berry phase

First we consider a physical system described by the Hamiltonian which depends on time through a set of parameter denoted by $\boldsymbol{R} = (R_1, R_2, R_3, \dots)$:

$$H = H(\boldsymbol{R}), \qquad \boldsymbol{R} = \boldsymbol{R}(t) \tag{2.13}$$

According to the adiabatic theorem, a physical system remains in its instantaneous eigenstate if a given perturbation is acting on it slowly, and if there is a gap between the eigenvalue and the rest of the Hamiltonian spectrum [32]. We are interested in the adiabatic evolution of the system as $\boldsymbol{R}(t)$ moves slowly along a path C. Next we introduce an orthonormal basis from the eigenstates of $H(\boldsymbol{R})$ at each value of parameter $\boldsymbol{R}$:

$$H(\boldsymbol{R})\big|n(\boldsymbol{R})\rangle = \varepsilon_n(\boldsymbol{R})\big|n(\boldsymbol{R})\rangle \tag{2.14}$$

Eq. (2.14) determines the basis function $\big|n(\boldsymbol{R})\big\rangle$ up to a phase factor.. One can make a phase choice, also known as a 'gauge', to remove this arbitrariness. According to the adiabatic theorem, if the system initially is in one of its eigenstates, $\big|n(\boldsymbol{R}(0))\big\rangle$, throughout the process it will stay in the same eigenstate while the Hamiltonian is changing with time [33]. Therefore, the only degree of freedom we have is the phase of the quantum state. We write the state at time t in the form:

$$\big|\psi_n(t)\rangle = e^{i\gamma_n(t)} e^{-\frac{i}{\hbar}\int_0^t dt'\,\varepsilon_n(\boldsymbol{R}(t'))}\big|n(\boldsymbol{R}(t))\rangle \tag{2.15}$$

where the second exponential factor is known as 'dynamical phase factor', and the $e^{i\gamma_n(t)}$ is the additional phase during the adiabatic evolution. When we insert Eq. (2.15) in the time-dependent Schrodinger equation we have:

$$H\big(\boldsymbol{R}(t)\big)e^{i\gamma_n(t)}e^{-\frac{i}{\hbar}\int_0^t dt'\varepsilon_n\big(\boldsymbol{R}(t')\big)}\big|n\big(\boldsymbol{R}(t)\big)\big\rangle =$$
$$i\hbar\frac{\partial}{\partial t}e^{i\gamma_n(t)}e^{-\frac{i}{\hbar}\int_0^t dt'\varepsilon_n\big(\boldsymbol{R}(t')\big)}\big|n\big(\boldsymbol{R}(t)\big)\big\rangle \tag{2.16}$$

In order to make writing the equations simpler we use a substitution of:

$$e^{i\gamma_n(t)}e^{-\frac{i}{\hbar}\int_0^t dt'\varepsilon_n\big(\boldsymbol{R}(t')\big)} : \aleph \tag{2.17}$$

If we solve Eq. (2.16) we will get to the position that we have:

$$H\big(R(t)\big)\aleph\big|n\big(\boldsymbol{R}(t)\big)\big\rangle =$$
$$-\hbar\gamma'_n(t)\aleph\big|n\big(\boldsymbol{R}(t)\big)\big\rangle + \varepsilon_n\big(\boldsymbol{R}(t)\big)\aleph\big|n\big(\boldsymbol{R}(t)\big)\big\rangle + i\hbar\aleph\big|\frac{\partial}{\partial t}n\big(\boldsymbol{R}(t)\big)\big\rangle \tag{2.18}$$

We can use Schrodinger equation for the left hand side of Eq. (2.18) and write:

$$\varepsilon_n\big(\boldsymbol{R}(t)\big)\aleph\big|n\big(\boldsymbol{R}(t)\big)\big\rangle$$
$$= -\hbar\gamma'_n(t)\aleph\big|n\big(\boldsymbol{R}(t)\big)\big\rangle + \varepsilon_n\big(\boldsymbol{R}(t)\big)\aleph\big|n\big(\boldsymbol{R}(t)\big)\big\rangle + i\hbar\aleph\big|\frac{\partial}{\partial t}n\big(\boldsymbol{R}(t)\big)\big\rangle \tag{2.19}$$

Since $\varepsilon_n\big(\boldsymbol{R}(t)\big)\aleph\big|n\big(\boldsymbol{R}(t)\big)\big\rangle$ term appears on both side of Eq. (2.19) and dividing by $\hbar$ and $\aleph$ and the equation is simplified to:

$$\gamma'_n(t)\big|n\big(\boldsymbol{R}(t)\big)\big\rangle = i\big|\frac{\partial}{\partial t}n\big(\boldsymbol{R}(t)\big)\big\rangle \tag{2.20}$$

In order to find the γ_n from Eq. (2.20) we need to multiply the equation with $\langle m\big(\boldsymbol{R}(t)\big)\big|$ from the left hand side:

$$\gamma'_n(t)\langle m\big(\boldsymbol{R}(t)\big)\big|n\big(\boldsymbol{R}(t)\big)\rangle = i\big\langle m\big(\boldsymbol{R}(t)\big)\big|\frac{\partial}{\partial t}n\big(\boldsymbol{R}(t)\big)\big\rangle \tag{2.21}$$

The Eq. (2.21) should be satisfied for all m.

First we consider $m \neq n$. The $\langle m(\boldsymbol{R}(t))|n(\boldsymbol{R}(t))\rangle$ will become zero and using $\frac{\partial}{\partial t} = \frac{\partial}{\partial \boldsymbol{R}}\frac{\partial \boldsymbol{R}}{\partial t}$, $\frac{\partial \boldsymbol{R}}{\partial t}: \boldsymbol{R}'$, $\frac{\partial}{\partial \boldsymbol{R}}: \nabla_{\boldsymbol{R}}$ we will have:

$$0 = \langle m(\boldsymbol{R}(t))|\nabla_{\boldsymbol{R}} n(\boldsymbol{R}(t))\rangle \boldsymbol{R}' \qquad (2.22)$$

The Eq. (2.22) is satisfied if $\boldsymbol{R}' = 0$ or if $\langle m(\boldsymbol{R}(t))|\nabla_{\boldsymbol{R}} n(\boldsymbol{R}(t))\rangle = 0$. First we check to see if $\langle m(\boldsymbol{R}(t))|\nabla_{\boldsymbol{R}} n(\boldsymbol{R}(t))\rangle = 0$. In order to do so we write the time-independent Schrodinger equation and multiply it with $\nabla_{\boldsymbol{R}}$ and $\langle m(\boldsymbol{R})|$ from left hand side. Since we assumed $m \neq n$, we will get:

$$\langle m(\boldsymbol{R})|\nabla_{\boldsymbol{R}} n(\boldsymbol{R})\rangle = \frac{1}{\varepsilon_n - \varepsilon_m}\langle m(\boldsymbol{R})|\nabla_{\boldsymbol{R}} H(\boldsymbol{R})|n(\boldsymbol{R})\rangle \qquad (2.23)$$

Assuming that the energy levels are not degenerate ($\varepsilon_n \neq \varepsilon_m$), then $\langle m(\boldsymbol{R})|\nabla_{\boldsymbol{R}} n(\boldsymbol{R})\rangle$ is zero if $\langle m(\boldsymbol{R})|\nabla_{\boldsymbol{R}} H(\boldsymbol{R})|n(\boldsymbol{R})\rangle$ is zero. To check if $\langle m(\boldsymbol{R})|\nabla_{\boldsymbol{R}} H(\boldsymbol{R})|n(\boldsymbol{R})\rangle$ is zero or not, we write it as:

$$\langle m(\boldsymbol{R})|\hat{O}_{\boldsymbol{R}}|n(\boldsymbol{R})\rangle: \quad \hat{O}_{\boldsymbol{R}} = \nabla_{\boldsymbol{R}} H(\boldsymbol{R}), \qquad \hat{O}_{\boldsymbol{R}}|X_a\rangle = \mu_a|X_a\rangle \qquad (2.24)$$

$$\begin{cases} |n\rangle = \sum_a \varphi^n{}_a|X_a\rangle \\ |m\rangle = \sum_{a'} \varphi^m{}_{a'}|X_{a'}\rangle \end{cases} \qquad (2.25)$$

Then if we put the set of eigenfunctions of (2.25) in (2.24) we will get:

$$\langle m(\boldsymbol{R})|\hat{O}_{\boldsymbol{R}}|n(\boldsymbol{R})\rangle = \sum_a \sum_{a'} \varphi *^m{}_{a'} \varphi^n{}_a \langle X_{a'}|\hat{O}_{\boldsymbol{R}}|X_a\rangle \qquad (2.26)$$

$$\langle X_{a'}|\hat{O}_{\boldsymbol{R}}|X_a\rangle = \mu_a \delta_{a,a'}$$

So the $\delta_{a,a'}$ will remove the summation over a' and we will leave with:

$$\sum_a \varphi^n{}_a \varphi *^m{}_a \mu_a \neq 0 \qquad (2.27)$$

Eq. (2.27) is not zero, implying $\langle m(\boldsymbol{R}(t))|\nabla_{\boldsymbol{R}} n(\boldsymbol{R}(t))\rangle$ is not zero, assuming non-degenerate states ($m \neq n$). This means that in Eq. (2.22):

$$\boldsymbol{R}' = 0 \qquad\qquad (2.28)$$

At the first look Eq. (2.28) suggests that $\boldsymbol{R}$ is not changing with time which is not the case. What Eq. (2.28) is actually showing is that $\boldsymbol{R}$ is changing extremely slowly in time ($\boldsymbol{R}' \rightarrow 0$). This conclusion is completely in agreement with the adiabatic theorem.

If we remember from Eq. (2.21) we considered that $m \neq n$. Now we consider the possibility of $m = n$. In this case $\langle m(\boldsymbol{R}(t))|n(\boldsymbol{R}(t))\rangle$ will change to $\langle n(\boldsymbol{R}(t))|n(\boldsymbol{R}(t))\rangle$ and will become 1 and if we use $\frac{\partial}{\partial t} = \frac{d}{d\boldsymbol{R}}\frac{d\boldsymbol{R}}{dt}$ in Eq. (2.20) we will get:

$$d\gamma_n(t) = i\, d\boldsymbol{R} \cdot \left\langle n(\boldsymbol{R}(t))\left|\frac{d}{d\boldsymbol{R}}\right|n(\boldsymbol{R}(t))\right\rangle \qquad\qquad (2.29)$$

In order to find $\gamma_n(t)$ we need to integrate both sides of Eq. (2.29) along a path C. Doing so we will get a set of equations as:

$$\gamma_n = i \int_c d\boldsymbol{R} \cdot \mathcal{A}_n(\boldsymbol{R}) \qquad\qquad (2.30\ a)$$

$$\mathcal{A}_n(\boldsymbol{R}) = \left\langle n(\boldsymbol{R}(t))\left|\frac{d}{d\boldsymbol{R}}\right|n(\boldsymbol{R}(t))\right\rangle \qquad\qquad (2.30\ b)$$

where vector $\mathcal{A}_n(\boldsymbol{R})$ is called the 'Berry connection' or 'Berry vector potential'. Eq. (2.30) shows that in addition to the dynamical phase, the quantum state will acquire an additional phase (γ_n) during the adiabatic evolution.

Moreover if we make a gauge transformation on the $\mathcal{A}_n(\boldsymbol{R})$:

$$\left|n(\boldsymbol{R}(t))\right\rangle \rightarrow e^{i\xi(\boldsymbol{R})}\left|n(\boldsymbol{R}(t))\right\rangle \qquad\qquad (2.31)$$

we will see that the Berry connection is gauge dependent:

$$\mathcal{A}_n(\boldsymbol{R}) \rightarrow \left\langle n(\boldsymbol{R}(t))\left|-\frac{\partial}{\partial\boldsymbol{R}}\xi(\boldsymbol{R})\right|n(\boldsymbol{R}(t))\right\rangle$$

$$\mathcal{A}_n(\boldsymbol{R}) \rightarrow \mathcal{A}_n(\boldsymbol{R}) - \frac{\partial}{\partial\boldsymbol{R}}\xi(\boldsymbol{R}) \qquad\qquad (2.32)$$

where $\xi(\boldsymbol{R})$ is an arbitrary smooth function. What we mean is that there is more than one choice of Bloch function $\left|n(\boldsymbol{R}(t))\right\rangle$, which satisfies the Bloch's theorem. This is due to the phase ambiguity in quantum mechanics, so a different gauge choice will give a

different connection. In addition, finding a set of Bloch functions which are continuous in the entire BZ is not always possible, so Berry connection can only be defined locally.

We put the Eq. (2.32) in Eq. (2.30) to see the results of gauge transformation on γ_n, in other words to check if γ_n is gauge invariant:

$$\gamma_n \rightarrow \gamma_n + \left[\xi\big(\boldsymbol{R}(0)\big) - \xi\big(\boldsymbol{R}(T)\big)\right] \tag{2.33}$$

This means that the phase γ_n will change under transformation, where $\boldsymbol{R}(0)$ and $\boldsymbol{R}(T)$ are the initial and final points of the path C. This made Fock [34] to conclude that one can always choose a suitable $\xi(\boldsymbol{R})$ such that γ_n accumulated along path C is cancelled out. As a result of this conclusion, the phase γ_n has long been considered as unimportant. This conclusion remained unchallenged almost for 20 years until Berry reconsidered the cyclic evolution of the system along the close path C where $\boldsymbol{R}(0) = \boldsymbol{R}(T)$ [22]. The phase choice we made on the basis function $n(\boldsymbol{R})\rangle$ requires $e^{i\xi(\boldsymbol{R})}$ in the gauge transformation to be single valued. This implies that we should have:

$$\xi\big(\boldsymbol{R}(0)\big) - \xi\big(\boldsymbol{R}(T)\big) = 2\pi \times integer$$

$$\gamma_n \rightarrow \gamma_n + 2\pi \times integer \tag{2.34}$$

This means that the γ_n can only change by an integer multiple of 2π under the gauge transformation and cannot be removed. Therefore, for a close path C, γ_n becomes a gauge-invariant physical quantity known as 'Berry phase' or 'geometric phase':

$$\gamma_n = i \oint d\boldsymbol{R} . \mathcal{A}_n(\boldsymbol{R}) \tag{2.35}$$

We can see from Eq. (2.35) that Berry phase only depends on the geometric aspect of the close path and is independent of how $\boldsymbol{R}(t)$ changes with time. Furthermore, by using Stokes's Theorem the Berry phase can be written as a surface integral, so in three dimensions (3D) we can write:

$$\Omega_n = \nabla_{\boldsymbol{R}} \times \mathcal{A}_n(\boldsymbol{R}) \tag{2.36}$$

$$\gamma_n = i \int_S \ d\boldsymbol{S} \cdot \Omega_n(\boldsymbol{R}) \tag{2.37}$$

Where Ω_n is called 'Berry Curvature'.

We note that one can also write the tensor form of Berry curvature as a summation over eigenstates as:

$$\Omega_{\mu\nu}^n(\mathbf{R}) = i \sum_{n'\neq n} \frac{\left\langle n\left|\partial H\middle/\partial R^\mu\right|n'\right\rangle\left\langle n'\left|\partial H\middle/\partial R^\nu\right|n\right\rangle - \left\langle n\left|\partial H\middle/\partial R^\nu\right|n'\right\rangle\left\langle n'\left|\partial H\middle/\partial R^\mu\right|n\right\rangle}{(\varepsilon_n - \varepsilon_{n'})^2}$$

(2.38)

This summation form has the advantage of not having any differentiation on the wave function; therefore it can be calculated under any gauge choice. Eq. (2.38) also shows that if we bring the two energy levels of $\varepsilon_n(\mathbf{R})$ and $\varepsilon_{n'}(\mathbf{R})$ together (equal to each other) at certain value of $\mathbf{R}$, the Berry curvature will become degenerate. This degeneracy point corresponds to a monopole in the parameter space.

The form of Berry connection resembles that of the electromagnetic vector potential, so using Berry curvature we can write Eq. (2.12) as:

$$v = \frac{1}{2\pi} \oint \Omega_n d^2 k$$
(2.39)

Notice that $\mathcal{A}_n(\mathbf{R})$ is similar to vector potential $\mathbf{A}$ while Ω_n is similar to the magnetic field $\mathbf{B}$ and the integral is over the BZ. This comparison makes it easier to see that the Berry curvature is also gauge-invariant. The analogy is no accident, in fact the equations of motions for a wave packet are [35]:

$$\mathbf{K}' = -\frac{e}{\hbar}\mathbf{E} - \frac{e}{\hbar}\mathbf{r}' \times \mathbf{B}$$
(2.40a)

$$\mathbf{r}' = \frac{1}{\hbar}\nabla_K E_K^\mu - \mathbf{K}' \times \Omega_n$$
(2.40b)

where $\mathbf{r}$ and $\mathbf{K}$ measure the average position and momentum of a wave packet. The first equation is the Lorentz force acting on an electron, but we can see that in the second equation (2.40b), we have an anomalous velocity $(\mathbf{K}' \times \Omega_n)$ term. From comparison between two velocities one can say that the curvature will deflect electron moving in $\mathbf{k}$-space in the same way that the magnetic field deflects a particle in real space.   This anomalous velocity is originated from the interaction between the electric field and the

Berry curvature. This velocity is always transverse to the electric field and will give rise to the Hall current.

In 1931, Dirac showed that the existence of a magnetic monopole will quantize the electric charge and vice versa [36]. In order for the quantum mechanical theory to be self-consistent, the magnetic flux through a closed surface must be multiple of the flux quanta $\Phi_0 = {h}/{e}$. To further explain the role of monopoles we briefly study the Berry phase and Berry curvature in a simple two-level system. The Hamiltonian of the two-level system can be written as:

$$H = \boldsymbol{h}(\boldsymbol{R}) \cdot \boldsymbol{\sigma} \tag{2.41}$$

where $\boldsymbol{\sigma}$ are the Pauli matrices:

$$\boldsymbol{\sigma}_x = \begin{pmatrix} 0 & 1 \\ 1 & 0 \end{pmatrix} \tag{2.42a}$$

$$\boldsymbol{\sigma}_y = \begin{pmatrix} 0 & -i \\ i & 0 \end{pmatrix} \tag{2.42b}$$

$$\boldsymbol{\sigma}_z = \begin{pmatrix} 1 & 0 \\ 0 & -1 \end{pmatrix} \tag{2.42c}$$

If we write the $\boldsymbol{h}$ in spherical coordination, $\boldsymbol{h} = h(\sin\theta\, cos\varphi, \sin\theta\, sin\varphi, \cos\theta)$, the two eigenstates with energies of $\mp h$ will have the forms of:

$$|u_-\rangle = \begin{pmatrix} sin\frac{\theta}{2}e^{-i\varphi} \\ -cos\frac{\theta}{2} \end{pmatrix}, |u_+\rangle = \begin{pmatrix} cos\frac{\theta}{2}e^{-i\varphi} \\ sin\frac{\theta}{2} \end{pmatrix} \tag{2.43}$$

We know that we are free to add an arbitrary phase to these wave functions. If we focus on the lower energy level $|u_-\rangle$, we can write the Berry connections as:

$$\mathcal{A}_\theta = i \begin{pmatrix} sin\frac{\theta}{2}e^{i\varphi} & -cos\frac{\theta}{2} \end{pmatrix} \begin{pmatrix} \frac{\partial}{\partial\theta} \end{pmatrix} \begin{pmatrix} sin\frac{\theta}{2}e^{-i\varphi} \\ -cos\frac{\theta}{2} \end{pmatrix} = 0 \tag{2.44}$$

$$\mathcal{A}_\varphi = i \begin{pmatrix} sin\frac{\theta}{2}e^{i\varphi} & -cos\frac{\theta}{2} \end{pmatrix} \begin{pmatrix} \frac{\partial}{\partial\varphi} \end{pmatrix} \begin{pmatrix} sin\frac{\theta}{2}e^{-i\varphi} \\ -cos\frac{\theta}{2} \end{pmatrix} = sin^2(\frac{\theta}{2}) \tag{2.45}$$

and the Berry curvature will be:

$$\Omega_{\theta\varphi} = \frac{\partial}{\partial\theta}\mathcal{A}_{\varphi} - \frac{\partial}{\partial\varphi}\mathcal{A}_{\theta} = \frac{1}{2}sin\theta \qquad (2.46)$$

However if we look at the lower energy in the south pole ($\theta = \pi$), we can see that the phase is not defined:

$$|u_-\rangle = \begin{pmatrix} e^{-i\varphi} \\ 0 \end{pmatrix} \qquad (2.47)$$

We can choose another gauge by multiplying the lower energy eigenstate by $e^{i\varphi}$, so the wave function be smooth and single valued everywhere except the north pole. Using this gauge we can see that our connections will become $\mathcal{A}_{\theta} = 0$ and $\mathcal{A}_{\varphi} = -cos^2(\frac{\theta}{2})$ while our curvature will stay the same as we expect from a gauge invariant physical quantity.

If $\boldsymbol{h}(\boldsymbol{R})$ depends on a set of parameters $\boldsymbol{R}$, then we can write the Berry curvature as:

$$\Omega_{R_1 R_2} = \frac{1}{2}\frac{\partial(\varphi, cos\theta)}{\partial(R_1, R_2)} \qquad (2.48)$$

and if we consider a specific case where $\boldsymbol{h} = (x, y, z)$, then the Eq. (2.48) in a vector form will become:

$$\Omega = \frac{1}{2}\frac{\boldsymbol{h}}{h^3} \qquad (2.49)$$

We note that the Eq. (1.49) is the same as the field generated by a monopole at the origin of $\boldsymbol{h} = 0$. Now if we integrate the Berry curvature that we found in Eq. (1.46) over a sphere containing the monopole, we will get the Berry phase on the sphere as:

$$\gamma_n = \int_S \Omega_{\theta\varphi} \cdot d\theta d\varphi = 2\pi \qquad (2.50)$$

We know that γ_n is an integer multiple of 2π, which in this case the integer value is 1. This integer number corresponds to the net number of monopoles inside the sphere and called 'Chern number'.

Dirac's argument was that if we consider an electron inside a 2D surface which has magnetic field inside, the Aharonov-Bohm phase ($\Phi = \frac{e}{\hbar}\oint \boldsymbol{A}.\,d\boldsymbol{r} = \frac{e}{\hbar}\iint \boldsymbol{B}.\,d\boldsymbol{s}$) is

proportional to the magnetic flux through the area enclosed by the loop. However, there are two areas which share the same closed loop (**Figure 2.5**).
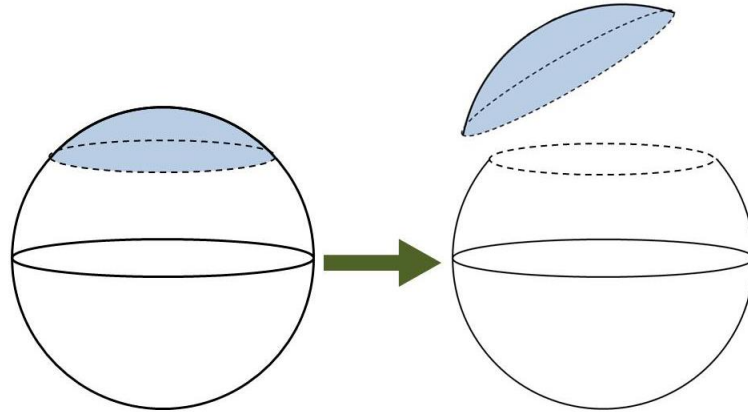
Figure 2.5: The loop divides the surface into two areas with the same boundary. The magnetic flux through both areas changes by multiple of h/e so the total flux of the sphere is quantised in the units of flux quanta.

The Aharonov-Bohm phase for both areas must be compatible so they should change by integer multiple of 2π; therefore the total flux of the sphere must be quantised and multiple integer of the flux quanta $\Phi_0 = h/e$.

Comparing the two stories of magnetism and Berry curvature, we can apply the same argument. In the Berry phase, the close surface is our BZ which is a torus due to the periodicity in the reciprocal space. Just as the magnetic flux is quantised the Berry flux (Eq. 2.39), must also be quantised and a multiple integer of 2π for the entire BZ. Now we know that this integer value is called Chern number and is a topological invariant in the sense that it cannot change when the Hamiltonian smoothly varies (For instance due to a weak perturbation coming from defect or dopant) [21, 31].

We have argued that Φ and the conductivity were quantised. In the magnetic monopole case the only way to change the number of flux is by moving a monopole in and out of the surface. Similarly for the quantum Hall system, it is possible to change the

Hall conductivity by passing a monopole through the BZ. We also showed that by doing this we need a singularity (Eq. 2.38) in the Berry connection and the Bloch functions. This only happens if the valence and conduction bands intersect which is one of the characteristic features of TIs.

2.5 Why Topological?

Topology is an area of mathematics focusing on the properties that are preserved under continuous deformations of objects. During these deformations the rule is that we cannot tear or glue the object and only deformations that involve stretching are accepted. In this area of mathematics, 2D surfaces can be topologically classified by their 'genus number', g, which basically counts the number of holes in the object. A mathematical theorem from Gauss and Bonnet, shows that if you know the Gaussian curvature of your object, which is basically the product of the two radii of the curvature in two perpendicular directions, by integrating the curvature over the surface we can get an quantised value in unit of 4π which will gives us the genus number [37]:

$$4\pi(1-g) = \int_s \boldsymbol{T}.d\boldsymbol{A}$$
(2.51)

where $\boldsymbol{T}$ is the Gaussian curvature. For example, in case of a sphere the Gaussian curvature will become $1/_{r^2}$ and we will get:

$$4\pi(1-g) = 4\pi \Rightarrow g = 0$$
(2.52)

By using the same method we can calculate the genus number of our BZ as a torus and we will get $g = 1$ (**Figure 2.6**). The genus number in mathematics works in the same way that the Chern number does in physics, which is why sometime genus number is used instead of the Chern number.

A TI can be explained as a material with an insulating state in the bulk and a quantum Hall state for the surface states. These two states are associated with different Chern numbers and as a result with two different topological phases; and we know that one cannot cross the material under the continuous deformation without changing the topological invariant. This explains why the name of TIs is chosen for this new class of material in the condensed matter society.
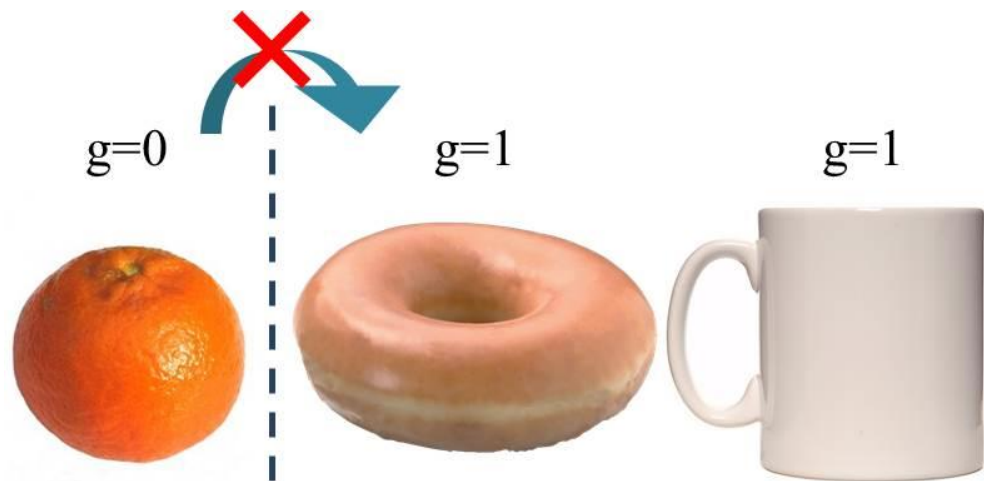
Figure 2.6: Different genus numbers. With stretching the doughnut, it can be changed to the mug so they have the same genus number, but we cannot do the same with the orange.

2.6   Chiral Edge States

One may ask the question, if the quantum Hall system is insulating, then how do they conduct the Hall current? As mentioned above the answer lies at the edge of the material. The quantum Hall system has gapless edge sates which are conducting and form current around the boundary of the material [19, 38]. The edge states are chiral which means that the current has a preferred direction. These conducting edge states will act as perfect 1D quantum wires even in presence of impurities and defects, and are topologically protected as long as the bulk electronic gap preserves.

Imagine a single wire in which we have left and right propagating modes. In absence of electron interaction or impurities, the electrons at the edge could travel smoothly in both directions of the material. This movement will produce a metallic behaviour in the sample. However, any small impurity or interaction will allow the electrons to backscatter. This will make the electrons to localise. In a quantum Hall system, the two propagating modes are separated from one another and placed at the two sides of the sample. This separation will make backscattering impossible.

The relation between the edge spectrum and the bulk one is usually referred to as the bulk-boundary correspondence. This means that a gapless excitation must exist at the interface of two topologically different classes of materials [19, 39, 40].

2.7   Anomalous Hall Effect

While Hall was working on different materials, he noticed that the transverse voltage was almost ten times bigger in ferromagnetic materials in comparison to the non-magnetic conductors [41]. He suggested that the Hall conductivity could be proportional to the magnetization M in a ferromagnetic metal:

$$R_H = R_0 B + R_A M \qquad (2.53)$$

This means that the Hall effect can persist even in the absence of the external magnetic field. This effect is known as anomalous Hall effect (AHE), **Figure 2.7**.
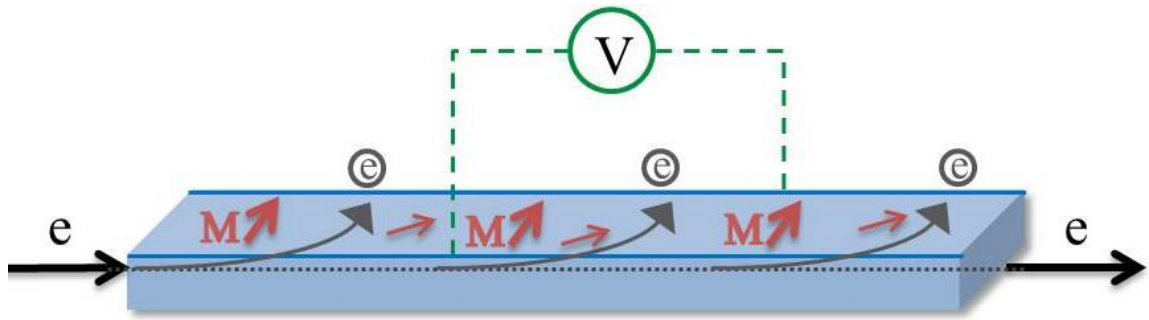
Figure 2.7: Illustration of anomalous Hall effect. The red arrows showing the magnetization (M) inside the sample.

Understanding of the AHE was an enigmatic problem for almost a century. The main reason seems to be the connection of AHE with topology and geometry that only became clear until much later. In 1954, Karpuls and Luttinger showed that electrons acquire an additional contribution to their group velocity when an external electric field is applied to a ferromagnet, in addition to magnetic field [42]. They named this additional velocity as 'anomalous velocity' which is now known as the Berry curvature. They suggested that the sum of the anomalous velocity over all occupied band states can be nonzero, implying a contribution to the Hall conductivity [43]. As this contribution depends on the number of filled bands, later on it referred to as the 'intrinsic' contribution to the AHE. The anomalous velocity can be related to the phase of Bloch state wave packets when an electric field causes them to evolve in the crystal momentum space [44]. Although the general mechanism of the AHE is complicated, the key components responsible for this effect are the electron scattering in ferromagnets in the presence of spin-orbit coupling (SOC).

After discovery of QHE from classical Hall effect, it is natural to ask if there is a quantum version of AHE, or the quantum anomalous Hall effect (QAHE). More precisely, the question is whether a state with a quantised Hall conductance can exist without external magnetic field at all. The answer to this question stayed unknown until the discovery of quantum spin Hall effect (QSHE).

2.8 Spin Hall effect and quantum spin Hall effect

The spin Hall effect (SHE) borrows its concept from the well established AHE. In AHE the relativistic SOC generates an asymmetric deflection of the charged carriers depending on their spin direction [43]. There are two different SHEs, direct and inverse SHE. In the direct SHE, an electrical current passing through a material can generate a transverse pure spin polarized current and in inverse SHE (ISHE), a pure spin current in the material can generate a transverse charge current, **Figure 2.8**.
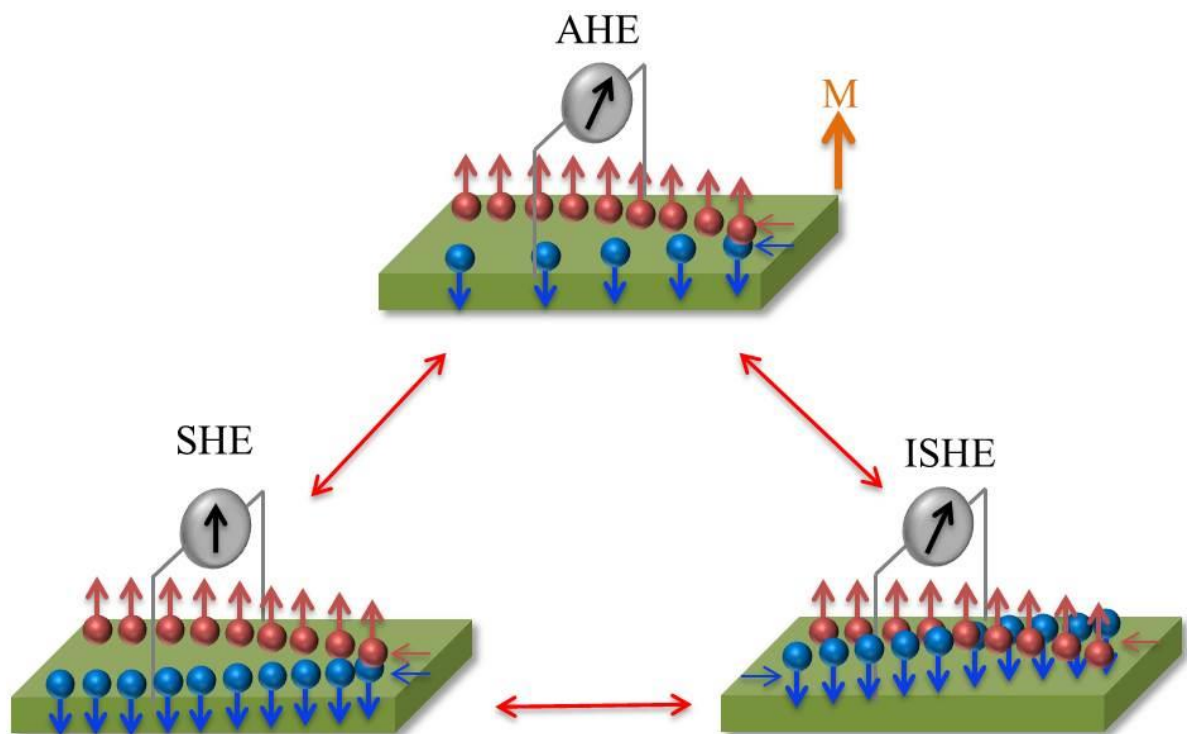
Figure 2.8: Illustration of the connection between AHE, SHE, and ISHE.

The SHE does not require time reversal symmetry (TRS) breaking so it can occur in a semiconductor without magnetic field [45].

Besides the Lorentz force which is caused by an external magnetic field, the electrons moving in a crystal can experience an internal magnetic field which comes from the SOC. This SOC depends on the $S \cdot L$ term and generates effectively magnetic field

which replaces the external magnetic field in QHE, and give rise to the QSHE. In solids, the description of SOC is complicated because of its dependence on the crystal lattice. However, if we imagine the electronic states in an atomic orbital picture, we can say that p-like bands (L=1) are affected by spin orbit, while the s-like bands (L=0) are not.

In 2005, Kane and Mele theoretically introduced the quantum spin Hall insulator, which is made of two copies of quantum Hall system with opposite spins and Chern numbers [3]. Their model was constructed on a honeycomb lattice based on the prior work by Haldane [46]. In this case time reversal will flip both spin and Chern number and introduce the two quantum Hall layers. The two chiral edge states are spin polarized and form a time-reversed pair to recover the overall TRS. This idea from Kane and Melle helped to understand the physics of the QSHE, however it is not completely realistic. When we put the two spin channels from the two QSH insulators at the edge of the sample, we assumed that there is no interaction between the spin layers.

Later on, in another remarkable paper [4], Kane and Mele showed that even in presence of spin mixing, we still have a topological distinction between the even insulators and odd insulators. This means that one can deform all the even subclasses to one another but these subclasses are still topologically distinct from the odd subclasses. Moreover, they showed that their honeycomb quantum spin Hall model belongs to the odd subclasses. Most importantly, they showed that the electronic states of their QSH insulator is characterised by a novel topology specified by a Z_2 index. This Z_2 index expresses whether the number of times that the 1D edge state crosses the Fermi level between 0 and π/a is even or odd (a is the lattice constant). Every time-reversal symmetric insulator is characterized by their Chern number being even or odd. The even subclasses like vacuum is commonly referred to as ordinary insulator while the odd subclasses are called 2D TIs. The Z_2 invariant can be formulated in terms of Bloch functions similar to the formulations in QHE. This means for any time-reversal invariant band structure we have an associated Z_2 which describes the topology of the Bloch functions. There are several ways of finding this Z_2 invariant. One can compute the Z_2 invariant from the Bloch functions as we mentioned, from an integral of Berry connection and curvature, or simply if we have crystal inversion symmetry by counting the number of band inversions [47] which is usually the case.

The edge states of 2D TIs consist of opposite spins moving in opposite directions, which is same as what we said for QSHE. As we mentioned earlier the two edge states are time-reversal conjugates and known as Kramers pair. Theoretically it is impossible to have backscattering within a Kramers pair with a time-reversal invariant potential. This will guarantee the stability of the TI edge spectrum [47-49]. However, we know that if we introduce magnetic impurities we will kill the TRS and will generate a gap at the edge band spectrum. So the TIs are only stable within the constraints given by the TRS.

Kane and Mele originally suggested that we can get the QSHE in graphene. However, soon scientist came to the conclusion that the SOC in graphene is not strong enough to observe the desired effect. Since the SOC is relativistic effect, heavier elements should have larger SOC. Later on, the QSHE was demonstrated experimentally for the first time in CdTe/HgTe/CdTe quantum well [8].

2.9   3D Topological Insulators

We introduced 2D TIs using quantum Hall and QSHE. It is natural to ask if we have 3D generalization of the TIs. It has been shown that there are four Z_2 invariants inside the 3D BZ for time reversal symmetric band insulators [2, 5, 6], as discussed below. As we mentioned before, the BZ is a torus in three momentum coordinates (k_1, k_2, k_3) changing between $-\pi$ and π. The time-reversal will change the sign of momentum from k to $-k$; however due to the periodicity of the reciprocal space there are some values of momentum that are invariant under time-reversal such as 0 and π. This means that in the BZ there are six planes that are time-reversal symmetric:

$$\begin{cases} k_1 = 0 \ and \ \pi \\ k_2 = 0 \ and \ \pi \\ k_3 = 0 \ and \ \pi \end{cases} \qquad (2.54)$$

Each of these six planes has its associated Z_2 invariant which we denote them as ν_i and μ_i where $i = 1, 2, 3$ in a way that ν_i and μ_i correspond to $k_i = 0$ and $k_i = \pi$, respectively. These six invariants are computed from the bulk 3D band structure but they are not independent. These invariants satisfy $\nu_1 + \mu_1 = \nu_2 + \mu_2 = \nu_3 + \mu_3$ which by defining $\nu_0 \equiv \nu_1 + \mu_1$ they will give us four independent topological invariants. These four invariants will provide a complete classification of the 3D TRS insulators. As we know, each of these four quantities can be even or odd so in total we will have 16 distinct classes.

➢ If all four invariants are even, then we will have an ordinary insulator such as vacuum.

➢ If ν_0 be even while at least one of the other three invariants is odd we will have a weak TI (WTI) and that is why we call ν_1, ν_2,and ν_3 as weak topological invariants.

➢ If ν_0 is odd we will have a strong TI (STI) or simply called TI and this is the reason we call ν_0 as the strong topological invariant.

The STIs have gapless surface states which are robust to disorder. These surface states look like massless Dirac cones where the dispersion relation is linear, **Figure 2.9**.
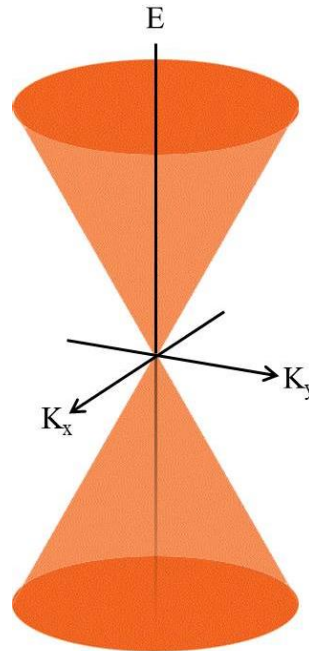
Figure 2.9: Dirac cone at the surface of STIs.

The Dirac Hamiltonian is proportional to $k_y \sigma_x - k_x \sigma_y$ where σ_x and σ_y are the Pauli matrices. According to the Hamiltonian the spin degree of freedom and the momentum are coupled which is known as 'spin-momentum locking'. These states also exist in graphene, while in graphene there are four Dirac cones; in TIs we always have odd number of Dirac cones on the surface.

In order to visualise the difference between the WTIs and STIs we consider two cases. A WTI can be formed by layering 2D QSH states. In this case a single surface band intersects the fermi surface in two places. It intersects once between Γ_1 and Γ_2 and once between Γ_3 and Γ_4, **Figure 2.10a**. Odd intersection between any pair of Γ points leads to the rise of a topological state. This WTI has $\nu_0 = 0$ because the Fermi surface enclosed even number of Kramers Points.
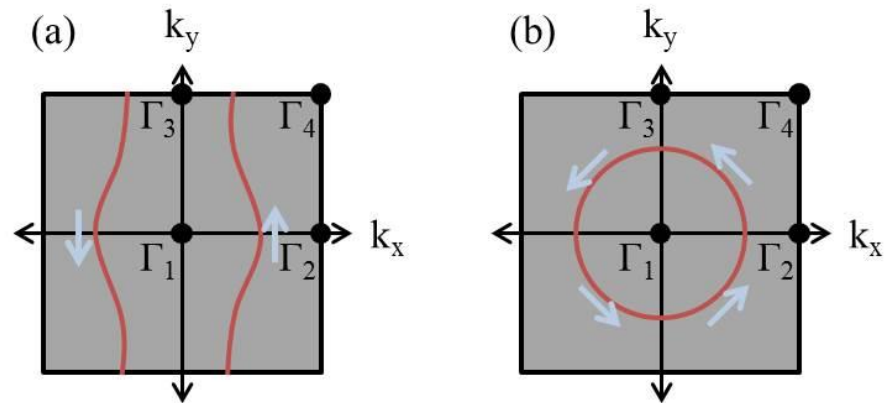
Figure 2.10: Sketch of the surface BZ with Fermi surfaces for (a) a WTI and (b) a STI.

In case of the STI, **Figure 2.10b**, we also have two intersections between the Γ points. However, our Fermi surface only enclosed one Karamers point which means the strong topological invariant odd.

Another way of finding TI materials from the band structures is to find some sort of band inversion at different points of the BZ [47, 50]. For example if the valence band of our material has s character at Γ point but has a p character in X point of BZ , while the conduction band has s and p reversed at these BZ points, then we have the inversion symmetry. This inversion means that our s orbitals are below the Fermi energy at some points and are above the Fermi energy at the other points. This band inversion is driven by the SOC, which means in order to find this effect we need to look at heavier elements [17]. At the same time our material should have a small band gap so that the SOC be able to modify the orbital energies to create the band inversion. For this reason, physicists typically calculate the band structure using DFT with and without SOC, to see if the SOC is strong enough to cause band inversions. If the calculations show that the material has odd number of these band inversions, then it will be a candidate for being STI and need to be examined experimentally. These criteria are usually the same for thermoelectric materials as heavy elements will reduce the thermal conductivity while the small band gap will increase the electrical conductivity.

2.10   3D Topological insulator materials

After the observation of QSHE in HgTe/CdTe quantum wells [50], the first 3D TI found was $Bi_{1-x}Sb_x$ using the link between these materials and thermoelectric materials. Soon after, the prediction was experimentally shown by Hsieh *et. al.* using angle resolved photoemission spectroscopy [9]. After the experiments from Hsieh *et. al.* new series of 3D TIs have been found in tetradymite semiconductors Bi_2Se_3, Bi_2Te_3, and Sb_2Te_3 [12, 26]. These new materials all share the same rhombohedral crystal structure with space group of $R\bar{3}m$. Unit cell of these materials consists of three so called QLs bonding to each other via a weak vdW bonding while the atoms inside the QL are bonded with a much stronger covalent bonding. The lattice parameters and the size of the band gaps for Bi_2Se_3 and Bi_2Te_3 are reported in **Table 2.1**.

Table 2.1: Lattice parameters for two well-known TIs.

Material	a (Å)	c (Å)	Band Gap (meV)
Bi_2Se_3	4.13	28.62	300
Bi_2Te_3	4.38	30.49	170

Each QL of these well-known TIs consists of three Se (Te) and two Bi atoms sitting in Se (Te)-Bi - Se (Te)- Bi- Se (Te) sequence, **Figure 2.11**. In order to see the perfect QL structure of these materials, we need to look them from one of the following main crystal planes which are 60 degrees apart: $(11\bar{2}0), (2\bar{1}\bar{1}0)$, and $(1\bar{2}10)$, **Figure 2.11c**. The other main crystal planes, **Figure 2.11d**, which are 30 degrees apart from the above mentioned crystal planes will show us the Se (Te) and Bi atoms sitting vertically on top of each other.
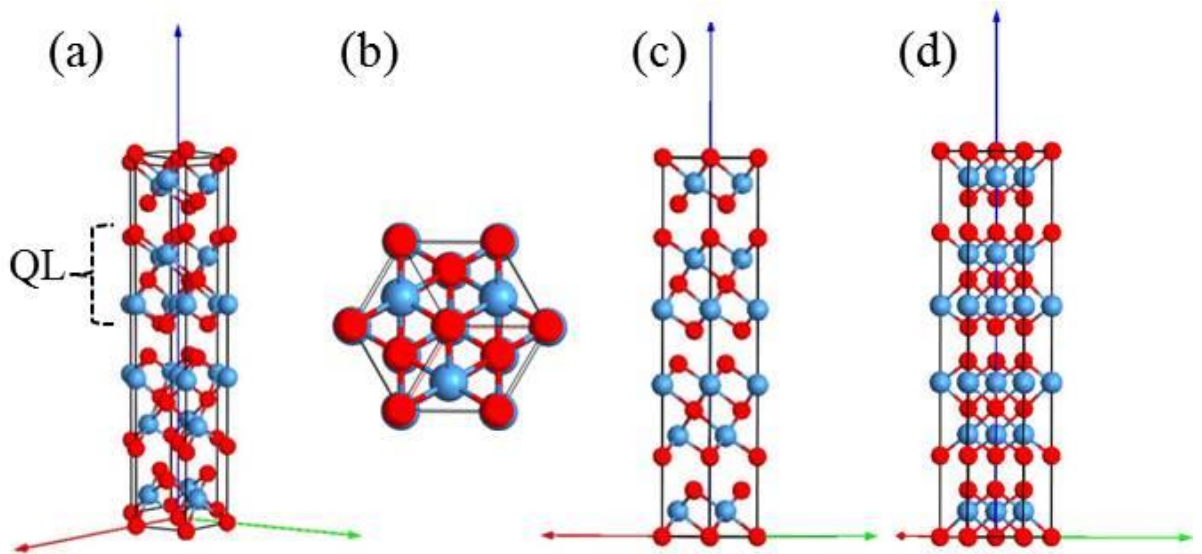
Figure 2.11: (a) Crystal structure of Bi(Sb)$_2$Se(Te)$_3$. (b), (c), and (d) show the crystal structure in (0001), the (11$\bar{2}$0), and (10$\bar{1}$0), respectively.

As we mentioned before, these materials should have a band inversion. To better explain the band inversion in these materials and for simplicity we only explain the origin of this band inversion in Bi$_2$Se$_3$. First we should note that the *s*-levels contribution can be neglected as these levels lie energetically much lower than the *p*-levels and are well separated. Starting from the *p*-levels of atomic Bi (6*p*) and atomic Se (4*p*) at the Γ point, the first energy shift happens due to chemical bonding between Bi and Se atoms within a QL. The formation of chemical bonding will hybridizes the states on Bi and Se atoms to become $|p1^{\pm}_{x,y,z}\rangle$, $|p2^{\pm}_{x,y,z}\rangle$, and $|p0^{\pm}_{x,y,z}\rangle$ where 1, 2, 0, and $\pm$ correspond to Bi, two neighbouring Se atoms, and the parity of the corresponding states (bonding and anti-binding), respectively. The two levels of interest for the formation of the conduction and valence bands are $|p2^{-}_{x,y,z}\rangle$ and $|p1^{+}_{x,y,z}\rangle$. In the next step according to the point group symmetry the crystal-field of the next neighbouring atoms will split the p_z orbitals from p_x and p_y whereas the last two remain degenerate. After this splitting the two states which are closest to the Fermi level are $|p1^{+}_z\rangle$ and $|p2^{-}_z\rangle$. In the last stage we consider the effect of the SOC. As we know the SOC Hamiltonian depends on the orbital and spin angular momentum ($S \cdot L$). It will preserve the total angular momentum while mixing the spin and

orbital angular momenta which leads to a level repulsion between $\left|p1_z^+,\uparrow\right\rangle$ and $\left|p1_{x+iy}^+,\downarrow\right\rangle$. This repulsion will push the $\left|p1_z^+,\uparrow(\downarrow)\right\rangle$ state down and with same analogy will push up the $\left|p2_z^-,\uparrow(\downarrow)\right\rangle$ state. If the SOC is large enough, it will reverse the order of these two levels and cause a band inversion. Note that in 3D TIs $\left|p1_z^+,\uparrow(\downarrow)\right\rangle$ and $\left|p2_z^-,\uparrow(\downarrow)\right\rangle$ states describing the upper valence and lower conduction bands, respectively, broaden into bands and lose their spin degeneracy for $k \neq 0$ [12].

2.11   Quantum anomalous Hall effect

After the discovery of QSHE, one can consider that each spin component is already a QAH state. However, the Hall conductance of two spin components will cancel each other due to the TRS. Therefore, the only task remains is to remove the QAHE of one spin component which leads to a non-zero net Hall conductance [51]. [39]. Two crucial conditions for realizing the QAHE are existence of 2D ferromagnetic (FM) insulator that breaks the TRS with band inversion transition with a strong SOC. The band inversion has to occur for one of the spin channels, while the TRS is broken. This can happen in FM materials with large spin splitting due to exchange coupling between magnetic moments and electron spin [51]. QSH insulators are good candidates because they satisfy the second criterion. In order to satisfy the first criterion doping these materials with magnetic elements is a common approach. The QAHE was achieved via Mn doping of HgTe/CdTe quantum wells in 2008 by Liu *et. al.* [52]. Since Mn dopants moments appear to be paramagnetically coupled (instead of ferromagnetically), in this material a small external magnetic field was required to realize the QAHE. The second criterion is not easy to satisfy because ferromagnetism usually coexists with metallic behaviour and ferromagnetic insulators are quite rare. The reason is that usually in FM systems, ferromagnetism originates from RKKY mechanism in which the FM coupling is mediated by free carriers. In case of the Mn doped HgTe quantum well, the lack of free carriers caused the magnetic moments of Mn atoms to couple paramagnetically.

Next a discussion of QAHE in Mn doped HgTe/CdTe quantum wells is given. HgTe and CdTe both are typical II-VI group compound semiconductors with zinc-blende lattice

structure. The band structure of HgTe and CdTe near the Fermi energy is formed by an *s*-type band (Γ_6) and a *p*-type band which is split to *J*=3/2 (Γ_8) and *J*=1/2 (Γ_7) bands by SOC (*J* is the total angular momentum). The CdTe has an energy gap of ~1.6 eV and its band ordering is normal with *s*-type bands (Γ_6) above *p*-type bands (Γ_7 and Γ_8). On the other hand, HgTe has an inverted band structure where Γ_6 bands are below the Γ_8 with a negative energy gap of ~0.3 eV. HgTe forms a quantum well with CdTe as a barrier, in which the conduction and valence bands split into subbands. In these subbands we use $|E_n\rangle$ and $|H_n\rangle$ for electron Γ_6 bands and heavy-hole Γ_8 bands (*n* = 1, 2,...). A topological transition phase exists in this quantum well at a critical thickness of 6.3 nm, due to the opposite band structures. When the thickness of the quantum well is larger than the critical thickness $|E_1\rangle$ is below $|H_1\rangle$ leads to an inverted band structure of the quantum well. Now we need to consider electron spin states for both $|E_1\rangle$ and $|H_1\rangle$ subbands.

Under the basis $|E_1,\uparrow\rangle, |H_1,\uparrow\rangle, |E_1,\downarrow\rangle$, and $|H_1,\downarrow\rangle$, the Hamiltonian describing the quantum well can be written as ($\uparrow$ and $\downarrow$ correspond to spin states) :

$$H = \begin{pmatrix} h(k) & 0 \\ 0 & h^*(-k) \end{pmatrix} \tag{2.55}$$

where $h(k)$ is given by the Hamiltonian of the minimal two-band model [53]. Thus, this Hamiltonian, known as Bernevig-Hughes-Zhang model, is basically just two copies of the two-band model for spins up and down which are related to each other by TRS [50]. The existence of band inversion in this quantum well is not enough for realisation of the QAHE since the TRS has not been broken yet. In order to break the TRS, Mn doping of the HgTe/CdTe quantum well is done. When the magnetisation is introduced to the system, the spin blocks will no longer relate to each other. Upon Mn doping, the Mn^{2+} atoms will substitute Hg^{2+} and the localised spin of Mn ions will couple with the spin of itinerant electrons through an exchange coupling:

$$H_s = \begin{pmatrix} G_E & 0 & 0 & 0 \\ 0 & G_H & 0 & 0 \\ 0 & 0 & -G_E & 0 \\ 0 & 0 & 0 & -G_H \end{pmatrix} \tag{2.56}$$

where splitting is $2G_E$ and $2G_H$ for the $\left|E_1, \uparrow\downarrow\right\rangle$, and $\left|H_1, \uparrow\downarrow\right\rangle$ bands. The corresponding energy gap is proportional to G_E-G_H and $-G_E$+G_H for spin up and spin down blocks, respectively.

In order to realise the QAHE we need that the state with one kind of spin become inverted and the entire system be in an insulating regime [53]. These two requirements suggest that the QAHE can be realised when $G_E G_H < 0$. This means that the spin splitting for electron and hole subbands should be opposite. This condition happens when HgTe/CdTe quantum well is doped with Mn. In this case there is large hybridization between the *p* orbitals of Te and the *d* orbitals of Mn which replaces cation position. This *p-d* exchange mechanism gives rise to an antiferromagnetic coupling between the Γ_8 bands and magnetic moments. On the other hand, the *s* orbitals of Hg cannot hybridize to the *d* orbitals of Mn, as it is forbidden by symmetry, and it will cause the direct exchange coupling to be dominant leading to a FM coupling. This opposite exchange coupling for electron and heavy-hole subbands, suggests that the inverted band structure can be achieved in this system. However, the problem with the Mn doped HgTe/CdTe quantum well is that it is a paramagnetic rather than FM material which shows a spin-glass behaviour at low temperatures. Therefore, a small magnetic field is required to magnetize the system to be able to realise the QAHE.

The governing concept for realisation of QAHE in TIs is similar to that of the Mn doped HgTe/CdTe quantum well. At 3D TIs the massless surface states are present at the top and the bottom surfaces of the thin film. The model of the Dirac cone on each surface is similar to the two-band model. When the magnetization (due to magnetic dopants) is introduced, it couples with the surface electron spins and opens a band gap in the surface Dirac cones. In the thin film with two surfaces, there will be a total number of two Dirac cones (as it is required by the fermion doubling theorem) [25].When the magnetic moments on both surfaces are parallel, we will see contribution to the Hall conductance from both surfaces with the same sign, leading to a total Hall conductance of $\pm e^2/\hbar$. This is exactly the QAHE that we are looking for. On the other hand, the Hall conductance for two surfaces will cancel each other, if the magnetic moments on the two surfaces are opposite. In this case the total Hall conductance will become zero.

In order to make this picture more realistic for thin film of TIs we need to consider the coupling effect of the top and bottom surfaces. A low energy model was introduced by Yu *et. al.* taking into account this type of interactions [54]. They introduced the quantum tunnelling between top and bottom surfaces in their Hamiltonian when the thickness of the film decreases, and then re-wrote the Hamiltonian as:

$$\begin{pmatrix} \hbar_k + g\mathcal{Z}\sigma_z & 0 \\ 0 & \hbar_k^* - g\mathcal{Z}\sigma_z \end{pmatrix} \tag{2.57}$$

where $h(k) = m_k\sigma_z + v_F(k_y\sigma_x - k_x\sigma_y)$ and v_F, $m_k = \mathcal{Z} + B(k_x^2 + k_y^2)$, $\sigma_{x,y,z}$, $\mathcal{Z}$, and g are the Fermi velocity, tunnelling effect, Pauli matrices, the exchange field along the z axis introduced by the FM ordering, and the effective g factor, respectively. The new basis of the Hamiltonian will be superposition of the old Hamiltonian as:

$$\left|\pm\uparrow\right\rangle = \frac{\left|t\uparrow\right\rangle \pm \left|b\uparrow\right\rangle}{\sqrt{2}}$$

$$\left|\pm\downarrow\right\rangle = \frac{\left|t\downarrow\right\rangle \pm \left|b\downarrow\right\rangle}{\sqrt{2}} \tag{2.58}$$

where t, b, ↑, and ↓ are representing the top surface, the bottom surface, spin up, and spin down, respectively. This is similar to the BHZ model describing the HgTe/CdTe quantum well [50].
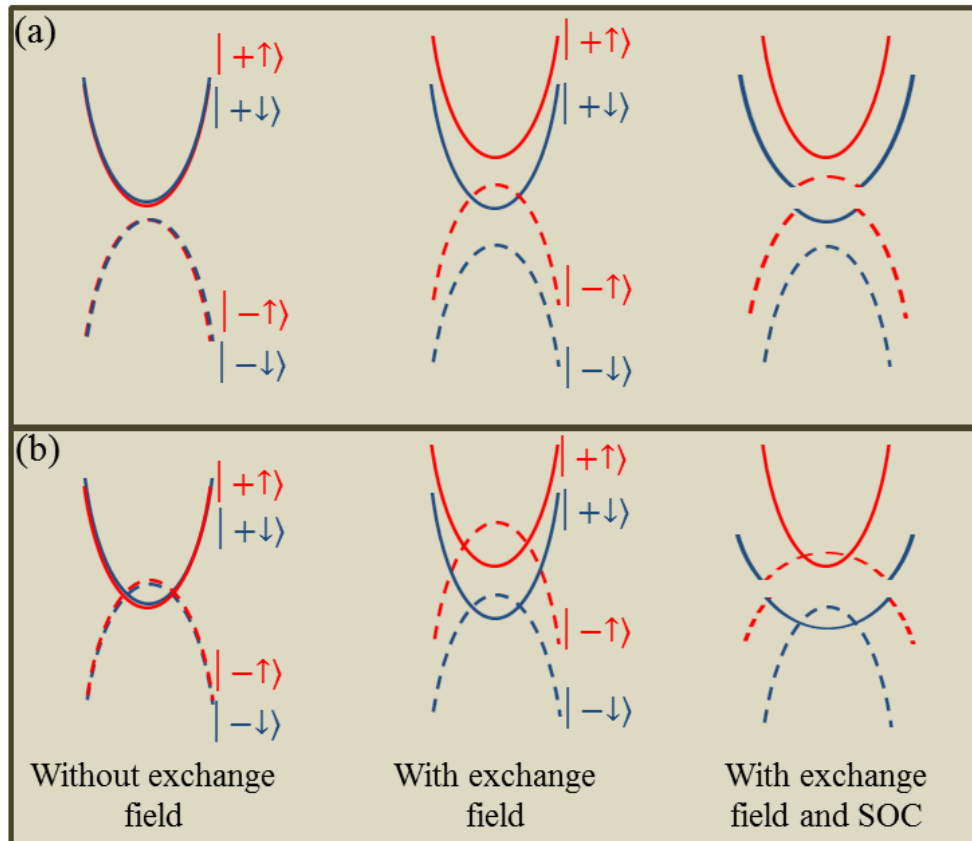
Figure 2.12 Evolution of the subband structure upon the increase of the exchange field. The solid and dashed lines show the subbands that have even and odd parity at Γ point, respectively.

According to the equation (1.55) due to to the presence of the σ_z matrix in the exchange field and the opposite signs of the gM, a strong enough exchange field will induce the QAHE in this system. The exchange field will break the TRS by increasing the mass term for the upper block of the Hamiltonian and reducing it for the lower block. If the four bands are originally in the topologically trivial phase, the exchange filed will induce a band inversion in the upper block while pushing the two subbands of the lower block even further away, **Figure 2.12a**. Therefore, the upper block will contribute to the Hall conductance ($e^2/\hbar$). However if the system is originally in the topologically non-trivial phase (both blocks have inverted band structure), a large enough exchange field can increase the band inversion in the upper block while removing it in the lower block, **Figure 2.12b**. Again the negative mass in the upper block will contribute to the Hall

conductance. Such a mechanism is applied to all the TI thin films which have FM ordering inside.

Several FM insulators such as EuO and GdN have been also considered, however due to their large band gap the inversion of their band structure are not feasible. These problems were overcome after the discovery of tetradymite TIs. Physicists predicted that thin films made out of this family of compounds doped with proper transition metal elements such as Cr and Fe could show the QAH state [54].

This theoretical prediction was first observed experimentally in Cr doped $(Bi,Sb)_2Te_3$ thin films [55]. Shortly after this observation, out-of-plane ferromagnetism was observed in Cr, V, and Mn doped Bi_2Te_3 or Sb_2Te_3 [56-61]. The first experimental observation of QAHE in Cr doped $(Bi,Sb)_2Te_3$ thin films was performed in 30 mK and the longitudinal resistivity dropped to ~2.53 kΩ while the corresponding Hall conductance was around $0.987\, e^2/\hbar$ [55]. However, if the temperature increases to 1 K, the longitudinal resistivity will increase significantly. Further improvement of the Cr doped $(Bi,Sb)_2Te_3$ thin films crystalline quality improved the Hall conductance and lowered the longitudinal resistivity to 15 Ω at 38 mK [62].

Moreover, several experimental studies have been performed in recent years on the electric and magnetic properties of Cr doped Bi_2Se_3 and Mn doped Bi_2Te_3 [63-65]. The ferromagnetism has been observed in Cr doped Bi_2Se_3 and Mn doped Bi_2Te_3 with a Curie temperature (T_c) of 8.5 and 12.5 K, respectively. Furthermore, it has been concluded that an effective incorporation of the magnetic dopants into the TIs lattice is important to improve the magnetic properties of these films for future applications. Therefore, an improvement of sample quality and study of the dopants position in the TIs at atomic level are required to demonstrate these effects in higher temperatures and lower thin films sizes [51, 65].

2.13   Applications

The QHE and QAHE have potential applications for future electronic devices. One of the most important features of the QH and QAH states is the chiral edge state which can carry electrical current without dissipation, because of their immunity from backscattering. Dissipationless transmission in materials is one of the most wanted features that have been studied for the electronic device applications in the past decades, since the Joule heating becomes bigger problem as the size of the electronic devices is reduced [66].

With emergence of the field of spintronics, it has been suggested that the TIs can also be used in spintronic device applications [7, 38, 67, 68]. One of the key aspects of spintronics is the generation, manipulation, and detection of spin currents. Among the several possibilities to create and control spin currents (such as half-metals), the TIs and doped TIs have gained a distinct place since its first observation a decade ago [33, 45].

One of the potential applications of using TIs is in spin orbit torque (SOT) magnetization switching. Different TI/magnet structures have been studied to probe the SOT effect [69-71]. Fan *et. al.* showed that by using TI/Cr doped TI bilayer heterostructure an efficient magnetic switching can be possible with a SOT ratio (strength of SOT per unit charge current density) which is almost three orders of magnitude larger than those reported in heavy metal/ferromagnet [71].

One of the other potential applications is in spin-electricity conversion induced by spin pumping. Shiomi *et. al.* showed that a spin-electricity conversion effect takes place in the surface states of bulk-insulating TIs $Bi_{1.5}Sb_{0.5}Te_{1.7}Se_{1.3}$ and Sn-doped Bi_2Te_2Se [72]. Although the efficiency of the measured spin-electricity conversion is low, due to the spin-momentum locking on topological surface states and by atomic engineering the interfaces this effect can, in principle, lead to efficient conversion between spin and electricity [72].

From the theoretical point of view, realisation of the QAHE also opened the door for experiments to observe other topological properties of TIs such as the topological

magneto-electric effect, the image monopole effect, and the topological Faraday rotation [73-75].

3   Methodology

The results in this thesis are obtained using both experimental and theoretical methods. In this chapter the methods that have been used during the development of this thesis are presented. Here we systematically and briefly explain the used methods in the following order: Thin film growth and *in-situ* characterisation, *ex-situ* characterisations on grown samples, both conventional and FIB cross-sectional sample preparation for electron microscopy, TEM, simulations and visualisations of microscopy data, data analysis, and density functional theory calculations.

3.1   Thin film growth and *in-situ* characterisation

In this section we briefly describe the molecular beam epitaxy (MBE) growth method that has been used for this work as well as the reflection high energy electron diffraction (RHEED) an *in-situ* characterisation tool. All the analysed samples have been grown by our collaborator Prof. Hesjedal from University of Oxford.

Most of the thin film deposition methods which are currently being used need some sort of reduced pressure ambient i.e. vacuum. This is due to the fact that growing crystals with high quality need an environment in which the deposited materials can travel long distances ($\sim$ metre scales) without being scattered [1], and also to avoid any contamination. This means that the mean free path of atoms in the environment should be large. Pressure reduction is one of the ways to achieve large mean free path according to the kinetic theory of gases [76]:

$$\lambda_{mfp} \propto 1/P \qquad (3.1)$$

If the pressure inside the growth chamber decreases to μtorr range, the mean free path will go to metre range which means that the atoms only will collide with the growth

stage/substrate.   However, achieving very low pressures (~ 10^{-10} torr) in a system is challenging and requires the use of various types of pumps.

3.1.1   Vacuum pumps

Pumping is the process of removing gas molecules from the system to obtain vacuum. There are four stages of vacuum depending on the chamber pressure, **Table 3.1.** For a successful crystal growth we need ultrahigh vacuum (UHV) in the growth chamber (10^{-8} Pa).

Table 3.1: Vacuum range.

Pressure range in Pa	Type of vacuum
$100 - 0.1$	Rough vacuum
$0.1 - 10^{-4}$	Low vacuum
$10^{-4} - 10^{-7}$	High vacuum
$< 10^{-7}$	Ultrahigh vacuum

There are various types of vacuum pumps categorised mostly into: gas-transfer pumps and entrapment pumps [76]. The gas-transfer pumps remove the atoms and molecules from the chamber and release them outside of the chamber. On the other hand, the entrapment pumps usually condense or bond chemically the molecules inside the chamber walls where they form layers of materials. These layers can be removed from the chamber by heating up the chamber to specific temperatures (depending on the used materials) or by manually polishing the chamber walls.

The gas-transfer pumps can be further divided to positive displacement and kinetic vacuum pumps. One of the most famous and used positive displacement pumps is the rotary mechanical pump. Rotary pumps usually contain a mounted rotary with spring-loaded vanes, **Figure 3.1**. During the rotation of the rotary, the springs will move the vanes in and out, enabling a quantity of gas to be confined and compressed and eventually sent out via the exhaust valve. Oil is added to the rotary pumps to seal and

lubricate the moving components. By using a rotary pump a vacuum of 10^{-1} Pa can be achieved. Rotary pumps are usually used to start the vacuum process in growth chambers. The rotary pumps are one of the cheapest pumps with a downside of the use of oil (hence potential contamination) as well as the noise that comes from the rotation of the rotary.
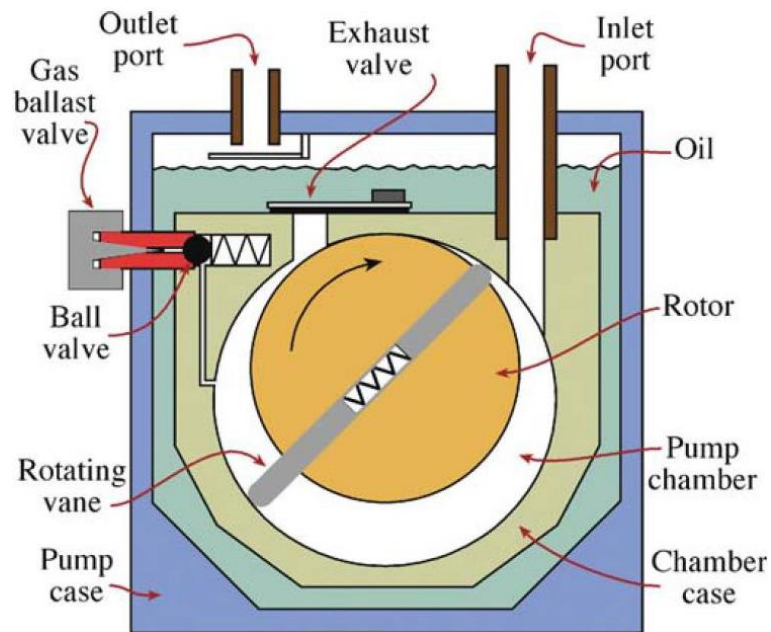
Figure 3.1: Cross-section of a rotary pump [1].

One of the well-known kinetic vacuum pumps is the diffusion pump. In contrast to the rotary pumps, the diffusion pumps have no moving parts which mean they produce much lower amount of noise. The diffusion pumps can work in a range of 10^{-1} to 10^{-9} Pa. Because they cannot directly release the atoms into the atmosphere, they usually need a mechanical pump at their outlet. The diffusion pumps can have pumping speeds from a few litres per seconds to 20,000 litres per second. In the diffusion pumps the low pressure is achieved by evaporating a fluid medium (oil) in multistage jet assembly as shown in **Figure 3.2a**. As the oil evaporates and streams out from the top nozzles, it collides with the residual gas which comes from the inlet and moves down towards the bottom of the pump and compressed to the exhaust and goes to the backing

pump. The region inside the pump will have lower local pressure with respect to the chamber due to this pumping process and cause the gas to flow inside the pump. Several jets can be used in series in order to improve the pumping rate. Although the diffusion pumps can achieve low pressures without using moving parts, they are not commonly used. This is due to the use of oil and the working mechanism of such pumps. In the diffusion pumps one of the biggest problems is the back-streaming of oil to the chamber itself. This problem is even more pronounced in the higher pressures. It is due to the low pressure difference between the jet area and the chamber which causes the oil to easily flow back to the chamber and contaminate both the chamber and the sample.
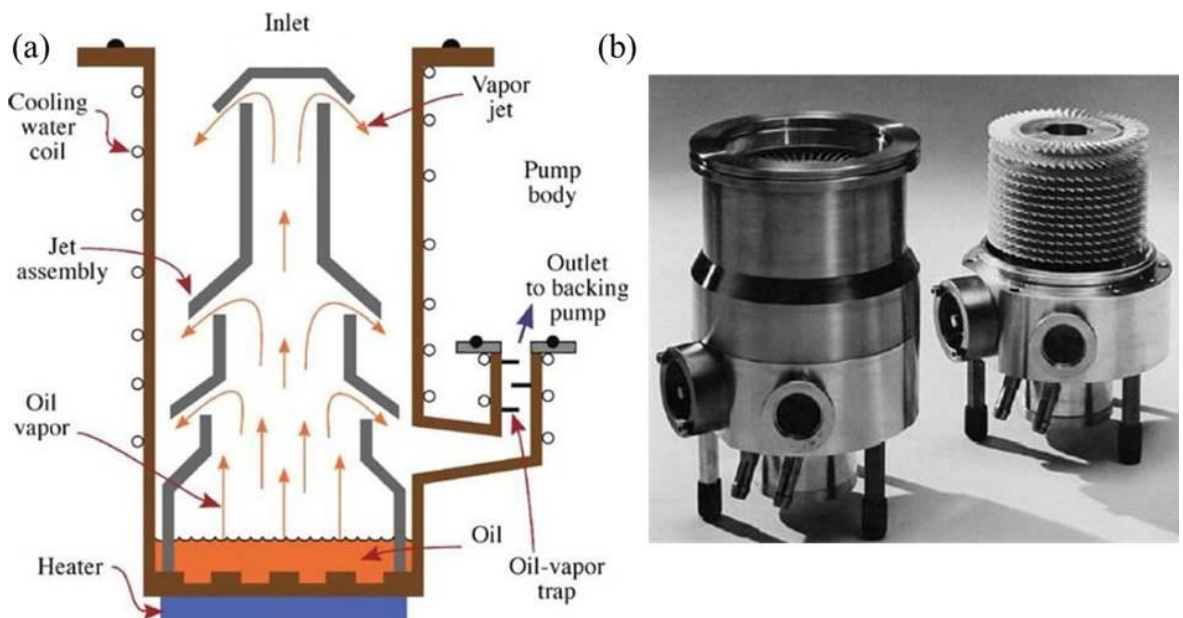
Figure 3.2: (a) Cross-section of a diffusion pump [1]. (b) Turbomolecular.

The problem of having back-streaming of oil inside the chamber spurred the development of an oil free pumps with capability of providing low pressures such as turbomolecular pumps. The turbomolecular pumps can achieve UHV conditions without using any fluid medium [76]. A turbomolecular pump is made of series of blades which act as rapidly rotating turbines as shown in **Figure 3.2b**. These blades can rotate easily up to 50,000 revolutions per minute. At each stage the blade will compress the molecules and

send it to the next stage which increases the pressure of the exhaust and that is why the turbomolecular pumps are also attached to a back-up mechanical pump. The turbomolecular pumps are generally the most important pumps used in the growth chambers, however due to the rotation of the blades they are not suitable for other applications which are sensitive to the noise such as the electron microscopes [1].

In order to solve the noise and the oil back-streaming problems, new generations of pumps have been developed such as the ion pump and Ti sublimation pump. These new pumps work by using reactive ions to bond with the residual ions inside the chamber and then attaching them to the pump pieces or the chamber walls. In the ion pump, a flow of Ti ions is generated by applying electric field between the cold Ti cathode and the stain-less steel anodes as shown in **Figure 3.3**. The Ti ions then travel spirally (due to a magnetic field) and interact with the residual ions in the pump which come from the chamber and then sit on the anode. Moreover, the applied electric field between the anode and the cathode will also attract some of the ions in the pump towards the Ti cathode. The ion pumps are only efficient at high vacuums, which is why they usually are switched on after a turbo pump (in growth chambers) or diffusion pump (in electron microscopy) has lowered the pressure to $<\sim 10^{-3}$ Pa. Similarly to ion pumps at sublimation pumps Ti ions are released inside the chamber and react to the reactive residual gases and attach them to the chamber walls. If there is a non-reactive molecule inside the chamber, it will be pushed to the walls and buried under the Ti atoms. That is why this pump is usually used before and after the use of chamber in order to avoid Ti contamination on the sample. It is obvious that this procedure will increase the pressure inside the chamber and then reduce it further down after the Ti ions are attached to the walls. Due to the working mechanism of this pump, it is not used in the vacuum systems for electron microscopes.
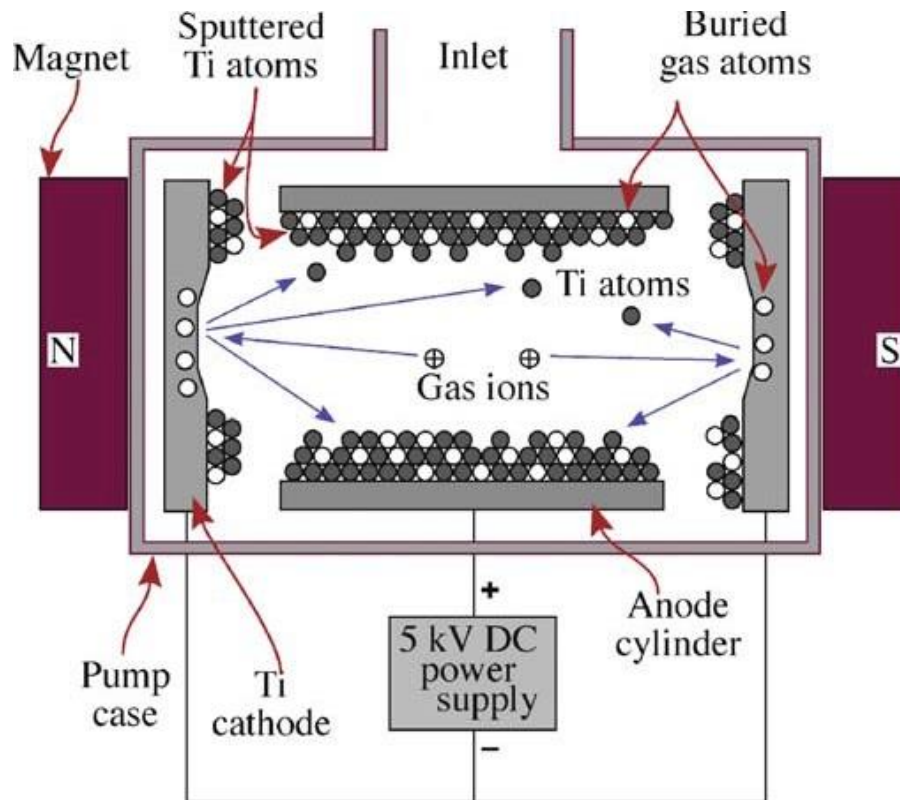
Figure 3.3: Schematic diagram of an ion pump [1].

3.1.2   Crystal growth using molecular beam epitaxy

Now that we explained the various pumps used to improve the vacuum in the growth systems, we focus on explaining the growth method itself. In this work we have used MBE growth technique to grow doped and un-doped TIs on Al_2O_3 and Ge substrates.

The MBE is well established growth technique for producing thin films. By using MBE we can precisely control the film stoichiometry, thickness, and the doping concentration. However, this method is slow and requires high degree of calibration to ensure the operating parameters are optimised. There are several parameters that are of great importance in order to achieve good crystallinity, these are: growth rate, growth temperature, vacuum pressure, partial pressure of each component/element, etc. In order to grow materials in a controllable manner, a good knowledge of the vapour pressure of the used elements is also needed. Generally, the increase of the source

temperature will increases the vapour pressure which increases the growth rate and also affects the stoichiometry of the grown materials.

There are usually several sources in a MBE chamber, as shown in **Figure 3.4**. Each source (Bi, Te, Se, Cr, Mn, Fe, or Cu) has its own heating unit which is used for heating up the source to the temperature that is needed to get the required vapour pressure.
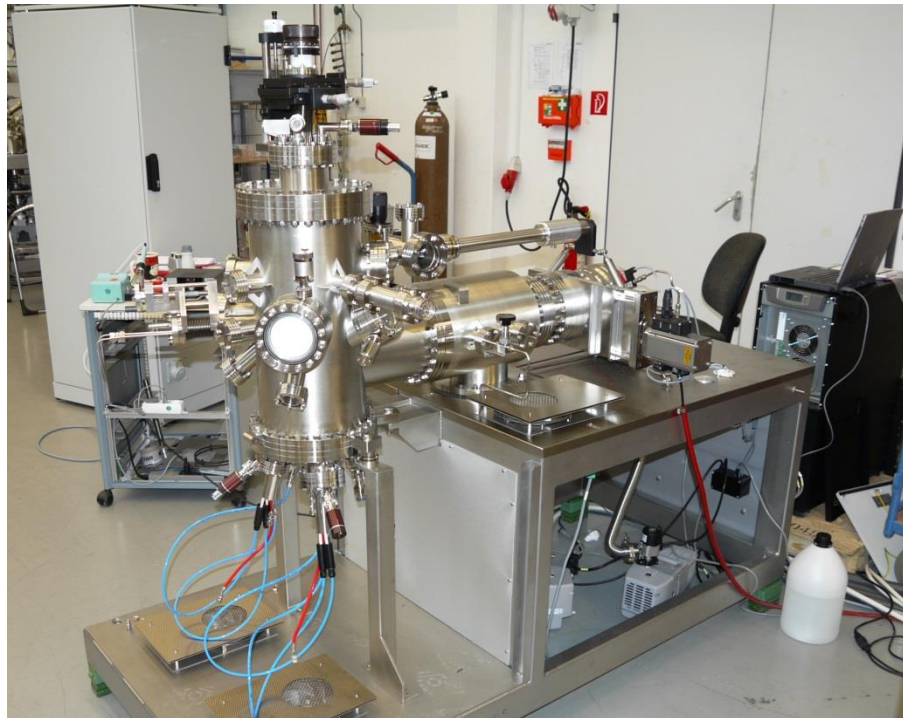
Figure 3.4: MBE chamber of Prof. Hesjedal at the University of Oxford.

There are many different ways to evaporate the materials from the sources. Two common evaporation techniques used in MBE are the electrically heated evaporation or an electron beam evaporations. The electrically heated evaporation usually heats up tungsten (W) wires, refractory metal sheets, crucibles, or sublimation furnaces. This technique has been used to evaporate the grown materials in this work.

On the other hand, in the electron beam evaporation, a beam of electrons is generated and then curved toward the crucible using a magnet which leads to melting of the source material. In contrast to the electrically heated evaporation, the electron beam

evaporation can minimise the contaminations coming from the heaters, crucibles, and support materials. Furthermore, materials with high melting points can be evaporated using the electron beam evaporation.

In contrast to other growth techniques such as sputtering in which the layers of materials are usually grown and then annealed, in MBE by using heating systems we can increase the substrate temperature in order to achieve good crystallinity upon growing the thin film layers. This is one of the other important factors that affects the growth quality.

There are various techniques to help the evaporated materials to reach to the substrate surface. The most commonly used technique is to put an aperture in front of the source to make a directional flow of ions towards the grounded substrate. In some MBE systems a bias voltage is applied between source and the substrate to accelerate the ions toward the substrate. The growth of thin films even with slow deposition rates can be extremely challenging due to the non-uniform growth of film on the substrate. There are three known growing scenarios of: island growth (Volmer-Weber), layer by layer growth (Frank-Van der Merwe), and the mixed growth (Stranski-Krastanov). In island growth, **Figure 3.5a**, the atoms are more strongly bounded to each other than to the substrate leading to growth of 3D islands of the film. In the layer by layer growth, **Figure 3.5b**, the film atoms are more strongly bounded to the substrate and the film tend to have a better crystal quality. This type of growth will produce films with highest quality.
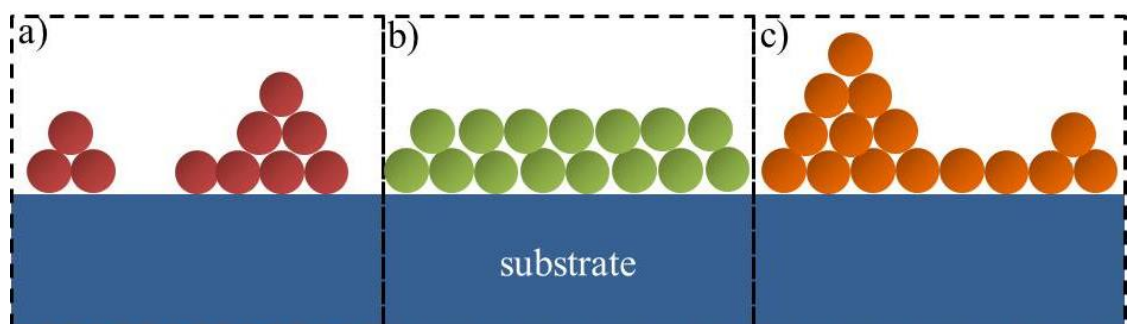
Figure 3.5: Three different growth mods of island, layer by layer, and mixed growth are shown in (a), (b), and (c), respectively.

In case of the mixed growth, **Figure 3.5c**, the film initially starts a layer by layer growth but then continues to form islands. This type of growth is fairly common specially in metal-metal systems [76].

3.1.3   RHEED *in-situ* characterisation

Growth systems generally allow basic *in-situ* characterisation of the specimen surface and structure. Electron diffraction based analysis can be performed during deposition using RHEED as well as low energy electron diffraction [77-84]. RHEED is one of the best *in-situ* surface characterisation methods used to monitor the growth process in real-time. In RHEED an accelerated beam of electrons will hit the sample in a grazing angle and then reflected to the electron fluorescent screen.
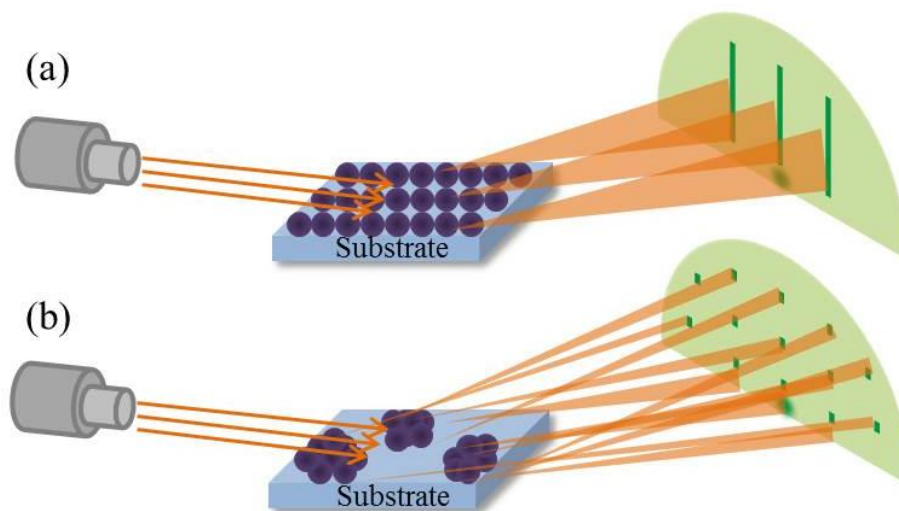
Figure 3.6: Schematics of RHEED pattern from (a) a flat surface and (b) a 3D nucleated surface. We note that the patterns appear on the screens are the superposition of the diffracted electrons wavefunctions.

As the angle of the incoming beam is extremely small, the RHEED probes the first few atomic layers of the surface. The reflected beam diffraction patterns can form dots, small streaks, diffused streaks, or long and sharp streaks. Flat surface form sharp diffraction streaks on the fluorescent screen (**Figure 3.6a**). On the other hand, the island

and 3D growth are identified when the diffraction pattern on the screen shows dots (**Figure 3.6b**).

3.2 *Ex-situ* characterisation techniques

Here we will briefly introduce the *ex-situ* characterisation techniques that have been used for the purpose of this thesis.

3.2.1 Atomic force microscopy

Atomic force microscope (AFM) provides a 3D profile of the surface on a nanometre scale by measuring the force between a sharp probe (diameter < 10 nm) and the film surface at very short distance (0.2-10 nm). The probe is attached to a flexible cantilever and the force between the material surface and the tip will bend the cantilever and these changes will be detected using a beam of laser. The AFM can work in contact, non-contact, and tapping modes. Although the tapping mode is the most commonly used mode, the other modes can be chosen depending on the material surface. In tapping mode, the cantilever is oscillating at its resonance frequency and touches the sample surface at the bottom of its swing. Using this mode high resolution images can be obtained even for the easily damageable materials such as TIs. The AFM can give a good understanding of the surface morphology and the roughness of the top surface [85, 86].

3.2.2 X-ray diffraction

In an X-ray diffraction (XRD) setup, the atomic planes of a crystal cause an incident beam of X-rays to diffract as they leave the crystal, hence forming diffraction pattern that reflects the symmetry of atomic ordering in the crystalline specimen [87-89]. The XRD can give useful information about the orientation of the single crystal, the average growth quality, and the crystallinity of a specimen. However, the signal of an XRD is an average

signal coming from relatively large area of the thin film and the substrate (depending on the film thickness) and cannot give information in on atomic level.

3.2.3   X-Ray absorption spectroscopy

X-ray absorption spectroscopy (XAS) measures the energy-dependence of the X-ray absorption coefficient near the absorption edge of a particular element [90-92]. In XAS a beam of X-rays will be transmitted through the sample. The transmitted intensity exponentially depends on the product of the X-ray absorption coefficient and the thickness of the sample. If the energy of the X-ray is equal to the binding energy of a core electron, the electron will jump to the higher energy level (or to the continuum) and an absorption peak can be seen in the intensity vs. energy plot. Two regions are commonly distinguished in this plot, known as the X-ray absorption near edge structure (XANES) and the extended X-ray absorption fine structure (EXAFS) (**Figure 3.7**).

The XANES is the region close to the absorption edge. This is due to the transition of the photoelectrons to the unoccupied bound states. Therefore, XANES is sensitive to chemical bonding and can features the different oxidation states of the absorbing atom. In order to reveal the oxidation state, the XANES of the sample is compared to standard samples with known oxidation states.
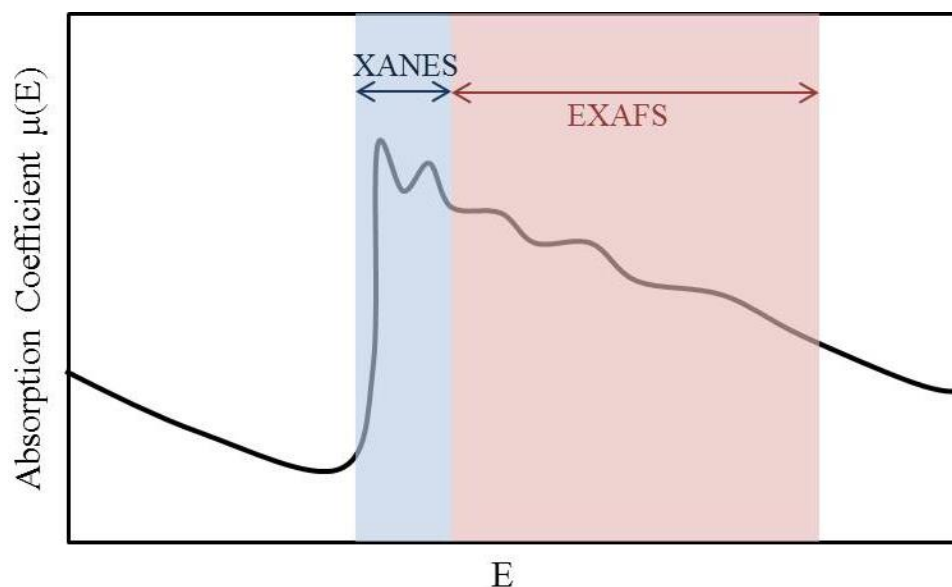
Figure 3.7: XAS absorption coefficient vs. energy plot showing XANES and EXAFS.

For photon energies higher than 30 eV above the absorption edge, known as EXAFS, the photoelectrons are excited to continuum. These waves then travel inside the sample and scatter from the neighbouring atoms and then the superposition of these scattered waves with the original wave will produce modulations. Therefore, the EXAFS depends on the atomic arrangement around the absorber atoms.

The downside of using XAS is similar to that of XRD. The XAS signal is an average signal generated from relatively large volumes. Furthermore, analysing the XAS data (specially the EXAFS) is extremely challenging and requires intensive fittings.

3.3   Conventional cross-sectional specimen preparation for transmission electron microscopy (TEM)

In this section, the conventional method for preparing cross-sectional specimens for TEM is described. In order to prepare thin enough specimens for electron microscopy the thickness of the specimen should be between 30 and 70 nm, such that the specimens become electron transparent. This preparation process happens in three major steps of: (1) cutting and gluing the material for polishing, (2) manually polishing the specimen, and (3) final polishing using Argon ion milling. The final ion milling stage continues till a hole appears inside the sample. The regions close to the hole are the regions of interest for electron microscopy as they are the thinnest parts of the sample. The general rule of thumb of specimen preparation for transmission electron microscopy is that the thinner the better.

In principle the whole specimen preparation process is straightforward; however, it can be extremely challenging in practice. This is due to the fact that, the process starts from a millimetre scale material and then the thickness manually goes down to μm scales. One of the most influential parameters that changes the preparation time is the substrate material. Depending on the substrate material the process can take up to 24 hours of work. Substrates such as Si and Ge require less time ($\sim$ 10 hours) while oxides such as Al_2O_3 need significantly more time. In addition to the fact that the whole process is extremely time consuming, the biggest down side of this preparation technique is that it is destructive. This means that from a 4 mm^2 sample only several μm^2 remains for performing electron microscopy; the rest of the initial material is either destroyed by polishing and cutting or remains thick (regions far away from the hole). Hence, the specimen preparation requires extreme focus specially if the initial material is not enough for multiple sample preparations.

The analysed specimens in this thesis are thin film TIs with either Ge or Al_2O_3 substrates with 10mm×10mm×0.5mm dimensions. The properties of the grown structure may significantly depend on the crystallographic orientation of both the substrates and the film. The TEM images are in projection along certain crystallographic directions so

knowledge of the in-plane orientations of the substrate in needed. These orientations can be investigated by XRD, RHEED, or are provided from the supplier of the substrates.

In other word, for [0001] growth orientation of hexagonal substrates which are frequently used in this thesis, the two mutually perpendicular standard in-plane orientations of [10$\bar{1}$0] and [11$\bar{2}$0] are used (both perpendicular to [0001]). In practice the substrate edges are either [10$\bar{1}$0] or [11$\bar{2}$0]. However, as we discussed in the introduction chapter, the [11$\bar{2}$0] is the preferred direction to observe the QL structure of TIs.

The sample preparation usually starts by cutting the material into pieces using a diamond pen. Then one of the cut pieces will be fixed to a glass slide by using 'crystal bond' for further precise cutting. In order to do so, the sample is placed on the glass slide and the solid 'crystal bond' will be placed on top of the sample; then the glass slide will be placed on top of a hot plate ($\sim$ 80°C) and the solid 'crystal bond' will melt down and cover the sample area. After properly fixing the sample with desired orientation, the glass slide will be taken off from the hot plate and the 'crystal bond' will re-solidify at room temperature in about one minute.

The precise cutting can be achieved using a diamond saw which is placed inside the wafer cutting machine (**Figure 3.8a**). By using the lowest possible speed rotation of diamond and low pressure on the sample, a sharp cut can be achieved. This stage takes approximately 5 minutes for single cut of Si substrate and will become more time consuming if the substrate material changes to harder oxides such as Al_2O_3. When the cutting is finished the next steps is to glue the samples to each other and Si supports and then thinning the specimen using a polishing table shown in **Figure 3.8b**.
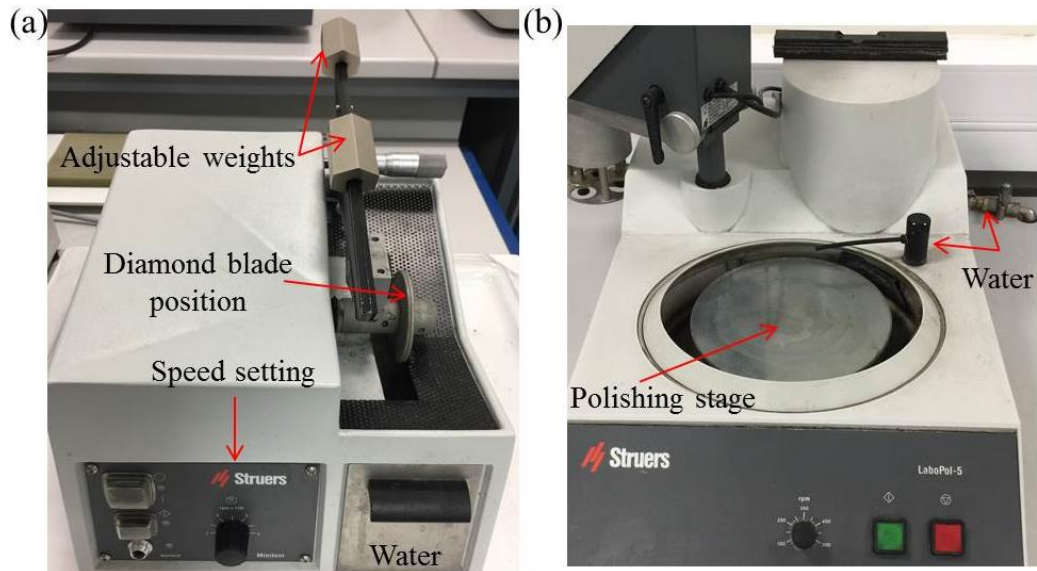
Figure 3.8: (a) Wafer cutting machine and its relevant components. The weights are used to counterbalance the weight of the sample which tunes the cutting speed. The water is used to clean the diamond blade continuously while cutting. (b) The polishing stage. The water is used to continuously clean the polishing pads while the specimen is being polished.

The diamond saw ideally cuts the initial 2mm×2mm sample to two smaller pieces of approximately 1mm×2mm (**Figure 3.9a**). The cut pieces then removed from the glass slide by heating and cleaning in acetone, ethanol, and isopropyl-alcohol (IPA). Each cleaning step should at least take 5 minutes to make sure that there is no residual glue or materials on the surfaces. These cleaning steps should be performed with care in case of TIs due to the weak bonding of these materials with their substrates. Another way of cleaning the cut samples is to put them in acetone and then use an ultrasonic bath. However, such method only works for materials which are strongly bonded to their substrate, and if used for TIs, which are weakly bonded, will leads to completely removing the TI thin film from the substrate.
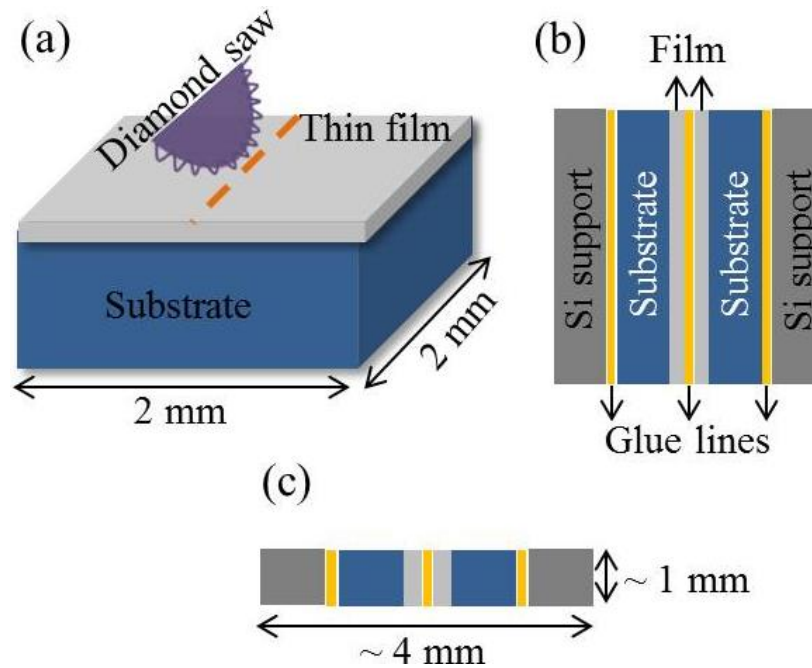
Figure 3.9: (a) Schematic of the specimen in the cutting step. (b) Top view schematic of the specimen ready to be mechanically polished. (c) Side view schematic of the specimen showing the 1 mm thickness of the sample before the mechanical polishing.

The next step is to prepare the glue for gluing the samples together. In order to do so, a 1:10 mixture of hardener and resin in made on a clean glass slide. In contrast to the 'crystal bond', this glue is liquid upon mixing and solidifies in less than 5 minutes when heated up to 100°C. In order to make sure that the glue is in perfect mixing ratio, we put small dot of the glue on a glass slide on top of the heating plate. As we mentioned before, the glue should solidifies in less than 5 minutes and change colour from light orange to dark red. After 5 minutes the glue should be tested using a tooth stick; if the glue fall apart new glue should be made and if the tooth stick breaks while putting pressure on the glue, the glue is in perfect mixture.

Once the glue hardness has been tested, the two 1mm×2mm pieces should be glued together in a way that the thin films face each other. We need to make sure that the glue line is as thin as possible by pressing the pieces together while heating them up. After the glued pieces are solidified on the hot plate, two Si supports are glued to the back of the

samples using the same glue (**Figure 3.9b**). These Si pieces will bring support to the glued sample as well as giving an indication of the sample thickness. The 1 mm thick sample (**Figure 3.9c**) then fixed on a glass slide using the 'crystal bond' and is ready for manual polishing.

The next step is to thin down the sample using diamond polishing pads. For this purpose, the specimen should be polished with 15, 6, 3, and 1 µm pads till a shiny and scratch free interface is observed under the optical microscope. The other side of the sample should also be polished with the same polishing pads. In order to do so, the sample should be place on the hot plate and removed from the 'crystal bond' and placed inside the acetone, ethanol, and IPA. After the cleaning process the polished side of the specimen will be attached to a Cu or Mo TEM grid using the same glue made for gluing the interfaces.

Once the grid is attached and the sample is fixed to the glass slide, polishing of the second side will be started. In this polishing step instead of checking the shininess of the specimen under the optical microscope, the sample should be judged by its thickness. The polishing starts with 15 µm pad and then the pad should be changed to 6 µm when the specimen thickness reaches 175 µm. When the thickness of the specimen becomes 135 µm, the polishing pad should be changed to 3 µm and polishing should be continued till reaching 100 µm of thickness. The last mechanical polishing then carried out using 1 µm pads. However, checking the thickness is not recommended at this stage as the thickness measurement itself can cause damage to the specimen. At this point the specimen polishing should be continued till the colour of the Si supports turn dark orange (best case light yellow) under the optical microscope (in transmission mode) (**Figure 3.10a**). Once the polishing is finished, the materials sticking outside of the Cu or Mo grid should be cut using a diamond pen, and the sample should be taken out of the 'crystal bond' and cleaned before Ar ion milling.
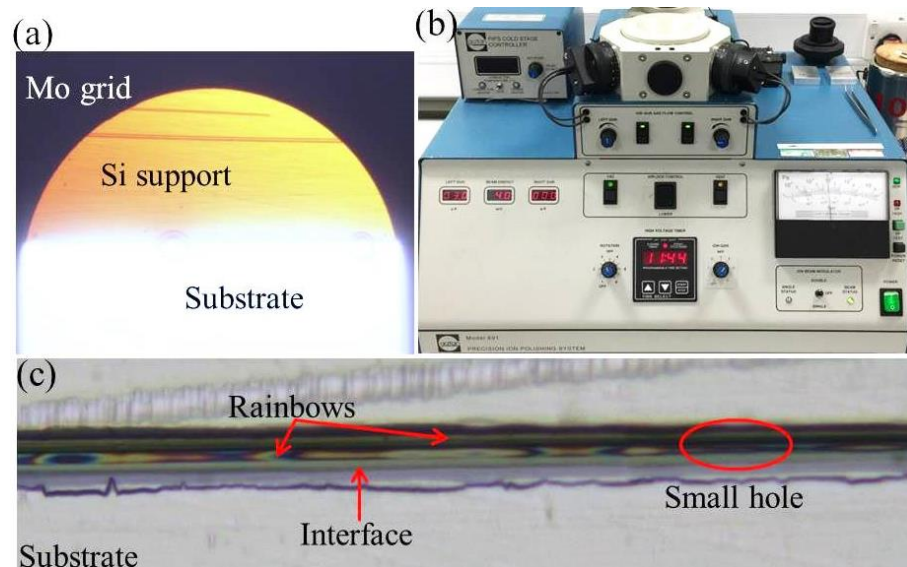
Figure 3.10: (a) Yellow colour of the Si support under the optical microscope in transmission mode. (b) The ion milling machine. (c) The rainbows and the hole at the interface glue line from Ar ion milling.

Once the cleaning is finished, the sample is loaded to the precision ion milling system (PIPS) holder and is ready to start the last thinning step. The PIPS can sputter materials using up to 6 keV of acceleration voltage. For the purpose of this thesis the PIPS were operated using ~ 3.5 keV of acceleration voltage. In order to achieve a homogeneous milling, right gun and the left gun were tilted to $\sim$ +6 and $\sim$ -6 degrees, respectively. The beams will hit the centre of the specimen from top and bottom and the hole should be observed in the same region. The most pronounce sign of sample being close to the stage that a hole appears inside the sample, is the thickness fringes (rainbow colours) inside the glue line. When the rainbow is observed the time steps should be reduced as the hole shall appear in a few minutes. After a few minutes we can see a hole appeared inside the glue line and the PIPSing should be stopped (**Figure 3.10c**).

One of the other downsides of the conventional sample preparation is that the whole procedure works easily if the bonding between the thin film and the substrate is strong. However, most of the samples used for this thesis are weakly bonded to their substrate making sample preparation extremely hard and even impossible for some of the cases. Hence, in order to solve these problems we started using FIB machines for cross-sectional specimen preparation.

3.4   Focused ion beam (FIB) for cross-sectional specimen preparation

In this section, the concept and the use of FIB instrument for preparing cross-sectional specimens for TEM is described. This preparation process happens in three major steps of: (1) milling the materials out and making the lamella, (2) lifting out the lamella, and (3) thinning down the specimen to electron transparency. The FIB machines are usually combined with scanning electron microscope (SEM); in which case the SEM column is used for imaging purposes. In order to understand the cross-sectional TEM preparation steps, a general knowledge of the instrument itself is needed.

3.4.1   Ion beam sources

The FIB instruments are generally divided to three types.   The main difference between these three types of FIB instruments coming from the ion sources which is used in their gun. The three different ion sources are the gas field ion source (GFIS), liquid metal ion source (LMIS) and plasma ion gun (PIG). The most common source type which is used in FIB instruments is the LMIS. The LMI sources usually use a liquid gallium (Ga) source. Using Ga in LMI sources is preferred because the high mass of Ga allows a reasonable high sputtering rate with a good resolution [93]. Furthermore, the Ga source has a long and stable lifetime ($\sim$ 1500 hours) with a resolution down to a few nm.

3.4.1.1   Liquid metal ion source structure

By far the most commonly used ion source in FIB instruments is the Ga LMIS. There are two important parts in the LMIS structure which are the source species and the needle (**Figure 3.11**). There are five important properties that need to be considered in order to choose the ion species:

- Low melting temperature
- Low vapour pressure at the melting temperature
- No chemically related effects with the needle

- High vacuum compatibility

- High mass for sputtering

The Ga source can offer a beam current from almost 1 pA to more than 50 nA, with very stable flux and has a low vapour pressure and low melting point (29.67 °C). Furthermore, the relatively high atomic number of Ga (Z=31) and the fact that it has low chemical reactivity will cause high sputtering rate with minimum damage.
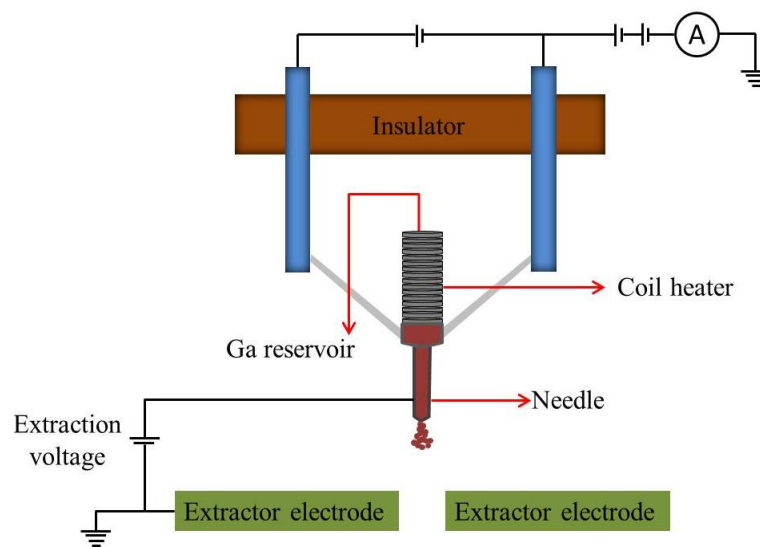
Figure 3.11: Sketch of an LMIS.

There are two major properties that should be considered in order to choose a suitable needle:

- Being hair pin type material such as W, nickel, tantalum, etc.

- Having low chemical interaction to the Ga.

W shows all the above mentioned properties as well as having high melting temperature (3422 °C) which makes it the most commonly used material for an LMIS needle.

The LMIS is approximately 1.5 cm in diameter and can be plugged to a low voltage power supply. The applied current will cause the Ga to melt and slowly flow to the tip. As with any other ion source, the successful operation depends on the geometry of the tip. However, this is not the case in LMIS as the Ga does not react with the tip and only wets it. The key to the LMIS operation is the formation of the Taylor-cone [94], which is effect of interactions between the W tip and the extractor electrodes. The electric field between the tip and the extractor will form a conical surface of Ga at the end of the W tip (**Figure 3.12**).
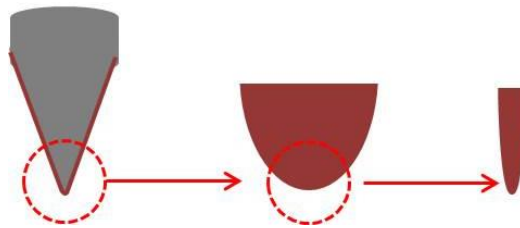
Figure 3.12: Formation of Taylor-cone at the tip of the W needle.

The electric field from the extractor electrodes attempts to pull the Ga ions from the W tip, but the surface tension of the liquid Ga formed on the tip will attempt to repulse. When the two forces are in balance, a cone shape begins to form with convex sides and a rounded tip with a radius of less than 10 nm. Upon a slight increase of the extractor voltage a stream of Ga ions will be emitted from the end of the cone and accelerated into the column.

3.4.1.2   Mass filter and FIB column structure

In order to collimate the extracted Ga ion beam, series of electrostatic lenses and blanking apertures have been used in FIB instruments. The use of electrostatic lenses is preferred over the electromagnetic lenses due to the relation between the strength of the electrostatic lens and the charge/mass ratio of the particles. One of the most important parts of a FIB instrument is the $E \times B$ mass filter (E and B are the electric and

magnetic fields, respectively) [95]. The $E \times B$ mass filter consists of two electrostatic plates and two magnet pole pieces sitting 90 degrees apart from each other, **Figure 3.13**.
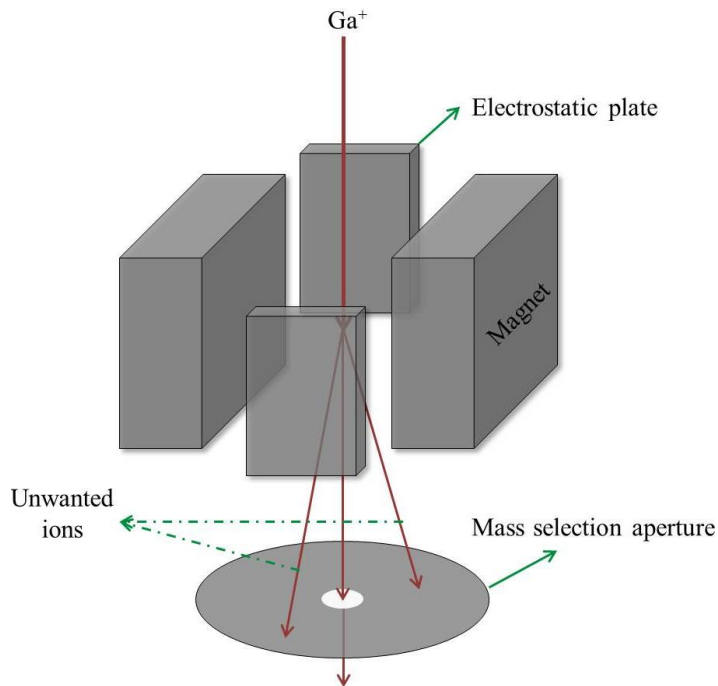
Figure 3.13: Schematic of the $E \times B$ mass filter used in FIB instruments.

The desired mass of Ga ions can be achieved by using the appropriate E, B, and selective aperture size. Generally speaking, as the diameter of the aperture reduces better resolution and milling precision can be achieved.

When the Ga ions pass the various lenses, filters, apertures and deflectors, they eventually hit the sample surface with specific energy and current. **Figure 3.14** shows a cross-sectional sketch of the path of Ga ions inside the FIB instrument. When the ions hit the sample surface they lose their kinetic energy through different types of interactions. This energy transfer from Ga ions to the surface atoms can cause many different phenomena such as:

- Atomic sputtering.
- Ion reflection and backscattering.
- Secondary electrons, auger electrons, and x-rays emission.
- Sample heating and damage e.g. amorphization and point defects etc.

- Ga ion implantations.
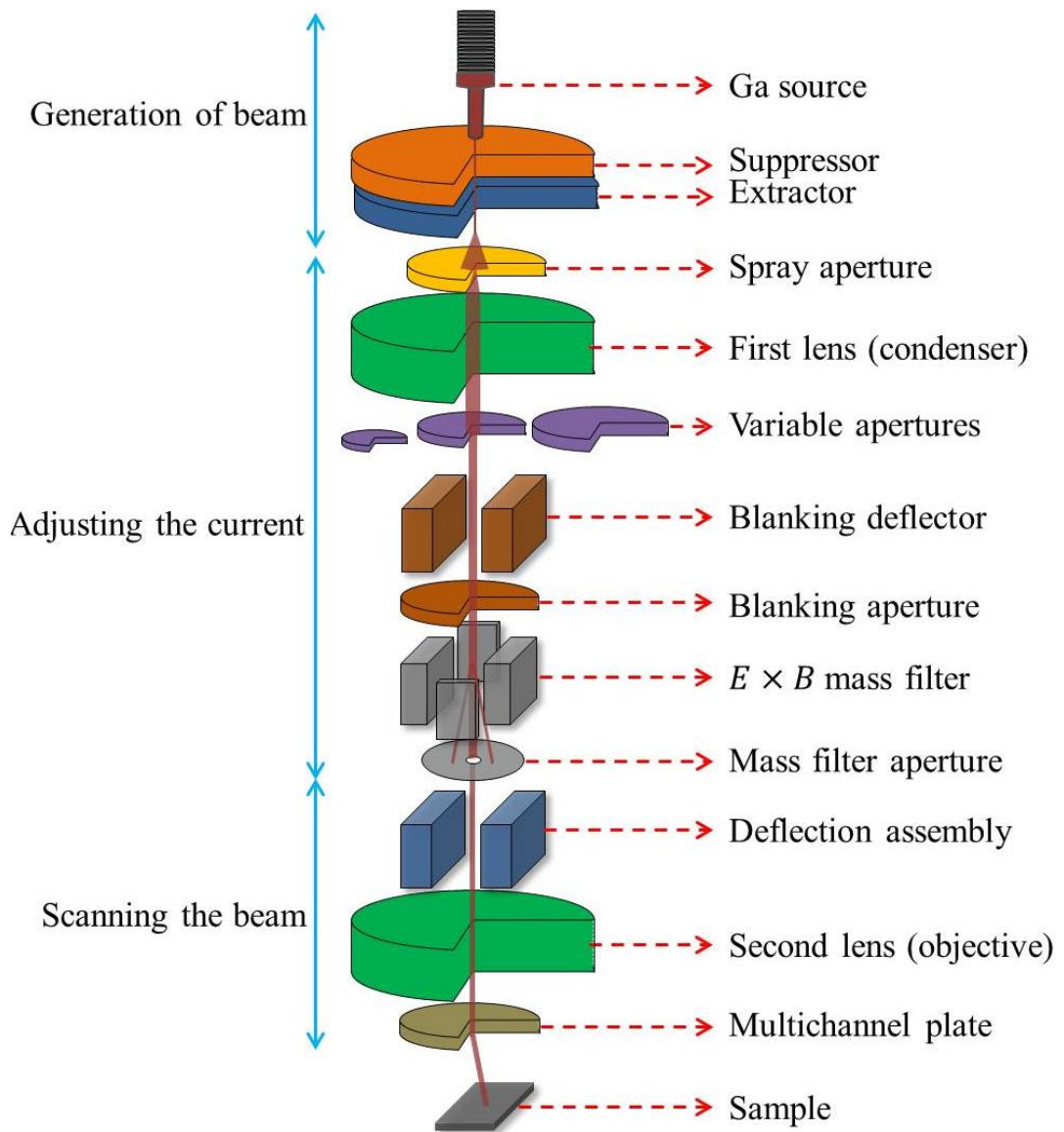
Figure 3.14: Schematic cross-section of the FIB instrument.

The Ga ion implantation and the sample damage are the two downsides of using FIB. However, there are two major ways to prevent these problems from happening. The first way of protecting the sample surface is to cover the region of interest with thick ($\sim$ 3µm) sacrificial layers and the second way is to use lower beam energies. The protective layers can be deposited on the sample surface by both electrons (SEM) and ions (FIB) using a gas injection system (GIS). In order to deposit materials on the sample surface, crucibles containing metalorganic platinum ($C_5H_4CH_3Pt(CH_3)_3$), carbon ($C_{10}H_8$), or

tungsten ($W(CO)_6$) can be heated up (< 100 °C) and the evaporated metalorganic materials can be directed to the sample surface via a needle tube. When the deposition gas locally reaches the sample surface the secondary electrons crack the gas molecules and deposit the desired species on the sample surface. Furthermore, the GIS can be also used for attaching the lamella to the lift-out needle as well as attaching it to the TEM grid.

3.4.2   FIB cross-sectional specimen preparation

Now we focus on the three step process of cross-sectional specimen preparation. As we mentioned before the first step is to mill the materials out and making the lamella. Prior to putting the specimen inside the FIB machine, a thin (10 nm) layer of C or Pt can be evaporated on the whole specimen to protect the sample from damage as well as reducing the charging effect caused by electron beam. Furthermore, small silver (Ag) contact from the sample surface to the sample stub can be made using Ag paint to further minimise the charging effect. After placing the sample and the TEM FIB grid inside the FIB chamber and venting the system, the ion source can be heated up to liquefy the Ga reservoir. When both sources are ready to be used (electron and ion guns pressure $\sim 10^{-5}$ Pa and chamber pressure $\sim 10^{-4}$ Pa), the sample should be moved to the eucentric height which depends on the initial positions of the lenses. In order to start the specimen preparation, a flat area close to a small particle should be found using the electron beam. The particle can be useful for focusing and checking the stigmatism of the beam in given energies and currents. Then the sample should be precisely rotated to make sure that the cross-sectional view is close to the desired zone axis. In order to protect the sample from Ga ion implantation and damage a 15×2×0.5 μm sacrificial layer of Pt should be deposited by the electron beam using 5 keV of acceleration voltage with 11 nA of current. Various beam energies and currents can be used for each deposition or milling steps, however here we state the values that are repeatedly used for the purpose of this thesis. After the Pt deposition using the electron beam a thicker layer (4 μm) of Pt can be deposited using the Ga ions with 8 keV of acceleration voltage with 0.66 nA of current (**Figure 3.15a**).
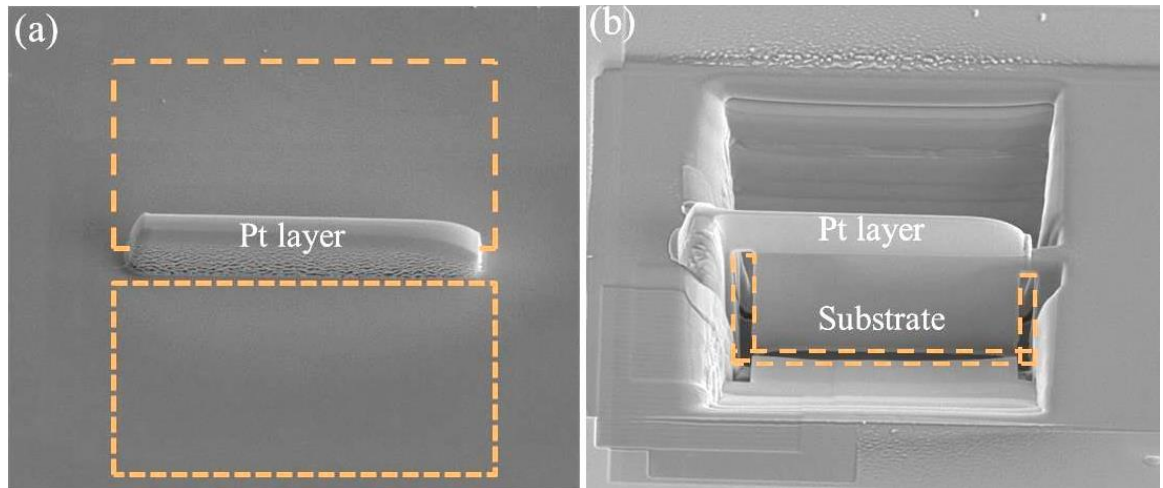
Figure 3.15: (a) Shows the deposited Pt on the sample surface. The orange dashed lines show the regions that the trenches are going to be sputtered out. (b) Shows the region of interest after the trenches have been milled out. The orange dashed lines show the regions of the U cut before the lift-out.

Next step is to mill the materials out from both sides of the Pt deposited area. For this step two rectangles should be placed on both sides of the Pt area as shown with orange dashed lines in **Figure 3.15a**. In order to mill these trenches out in a way that the bottom of the trenches be thinner than the top Pt layer, the sample can be tilted for ±2 degrees (from 52°). Then using an acceleration voltage of 30 keV and a beam current of 6.5 nA, the ion beam cuts out the trenches. To make sure that the materials are completely removed from the trenches we will repeat the last step several times depending on the substrate milling rate (e.g. the milling rate of Si and Ge are much faster than Al_2O_3). When the cutting of the trenches is finished the thickness of the lamella will be approximately 1.5 µm (**Figure 3.15b**). If the thickness of the lamella goes less than 1 µm, the lift-out becomes extremely hard and in some cases impossible. In order to make the lamella ready for the lift-out procedure a U shape shall be cut out from the sample (**Figure 3.15b**). In order to do so, an acceleration voltage of 30 keV with beam current of 2.8 nA can be used.

When the U cut is finished, the lift-out needle shall be inserted to the chamber and slowly placed on top of the Pt layer. The needle should only touch the surface of the Pt layer without putting any extra pressure on the lamella. If any pressure is placed on the lamella, the lamella and the needle will crash to the bottom of the trenches after the full cut out and the sample will be unreachable or fly into the vacuum pumps. In order to attach the lift-out needle to the lamella the GIS should be inserted to the chamber and using 8 keV of acceleration voltage and 0.66 nA of current we deposit 1 µm Pt at the touching point and the needle will be attached to the lamella (**Figure 3.16a**).
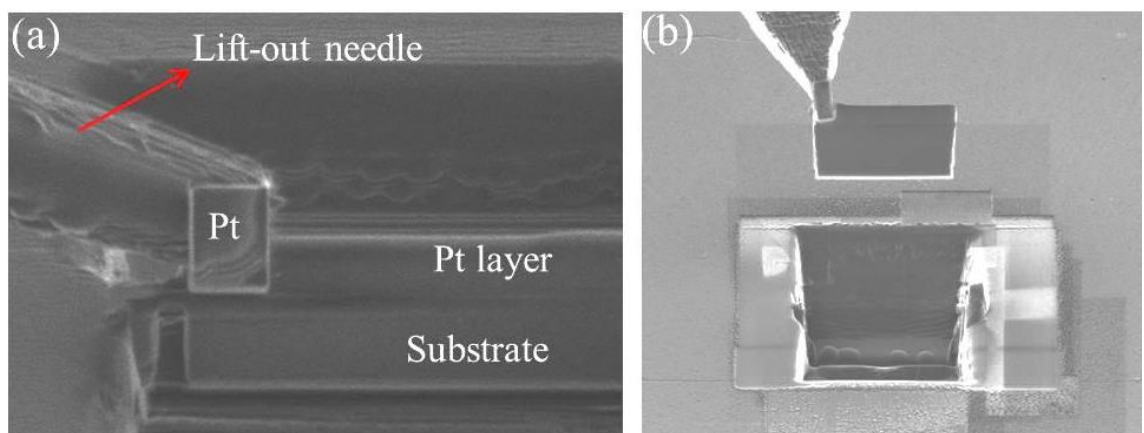
Figure 3.16: (a) Shows the deposited Pt to fix the lamella to the lift-out needle. (b) Shows the lamella after the full cut out.

When the lift-out needle is attached, the rest of the U shape shall be cut in order to completely free the lamella from the sample. To cut the rest of the U shape we change the ion beam energy to 16 keV without changing the current. This is due to the fact that changing the beam current will mechanically change the aperture and causes small amount of vibrations. These vibrations can move the needle and crash the lamella to the sample. After completely cutting the U shape out, the lamella can be moved out by changing the height of the needle as shown in **Figure 3.16b**, and the lift-out and GIS needles can be retracted.

The next step is to attach the lamella to the TEM FIB grid. Once the TEM FIB grid location has been found and moved to the eucentric height, the lift-out needle can be inserted. After carefully moving the lamella close to the one of the posts on the TEM FIB grid, the GIS needle shall be inserted. Then the lamella can be completely touching the grid post and by using 8 keV of acceleration voltage and 0.66 nA of current the lamella can be attached to the side of the grid post (**Figure 3.17a**).
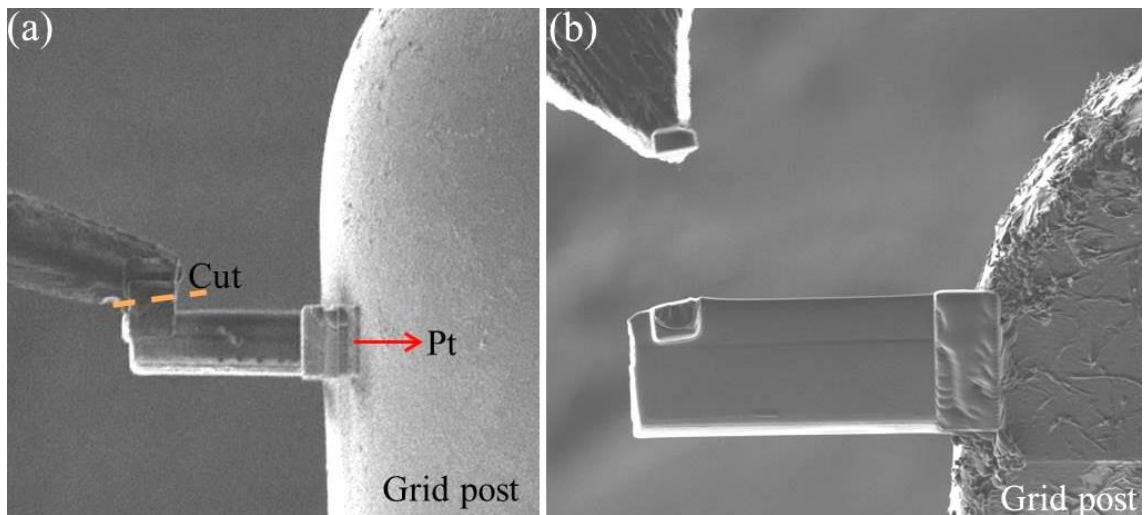
Figure 3.17: (a) Show the deposited Pt which fixed the lamella to the grid as well as the cutting point for removing the needle. (b) Shows the lamella fixed to the grid and the cut outed lift-out needle.

Once the lamella is fixed to the grid, by using 30 keV of acceleration voltage and 2.8 nA the lift-out needle can be cut and separated from the lamella as shown in **Figure 3.17b**. We note that at this point we only change the acceleration voltage. The 0.66 nA current value will be changed to 2.8 nA because it is the pre-set values. This pre-set value will not change the mechanical aperture inside the FIB which means no vibrations will be made during this change.

Now we focus on the next step which is the thinning procedure. In order to do so, the sample should be tilted to 52° which is the position in which the ion beam is parallel and the electron beam is looking down on the lamella side planes (top view and side view). In order to thin down the specimen, five steps with different beam energies, beam

currents, and beam angles should be used. For each step the thickness of the sample should be reduced and as the sample goes thinner and thinner the thinning length should become smaller and smaller to avoid bending of the lamella (**Figure 3.18a**).

For the first step the sample will be tilted for ±2° to 54 and 50 degrees and an acceleration voltage of 16 keV with a beam current of 0.47 nA can be used. If the milling speed of the substrate is slow each step shall be repeated until the desired thickness is achieved. After this step the thickness of the lamella should be reduced to 1 μm. For the second step the sample should be tilted for ±1.5° and an acceleration voltage of 16 keV with a beam current of 0.13 nA is used. In this stage the thickness of the lamella should reach approximately 0.6 μm. After achieving the desired thickness, the beam current is reduced to 45 pA and the step shall be repeated to reduce the thickness to 0.4 μm. For the third stage the lamella will be tilted for ±1° and an acceleration voltage of 8 keV with a beam current of 21 pA shall be used. At the end of the third stage the lamella shall reach the thickness of 0.25 μm and the Pt layer and the specimen shall become brighter. In the fourth step the lamella will be tilted for ±0.5° and an acceleration voltage of 5 keV and a beam current of 16 pA are used. In this step the thickness should be reduced to approximately 100 nm and the lamella should become more and more transparent. **Figure 3.18b** shows the side view of the lamella after performing the aforementioned steps.

(a) Top view

±7°   ±0.5° ±1° ±1.5°   ±2°   Post

(b) Side view

Interface   Post
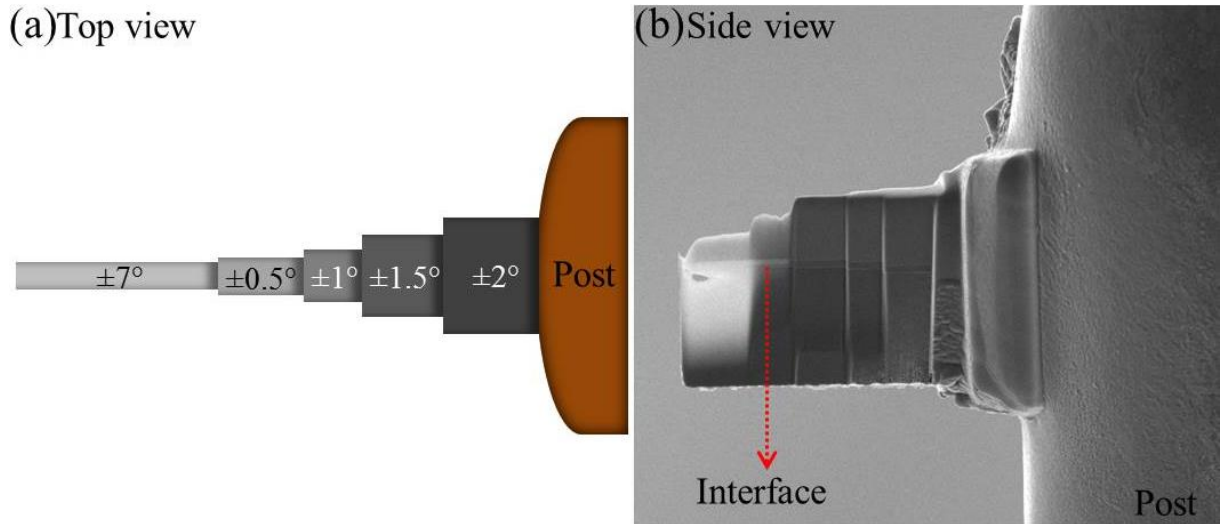
Figure 3.18: (a) Shows the schematic top view of the thinning steps. (b) Shows a side view SEM image of the thinning steps.

For the last step the specimen should be tilted to 45° (±7°) and an acceleration voltage of 2 keV with a beam current of 10 pA should be used to completely clean and thin down the lamella. After this step the thickness of the specimen should be decreased to ∼ 50 nm. Towards the end of the cleaning steps a small hole may appear inside the substrate which indicates the achieving desired thickness of the sample (**Figure 3.18b**). While the appearance of the hole can be a good sign, the hole usually can locally bend the specimen and makes the orienting of specimen on the zone axis rather challenging.

Although the cross-sectional specimen preparation using FIB is usually better than the conventional method in all aspects, it needs more learning time and care; for example, in FIB preparation of organic or other beam sensitive materials even lower energies should be used to avoid beam damage.

3.5   Electron microscopy

Electron microscopy is the most powerful and commonly used technique for characterization of materials at atomic scale. Historically the TEM was developed because of the limited imaging resolution of the conventional light microscopes. The difference comes from the wavelength of the used sources which in this case are light and electrons. In 1927 just 2 years after the theoretical prediction of the wave properties of electrons by de Broglie [96], two research groups, Davisson and Germer [82] and Thomson and Reid, independently carried out their classic electron diffraction experiment which confirmed the wave nature of electrons [1].

There are two main reasons for preferring the electron microscopes over the optical or visible-light microscopes (VLM). The first reason is that the electrons can be easily and efficiently manipulated by the lenses inside the microscope column which is due to the charge of the electrons. The second reason is the very small wavelengths of electrons which gives a better resolution in contrast to the VLM.

The resolution of microscopes mostly depends on the wavelength of the source. The de Broglie formula (Eq. (3.2)) is the equation which enables us to compute the wavelength of the electrons depending on their energy [96].

$$\lambda = \frac{h}{p} \tag{3.2}$$

where h is the Plank's constant and p momentum. Taking into account the kinetic energy of the electrons leaving the gun and accelerating in potential difference (V), the relativistic electron wavelength can be written as:

$$\lambda = \frac{h}{\left[2m_0 eV \left(1 + \frac{eV}{2m_0 c^2} \right) \right]^{1/2}} \tag{3.3}$$

A simpler non-relativistic approach will give similar electron wavelength equation as the Eq. (3.3) without the relativistic part of $\left(1 + \frac{eV}{2m_0 c^2} \right)$; however the relativistic effects cannot be ignored at energies > 100 KeV because the velocity of the electrons becomes greater than half of the speed of light.

As it may be obvious from the name 'transmission electron microscopy', the image in an electron microscope forms using the transmitted electrons. In order for electrons to transmit through a sample, a very thin specimen ($\sim < 80$ nm) is needed. Thinning the specimens to the required thickness for atomic resolution imaging or spectroscopy can be extremely challenging. One way of looking at thicker specimens is to use electron microscopes with high acceleration voltage (200 keV or 300 keV). One of the downsides of using electron microscopes with such high acceleration voltages is the beam damage that can destroy the beam sensitive materials. However, the specimens used in this thesis are beam resistant and are carefully made by the conventional and FIB sample preparation techniques for high resolution electron microscopy and spectroscopy.

The electron microscopes are expensive and complex machines. In order to get atomic resolution imaging these machines use many functional parts such as lenses, apertures, etc. Generally speaking an electron microscope is a machine that generates high energy electrons (typically 100 – 200 KeV), has complex series of electron lenses to focus the beam on the specimen, and uses another set of lenses to magnify and form an image after electron being transmitted from the specimen. The electrons generated from the gun will be deflected and focused many times inside the microscope column using electromagnetic lenses and eventually will be detected either by a charge-coupled-device (CCD) camera or using an old style fluorescent viewing screen. One of the most important parts of any electron microscope are the electromagnetic lenses.

3.5.1   Lenses in an electron microscope

Similar to a VLM, the lenses in TEM control all the basic operational functions. A typical lens in a VLM focuses the beam of light due to the refraction of light at the lens (**Figure 3.19a**). On the other hand, in an electromagnetic lens the focusing is achieved using a strong magnetic field which is generated by the electric current that flows in the Cu-coils (**Figure 3.19b**). In contrast to the VLM, where the strength of the focusing is fixed and defined by the glass lens, in an electron microscope the position of the lenses are fixed but the strength of the lens can be changed by changing the current flows in the Cu-coil.
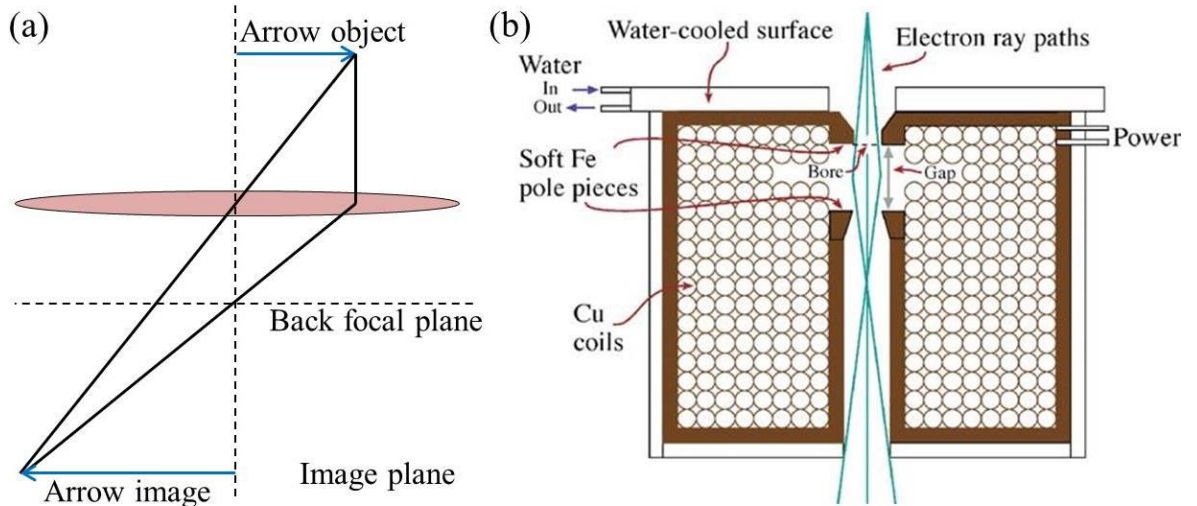
Figure 3.19: (a) Schematic of a conventional optical lens. (b) Cross-sectional schematic diagram of a magnetic lens [1].

Now we focus on the principals of how the electromagnetic lenses work. When the electrons enter an electromagnetic field introduced by the lenses they experience the Lorentz force (Eq. (2.1)). The radial distance of the electrons from optic axis can be found using the relativistic force acting on an electron entering a uniform magnetic field with an angle of 90°:

$$r = \frac{\left[2m_0 E \left(1 + \frac{E}{2E_0}\right)\right]^{1/2}}{eB} \tag{3.4}$$

However, in order to find the above radial distance an oversimplification has been made. If the angle between the incoming electrons and the magnetic field set to 90° then the electrons will travel straight down the optic axis without even noticing the lens. The actual lens effect comes from the deviation from the 90° angle. Therefore, the electron velocity should be divided to parallel and perpendicular components (with respect to the magnetic field). The parallel component which is in z direction results in motion parallel to the optical axis, while the perpendicular component produce a circular motion with a radius given by Eq. (3.4). From the various relationships the path of electrons through the

lens can be calculated. The most important equations are for the electrons travelling near the optic axis which are called paraxial equations.

Although the magnetic field inside the electromagnetic lenses provides a controllable mechanism for changing the trajectories of the electrons, the electromagnetic lenses are much more imperfect than the optical lenses. The challenge comes from the point that creating a magnetic field that acts in the same way on all the electrons is extremely difficult. The spherical aberrations, chromatic aberrations and astigmatism are the most important factors to be considered to achieve even higher resolutions [1].

(a) $C_s > 0$ (b) $C_s = 0$
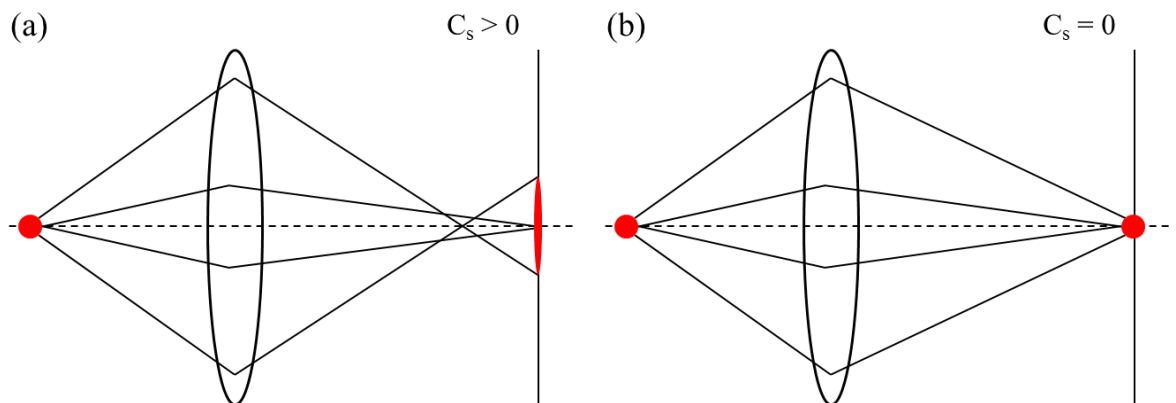
Figure 3.20: (a) and (b) show the schematics of imaging a point object using an electromagnetic lens with and without having spherical aberration, respectively.

The spherical aberration is the inability of the electromagnetic lens to act in the same way on both the off-axis and paraxial electrons [1]. In other words the electrons that are coming close to the optical axis would be focused differently to ones coming with higher angle, far from optical axis. This causes formation of a blurred disk instead of the original point (**Figure 3.20**).

Nowadays, many microscopes have C_s correctors (C_s is the spherical aberrations coefficient) which are computer controlled complex systems of lenses (quadrupole, hexapoles, and octapoles). The correctors are designed to optimise the effect of the

electromagnets on all the electrons so that any electron whether it travels under paraxial condition or far away from the optical axis will be focused in the same point. Microscopes with C_s correctors have significantly improved spatial resolution. We note that one of the microscopes used in this work has been reached the spatial resolution value of 0.8 Å (at 100 keV) operating on the specimens investigated in **chapter 7**.

Another type of aberration is the chromatic aberration which is caused by the difference in the electrons wavelength in the microscope. Such difference appears due to the energy spread of the electrons coming out of the electron gun. The electrons with lower energy will be deflected more and using the same argument as before, they will form a blurred disk on the imaging plane instead of the original (source) point. Modern microscopes have better electron guns (based on field emission) which can produce beam of electrons with an energy spread of ~0.3 eV. Recently, further improvement is achieved by using monochromators which can provide a beam of electrons with energy spread of ~0.015 eV. Besides the energy dispersion due to the source, chromatic aberration can also happen due to energy losses of electrons after their interaction with the specimen. This can be mostly solved by using energy filtering.

Astigmatism is another imperfection which affects the spatial resolution of the microscope. This effect arises due to inhomogeneities of the magnetic fields around the microscope optical axis. Main contributors of the astigmatism are the lenses, but some might also appear due to the charged accumulation on the microscope apertures when they are not perfectly cleaned. This imperfection can be corrected using the stigmator coils generating small compensating magnetic fields and can be controlled manually using stigmator knobs.

3.5.2   Electrons interacting with matter

Electrons interact with matter of all kinds due to their charge. This means electrons will interact and will be involved in many energy transfer mechanism in samples (**Figure 3.31**).
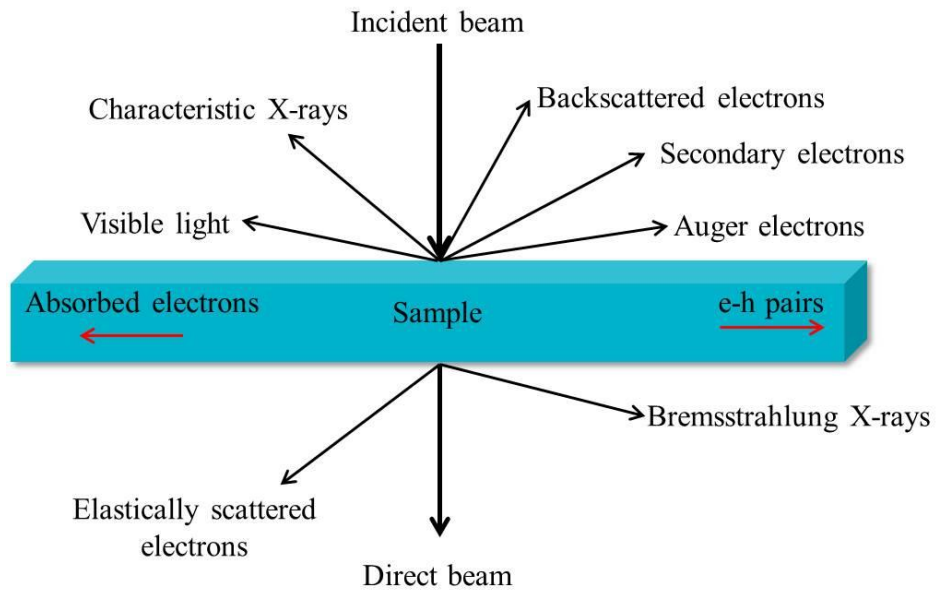
Figure 3.21: Schematic diagram of the main signals generated as an electron beam interacts with sample.

The interactions are classified into two different types, namely elastic and inelastic interactions. In elastic interactions, no energy is transferred from the electron to the sample. As a result, the electron leaving the sample still has its original energy. Elastic scattering happens if the electron is deflected from its path by Coulomb interaction with the positive potential inside the electron cloud. In this case, the primary electron loses no energy or only a negligible amount of energy. These signals are mainly used in TEM and electron diffraction methods.

If energy is transferred from the incident electrons to the sample, then the electron energy of the electron after interaction with the sample is consequently reduced and this is called inelastic interaction. The energy transferred to the specimen can cause generation of different signals such as X-rays (characteristic and Bremsstrahlung), Auger or secondary electrons, plasmons, phonons, UV quanta or cathodoluminescence.

When an electron traveling through the electron cloud of an atom transfers a part of its energy to an electron of any localised atom and if the transferred energy be sufficient, an electron from the localised atom will be ejected to the vacuum. To achieve the energetically favorable ground state again, an electron drops down from a higher level to fill the vacancy. By this process, the atom can relax but the excess energy has to

be given away. Getting rid of the additional energy can generate a characteristic X-ray or if the released photon is absorbed by an outer shell electron and that electron gets ejected out of the atom an Auger electron will be generated.

An electron passing an atom within its electron cloud may also be decelerated by the Coulomb force of the nucleus. This inelastic interaction generates X-rays that can carry any amount of energy up to that of the incident beam. These generated X-rays are called Bremsstrahlung X-rays.

Phonons are collective oscillations of the atoms in a crystal lattice. If an incident electron hits an atom and transfers a part of its energy to it, this atom begins to vibrate. Since all atoms are linked together in a crystal, the vibration of an atom is felt by others that also start to vibrate. By this process, the absorbed energy is distributed over a large volume. The resulting collective vibrations are equivalent to heating up the specimen. Phonons can be generated as the main effect or as a by-product of any inelastic electron-matter interaction.

If the electron beam passes through an assembly of free electrons, like in the conduction band of metals, the transfer of energy can induce collective oscillations inside the electron gas that are called plasmons. They can occur in any material with free or weakly bound electrons and are the most frequent inelastic interaction in metals.

From the spectroscopic point of view, the energy dispersive X-ray (EDX) chemical mapping can be performed using characteristic X-rays both in a TEM and a SEM. Furthermore, the EELS chemical analysis can be performed using the inelastically scattered electrons in a TEM.

3.5.3   Imaging and diffraction in a TEM

In this section, the four basic TEM methods of selected area electron diffraction (SAED), high resolution TEM (HRTEM), bright field TEM (BF-TEM), and the dark field TEM (DF-TEM) will be explained. All these modes can provide particular information about the sample under investigation.

The system of lenses between the electron gun and the specimen is called illumination system [1]. These lenses collect the electrons coming out of the electron gun and 'focus' them on the specimen either as a parallel beam (required for SAED) or convergent beam (as it is the case in scanning TEM (STEM) mode). Once the electrons have interacted with the specimen, another complex system of lenses is used to record either an image or a SAED. Although the actual TEM has more complex lenses, a simplified schematic of the microscope in diffraction and imaging modes is shown in **Figure 3.22**. In a simple approximation, there are three sets of objective, intermediate and projector lenses used in a TEM below the sample.

In the diffraction mode, **Figure 3.22a**, the strength of the intermediate lens is chosen so that it takes the back focal plane (of the objective lens) as its object, while in the imaging mode ,**Figure 3.22b**, the image plane (of the objective lens) acts as an object for the intermediate lens [95]. First let consider the diffraction mode (**Figure 3.22a**). In the back focal plane of the objective lens we have the diffraction pattern of the illuminated area of the specimen. In crystalline samples, this diffraction pattern will be seen as sharp spots which are due to the scattering of the electron from the corresponding atomic planes. This point is then imaged by the intermediate lens into a point at the second intermediate image plane. This image is then magnified by the projector lens and focused on the screen. Hence this setup gives a magnified image of the back focal plane of the objective lens. In many cases, it is proving very useful to acquire a SAED pattern. This is due to the fact that we can choose the area of which we want to from a diffraction pattern from. In order to achieve this, we insert a SAED aperture in the first intermediate image plane, as shown in **Figure 3.22a**. We need to note that since in this plane an image of the specimen is formed, by moving the aperture we can choose only the area which we are interested in. Hence by using the SAED aperture contributions from the rest of the sample can be avoided.
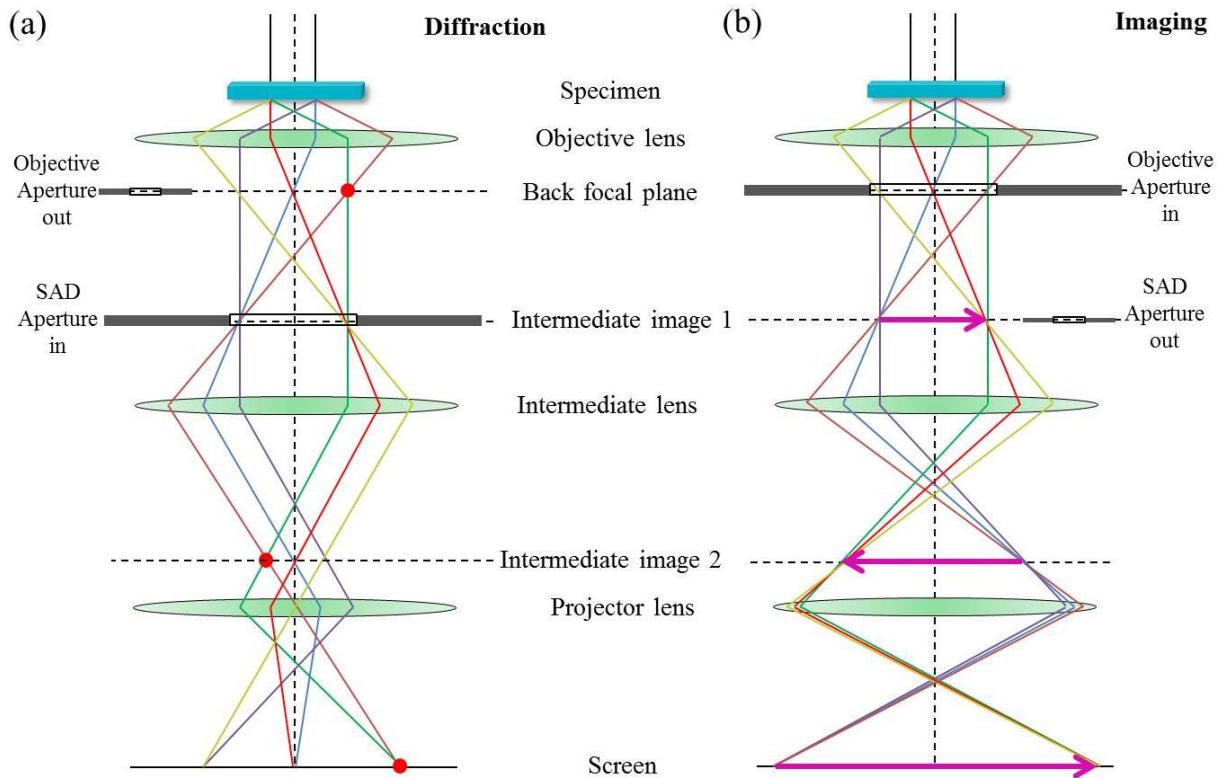
Figure 3.22: (a) and (b) show schematics of the lenses and apertures in diffraction and imaging mode, respectively.

In the imaging mode, **Figure 3.22b**, the intermediate lens strength is chosen so that it takes the image at the first image plane as its object, and then this image is further magnified by the projector lens [1]. There is no need of using the SAED aperture in this mode, however sometimes it is very useful to insert the objective aperture. The objective aperture is at the back focal plane of the objective lens (**Figure 3.22b**) and has the purpose to select desired area of the diffraction pattern. There are two general imaging modes depending on the position of this aperture. If we put the aperture at the centre (central beam) it will transmit only the central spot from the diffraction pattern and the final image on the screen in such case is called a bright field image. We can also choose another i.e. non-central diffraction spot, in which case we form a so called dark field image (**Figure 3.23**) [1].
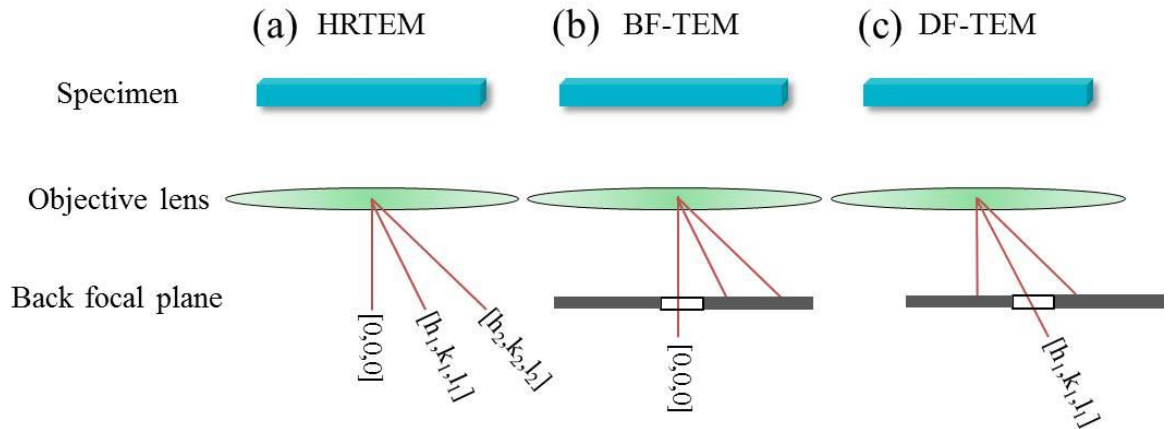
Figure 3.23: (a), (b), and (c) Show the schematics of HRTEM, BF-TEM, and DF-TEM.

By choosing the central unscattered beam with the objective aperture we get a BF image, while if we move the aperture so that it transmits the $[h_1, k_1, l_1]$ diffraction spot we get the corresponding DF image. The BF and DF-TEM images can give extremely useful information about the specimen structure, since the contrast (diffraction contrast) in these images depends on the scattering properties of given specimen area. For instance, if we perform DF imaging on a polycrystalline specimen, the bright regions which will show up in the image are the domains which are oriented in a way to satisfy the Bragg condition.

The HRTEM is the third mode that the TEM can be operating in. In this case, we remove the objective aperture so that the whole transmitted diffraction pattern can pass from the back focal plane. In this mode, we get much more information about the specimen since we have allowed all diffraction spots to participate in the resultant image on the screen. Hence, the HRTEM image is actually a complicated interference pattern [1]. This imaging mode can give us some useful information about the specimen e.g. lattice fringes. The HRTEM contrast for crystals is a complex periodic pattern and the atomic columns cannot be straightforwardly determined from such patterns since the contrast depends on the imaging conditions and specimen thickness.

To better understand and to be able to interpret the images in HRTEM mode, we need to develop atomistic models and perform image simulations. Most of the electron

microscopy images in this thesis are HAADF-STEM images. As the contrast in HAADF-STEM images is more straightforward to be interpreted we can extract much more directly interpretable information from the specimen. TEM imaging in this thesis is used to obtain overall information such as film thickness, but not for analysis of the specimen structure at the atomic level, where the HAADF-STEM imaging is more suitable.

3.5.4   Scanning transmission electron microscopy

The STEM technique is very frequently used in this thesis to extract information about the atomic structure of the film and heterostructured interfaces. This microscopy technique is widely used in material sciences due to its sub-angstrom resolution [1, 97, 98]. The STEM microscope is a complex system in which the careful design of lenses outstanding stability and atomic resolution imaging has been achieved.

As the name suggests, the STEM mode operates by scanning/rastering a sub-angstrom probe across the specimen surface [1]. The condenser and objective lenses which are located above the specimen have the purpose to create a convergent beam which is focused to a sub-angstrom region, 'probe' [1]. The specimen is positioned along the optical axis so that its position matches with the position where the beam converges and the probe is formed. In order to obtain local information in STEM we use a point-like illumination in contrast to the TEM. In this way, we can obtain local information of the specimen structure on angstrom scale. The probe will scan the sample and stays at each point for a certain time (microseconds); hence, pixel-by-pixel we generate information for certain specific area of interest. The scanning is achieved by shifting the probe with helps from system of scanning coils (**Figure 3.24a**) which create controlled magnetic fields required to deflect the probe from the central to a desired (x, y) position [1]. This is in contrast with the TEM in which the image is formed in a parallel mode.

Another fundamental difference between STEM and TEM is the position of the lenses. In STEM all important lenses are above the specimen while below the specimen, we do not use lenses to magnify/construct an image. In STEM we only use detectors to record either BF-STEM or HAADF-STEM [1].
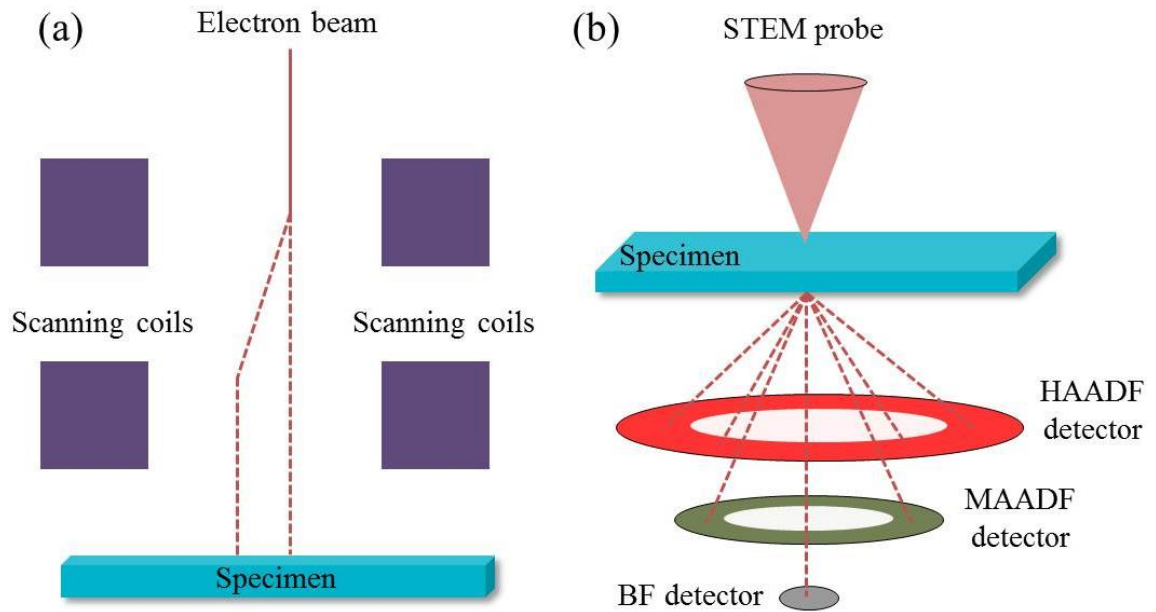
Figure 3.24: (a) shows schematic of the scanning coils above the specimen in STEM and (b) shows the HAADF, MAADF, and the BF detectors presence below the specimen.

The electrons that interact with the specimen scatter under different angles; some of them at very low angles but some of them at high angles. Using the different collection angles three types of images can be formed. The low angle electrons (up to ~ 20 mrad) form so called BF-STEM images while the electrons scattered at very high angles form HAADF-STEM images [1]. Meanwhile, the rest of the electrons which scatter in the mid-range can be detected in middle-angle-annular-dark-field (MAADF) detector. The schematic geometry of the BF-STEM, MAADF-STEM, and HAADF-STEM detectors are illustrated in **Figure 3.24b**. The HAADF detector typically covers an angle range of 70 to 200 mrad.

The electrons scattering under low angles go through the centre of the HAADF and MAADF detectors and are detected by the BF detector. Similar to TEM images the BF-STEM images are also challenging to interpret. This is due to the fact that these images are dominated by the phase contrast. An annular BF-STEM detectors can be used to image light elements [1]. On the other hand, the high angle electrons are incoherent making the signal more straightforward to interpret. A bright pixel in HAADF images corresponds to scattering inside the specimen, the more intensity is collected at given

pixel the heavier are the elements along that atomic column. The correlation between the atomic number and the intensity in the HAADF images is the reason why this imaging mode is widely used in the scientific community [58, 97-116].

Another difference between TEM and STEM is in the magnification process. In a TEM the magnification happens after the electrons exit the sample similar to the conventional optical microscope i.e. by carefully setting the focal lengths of the lenses so that the final image dimensions are much bigger than those of the object [1]. On the other hand, taking into account that there are no lenses in STEM microscope below the specimen, the image dimensions are defined by the scanning window, which is the region of the specimen surface being scanned by the beam [1].

In the STEM we program the microscope in a way that this window is sampled equidistantly in both x and y directions and at each 'pixel' of this area the beam scans for a very short time interval. If we work at high magnification the distance between these pixels is very small; on the other hand, in the case of low magnification these pixels are far away. Therefore, the magnification in STEM images is directly determined by the dimensions of the scanning window or in other word the frame size [1].

The STEM probe is fundamentally important as the magnification/resolution depends on the scanning of the probe. For instance, the probe size determines the image resolution, while its shape is directly related to the quality of the image [1]. Since the probe is an image of the electron source, we need sources that are extremely sharp and symmetric to produce highest possible brightness. In addition, the probe diameter can be controlled by the convergence semi-angle of the beam below the objective lens [1]. With bigger convergence semi-angles we can get smaller probes. However, this reduction of the probe size is limited by the aberrations of the objective lens [1]. Hence, to further reduce the probe size, a reduction of the spherical aberration coefficient is required. As mentioned in TEM aberrations, the off-axis electrons are deflected more than the paraxial ones which make them focus closer to the lens. The C_s corrector diverges the off-axis electrons in a way that the additional angle would compensate for the over-deflection caused by the objective lens [116].

In 1936, Scherzer proved that any electron optical system will always suffer from spherical aberration and chromatic aberration if simultaneously:

- the optical system is rotationally symmetric
- the system produces a real image of the object
- the fields of the system do not vary with time
- there is no charge on the axis

Breaking the first of Scherzer's assumptions is the basis of currently commercially available aberration correction technologies which is achieved using multipole lenses. Multipole lenses come in a series with 2, 4, 6, and 8 poles named dipole, quadrupole, sextupole, and octapole, respectively. The idea behind the current spherical aberration correctors is to introduce a corrector that produces negative spherical aberration. This then combines with the positive aberration of the objective lens to give a total of zero spherical aberration. There are two approaches both using multipole lenses: the so-called quadrupole-octupole corrector and the hexapoles (sextupole) corrector [1].

Quadrupole-octupole correctors are consisting of four quadrupoles and three octapoles as: Q1, O2, Q3, O4, Q5, O6, and Q7. The progress of the beam through the corrector is as follows:

- Q1 produces a crossover at Q3 in *x* direction and a highly elliptical beam at O2.
- O2 corrects spherical aberration in *x* direction and introduces some four-fold astigmatism.
- Q3 has little effect in *x* direction because the ray is almost on axis but produces a crossover in *y* direction at Q5.
- O4, acting on an approximately round beam, corrects the four-fold astigmatism introduced by the combination of O2 and O6.
- Q5 has little effect in *y* direction as it is on axis but deflects the electrons in *x* direction so that a round but convergent beam in *x* (*y*) arrives at Q7.
- O6 corrects spherical aberration in *y* direction and introduces some four-fold astigmatism.

- Q7 returns the beam to a round beam that now has acquired negative spherical aberration.

The Hexapole correctors rely on two hexapoles, Hex1 and Hex2 that are rotated by 60° with respect to each other so that the first order effect of the Hex1 is cancelled by the first order effect of the Hex2. However, for this to happen precisely, two hexapoles must occur in equivalent optical planes. To achieve this pair of projector lenses or as called transfer lenses of TL21 and TL22 are placed between the two hexapoles in the following order: TL11, TL12, Hex1, TL21, TL22, and Hex2 [1].

Such correctors have enabled sub-angstrom probe size, which leads to a spatial resolution of up to 0.8 angstrom.
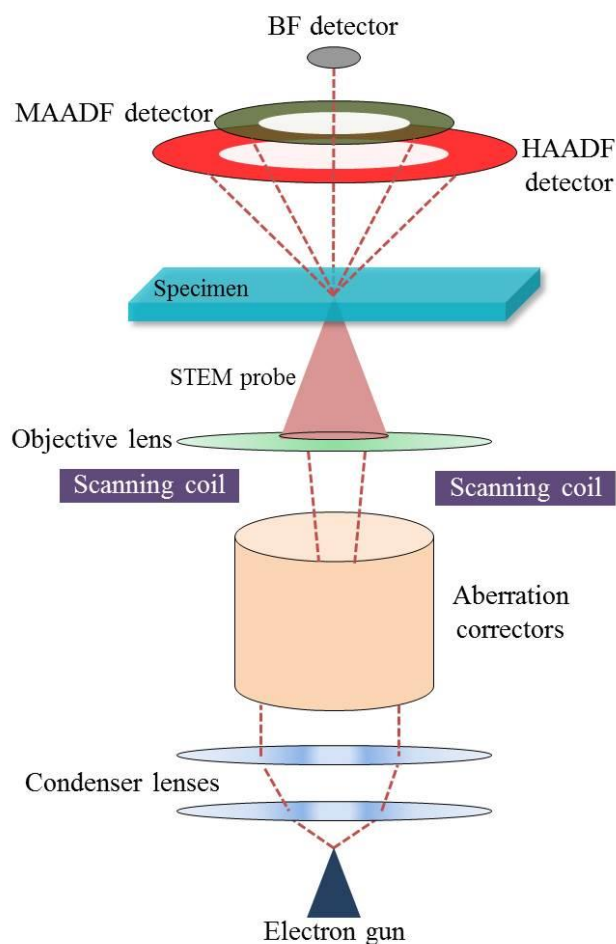
Figure 3.25: Simplified schematic of a STEM microscope.

A simplistic schematic of the functional parts of a dedicated STEM microscope is shown the **Figure 3.25**. We shall note that in many of the dedicated STEM instruments the gun is located at the bottom. This is due to the fact that the gun is usually the heaviest part of a microscope and locating it closer to the ground will cause a better mechanical stability.

3.5.5   High angle annular dark field-STEM

When the electrons travel very close to the positively charged core of given atom they will experience Rutherford scattering (proportional to the atomic number (Z) as $\sim Z^2$) [1]. Hence, unlike TEM an image recorded in this mode is not a phase contrast/interference image. Due to the incoherency of scattered electrons in HAADF-STEM imaging, the intensity recorded by the HAADF detector can be represented as a sum of all scattering intensities coming from the specimen's 'scattering centres' (atomic columns) which have interacted with the probe [1]. This allows the atomic columns to be treated as independent scattering centres and certainly enables more straightforward interpretation of the resultant images.

As we mentioned earlier the probe size for modern dedicated STEM microscopes is in sub-angstrom region. This will allow us to be able to visit several pixels in-between two neighbouring atomic columns when operating in very high magnification. This condition makes the signals coming from two neighbouring atomic columns practically independent. Hence, atomic columns that contain elements with higher atomic number Z (e.g. Bismuth) appear brighter in the image compared to lower Z elements (e.g. Tellurium). This property of the HAADF-STEM imaging illustrates its usefulness as well as potential and explains the wide applicability of this technique in physical sciences. Moreover, in this thesis we also used EELS elemental mapping which is acquired at the same time with the HAADF-STEM image to get both structural and chemical information of the specimen [117-119].

Figure 3.26 shows the difference between the HAADF and BF-STEM images of a Bi_2Te_3 thin film grown on Ge substrate. As we mentioned before, due to the atomic number dependence of HAADF-STEM imaging we can easily distinguish between the Bi and Te atomic columns as well as the vdW gap between the QLs of the film.
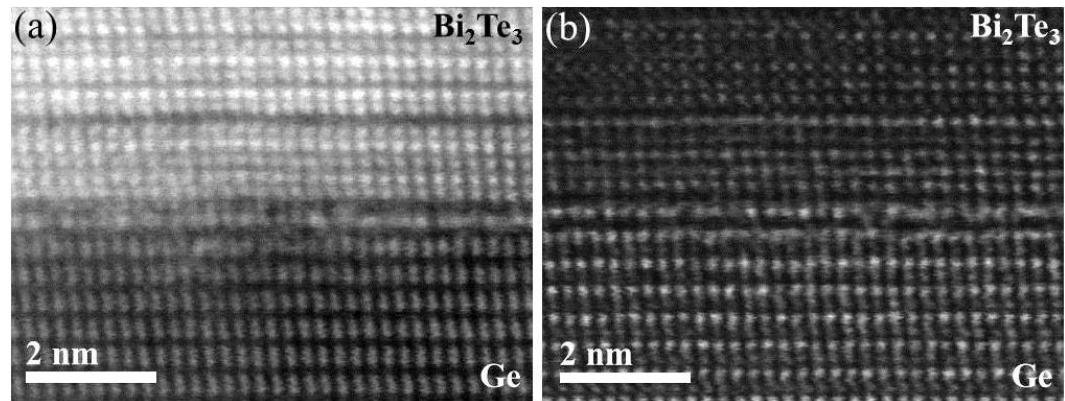
Figure 3.26: (a) and (b) show HAADF and BF-STEM images of the Bi_2Te_3 on Ge substrate.

There are also some challenges of using STEM. Due to the sub-angstrom probe size, some specimens may suffer damage when exposed with the beam [1]. The samples analysed in this thesis are in general resistant to beam exposure. The HAADF-STEM imaging has been performed using a 100 keV microscope to lower the probability of damaging the specimens. The probe may also attract contaminations present at the specimen surface, and make the imaging impossible. In order to use a 100 keV STEM the specimen thickness should be thinner than normal specimens prepared for 200 keV or 300 keV microscopes (both TEM and STEM). These challenges can be avoided with a very well-prepared specimen.

While operating the microscope, there is always a possibility that the probe's axis is slightly misaligned with respect to an atomic column or slightly off from ideal convergent beam, which can reduce the spatial resolution of the acquired HAADF-STEM image. However, such small effects to some extent can be compensated by the phenomenon called channelling [1]. The physics behind this phenomenon is that when the electrons travel to the specimen they feel two different potentials, one from the atomic column and one from the interstitial positions between the columns. The atomic columns are positively charged and attract the electrons from the probe more compared

to the interstitial region. Hence, the atomic columns can act as channels which the probe electrons tend to follow as they travel through the specimen. This will reduce the beam broadening and consequently improve the spatial resolution [1]. This means that the STEM imaging is to some extent resistant to small deviations of the incident angle up to the critical angle (few milliradians). In other words, the electrons coming to the specimen under smaller angle will travel all the way down the column similarly as the light in optical fibre.

From the quantum mechanics point of view, there is another important factor which can happen. This phenomenon is called cross-talk of electrons between neighbouring atomic columns. It was discussed above that the electrons traveling along the atomic column are effectively confined due to the channelling effects. From quantum mechanics is known that as long as the distance between two atomic columns is small there is a considerable probability for the electron to cross-talk from the initial atomic column to the neighbouring one. This process is a probabilistic; hence the likeliness of realisation increases with the specimen thickness along the beam direction [1]. As a result, a very thin specimen is needed in order to reduce this term.

3.6   Software for analysis, visualisation, and simulations of microscopy images

Digital Micrograph is the software which communicates between the operator and the microscope (both TEM and STEM). Besides this primary function this software has implemented many post-processing tools and is widely used in the microscopy community and in this thesis. Digital Micrograph is used in this thesis for purposes such as image rotation, measuring distances, plotting intensity profiles, image alignment, PCA and etc. [120].

In order to acquire high quality images and to reduce the exposure on the specimen, often, instead of acquiring a single image, quick acquisition of several (~30) images is performed. During this process the specimen can drift; hence the collected series of images have been aligned using a spatial drift correction script which is based on

statistical correlations [121]. The algorithm takes a reference image and calculates the amount of shift along (*x, y*) directions for each image of the series. After this step, a final image is constructed as an average of the drift-corrected images from the series. Digital Micrograph will be also used to plot the element specific maps of the EELS measurements.

The Digital Micrograph can also be used to perform variety of component analysis such as PCA and independent component analysis (ICA) [122]. The EELS elemental maps in this thesis have been treated by the PCA scripts [123, 124]. The PCA is a series of statistical methods to identify patterns and to express the data in such a way as to highlight their similarities and differences. The general and simplified version of the process goes as following steps: subtracting the mean in each direction, calculating the convergence matrix, and calculating the eigenvectors and eigenvalues of the covariance matrix which generates the components. The generated components can be either meaningful or just noise. Next step is to check and plot each component to choose the components that we want to include in the final image or signal. We note that the users should be extra careful working with the PCA as they can remove the components containing useful information. This has been discussed in more depth on an example in the **chapter 4**.

Also there are other useful tools for material scientists to create and visualize atomistic models; such as VESTA [125], JEMS [126], and CrystalKit [127] software packages. Majority of the atomistic models presented in this thesis are visualized using VESTA. We also often need information about material structures as a .cif file. For this purpose there are many free databases available online such as ICSD [128].

As mentioned before, the HRTEM images are phase contrast images so they require image simulations to check and reveal the underlying atomic structure. Although the HAADF-STEM images are much more straightforward to be interpreted, image simulations are also in some cases are required. In the **chapter 6** HAADF-STEM image simulations are performed using QSTEM [129] in order to show the correct zone axis of the FeSe inclusion inside the Bi_2Te_3 film.

3.7   Electron energy loss spectroscopy

One of the other most important benefits of using STEM is the ability to simultaneously perform EELS measurements [1]. In other words, the extremely small STEM probe enables us to reveal the local chemistry by analysing the energy losses of the transmitted electrons. This technique has been used throughout this thesis firstly to identify the chemical environment of the dopants inside the TIs, and secondly to confirm the chemical structure of TIs and their interface chemical abruptness.
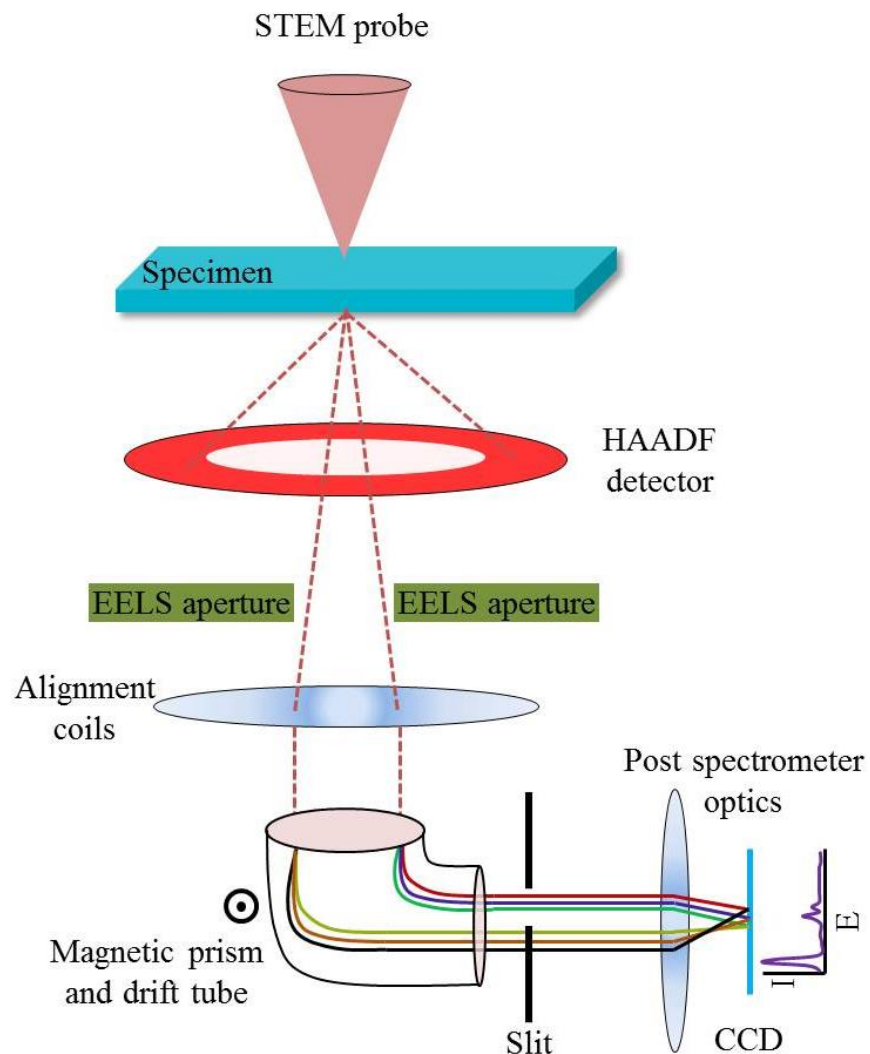
Figure 3.27: Schematics of an EELS post column filter.

There are two different types of EELS filters, the in-column omega filter and post column filters. The STEM instrument used in this thesis to perform EELS mapping has the post column filter. Post column filter is ideally suited for high spatial resolution STEM-EELS analysis as this detector is spatially separated from the annular dark field detectors of the STEM, and performs energy filtering after the sample interaction and imaging mode of the STEM has been performed. In this way the detector itself has no impact on the microscope imaging condition [1]. A schematic of the post column EELS filters has been shown in **Figure 3.27**.

Electrons while traveling through the specimen can experience scattering events or transmit without being affected. The high angles scattered electrons are detected by the HAADF detector. The electrons that passed the hole in HAADF detector are then directed to a spectrometer which can spatially separate them into different channels according to their energy. The electrons which have not lost energy form the most intense contribution of the whole energy spectra. This peak is much bigger than the other peaks and is called 'zero-loss' peak, **Figure 3.28**.
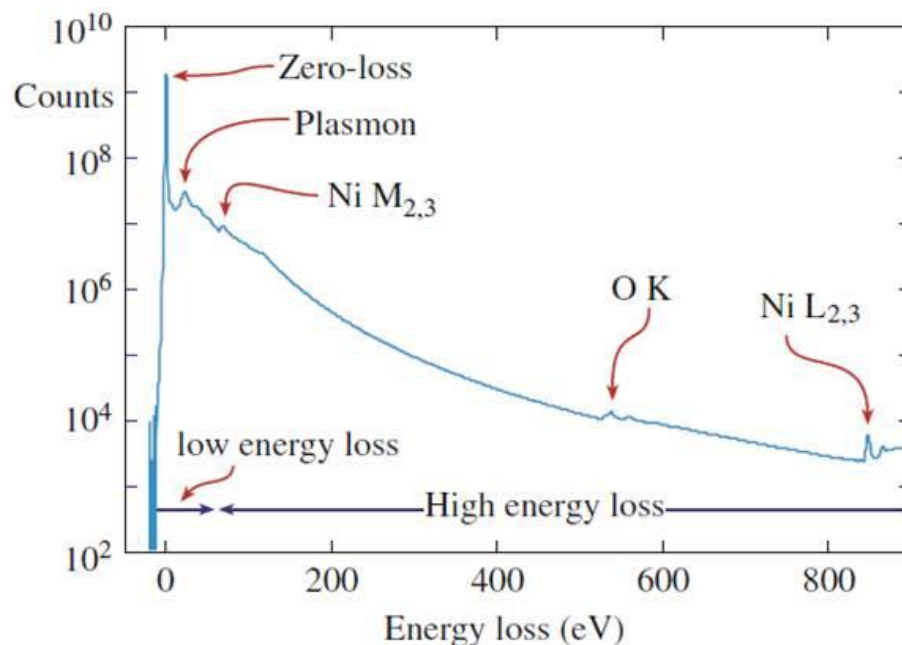
Figure 3.28: EELS map of NiO specimen showing the zero loss, low loss, and the core loss regions as well as the plasmon peak [1].

One of the most important peaks in the so called low loss region (energy losses below ~50 eV) is the plasmon peak. It generates as a result of energy lost which is transferred to excite a plasmon (collective oscillatory mode for the weakly bounded electrons). We can think about the plasmons as being like the ripples that spread out from where a stone is dropped into the water. But unlike the water, these oscillations are damped rapidly and they have an average life time of 10^{-15} s. therefore these oscillations are quit localised < 10 nm. The plasmon peak is the second dominant peak in EELS spectra after the zero loss peak. The plasmon peak usually appears in the energy range of 5-25 eV [1].

Furthermore, in the low loss region there are other features which can give an opportunity to determine finer details such as inter-band transitions, band gaps etc. [1]. One of these features is positioned immediately after the zero loss peak and before the rise of the plasmon peak. If no inter-band transitions occur, the intensity in this region of the spectrum approaches the dark-current (noise) level of the detector. This low intensity implies that there is a forbidden-transition region, which is simply the band gap, between the valence and conduction bands in semiconductors and insulators [1].

Although the plasmon peaks can be used as chemical fingerprints, core-loss region is the main region for the EELS chemical mapping. The core-loss shows characteristic features for each element, in addition to the power law decaying background. The energy loss of electrons is transferred to 'ionize' the atom by ejecting an electron from the core shells. In this work, EELS was used to confirm the HAADF conclusions about the spatial distribution of Te, Se, Cr, Mn, Fe, Cu, and O in specimens studied in this thesis.

3.8   Density functional theory (DFT)

DFT calculations are computational methods to model and solve the Schrodinger equation of many body systems. These calculations rely on the Hohenberg-Kohn theorems which demonstrate that the external potential which in turn determines the total energy of the system is a unique functional of the electron density; the electron density which minimizes this total energy functional describes the ground state of the

system. This is in fact a reformulation of the quantum mechanics from Schrodinger equations approach into electron density approach [130].

Within Kohn-Sham DFT the extremely hard and unsolvable many-body problem of interacting electrons is reduced to a problem of non-interacting electrons in an effective potential. This effective potential includes external potentials and the effects of Coulombic interactions between electrons including the exchange and correlation interactions. The total energy functional (Eq. (3.5)) can be written as [131]:

$$E[\rho] = T[\rho] + \int \rho(\boldsymbol{r}) v_{ext}(\boldsymbol{r}) d^3\boldsymbol{r} + E_H[\rho] + E_{xc}[\rho] \qquad (3.5)$$

where the terms are the kinetic energy, energy due to the external field (all external potentials including the electron-nuclei interactions), the Hartree term (Coulomb interactions between electrons), and the exchange-correlation term (which does not have a classical equivalent), respectively.

Modelling of exchange and correlation is the greatest difficulty for DFT as the exact behaviour of these interactions are only known in the case of free electron gas [132]. Hence, approximations are used for exchange and correlation using the local density approximation (LDA) and local spin density approximation (LDSA) to give local solutions as a function of the local electron density or generalised gradient approximations (GGA) to give solution to the local electron density and its local gradient.

In this thesis, the DFT calculations have been used to find the minimum energy of different systems as well as crystal relaxations and to calculate the electronic band structure of the materials studied. For these purposes two different codes have been used. The CASTEP code [133] which is used in calculations which are performed in York and an all electron code (full potential approach) from the Mie University in Japan. In contrast to the code used in Japan, the CASTEP code is an outer shell code which means the energy equation is only being solved for the outer shell electrons. This method can reduce the time and the cost of calculations due to the much smaller number of electrons in outer shells. This approach in case of bismuth and tellurium is extremely faster.

In order to start the calculations first we need to generate an input file, which consist of atoms positions in the unit cell representing studied system. Next a parameter file is needed. As it is obvious from its name the parameter file contains the parameters of the calculations such as the type of exchange-correlation, the cut off energy , the speed of the calculations, number of cycles, sampling area etc. Furthermore, we put the task that we want to calculate in the parameter file, e.g. energy calculation or band structure calculation.

The next step is to keep increasing the cut off energy, which is basically the amount/length of interactions, till the free energy value does not change more than 5 in meV scale. After finding the appropriate cut off energy, the number of sampling point (k-point) should be converged. Knowing the cut off energy value and the k-point is starting point for the system geometry optimisation.

Often, for example for supercells which contain interfaces between two materials, defects or even bulk materials, we do not know the exact positions of the atoms neither the precise value of the supercell lattice parameters. In this step we run the calculations with parameters we achieved from the previous cut off and k-point calculations and allow the atoms to move around their positions to find their lowest energy states. This lowest energy state is also known as the relaxed state. This calculation can be used to confirm the possibility of the formation of materials consist of different atoms by comparing to the crystal values of HAADF-STEM images.

The total energy calculations can also be used to calculate the formation energy of ad-atoms. Furthermore, by moving the ad-atom and placing it on various positions we can calculate the possible position of the ad-atom binding energy difference. This has been done in **chapters 5 and 6**, where we calculated the formation energy of Mn dopants and selenium ad-atom inside and on top of the Bi_2Te_3 film, respectively.

In order to plot the electronic band structure we plot the energy levels for all characteristic k directions in the BZ. Bands are usually plotted in two dimensions by projecting the band structure along certain desired paths in the k-space. By counting all states in extremely small energy interval around energy E, the density of states (DOS) can

be calculated. Very useful information can be obtained by analysing the DOS such as conductivity or insulating behaviour of the sample.

More details about each calculation performed are presented in results presentations in **chapters 5, 6, and 7**.

4   Atomic-level structural and chemical analysis of Cr-doped Bi$_2$Se$_3$ thin films

This chapter is based on the work published in [117] and forms a natural comparison with the works performed in the next chapters.

In this chapter, a study of the structure and chemical composition of the Cr-doped 3D TI Bi$_2$Se$_3$ is demonstrated. Single-crystalline thin films were grown by MBE on Al$_2$O$_3$ (0001) substrate. The structural and chemical properties of the sample were determined on an atomic level by aberration-corrected STEM and EELS.

Bi$_2$Se$_3$ film and the Al$_2$O$_3$ substrate belong to trigonal crystal system which contains both hexagonal and rhombohedral lattice systems. The Bi$_2$Se$_3$ film and Al$_2$O$_3$ substrate have $R\bar{3}m$ and $R\bar{3}ch$ space groups, respectively.

The Cr dopants can occupy various places in the Bi$_2$Se$_3$ lattice. They can substitute Bi and Se atoms as well as sitting in the vdW gap between the QLs of Bi$_2$Se$_3$ film.

In this work the film was grown by Dr. L. J. Collins-McIntyre and Dr. T. Hesjedal in the Physics department of University of Oxford, Oxford. Furthermore, the atomically resolved STEM-EELS have been performed by Dr. D. Kepaptsoglou and Prof. Q. Ramasse in the SuperSTEM national laboratory, Daresbury.

4.1.   Introduction

Among the various Bi-based TIs that have been studied, Bi$_2$Se$_3$ is one of the most promising candidates for future device applications. Crystalline Bi$_2$Se$_3$ has a rhombohedral structure and its unit cell is made up of three weakly bonded QLs [134]. It has a single Dirac cone in the BZ and a nontrivial (bulk) band gap of 0.3 eV [12]. Upon doping with

magnetic dopants, time-reversal symmetry (TRS) may be broken and Dirac electrons may become effectively massive [135]. According to first-principle calculations, doping TIs with V, Cr, Mn or Fe can break TRS and open a band gap in the surface bandstructure [136]. Long-range ferromagnetic order has been reported in materials such as Cr- and Sm-doped Bi$_2$Se$_3$ [51, 137-139] and Mn-and Fe-doped Bi$_2$Se$_3$ [63, 140]. Most importantly, the interaction between topologically protected surface states and ferromagnetism is expected to give rise to different unconventional spintronic effects for device applications. The location of the dopants in the Bi chalcogenide matrix depends highly on the type of dopant, e.g., its ionic radius and ability to form undesired chalcogenide compounds, its concentration and the growth conditions. In Cr:Bi$_2$Se$_3$, dopants can either substitute for Bi or incorporate between the QLs in the vdW gap [65, 141]. First principle calculations predict that the Bi sites are the most energetically favorable substitutional sites for Cr [134, 136]. Formation energies of Cr being in the vdW gap are 0.29 eV higher compared to the substitutional scenario, and interstitial Cr within the QLs is much less favorable [134].

In this chapter it is directly shown that 4.6 at-% of Cr is incorporated substitutionally on Bi sites as predicted by calculations. Furthermore, it is demonstrated that the Cr dopants can be incorporated in the Bi$_2$Se$_3$ structure with no phase segregation. In addition, it is shown that Cr can segregate on the grain boundaries which are inevitably present in thin film growth. This segregation of Cr is correlated to the grain boundary density. Their effect on the surface state of Bi$_2$Se$_3$ would depend on the geometry and the spatial extension of the boundary defects. By controlling the defect density, the amount of Cr that segregates can be minimized; hence a homogeneous Cr distribution could in principle be achieved even at higher Cr-dopant concentrations.

4.2. Methods

The Cr doped Bi$_2$Se$_3$ thin film samples were prepared by MBE. Samples were deposited on solvent-cleaned *c*-plane sapphire substrates in a growth chamber with a base pressure of 1×10^{-10} Torr. The doping concentration has been measured with an *in-*

situ beam-flux monitor (BFM) with respect to the Bi flux. The typical film thickness was ~100nm. Standard effusion cells were used for the co-deposition of Bi and Cr, while Se was sublimated from a bespoke hot-lip cracker source. All evaporation materials used were of 99.9999% purity and the films were deposited in a Se-rich environment to reduce the formation of BiSe anti-site defects and Se vacancies. Growing with a Bi:Se flux ratio of 1:10, the deposition rate is Bi-limited at ~0.4 nm/min. We note that the Se concentration was lower at the beginning of the growth to avoid formation of Se layers at the interface (as can be observed in **Figure 4.6c**). Films were deposited at a constant substrate temperature of 200 °C, and then cooled under a residual Se background to room temperature (25 °C). The low growth temperature and cooling slowly in the Se rich environment inhibit the formation of defects in the sample.

RHEED was used to monitor the growth *in-situ*, and showed streaky patterns which are indicative of 2D growth. The sample composition was determined by Rutherford backscattering spectrometry (RBS) to be 4.6 at-% Cr, 35.3 at-% Bi, and 60.1 at-% Se, bringing the (Cr+Bi):Se ratio to 2:3, indicative of Cr being substitutional on Bi sites [138].

The AFM images were acquired using a Veeco Multimode V AFM in tapping mode to check the growth mode and morphology of the film. The XRD and rocking curve measurements were carried out on a Bruker D8 x-ray diffractometer with a Cu anode (λ = 1.54 Å). Incident optics were set with a Ge (220) 2-bounce monochromator, 2.5° Soller slits and 1 mm beam mask. The receiving optics used 2.5° Soller slits arriving at either an area detector (XRD) or a scintillator counter (rocking curves).

Cross-sectional TEM specimen preparation was carried out by FIB methods using a FEI Nova 200 NanoLab high-resolution field emission gun scanning electron microscope (FEGSEM). Layers of Pt were deposited to protect the film from Ga ion implantation and damage.

Structural characterization has been performed by TEM. The SAED were obtained using a JEOL 2000 EX. STEM imaging and EELS measurements were performed in a Nion UltraSTEM100TM equipped with a Gatan Enfina spectrometer. The microscope was operated at 100 kV, with a convergence angle of 30 mrad; at these optical conditions the

electron probe size is determined to be 0.9 Å. The inner detector angle for high-angle annular dark-field (HAADF)-STEM imaging was 76 mrad. The native energy spread of the electron beam for EELS measurements was 0.3 eV; with the spectrometer dispersion set at 0.2 eV/channel & 1 eV/channel, yielding an effective energy resolution of 0.6 eV and 3 eV, respectively. The EELS collection angle was 33 mrad. For enhancing the contrast of the atomically-resolved spectra, a noise-reduction routine was applied using PCA (CiMe-plugin for Gatan's Digital Micrograph 2.3 software suite [124]). Chemical maps were created by integrating at each point of these spectrum images the spectrum intensity over a ~20 eV window above the Cr $L_{2,3}$, Se $L_{2,3}$, EELS edge onsets after background subtraction using a power law model.

4.3.   Results

In order to determine the location and distribution of Cr dopants in the film state of the art HAADF imaging and atomically resolved EELS in an aberration corrected STEM have been performed.
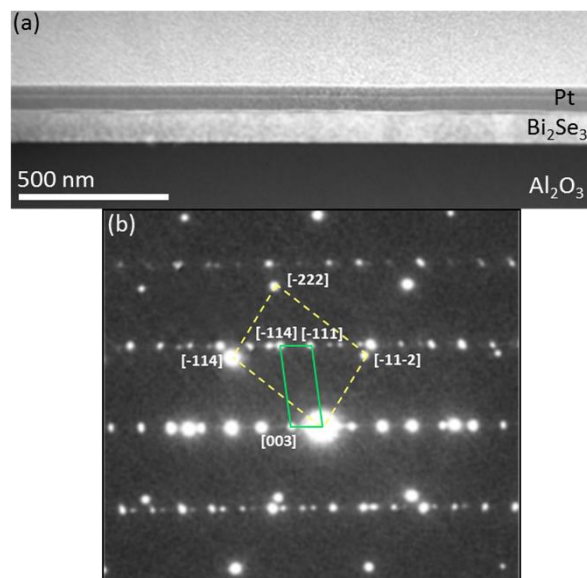
Figure 4.1: (a) Low magnification HAADF-STEM image of the Bi$_2$Se$_3$ film on Al$_2$O$_3$ (0001). (b) SAED from the Bi$_2$Se$_3$/Al$_2$O$_3$ interface region along the [11$\bar{2}$0] crystallographic direction. The dashed (yellow) and solid (green) rectangles are showing the projected unit cells of Al$_2$O$_3$ and Bi$_2$Se$_3$, respectively.

Figure 4.1a shows a low magnification cross-sectional view of the MBE -grown Cr doped Bi$_2$Se$_3$ thin film on *c*-plane Al$_2$O$_3$.

The atomic number dependence ($\sim Z^2$) of HAADF-STEM images clearly outlines the Bi$_2$Se$_3$ film (bright contrast) and the Al$_2$O$_3$ substrate (darker region). The SAED pattern (**Figure 4.1b**) obtained from the substrate-film interfacial region shows that the Cr doped Bi$_2$Se$_3$ is single-crystalline and that it is grown epitaxially on Al$_2$O$_3$ (0001) with the following crystallographic relationships: Bi$_2$Se$_3$ [11$\bar{2}$0]||Al$_2$O$_3$ [11$\bar{2}$0] and Bi$_2$Se$_3$ (0001)||Al$_2$O$_3$ (0001). We note that no obvious twinning of Bi$_2$Se$_3$ is observed.

The growth of the Cr doped Bi$_2$Se$_3$ film (thickness ~100nm) is mediated by granular growth driven by screw dislocations as shown in **Figure 4.2**.
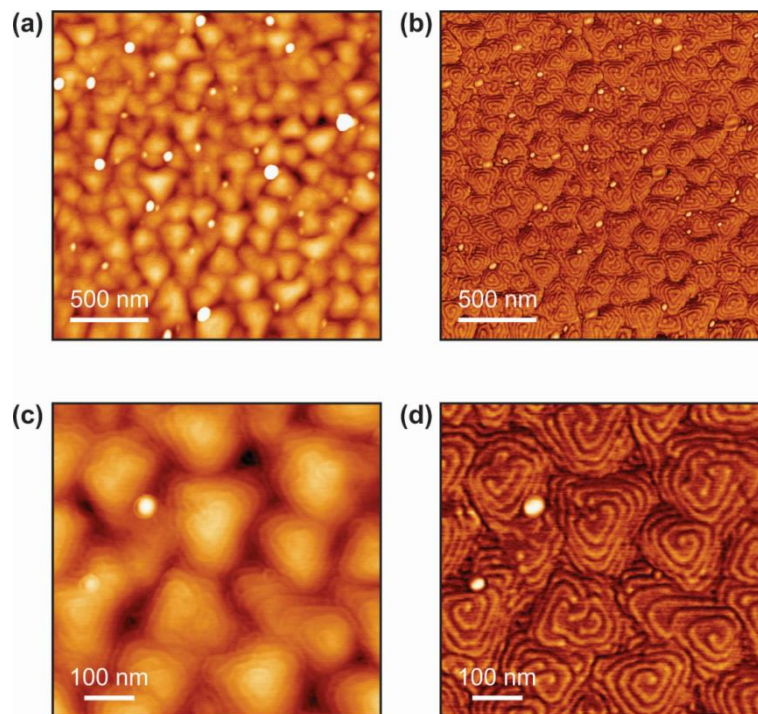
Figure 4.2: Tapping mode AFM images showing the height in the left column (a) and (c) and the phase in the right column (b) and (d). The overview scans (a) and (b) illustrate the dominance of the triangular growth islands, separated by trenches. The bright spots are due to surface contamination as a result of sample cleaving. The zoomed-in images in (c) and (d) show an average triangular island size of ~150 nm. The ~1-nm-high QL steps of the terraces are clearly resolved. In the phase image the spiral growth mode is visible and shows 7 nm height for the terraces.

The AFM image in **Figure 4.2** illustrates the spiral islands, common for *c*-axis oriented Bi$_2$Se$_3$ films, with QL-high steps (~1 nm). The islands (or grains) have a lateral dimension of typically ~150 nm, and are separated by trenches (grain boundaries). This growth process results in a film of uniform thickness with a smooth surface morphology as indicated also by the RHEED patterns taken at the end of the film growth, **Figure 4.3**.
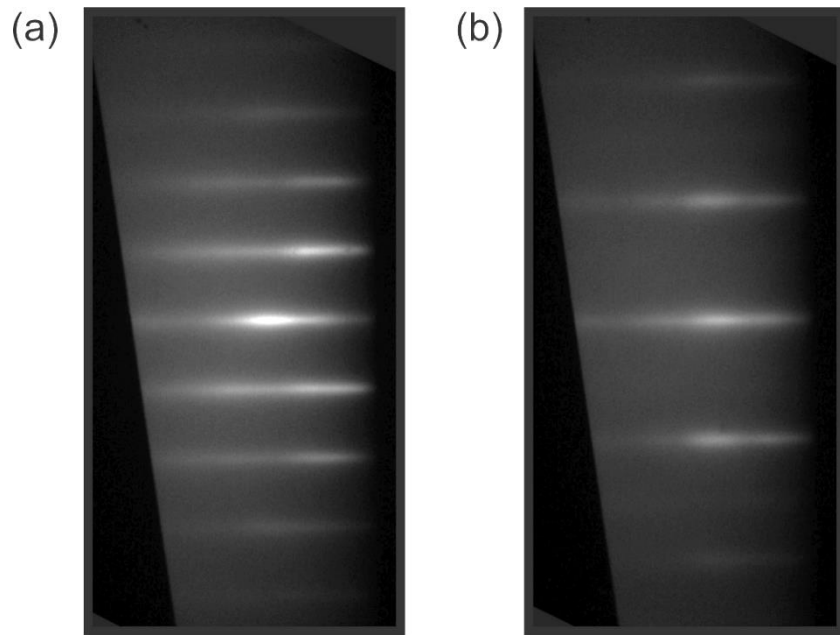
Figure 4.3: RHEED images of the Cr doped Bi$_2$Se$_3$ film recorded in-situ at the end of the film growth along the (a) $[10\bar{1}0]$ and (b) $[11\bar{2}0]$ azimuths, respectively.

Furthermore, the overall quality of the grown film is shown by performing XRD (**Figure 4.4**). **Figure 4.4** shows a 2Θ-ω scan of the Cr doped film. The film only exhibits the (000*l*) family of peaks representative of Bi$_2$Se$_3$, and the extracted *c*-axis lattice parameter of ~28.65 Å is slightly larger than the literature value for Bi$_2$Se$_3$ (ICSD 617072). The sapphire peaks are indicated as well. In general, the crystalline quality of the film as evidenced by the peak width is very good.
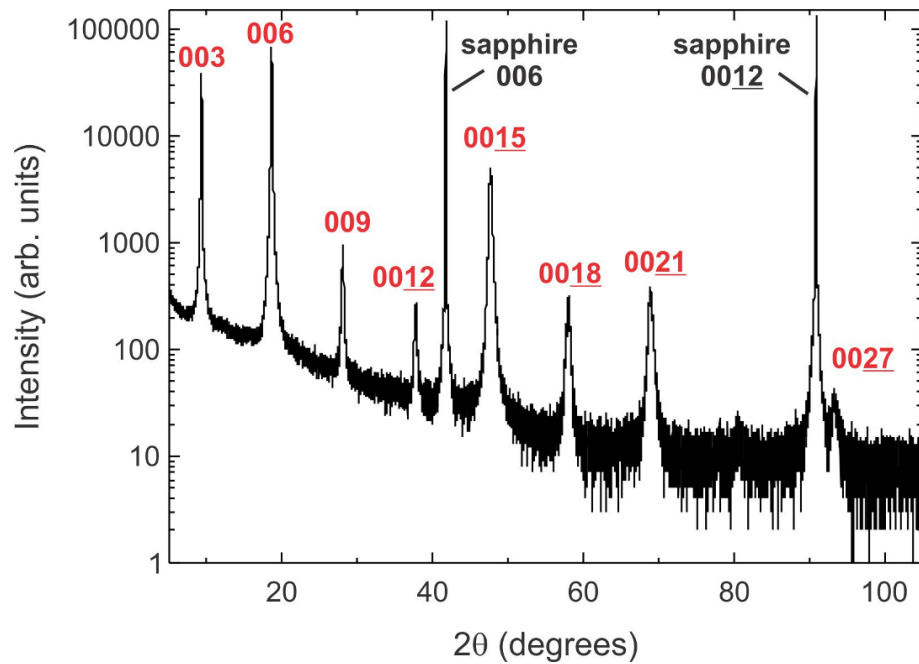
Figure 4.4: XRD of the Cr doped thin film using for this investigation. The film peaks are labeled in red and the sapphire substrate peaks in black.

The structural ordering of the film is shown in HAADF images acquired along the [11$\bar{2}$0] zone axis in **Figure 4.5**. The abrupt change in the HAADF image contrast indicates a chemically abrupt substrate-film interface, and the white fringes are showing the continuous QL structure of the film.

Figure 4.5b gives a closer view of the interfacial region between the Al$_2$O$_3$ and Cr doped Bi$_2$Se$_3$ film. It shows that, while interface with the Al$_2$O$_3$ is chemically abrupt - the film is not fully ordered at the initial stage of the growth. In fact, it requires about 3-4 atomic layers before the regular QL growth of Bi$_2$Se$_3$ is achieved. Along this crystallographic orientation Bi and Se atomic columns do not overlap, hence Bi and Se atomic columns are easily distinguishable due to the much higher atomic number of Bi compared to Se. The inset in **Figure 4.5b** is a high-magnification HAADF image of a QL clearly showing the atomic stacking of the Bi and Se atomic columns.
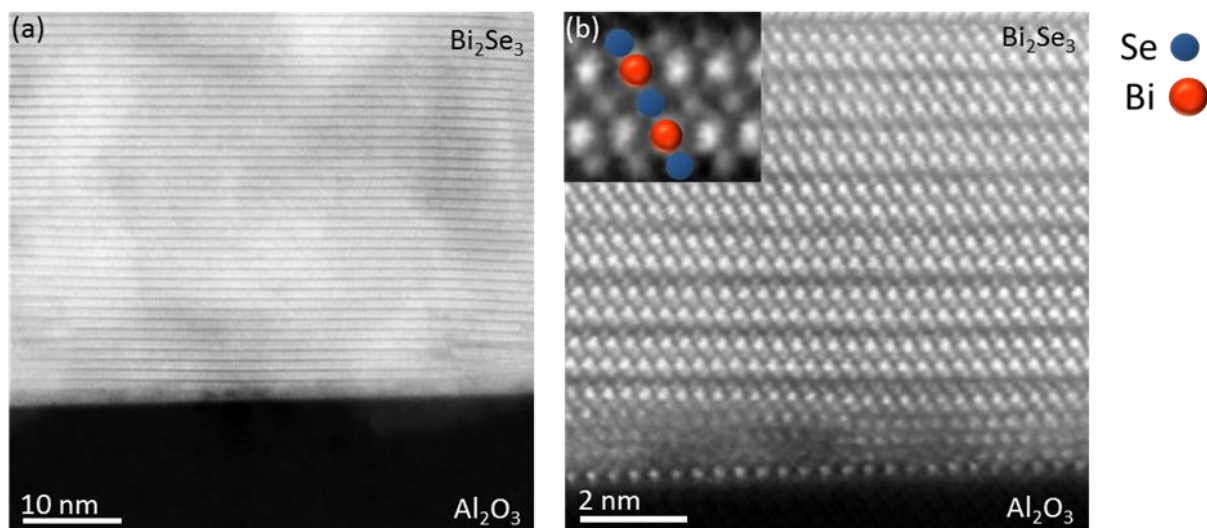
Figure 4.5: (a) HAADF-STEM overview image from the interfacial region between the film and substrate. (b) Magnified image of the film at the interface. A smooth interface and regular Bi_2Se_3 QLs are found, except for the first layer which appears to be highly disordered. The inset shows magnified image of a QL with overlaid structural model; Bi (red) and Se (green) atomic columns.

Next the location of the Cr dopants in the Bi_2Se_3 matrix is investigated. Direct imaging of Cr by HAADF is not feasible due to the low Z of Cr (Z_{Cr}=24) in comparison to Bi and Se and the low concentration of Cr in the film. In order to get an unambiguous signature of the Cr present in the film, spatially resolved EELS mapping, by rastering the electron probe serially across a defined region and collecting an EEL spectrum at each point has been performed. Chemical maps where then created by integrating at each point of these spectrum images the spectrum intensity over a $\sim$20 eV window above the EELS edge onsets, while HAADF intensity signal was simultaneously acquired allowing for unambiguous correlation of the chemical information to the structural image.

Figure 4.6a shows a HAADF-STEM survey image in which the region selected for EELS measurements is highlighted (**Figure 4.6b**). The map of the Cr $L_{2,3}$ signal intensity is shown in **Figure 4.6c** (we note that the data treated by PCA).
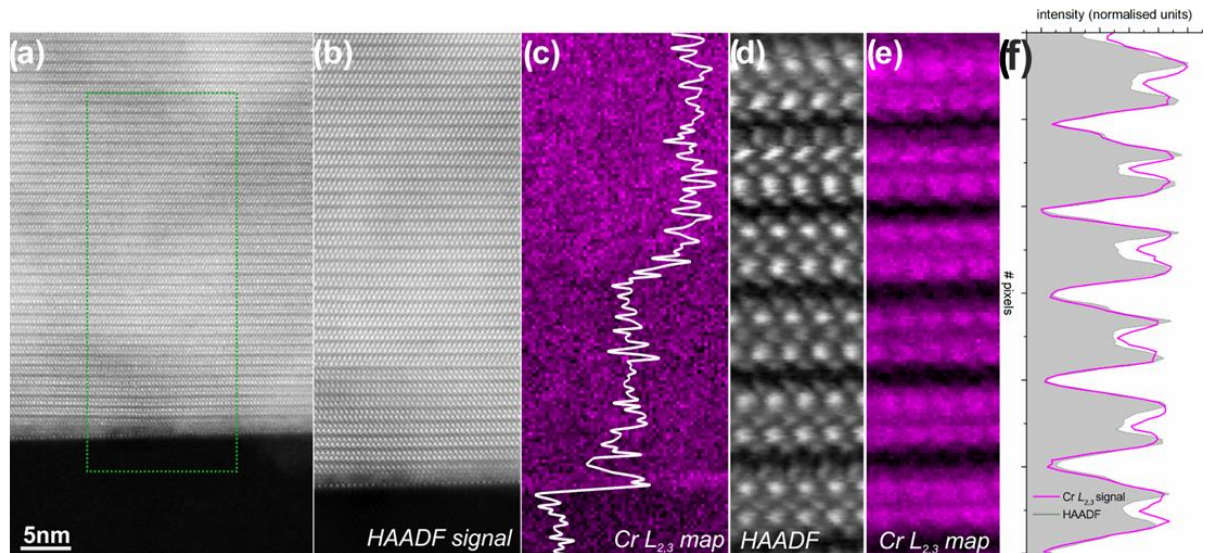
Figure 4.6: Elemental mapping of 4.6% Cr doped Bi$_2$Se$_3$. (a) HAADF-STEM survey image from Bi$_2$Se$_3$ film and Al$_2$O$_3$ substrate. (b) HAADF-STEM signal from the region of interest outlined in (a) produced simultaneously with the EELS acquisition. (c) Cr $L_{2,3}$ EELS signal showing uniform distribution of Cr throughout the QLs contained within the region of interest. (d) The atomically resolved HAADF-STEM image from the film area recorded simultaneously with the EELS signal shown in (e). (e) Spatially resolved intensity of Cr $L_{2,3}$ edge signal, showing that Cr is substituting Bi in the QLs shown in (d). (f) Intensity profiles of Bi atomic columns and Cr elemental map showing the direct spatial correlation between these two signals.

Similar to previous reports on the same system [10], the map shows a uniform Cr distribution throughout the film without any signs of Cr diffusion into the substrate. In order to determine the position of Cr dopants in the Bi$_2$Se$_3$ structure atomically resolved EELS measurements of the bulk of the film has been performed.

Figure 4.6e shows an atomically resolved Cr $L_{2,3}$ EELS map (data treated by PCA). Direct comparison of the Cr chemical map intensities (see plotted integrated intensities in **Figure 4.6f**) with the simultaneously acquired HAADF signal (**Figure 4.6d**), shows that Cr is in registry with Bi columns, i.e., Cr is substituting for Bi, a direct confirmation of the first principles calculations [134, 137]. It should be noted that the Cr elemental maps are displayed as normalised intensities (stretching the image contrast, for visual convenience). While these maps are indicative of the relative spatial distribution of the

elements, they should therefore not be interpreted as a quantification of the sample composition

In addition to the Cr substitution of Bi atoms, it is also found that Cr segregates at the grain boundaries which are rather common in MBE-grown Bi$_2$(Se,Te)$_3$ films due to the vdW epitaxy and substrate surface steps [100, 142]. **Figure 4.7** shows an elemental map of Cr in the region where grain boundaries are present.
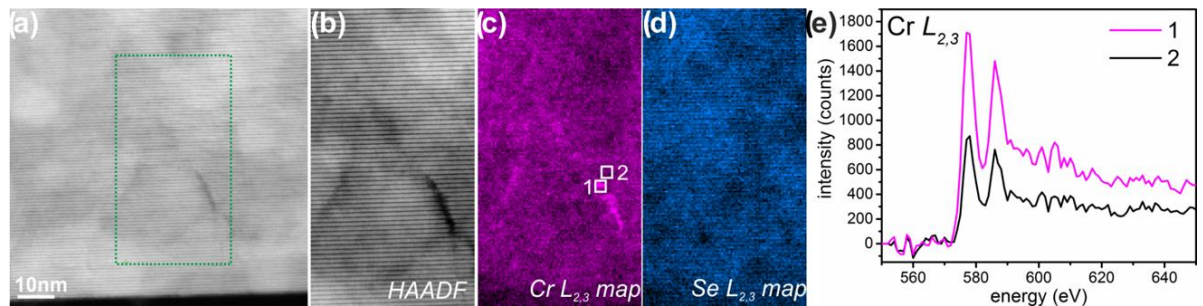
Figure 4.7: (a) HAADF-STEM survey image. (b) HAADF-STEM signal from the region of interest outlined in (a) produced simultaneously with the EELS acquisition. (c) Cr $L_{2,3}$ EELS signal showing Cr segregation along the grain boundaries. (d) Se $L_{2,3}$ EELS signal showing uniform distribution of Se in the film. (e) Cr $L_{2,3}$ edges obtained from the grain boundary and off boundary regions labeled as number 1 and 2 in (c), showing enhanced Cr signal at the grain boundary.

In the survey scan (**Figure 4.7a**), the area including the boundary is indicated. Comparing the HAADF-STEM image (**Figure 4.7b**) simultaneously acquired with the EELS signal, to the Cr $L_{2,3}$ intensity map (**Figure 4.7c**), a clear increase of the Cr $L_{2,3}$ signal is seen at the grain boundary (dark contrast in **Figures 4.7a and 4.b**) compared to regular QL regions (**Figures 4.7c and 4.7e**) (data treated by PCA). This implies that grain boundaries act as 'sinks' for Cr dopants. It is to be expected that segregation of Cr at the boundaries can be significant when Cr concentrations in the films are large. On the other hand, the corresponding Se map of the same region shows a uniform distribution throughout the sample (**Figure 4.7d**).

In order to assess whether the Cr segregated at the grain boundaries has a different chemical state than the fully substitutional Cr in the film, near edge fine structure of the Cr $L_{2,3}$ EELS signal is investigated. More specifically the ratio between the L_2 and L_3 peaks of the Cr core loss edge has been investigated, a method commonly used to access the valence state of transition metals. For this, the background subtracted Cr $L_{2,3}$ edge of the areas highlighted in **Figure 4.7b** are normalized to the maximum of intensity of the L_3 peak (**Figure 4.8**).
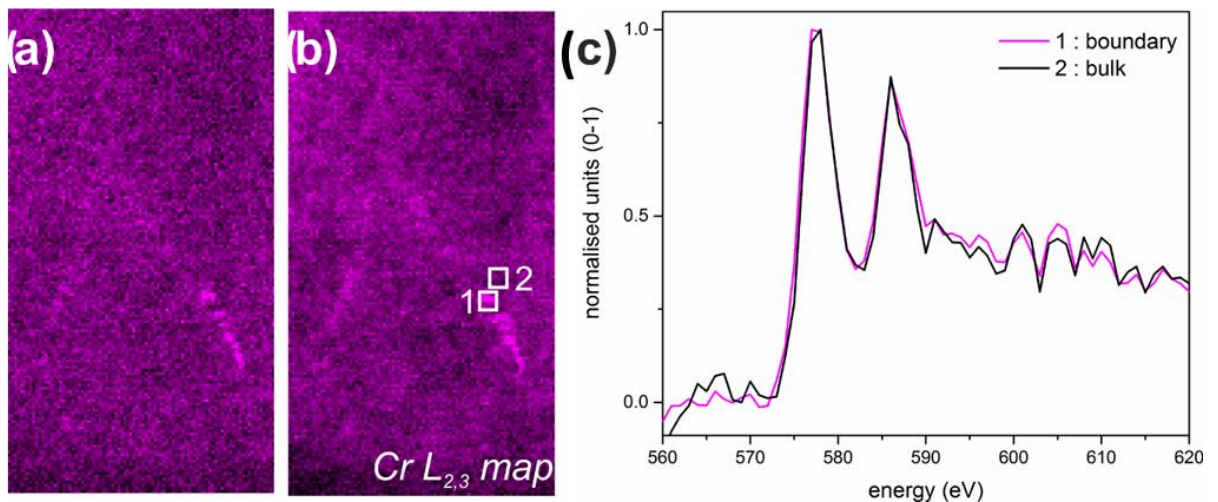
Figure 4.8: EELS maps of the Cr $L_{2,3}$ edge produced using (a) raw and b) PCA treated data respectively., showing enhanced Cr signal at the grain boundary. The map in (b) corresponds to the map showing in Figure 7c. (c) background-subtracted Cr $L_{2,3}$ edge extracted from the grain boundary and bulk regions (same as **Figure 4.7e**), normalized to the maximum of the L_3 peak.

It can be seen that L_3/L_2 intensity ratio does not appear to change between the bulk and of grain boundary regions indicating that the nominal valence state of Cr is similar throughout the specimen [23,24].

The uniform distribution of Cr in the film agrees well with the measured ferromagnetic properties [143], in contrast to a recent report of Cr segregation at the surface resulting in superparamagnetic behavior of Cr doped Bi_2Se_3. Even though the segregation of the Cr is not desired in the films, as long as the majority of the grain

boundaries are within the interior of the film (as observed in this study) they should not strongly affect the Dirac surface states, which are macroscopic states spanning over the entire surface of the contiguous film. In order to suppress the formation of grain boundaries, a growth at lower growth temperatures and lower growth rates is suggested.

4.4.   Discussion

The results presented clearly show a regular QL stacking of the Bi$_2$Se$_3$ film, with the exception of the first several atomic layers in the initial growth. The spectroscopy data gives direct evidence that Cr is preferentially substituting for Bi in the Bi$_2$Se$_3$ host. Furthermore, the results show that Cr has a tendency to segregate at internal grain boundaries of the Bi$_2$Se$_3$ film.

In the case of PCA, the choice of 3 components was based on the scree plot of the datasets, which flattens out after component 3, indicating that the remaining factors relate to a very small proportion of the variability and are likely attributed to noise [144]. Although not atomically resolved the raw data already shows a Cr signal variation, with the higher intensity localized in the QL. Data treated by PCA reveal that the maxima of EELS intensities are localized in the Bi columns. To make this point clear, the integrated intensity profiles of the maps in **Figure 4.6** against the integrated intensity profile of the simultaneously acquired HAADF signal (**Figure 4.9b**) is plotted. The intensity profile of the unprocessed data follows the general trend of the HAADF signal, localizing the Cr signal within the quintuple Bi$_2$Se$_3$ layers. Upon PCA treatment it is evident that the maxima of the Cr $L_{2,3}$ intensity profile coincide with the maxima of the HAADF intensity profile (**Figures 4.9c and 4.9d**) ; confirming that the Cr dopants are localized in the Bi sites. In order to exclude any processing artefacts, the background subtracted Cr $L_{2,3}$ edges before and after PCA (3 components) are plotted in **Figure 4.9c**. Both spectra show a clear Cr $L_{2,3}$ signal with the treated spectra being denoised.
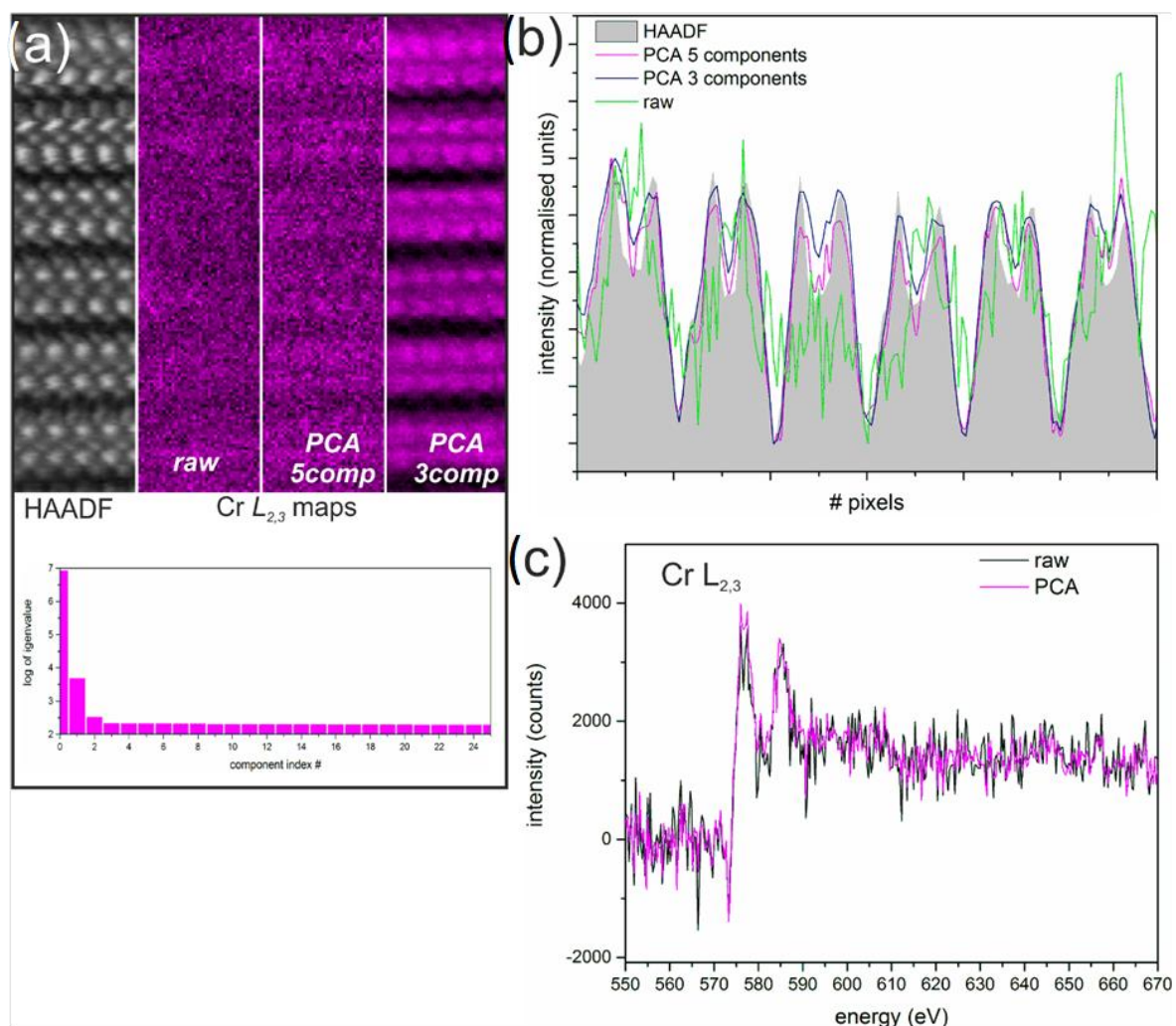
Figure 4.9: (a) HAADF-STEM signal, Cr $L_{2,3}$ intensity maps (raw and treated by PCA, respectively) and Scree plot, (b) integrated intensity profiles of the HAADF signal and Cr $L_{2,3}$ maps corresponding to (a). (c) Background subtracted Cr $L_{2,3}$ EELS edge before and after PCA (3components) showing the reduction of noise.

Similarly data acquired at a dispersion of 1eV/channel, including both Cr and Se $L_{2,3}$ edges show the anti-correlation relationship between Cr and Se signals, confirming that the Cr atoms reside in Bi sites.

Further overview and high magnification HAADF and BF-STEM images taken from the JEOL 2200 microscope in York are presented as **Figure A1** and can be found in appendix section.

4.5.   Conclusion

In this chapter, a structural study of a single-crystalline, Cr doped Bi$_2$Se$_3$ film on Al$_2$O$_3$ (0001) was shown. Structural and spectroscopic studies using aberration-corrected STEM-EELS have shown that Cr incorporation in Bi$_2$Se$_3$ film proceeds via substitution of Bi atoms. For the investigated Cr concentration of 4.6 at-% the dopant does not disturb the rhombohedral Bi$_2$Se$_3$ structure. Additionally, segregation of Cr at the grain boundaries of the film was found. By controlling the density of defects and controlling the growth conditions Cr segregation at the boundaries can be minimized and incorporation of Cr in Bi$_2$Se$_3$ films can be achieved via uniform substitution of Bi.

5   Experimental and density functional study of Mn doped Bi$_2$Te$_3$ topological insulator

This chapter is based on the work published in [118] and forms a natural comparison with the work performed in the previous chapter and next chapters.

In this chapter, a nanoscale structural and density functional study of the Mn doped 3D TI Bi$_2$Te$_3$ is demonstrated. XANES shows that Mn has valency of nominally 2+. EXAFS in combination with EELS shows that Mn is a substitutional dopant of Bi and Te and also resides in the vdW gap between the QLs of Bi$_2$Te$_3$. Combination of aberration-corrected STEM and EELS show that Mn substitution of Te occurs in film regions with increased Mn concentration. First-principles calculations show that the Mn dopants favor octahedral sites and are ferromagnetically coupled.

Bi$_2$Te$_3$ and Al$_2$O$_3$ both belong to trigonal crystal system which contains both hexagonal and rhombohedral lattice systems. The Bi$_2$Te$_3$ film and Al$_2$O$_3$ substrate have $R\bar{3}m$ and $R\bar{3}ch$ space groups, respectively.

the Mn atoms can occupy various places in the Bi$_2$Te$_3$ lattice. They can substitute Bi and Te atoms as well as sitting in the vdW gap between the QLs of Bi$_2$Te$_3$ film.

In this chapter the film was produced by Prof. Hesjedal in the Physics department of University of Oxford, Oxford. The atomically resolved STEM-EELS have been performed by Dr. D. Kepaptsoglou and Prof. Q. Ramasse in the SuperSTEM national laboratory, Daresbury. Moreover, the XANES and EXAFS measurements and fittings have been performed by Dr. A. I. Figueroa and Prof. G. van der Laan at Diamond Light Source, Didcot. Furthermore, the DFT calculations have been performed in York using the CASTEP code.

5.1.   Introduction

A typical representative of a 3D TI is Bi_2Te_3, a narrow-gap semiconductor with an indirect band gap of 160 meV at 300 K. The unit cell of Bi_2Te_3 is composed of three weakly bonded Te-Bi-Te-Bi-Te QLs with a hexagonal crystal structure [134]. However, Bi_2Te_3 exhibits no magnetic ordering, and single crystals are typically p-type semiconductors that can become superconducting under pressure [145].

In order to induce magnetic ordering in Bi_2Se_3 or Bi_2Te_3, doping with transition metals is an established route [117, 134]. Upon doping with magnetic elements, TRS can be broken and the Dirac electrons can become effectively massive [135]. According to first-principles calculations, this is the case when TIs are doped with V, Cr, Mn, or Fe, which can break TRS and open a band gap in the surface band structure [136]. Even though long-range ferromagnetic order has been reported at low temperatures in materials such as Cr-doped Bi_2Se_3 [137, 146], Mn- and Fe-doped Bi_2Se_3 [63, 65], and Bi_2Te_3 [147] the correlation between local chemical environment of magnetic dopant and magnetic order is not well understood. Indeed, direct correlation between the magnetic dopants concentration and functional properties of TIs could be rather challenging, for example doping with Mn in many host materials results in structural or chemical inhomogeneities affecting the magnetic properties [63]. The main goal of achieving room-temperature ferromagnetism in homogeneously doped 3D TIs has therefore proven difficult to achieve [148]. Although Mn doped Bi_2Te_3 crystals and thin films with doping concentrations of up to 10% were found to be ferromagnetic with Curie temperatures of around 10 K [149], it is not clear if ferromagnetism is due to secondary, undesirable Mn-containing phases or the homogeneous doping of Mn into the Bi_2Te_3 matrix, i.e., as a substitutional dopant. Due to the layered crystal structure of these materials, several possible lattice sites exist for the incorporation of magnetic dopants. These include substitutional incorporation on Bi or Te sites within the QLs, as well as interstitial incorporation within the QLs, and the incorporation in the vdW gap between the QLs [149].

In these ternary systems, it is of great importance to preserve the overall bulk electronic properties upon doping, and, moreover, to reduce the defect densities in

general. In this chapter it is demonstrated that the low Mn doping concentrations (~ 2.5 at-%) in the Bi$_2$Te$_3$ preserved the structural integrity of the thin film. It is also shown that, by using real space atomic imaging and X-ray spectroscopy, even at this low doping concentrations Mn is substitutionally incorporated into Bi$_2$Te$_3$, as well as in the vdW gap. First principle calculations performed for number of Mn configurations as a substitutional and interstitial dopant show that ferromagnetic ordering is favored. At higher doping concentrations (*e.g.* ~ 6 at-%) secondary phases appear and the crystallinity of the matrix is significantly deteriorated. This work show that inducing long range ferromagnetic order by Mn doping Bi$_2$Te$_3$ can be achieved even at low concentrations, independent of the local chemical environment.

5.2.   Methods

The Mn doped Bi$_2$Te$_3$ thin films were grown by MBE on *c*-plane sapphire substrates. Prior to growth, the samples were solvent-cleaned and baked in the load-lock for 8 hours. First, a Bi$_2$Te$_3$ buffer layer was deposited at a substrate temperature of 200°C. The doped layers were then grown with a Mn doping concentration ranging from ~2% to 9%, measured with an *in-situ* beam-flux monitor (BFM), and given in % with respect to the Bi flux, at a substrate temperature of 250°C. Standard effusion cells were used for the co-deposition of Bi, Mn, and Te. All evaporation materials used were of 99.9999% purity and the films were deposited in a Te-rich environment to reduce the formation Bi-Te anti-site defects and Te vacancies. Growing with a Bi:Te flux ratio of 1:10, the deposition rate is Bi-limited at $\sim$ 0.4 nm min^{-1}. Nominal Mn-doping concentrations were adjusted using the Mn:Bi flux ratio, as measured by the BFM.

The film quality was evaluated using XRD. Judging from the film peaks observed in the out-of-plane XRD spectra, the 2.5% Bi$_2$Te$_3$ film is rhombohedral, *c*-axis oriented, and free of peaks from secondary phases.

Cross-sectional TEM specimen preparation was done by FIB methods using a FEI Nova 200 NanoLab high-resolution field emission gun scanning electron microscope. A protective layer of C was thermally evaporated onto the film surface outside of the FIB

chamber; two further sacrificial layers of Pt were deposited by the electron and ion beams to protect the film from Ga-ion implantation and damage.

Structural characterization STEM imaging and EEL Spectroscopy measurements were performed in a Nion UltraSTEM100^{TM} equipped with a Gatan Enfina spectrometer. The microscope was operated at 100 kV, with a convergence angle of 30 mrad; at these optical conditions the electron probe size is determined to be ~0.9 Å. The inner detector angle for high-angle annular dark field (HAADF)-STEM imaging was 76 mrad. The native energy spread of the electron beam for EELS measurements was 0.3 eV, with the spectrometer dispersion set at 0.3 and 1 eV/channel, depending on the required energy range. The EELS collection angle was 31 mrad. For enhancing the contrast of the atomically-resolved spectra, a noise-reduction routine was applied using PCA (CiMe-plugin for Gatan's Digital Micrograph 2.3 software suite) [124]. Due to the overlap of the Te $M_{4,5}$ and Mn $L_{2,3}$ core loss edges (and O K at the interface), elemental maps were are created by multiple linear least squares (MLLS) fitting [150] or reference spectra, after background subtraction using a power law. The fitting was performed using the routine built in Gatan's Digital Micrograph software suite and reference Te $M_{4,5}$ and Mn $L_{2,3}$ edges (available in the Gatan EELS atlas) and where applicable the O K edge (acquired from the Al$_2$O$_3$ substrate) as fitting components, respectively.

XANES and EXAFS spectra were collected at room temperature at the Mn K edges of Mn doped Bi$_2$Te$_3$. A Mn foil and powdered MnO, Mn$_2$O$_3$ and MnTe compounds were measured as references. The powdered standards were pressed into pellets with the optimized quantity for measurements in transmission mode. A nine-element Ge fluorescence detector was used to measure the thin films, with the beam at grazing incidence (<5°) with respect to the sample plane. All spectra were acquired in quick-EXAFS mode with monochromatic beam from the Si(111) crystals. The energy range for each scan allowed us to extract information in the extended region up to $k = 12$ Å^{-1}. EXAFS spectra were processed and analyzed using different tools of the IFFEFIT XAFS package [151]. Fits of the EXAFS signal were performed on the R space in a range from 1.5 to 3.2 Å using a sinusoidal window function, so that it covered Mn in the first coordination shell. The parameters fitted were the interatomic distance (R), the Debye-Waller factor (σ^2) for each scattering path, and a general shift in the threshold energy (ΔE_0). The amplitude

reduction factor S_0^2 was set to that obtained for the fit of the MnTe standard ($S_0^2 = 0.71$). Data analysis and fitting on all references and samples were performed in ARTEMIS, making use of models based on crystallographic information obtained from the ICSD database. The atomic clusters used to generate the scattering paths for fitting were generated with ATOMS [152].

Structure optimization, total-energy and electronic-structure calculations were performed from first-principles using the plane-wave DFT program CASTEP [133] with the generalized gradient approximation (GGA) of Perdew-Burke-Ernzerhof (PBE) [153] for the exchange-correlation functional. Ultrasoft pseudopotentials were used for each element, with a 500 eV plane-wave cut-off energy. Internal atomic positions were fully optimized until the force on each atom is ≤ 0.05 eV Å^{-1} and the total energy converges within 0.02 meV/atom. The BZ was sampled using a Monkhorst-Pack [154] k-mesh of 5×5×1 for bulk Bi$_2$Te$_3$ and a k-mesh of 3×3×1 for all 2×2×1 supercell systems with Mn. Hexagonal lattice constants for bulk Bi$_2$Te$_3$ ($a = 4.43$ Å and $c = 30.53$ Å) were also calculated from first-principles. Semi empirical dispersion correction (SEDC) [155] is included to account for the weak vdW interactions between Bi$_2$Te$_3$ QLs. All calculations were taking spin polarization into account. SOC was not included as initial tests showed that it does not play an important role with respect to relative energy differences between different configurations.

5.3.   Results

Figure 5.1a shows a cross-sectional overview of a Mn$_x$Bi$_{2-x}$Te$_3$ thin film grown on c-plane Al$_2$O$_3$ by MBE. The atomic number dependence (~Z$^{1.8}$) of the HAADF contrast clearly outlines the Bi$_2$Te$_3$ film and the Al$_2$O$_3$ substrate. The film has uniform thickness with a good crystallinity. Atomic resolution HAADF imaging (**Figures 5.1b, 5.1c, and 5.1e)** show the good structural ordering of the film, with distinctive QL repeat unit in different regions of the sample. The abrupt change in HAADF image contrast between substrate and film indicates a chemically abrupt substrate-film interface, while the white fringes are

showing the continuous QL structure of the film. The XRD further shows the single crystalline nature of the grown films on a larger scale (**Figure 5.1d**).
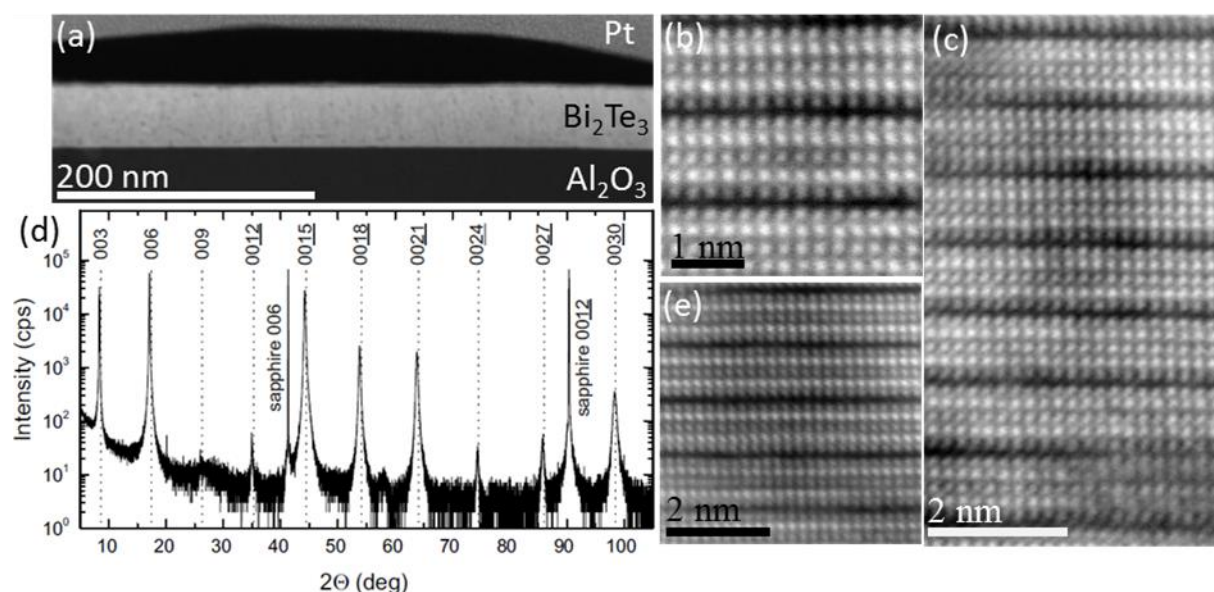
Figure 5.1: (a) Low magnification HAADF-STEM image of the Bi$_2$Te$_3$ film on Al$_2$O$_3$ (0001) substrate. (b), (c), and (e) are atomically resolved HAADF-STEM images of different places of the Bi$_2$Te$_3$ film. Good crystalline QL structure of the Bi$_2$Te$_3$ film is present. (d) XRD diagram showing both film and substrate peaks as labelled.

The presence of transition-metal (TM) and rare-earth dopants in the grown film, as well as their chemical state, can be studied by XANES [156], hence this technique is employed to reveal the Mn chemical environment in the grown films. **Figure 5.2a** shows the normalized XANES spectra at the Mn K edge of the doped Bi$_2$Te$_3$ thin film. Comparison of the energy position of the absorption jump for the thin film with the references of the relevant standard compounds suggests that the Mn dopants in Bi$_2$Te$_3$ have a valence state close to that of the MnTe, implying 2+. These results are in good agreement with TM dopants, such as Cr, Mn and Fe, in Bi$_2$Se$_3$ TI thin films determined by XAS and x-ray magnetic circular dichroism at the TM $L_{2,3}$ and K edges [65, 140, 141].

The local ordering structure of the Mn doped Bi$_2$Te$_3$ thin film can be studied from the $\chi(k)$ EXAFS signal through a Fourier transform (FT) analysis, shown in **Figure 5.2b**,

performed over a k range of 2.5 to 10.5 Å^{-1} using a k^2 weight, a $\Delta k = 1$ Å^{-1}, and a sinusoidal window function.
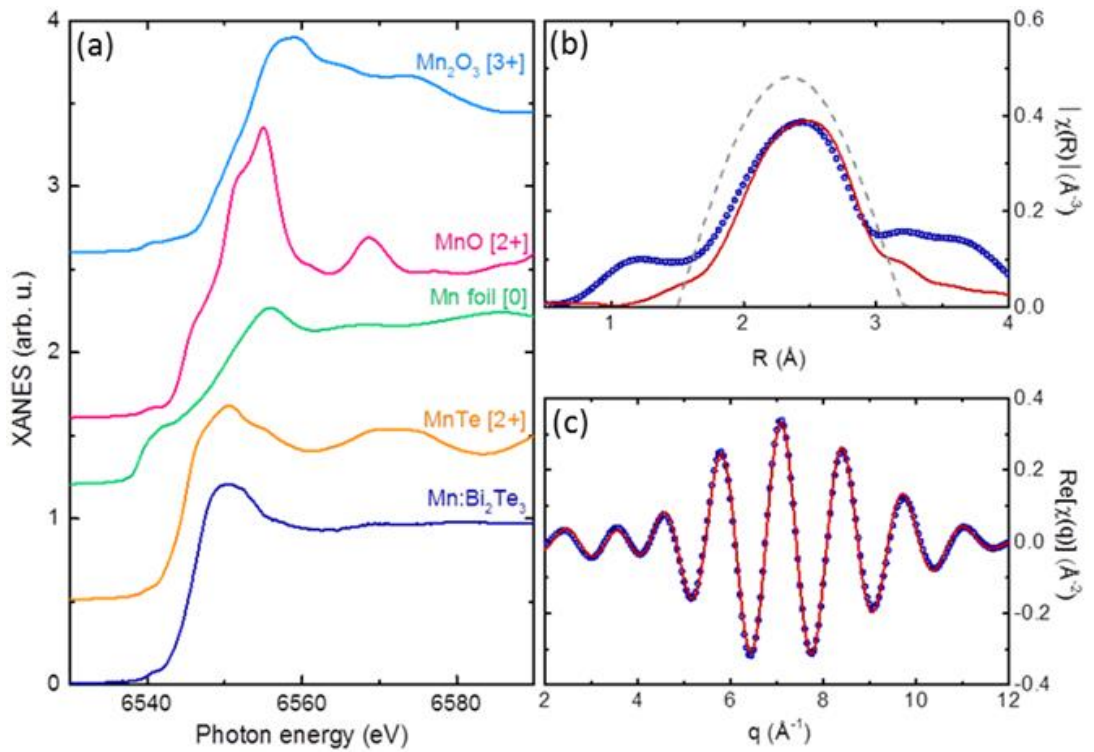
Figure 5.2: (a) Mn K edge XANES for a Mn doped Bi$_2$Te$_3$ thin film and comparison with MnTe, MnO, and Mn$_2$O$_3$ powder samples, and Mn foil for reference. The Mn oxidation state is indicated in square brackets. The spectra have been offset vertically for clarity. (b) Fourier transform of the EXAFS signal at the Mn K edge on the thin film (symbols) together with the best fit to the first coordination shell (solid line). The dotted curve shows the sine window function. (c) Contribution of the first coordination shell to the EXAFS signal (symbols) together with its best fit (solid line).

The best fits of the FT magnitude, $|\chi(R)|$ (**Figure 5.2b** and the real part of its inverse FT, Re $|\chi(q)|$, in **Figure 5.2c**) were achieved with Mn in an octahedral environment of Te (and Se) atoms. We note that the presence of Se in the samples was due to unintentional Se doping during growth in the Se-Te MBE system. The values of the structural parameters obtained from the fit are listed in **Table 5.1**, together with the

nominal coordination and bonding of Bi atoms in Bi$_2$Te$_3$ and Bi$_2$Se$_3$. Comparison of Mn-Te and Mn-Se distances with Bi-Te and Bi-Se of the undoped structure (**Table 5.1**) shows a strong local contraction of the bonds, which has been observed in similar TM-doped structures [65, 141]. The σ^2 values are high in all cases, which can be understood as a high dispersion of bond distances and an increasing structural disorder in the crystal with incorporation of Mn, suggesting that Mn neighbourhood is rather heterogeneous.

Table 5.1: Structural parameters obtained from Mn K edge EXAFS fits for the Mn doped Bi$_2$Te$_3$ thin film shown in **Figure 5.2b**. Nominal coordination and bonds of Bi$_2$Te$_3$ and Bi$_2$Se$_3$ according to the crystallographic information in ICSD database are listed for comparison. Coordination number, N, interatomic distance, R, and Debye-Waller factor, σ^2, for each path are shown. A value of ΔE$_0$ = (3.3 ± 0.9) eV was obtained from the fit.

Mn:Bi$_2$Te$_3$	Mn-Te1	Mn-Te2	Mn-Se
N	1.5	1.5	3
R (Å)	2.93 ± 0.02	3.07 ± 0.02	2.70 ± 0.02
σ^2 (Å^2)	0.026 ± 0.005	0.026 ± 0.005	0.009 ± 0.005
Bi$_2$Te$_3$	**Bi-Te1**	**Bi-Te2**	-
N	3	3	-
R (Å)	3.033	3.248	-
Bi$_2$Se$_3$	**Bi-Se1**	**Bi-Se2**	-
N	3	3	-
R (Å)	2.952	3.021	-

Oxidation effects might also play a role in the structural disorder, as observed for Fe dopants in Bi$_2$Se$_3$ [65] and rare-earth dopants in Bi$_2$Te$_3$ [156]. However, the extracted contributions of MnTe, MnSe, and Mn$_2$O$_3$ from the linear combination fit of the XANES region shows that the electronic structure of the Mn doped Bi$_2$Te$_3$ is more similar to the MnTe than the oxides, **Figure 5.3** and **Table 5.2**.
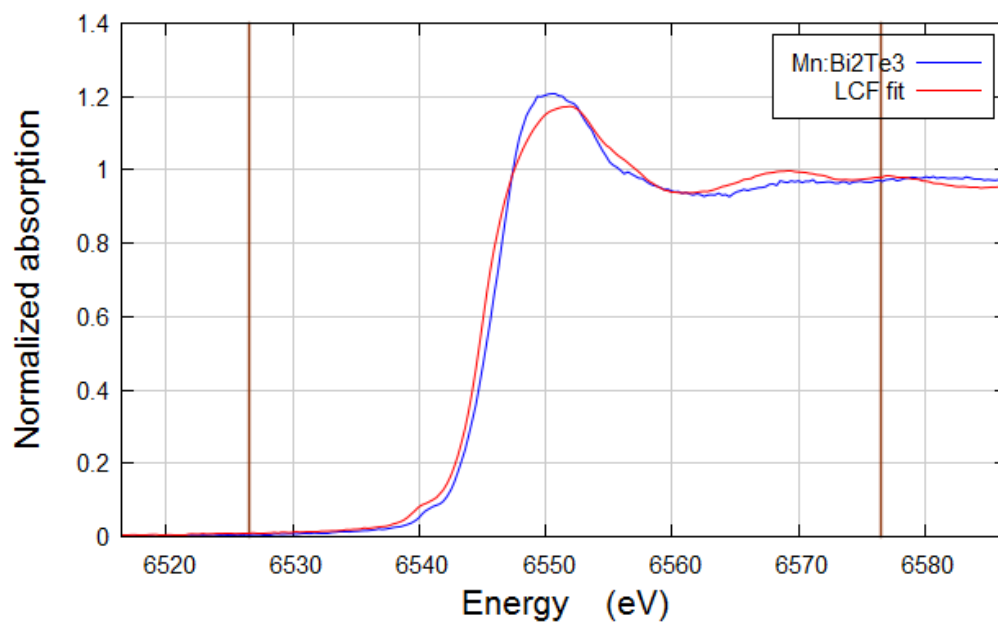
Figure 5.3: Linear combination fit (LCF) of the XANES region using MnTe, MnSe and Mn_2O_3 as standards (red) with the XANES signal of the Mn doped Bi_2Te_3sample (blue).

Table 5.2: Contribution from each component extracted from the fitting shown in **Figure 5.3.**

Standard	Weight
MnTe	0.470 ± 0.027
MnSe	0.498 ± 0.030
Mn_2O_3	0.032 ± 0.004
TOTAL	1.000

These results point to Mn dopants incorporating heterogeneously, both as a substitutional and interstitial in the vdW gap within the structure; hence, the varied bonding environment rather than at well-defined crystallographic positions.

Next spatial distribution of the Mn dopants on a nanoscale in the Bi$_2$Te$_3$ film is investigated. Direct imaging of Mn dopants at atomic resolution by Z-contrast in the HAADF images is particularly challenging due to the low Z of Mn (Z_{Mn}=25) in comparison to Bi (Z_{Bi}=83) and Te (Z_{Te}=52), as well as the low concentration of Mn in the film.

In order to get an unambiguous signature of the Mn spatial distribution in the film on nanometer scale, spatially resolved STEM-EELS measurements is employed. A large field-of-view HAADF-STEM image of the film in cross-section shows the characteristic QL structure of the Bi$_2$Te$_3$ film, **Figure 5.4a**. At closer inspection it can be seen that the HAADF image intensity of the film is not uniform; patches of lower intensity (dark patches) can be observed throughout, indicating a compositional variation across the film, possibly due to a non-uniform distribution of the Mn dopants.

In order to test this hypothesis, EELS elemental mapping has been performed, as marked by a brown rectangle in **Figure 5.4a** and enlarged in **Figure 5.4b**. Simultaneous acquisition of EELS has been used to produce elemental maps of Mn and Te shown in **Figures 5.4c and 5.4d**. The elemental maps show that Mn is present throughout the film (**Figure 5.4c**), although its distribution is not uniform. In fact, the observed dark patches in the HAADF images correlate directly with the regions of higher Mn presence, confirming that the observed dark patches have increased Mn concentration, compared to the rest of the film. Moreover, comparing the Te elemental map (**Figure 5.4d**) to Mn and the HAADF signals (**Figures 5.4c, 5.4b,** and extracted spectra in **5.4e**), one finds that the dark regions in HAADF have a lower Te concentration.
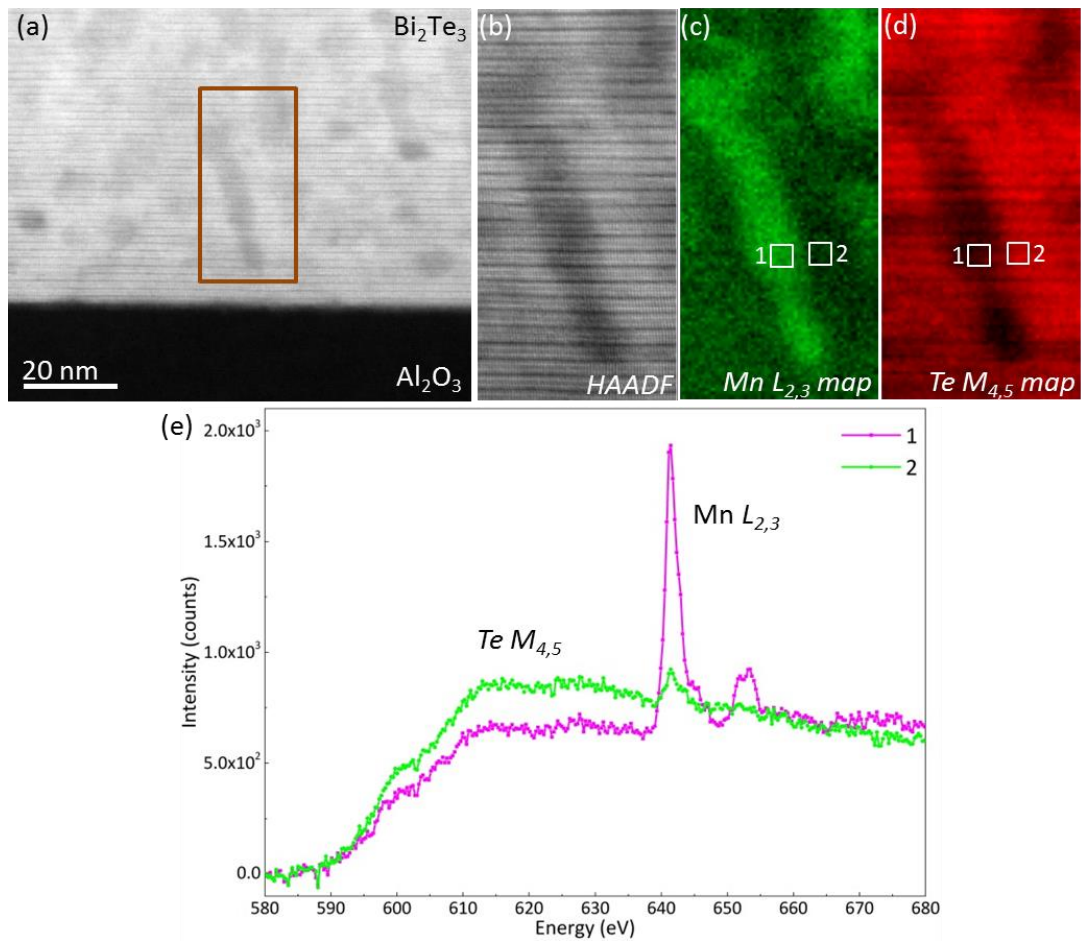
Figure 5.4: (a) HAADF-STEM survey image from the Bi$_2$Te$_3$. (b) HAADF-STEM signal from the region of interest outlined in (a), produced simultaneously with the EELS acquisition. (c) Mn $L_{2,3}$ EELS signal showing higher concentration of Mn in the dark patch areas visible in (b). (d) Te $M_{4,5}$ EELS signal showing a distribution anti-correlated to that of Mn. (e) Background-subtracted Mn $L_{2,3}$ and Te $M_{4,5}$ edges obtained from the grain-boundary and off-boundary regions labelled as 1 and 2 in (c) and (d), showing enhanced Mn signal and decreased Te signal at the grain boundary.

The decrease of the Te signal in these areas (and relative increase in Mn content) while clearly retaining the ordered atomic structure of the QLs suggests that in regions with increased Mn concentration Mn also substitutes Te– in addition to the predicted more energetically favorable Bi atomic positions, as has been reported previously [157].

Furthermore, the correlation between the dark patches and the Mn signal in other regions of the sample as shown in **Figure 5.5** is also investigated. **Figure 5.5a** shows an overview HAADF-STEM image from another region of the sample with dark patches. **Figure 5.5b** shows the magnified region outlined with a brown rectangle in **Figure 5.5a**. Four regions with different contrasts of dark patches, as outlined with blue, red, green, and black rectangles in **Figure 5.5b**, is investigated. **Figure 5.5c** shows the background subtracted Mn $L_{2,3}$ and Te $M_{4,5}$ edges from simultaneously collected EELS spectra.
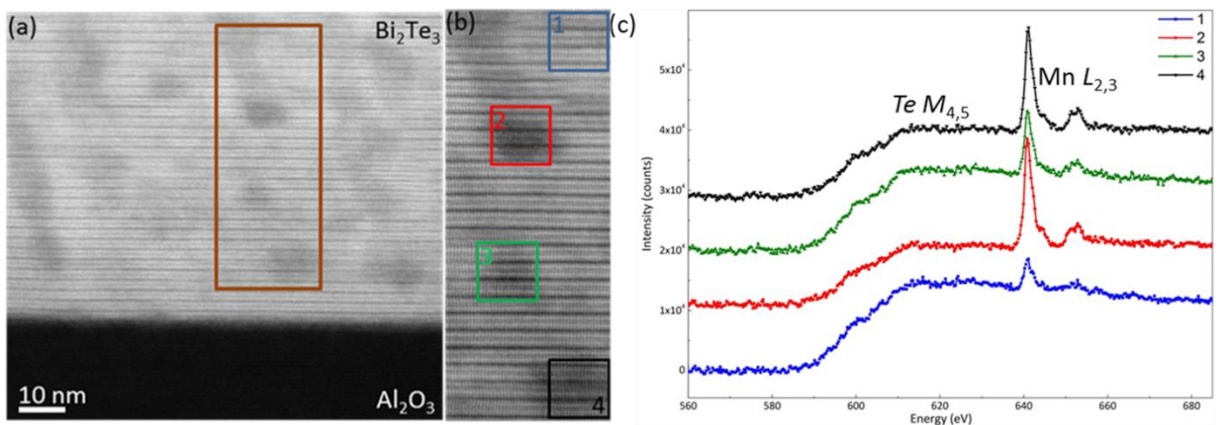
Figure 5.5: (a) Low magnification HAADF-STEM image of the Bi_2Te_3 film and the Al_2O_3 substrate. (b) HAADF-STEM signal from the region of interest outlined in (a). (c) Background-subtracted Mn $L_{2,3}$ and Te $M_{4,5}$ edges extracted from the regions shown in (b). Spectra have been shifted vertically for clarity.

The extracted EELS spectra show that the region with higher dark contrast (Red) has the highest Mn $L_{2,3}$ signal and the region with lower dark contrast (Blue) has the lowest Mn $L_{2,3}$ signal.

Similar analysis at the interface region is shown in **Figure 5.6**, which also indicates the Mn segregation at the interface within 1 nm region. As for the presence of oxygen in the EELS map (**Figure 5.6d**) , the EELS measurements were performed on thin foils, which have been exposed to air for some time before observation in the electron microscope, and therefore the presence of some degree of surface oxidation cannot be avoided.
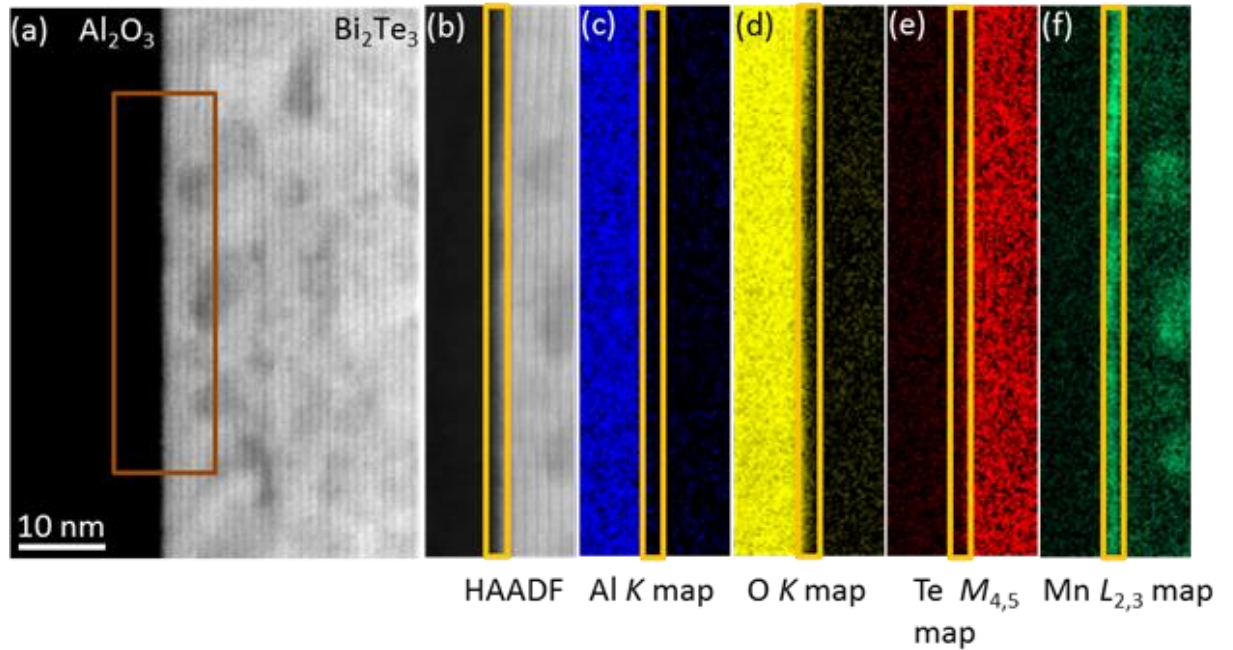
Figure 5.6: (a) HAADF-STEM survey image in which the region selected for simultaneous acquisition of EELS for elemental mapping is highlighted. (b) Magnified HAADF image outlined with brown rectangle in (a). The elemental Al, O, Te, and Mn maps are shown in (c), (d), (e), and (f), respectively. Al and Te elemental maps in (c) and (e) show no intermixing between substrate and film. The Mn elemental map (f) shows the segregation of Mn at the interface.

The results from STEM-EELS confirm the EXAFS results showing that the local environment of the Mn atoms in the Bi$_2$Te$_3$ thin film is heterogeneous. The large variability in measured Mn-Te distances, as shown in **Table 5.1**, is consistent with Mn incorporating substitutionally on Bi sites but also as interstitials in the vdW gap.

In order to shed light on the atomic coordination sites of the Mn presence in the Bi$_2$Te$_3$ film, as well as for understanding the magnetic ordering in the material due to incorporation of Mn in the possible substitutional and interstitial sites, first-principle calculations has been performed. On a 2×2×1 supercell, the energetics and magnetic ordering of the preferred site of the Mn in the vdW gap, Bi, and Te substitutions are investigated. For this purpose 16 different configurations have been considered, as the

two Mn atoms can occupy multiple sites in the vdW gap as well as in the same or in different QLs.

First the results for the Mn residing in the vdW gap will be given. **Figure 5.7a** shows the typical QLs bulk-structure of Bi$_2$Te$_3$. **Figure 5.7b** shows the model of the energetically most favorable configuration of Mn atom residing in the interstitial sites, i.e., the octahedral (B-B$_1$) sites. Total-energy calculations found that Mn on the B site is by 0.19 eV energetically more favorable than the tetrahedral (A) site. In all considered configurations of Mn in the vdW gap the preferred Mn positon remains on the octahedral B sites.

These calculations are consistent with the EXAFS results presented above. In addition, the calculations show that Mn atoms prefer to stay in the same vdW gap rather than move to the next gap.
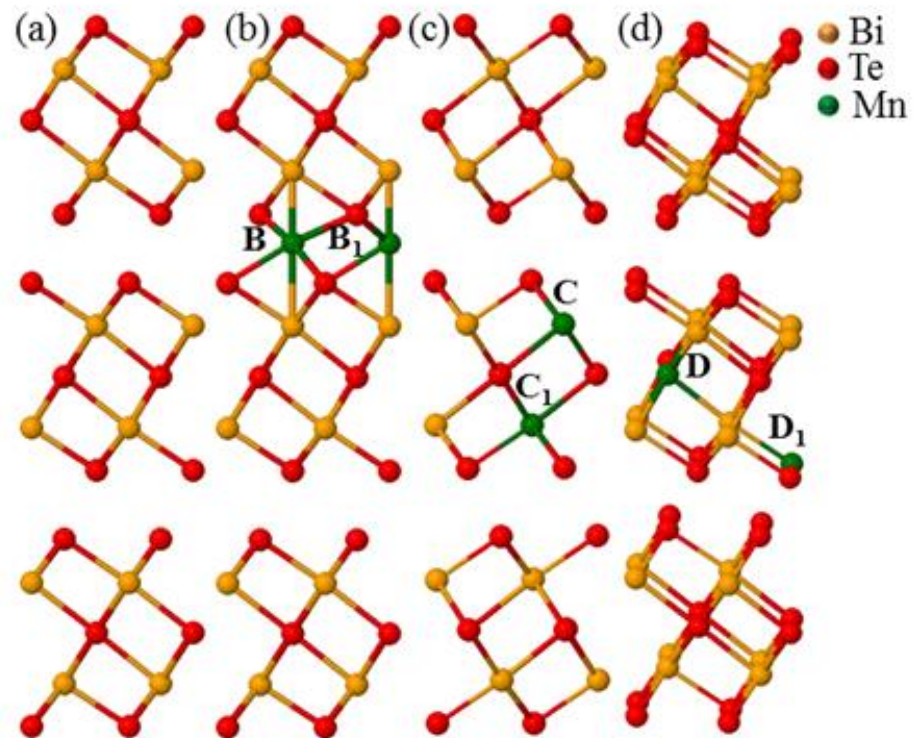
Figure 5.7: The most energetically favorable configurations for Mn occupying the available interstitial and substitutional sites. (a) Shows the QL structure of Bi$_2$Te$_3$ with no Mn dopant. (b) Shows the most favorable configuration when Mn dopants octahedrally occupy the van der Waals gap (B and B$_1$). (c) The most favorable configuration when Mn atoms substitute the closest Bi sites in two different Bi planes (C and C$_1$). (d) Shows the energetically favorable position when Mn dopants occupy the furthest Te sites in two nearby Te planes (D and D$_1$). The model has been tilted for clarity. Bi, Te, and Mn atoms are represented by yellow, red, and green spheres, respectively.

Next the energetics of Mn dopants occupying Bi and Te substitutional sites is considered. **Figures 5.7c and 5.7d** show the most favorable configurations of Mn dopants occupying Bi and Te atomic sites, respectively. For Bi substitution most favorable configuration is when Mn atoms occupy the closest Bi sites in two different Bi planes denoted as C and C$_1$, **Figure 5.7c**. In case of Te substitution (**Figure 5.7d**), Mn atoms are most energetically stable when they occupy the furthest Te sites in the same QL, the D

and D_1 sites. For all of the configurations presented above, the ferromagnetic ordering with values of magnetic moment is shown in **Table 5.3**.

Table 5.3: The final magnetic moments for the most energetically favorable configurations of Mn dopants in the Bi_2Te_3 structure. The labels (b, c, and d) refer to the illustrations in **Figure 5.7**.

Model	Mn position	Magnetic moments (μ_B)
(b) **B-B$_1$**	Van der Waals gap	+4.10 − +4.10
(c) **C-C$_1$**	Bi substitution	+4.44 − +4.41
(d) **D-D$_1$**	Te substitution	-5.04 − -5.11

These results show that for considered atomic configurations, independent of Mn occupation site, Mn dopants will tend to be ferromagnetically ordered in Bi_2Te_3 films.

Finally it is shown that films with increased Mn doping concentration (~ 6 at-%) have significant change of their atomic structure and local chemistry, **Figure 5.8**. In these films the QL structure of Bi_2Te_3 is deteriorated and presences of secondary phases, rich in Mn, are observed (**Figures 5.8b and 5.8c**). Hence the benefit of Mn dopants for magnetic 3D TIs based on Bi_2Te_3 is limited to lower Mn dopant concentrations.

We note that further HAADF and BF-STEM images and energy-dispersive X-ray spectroscopy results confirming the EELS analysis are presented as **Figures A2, A3, and A4** of appendix section.
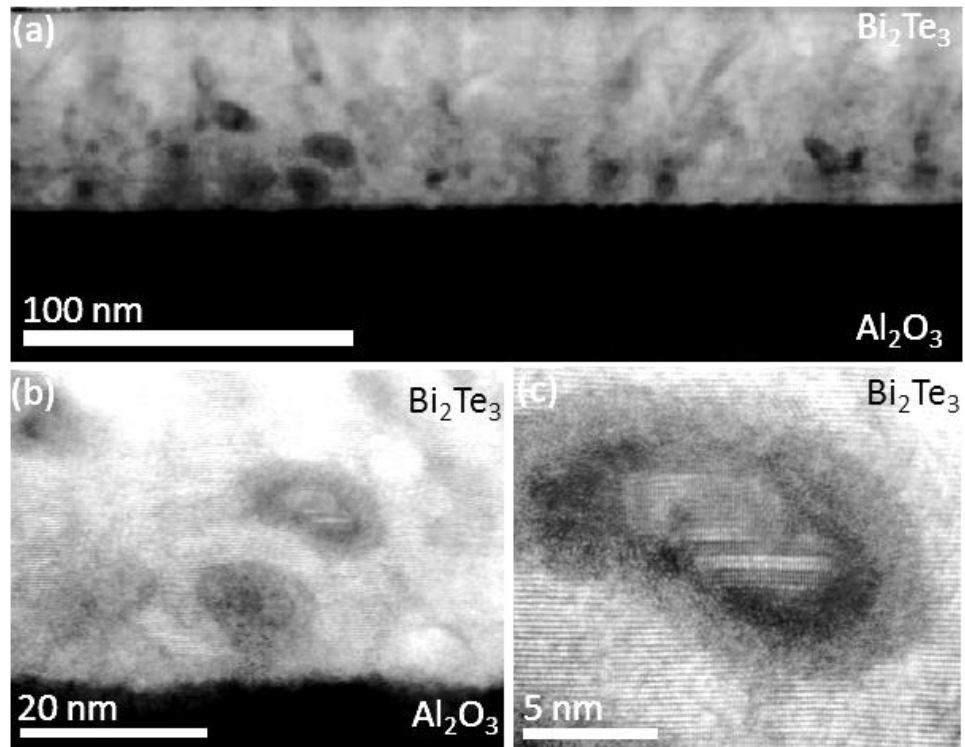
Figure 5.8: (a) Low magnification HAADF-STEM image of the Bi$_2$Te$_3$ film and the Al$_2$O$_3$ substrate with ~ 6 at-% of Mn doping. (b) Shows the regions of the film with dark patches. (c) Shows higher magnification image of the patch area forming secondary phases with deteriorated crystallinity.

5.4. Discussion

The results presented clearly show a regular QL stacking of the Bi$_2$Te$_3$ film. The EELS data gives direct evidence that Mn is substituting in the vdW gap and Te sites in the Bi$_2$Te$_3$ host. The XANES and EXAFS results show that the local environment of Mn is heterogeneous with a tendency of 2+ valency.

In the case of the DFT calculations, the total number of 16 different configurations has been investigated to find the most favorable substitutional sites of Mn. 8 configuration of having the Mn atoms in the vdW gap (**Figure 5.9**).
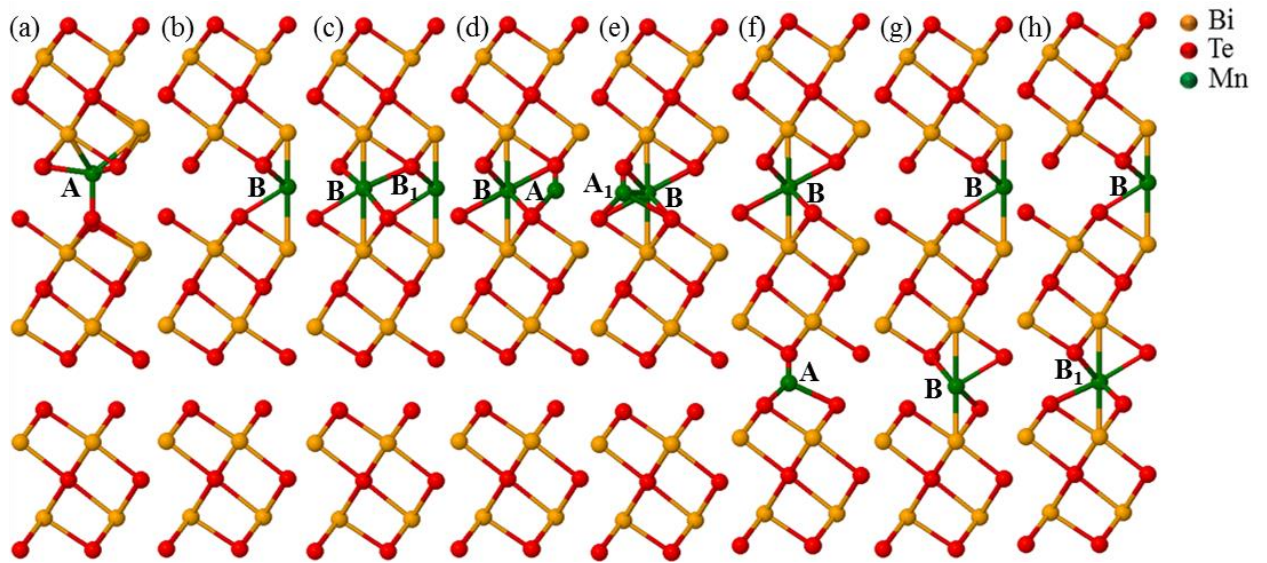
Figure 5.9: Simulation models for Bi_2Te_3 with Mn atoms placed in the van der Waals gap. (a) and (b) show one Mn atom being placed at the tetrahedral (A) and octahedral (B) interstitial sites, respectively. (c) Shows two Mn atoms placed at the two available octahedral sites (B and B_1). (d) and (e) show one of the Mn atoms occupying the B site and the other one occupying the two different available tetrahedral sites (A and A_1). The distance between the two Mn atoms in panel (e) is shorter compared to (d). (f) Shows Mn atoms in a B-A arrangement in two different van der Waals gaps. (g) and (h) show the B-B and B-B_1 arrangements, respectively. The distance between the two Mn atoms in panel (g) is shorter compared to (h). Bi, Te, and Mn atoms are represented by yellow, red, and green spheres, respectively.

As we mentioned in the results section the most favorable position for Mn atoms to occupy in the vdW gap is the B-B_1 site shown in **Figure 5.9c**. Comparing to the B-B_1 site, the rest of the configurations shown in **Figure 5.9d to 5.9h** are less favorable by 0.056, 0.363, 0.38, 0.146, and 0.141 eV, respectively.

3 and 8 different configurations of having the Mn atoms in the Bi and Te atomic sites are also investigated, respectively (**Figure 5.10** and **Figure 5.11**).
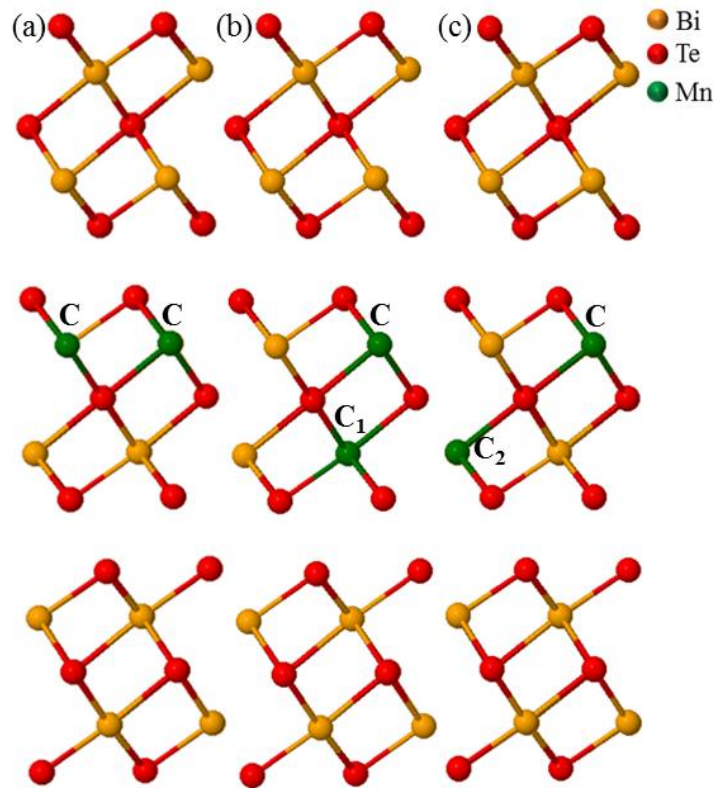
Figure 5.10: Simulation models for Bi_2Te_3 with Mn atoms substituting Bi. (a) Shows two Mn atoms occupying the two nearest Bi atoms denoted as C. (b) Shows the Mn atoms occupying the closest Bi sites in two different planes of the Bi_2Te_3 QL (C and C_1). (c) Shows the Mn atoms occupying the furthest Bi sites in two different planes of the Bi_2Te_3 QL (C and C_2). The Bi, Te, and Mn atoms are represented by yellow, red, and green spheres, respectively.

As we mentioned in the results section the most favorable position for Mn atoms to occupy the Bi atomic column is the C-C_1 site shown in **Figure 5.10b**. Comparing to the C-C_1 configuration, the rest of the configurations shown in **Figure 5.10a and 5.10c** are less favorable by 0.093 and 0.201 eV, respectively
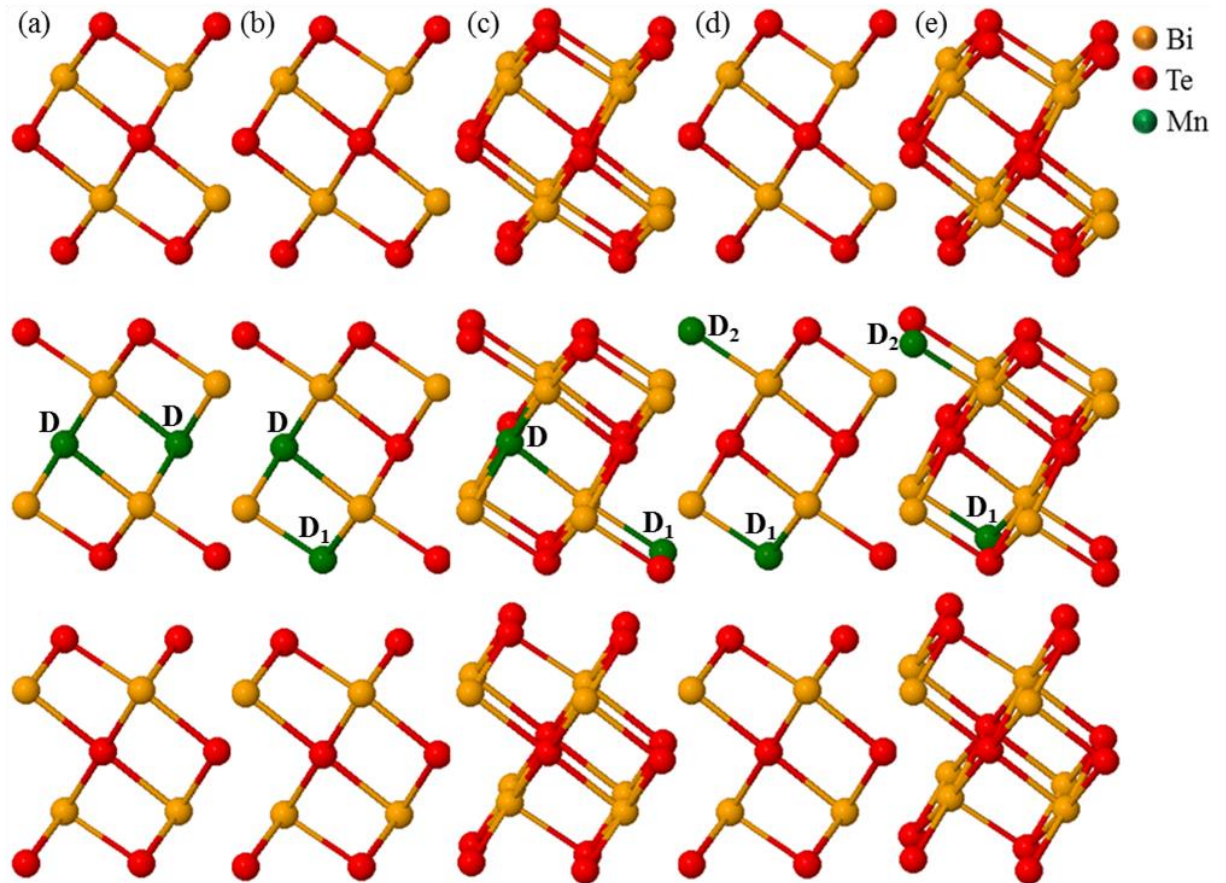
Figure 5.11: Simulation models for Bi_2Te_3 with Mn atoms substituting Te. (a) Shows two Mn atoms occupying the two Te atoms in the same plane (D). (b) and (c) Show the Mn atoms occupying the closest and furthest Te sites in two nearby planes of the Bi_2Te_3 quintuple layer respectively (D and D_1). The distance between the two Mn atoms in panel (b) is shorter compared to (c). (d) and (e) Show the Mn atoms occupying the furthest Te sites possible in a Bi_2Te_3 quintuple layer (D_1 and D_2). The distance between the two Mn atoms in panel (d) is shorter compared to (e). Models in panel (c) and (e) have been tilted for clarity. The Bi, Te, and Mn atoms are represented by yellow, red, and green spheres, respectively.

As we mentioned in the results section the most favorable position for Mn atoms to occupy the Te atomic column is the D-D_1 site shown in **Figure 5.11c**. Comparing to the **Figure 5.11c**, the rest of the configurations shown in **Figure 5.11a, b, d, and e** are less favorable by 1.728, 0.579, 0.297, and 0.481 eV, respectively.

5.5.   Conclusion

In summary, a structural study of Mn doped Bi$_2$Te$_3$ thin films on Al$_2$O$_3$ (0001) substrates was presented. Structural and spectroscopic analysis using aberration-corrected STEM-EELS and EXAFS have shown that Mn dopants in Bi$_2$Te$_3$ film tend to accumulate in the vdW gap as well as enter the lattice substitutionally on Bi sites. In addition, Mn can also substitute Te in regions of very high Mn concentration. Structural optimizations and energy calculations suggests that octahedral sites are the most favorable positions for Mn occupation in the vdW gap. Furthermore, they showed that the closest Bi sites in different planes and furthest Te sites in nearby planes are most favorable configurations for Mn occupying Bi and Te sites, respectively. The DFT calculations for Mn atoms occupying all the different possible sites predict ferromagnetic coupling. This study shows that at low concentrations (*e.g.* ~ 2.5 at-%) Mn can be readily incorporate as a dopant in Bi$_2$Te$_3$ thin films, fully preserving the crystal structure of Bi$_2$Te$_3$ without inducing secondary phases, and hence presents a system with promising properties as a magnetic 3D TI.

6   Van der Waals epitaxy between the highly lattice mismatched Cu doped FeSe and Bi_2Te_3

This chapter is based on the work published in [119] and forms a natural comparison with the works performed in the next chapter.

In this chapter, a structural and DFT study of $Fe_xCu_{1-x}Se$ within the 3D TI Bi_2Te_3 is demonstrated. The $Fe_xCu_{1-x}Se$ inclusions are single-crystalline and epitaxially oriented with respect to the Bi_2Te_3 thin film.

Aberration-corrected STEM and EELS show an atomically-sharp $Fe_xCu_{1-x}Se/Bi_2Te_3$ interface. The $Fe_xCu_{1-x}Se$ /Bi_2Te_3 interface is determined by Se-Te bonds and no misfit dislocations are observed, despite the different lattice symmetries and large lattice mismatch of $\sim$ 19%.

Furthermore, the first-principle calculations show that the large strain at the $Fe_xCu_{1-x}Se$ /Bi_2Te_3 interface can be accommodated via vdW -like bonding between Se and Te atoms.

In this work the film was grown by Prof. T. Hesjedal in the Physics department of University of Oxford, Oxford. Furthermore, the atomically resolved STEM-EELS have been performed by Dr. D. Kepaptsoglou and Prof. Q. Ramasse in the SuperSTEM national laboratory, Daresbury. Prof. P. L. Galindo (Universidad de Cádiz, Spain) using matlab script, on the HAADF image, has provided us with the (x,y) position of the atoms for the displacement calculations.

6.1.   Introduction

Heterostructured materials are the basis of metal–oxide–semiconductor transistor and data storage technologies. Besides the tremendous importance of multi-layered thin films for device applications, heterostructured interfaces have also been for the past decades a playground for the discovery of novel physical phenomena, e.g., the QHE [30]. One of the main criteria for realising new, interface-related heterostructure behaviours is the ability to control the atomic and electronic properties on an atomic level. This typically requires creating epitaxially matched superlattices. One of the main challenges in creating such superlattices is the lattice mismatch between the individual single crystal components [158, 159]. Having different symmetries and lattice parameters lead to built-in strain in the interface region [160], which ultimately changes the electronic properties of the system [161]. Due to the strong chemical bonds between the atomic layers at the heterostructure interface, this effect already occurs at very low values of the lattice mismatch.

In contrast to strongly-bonded heterointerfaces, epitaxial heterostructures can also be realised via weak vdW interactions [162], as demonstrated for heterostructures comprising, e.g., 2D materials, graphene, boron nitride, and transition metal dichalcogenides [104, 112, 163] and layered materials such as Bi_2Se_3 and Bi_2Te_3 [12, 164]. Here, despite the constraints such as large lattice mismatch (up to 19%) and different crystallographic orientations, novel heterostructures can be realized, using these layers as Lego-like building blocks, allowing for the design of atomically thin electronic device materials with outstanding properties [163].

Heterointerfaces have recently also attracted attention as a platform for realizing exotic quantum phenomena, e.g., by combining a superconductor with a TI [109, 165-169]. Proximity effects in this type of interface are predicted to give rise to so-called Majorana fermions [166, 170, 171]. Experimentally, the proximity effect at the superconductor/TI interface has been investigated in $FeTe/Bi_2Te_3$ heterostructures [109, 169, 170, 172, 173], and induced superconductivity in the TI has been observed with a transition temperature (T_c) of around 12 K [109]. Due to the much higher T_c of Cu-based superconductors, other candidates for these heterostructures include CuSe and Cu doped

FeSe and FeTe [174]. The main issues in fabricating such heterostructures are the different crystallographic structure, FeSe has tetragonal structure (*P 4/nmmS*) and Bi$_2$Te$_3$ has trigonal structure ($R\bar{3}m$), and the very large lattice mismatch of 19%.

In this work, it is demonstrated that single-crystalline, misfit-dislocation free interfaces between tetragonal Cu doped FeSe and trigonal Bi$_2$Te$_3$ symmetry lattices with very large lattice mismatch (19%) can be realised, using STEM and EELS. Large inclusions of Fe$_x$Cu$_{1-x}$Se are fully epitaxially embedded in the Bi$_2$Te$_3$ film-matrix. It is shown that the calculated strain energy associated with the large mismatch is rather small; hence no misfit lattice dislocations are formed. An atomically-resolved interface structure analysis of Fe$_x$Cu$_{1-x}$Se /Bi$_2$Te$_3$ shows that the Se and Te atomic columns are relaxed in-plane, so the overall strain is less than 10%. According to DFT total energy calculations, the energy cost associated with such displacements of the atomic columns is less than 0.01 eV, which is significantly lower than the thermal energy at room temperature (0.0257 eV).

6.2.   Methods

The Bi$_2$Te$_3$ thin films were grown by MBE on *c*-plane sapphire substrates using a growth protocol described in detail in Ref [175]. Bi, Fe, Cu and Te were evaporated from standard effusion cells, whereas Se was supplied out of a cracker cell. All elements were of 99.9999% purity. Their flux was monitored using a beam-flux monitor. Fe, Cu, and Se were introduced to the system after growth of several QLs of Bi$_2$Te$_3$. The base pressure of the growth chamber was 1×10^{-10} Torr. The XRD measurements were carried out on a Rigaku Smartlab diffractometer using a rotating Cu anode (incident Cu K-α$_1$ radiation) in the standard Bragg-Brentano geometry.

Cross-sectional TEM specimen preparation was carried out by FIB using a FEI Nova 200 NanoLab instrument. First a ∼ 10-nm-thick layer of carbon was thermally evaporated onto the film surface outside of the FIB chamber to reduce possible charging effects, as well as protecting the surface from damage. Before starting the milling procedure in the FIB, a ∼ 500-nm-thick Pt sacrificial layer was deposited using the electron beam to protect

the film from Ga-ion implantation, followed by a $\sim$ 3-nm-thick Pt layer using the Ga beam to further protect the surface from any implantations and damage during the FIB process. For milling the trenches on both sides of the Pt-deposited area, first the stage is tilted $\pm 2°$ from the position in which the Ga beam is perpendicular to the surface (52°), and then used an ion beam at 30 kV acceleration voltage and 6.5 nA beam current to mill the material out. In order to thin down the sample to the thickness required for 100 kV STEM imaging, after attaching the lamella to the Cu grid, a four steps procedure is used. First, the lamella is tilted by $\pm 2°$ and used a 16 kV beam with 0.47 nA, then tilted $\pm 1.5°$ and used a 16 kV beam, with 0.13 nA and 45 pA. After that, the specimen is tilted for $\pm 1°$ and used a current of 21 pA. For the last thinning step, the lamella is tilted by $\pm 0.5°$ and used 5 kV and 16 pA as beam parameters. When the sample approximately reached the required thickness, a cleaning step is performed by tilting the lamella by 45° and using a 2 kV Ga beam with 10 pA of current.

STEM imaging and EELS measurements were performed in a Nion UltraSTEM100 equipped with a Gatan Enfina spectrometer. The microscope was operated at 100 kV, with a convergence angle of 30 mrad; in these optical conditions the electron probe size is estimated to be $\sim$ 0.9 Å. The inner detector angle for high-angle annular dark field (HAADF)-STEM imaging was 76 mrad. The native energy spread of the electron beam for EELS measurements was 0.3 eV, with the spectrometer dispersion set at 1 eV/channel. The EELS collection angle was 33 mrad. For enhancing the contrast of the atomically-resolved spectra, a noise-reduction routine was applied using PCA (CiMe- plugin for Gatan's Digital Micrograph 2.3 software suite) [124].

Structure optimization, total-energy and electronic-structure calculations were performed from first-principles using the plane-wave DFT program CASTEP [133] with the generalized gradient approximation (GGA) of Perdew-Burke-Ernzerhof (PBE) [153] for the exchange-correlation functional. Ultrasoft pseudopotentials were used for each element, with 600 eV plane-wave cut-off energy for FeSe and FeTe formation energy calculations. Furthermore, a 500 eV plane-wave cut-off energy has been used for the Se bonding energy calculations to investigate the bonding nature of Se atoms in various positions on top of the Bi$_2$Te$_3$. Internal atomic positions were fully optimized until the force on each atom is $\leq$ 0.05 eV Å^{-1} and the total energy converges within 0.02 meV/atom. The BZ was

sampled using a Monkhorst-Pack [154] **k**-mesh of 6×6×6, 5×5×5, 7×7×7, 6×6×4, 9×9×6, and 5×5×1 for bulk Fe, Se, Te, FeSe, FeTe, and Bi_2Te_3, respectively. Trigonal and tetragonal lattice constants for bulk Bi_2Te_3 (a = 4.43 Å and c = 30.53 Å) and FeSe ($a = b$ = 3.68 Å and c = 5.03 Å) were also calculated from first-principles. A semi-empirical dispersion correction (SEDC) [155] is included to account for the weak vdW interactions, as well as a 30 Å-thick space of vacuum on top of the Se atom in the bonding energy calculations.

6.3.   Results

Figure 6.1a shows a cross-sectional HAADF-STEM overview of the Bi_2Te_3 thin film grown on c-plane Al_2O_3 by MBE. Due to the atomic number dependence of the HAADF imaging ($\sim Z^{1.8}$), the Bi_2Te_3 film is clearly outlined with respect to the Al_2O_3 substrate. The film has a uniform thickness of 120 nm and a flat surface morphology. The XRD results further shows the single-crystalline nature of the grown film on a larger length scale (**Figure 6.1b**). The observed family of (003) peaks are representative of the rhombohedral symmetry class of Bi_2Te_3 ($R\bar{3}m$).

Note, however, that the occurrence of the (009), (00$\underline{12}$), and (00$\underline{24}$) peaks is characteristic of until cells distortions, e.g., due to doping [107, 118]. Atomic-resolution HAADF imaging (**Figure 6.1c**) shows the distinctive Te-Bi-Te-Bi-Te QL repeat unit of the Bi_2Te_3 film. The lower intensity regions, close to the interface, correspond to $Fe_xCu_{1-x}Se$ inclusions, as outlined with dashed arrows in **Figure 6.1a**.
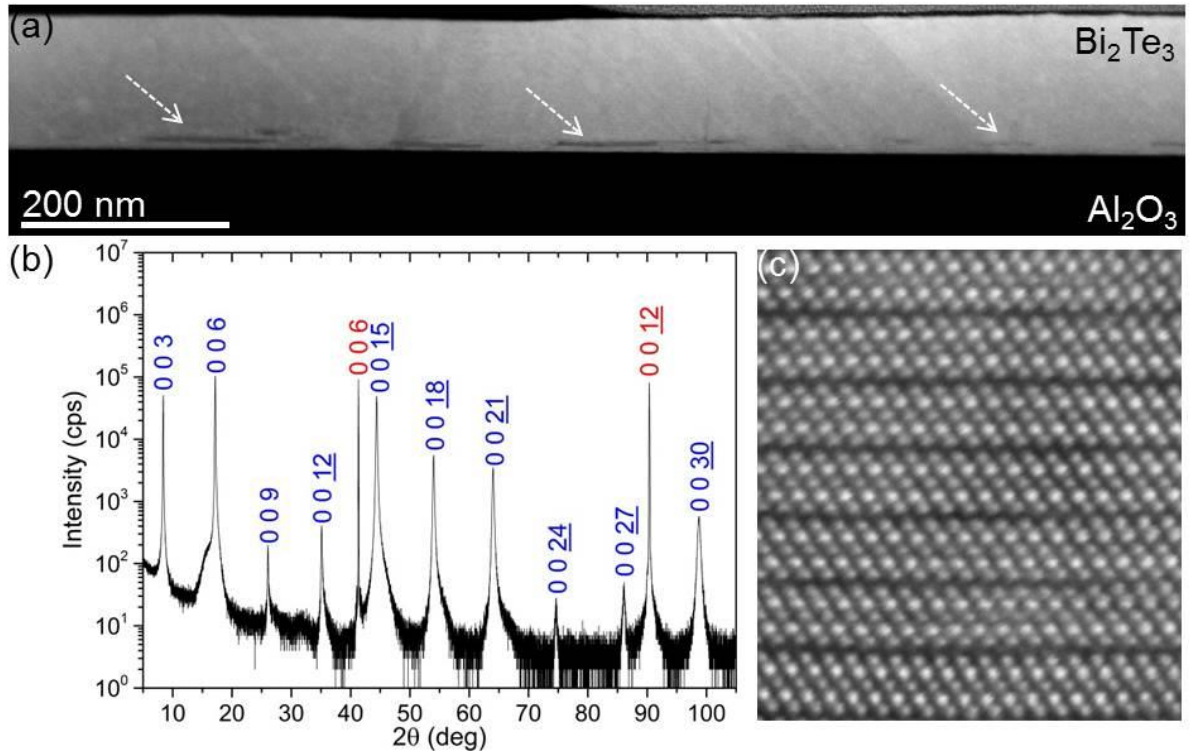
Figure 6.1: (a) Low-magnification HAADF-STEM image of the Bi_2Te_3 film on the Al_2O_3 substrate. The dashed arrows outline the $Fe_xCu_{1-x}Se$ inclusions in the Bi_2Te_3 film. (b) XRD spectrum showing both Al_2O_3 substrate (red labels) and Bi_2Te_3 film peaks (blue labels). (c) Atomically resolved HAADF-STEM image shows the QL structure of the Bi_2Te_3 film.

In order to reveal the atomic structure of the $Fe_xCu_{1-x}Se$ phase, and the ordering at the $Fe_xCu_{1-x}Se$ /Bi_2Te_3 interface, atomically resolved HAADF-STEM imaging has been performed. **Figure 6.2** shows a typical region of $Fe_xCu_{1-x}Se$ /Bi_2Te_3 acquired in a $[11\overline{2}0]$ zone axis. **Figure 6.2a** shows details of the interfacial region containing the $Fe_xCu_{1-x}Se$ inclusion. Higher magnification HAADF-STEM images from the regions outlined in **Figures 6.2a and 6.2b** show the atomic stacking of $Fe_xCu_{1-x}Se$, as well as the interface between $Fe_xCu_{1-x}Se$ and Bi_2Te_3 (**Figures 6.2b and 6.2c**). The $Fe_xCu_{1-x}Se$ inclusion is crystalline, with an atomically sharp interface with the Bi_2Te_3 film. Based on the atomic column *Z*-dependent contrast, the identification of the atomic structure at the interface can be carried out. The large difference between the atomic number of Bi and Te enables an easy differentiation between Bi and Te atomic columns. Similarly, the difference

between the Cu and Se columns can be established, even though the intensity change is much smaller due to low difference in Z (**Figure 6.2c**). The HAADF intensities indicate that the bonding across the interface consists of Se-Te bonds.
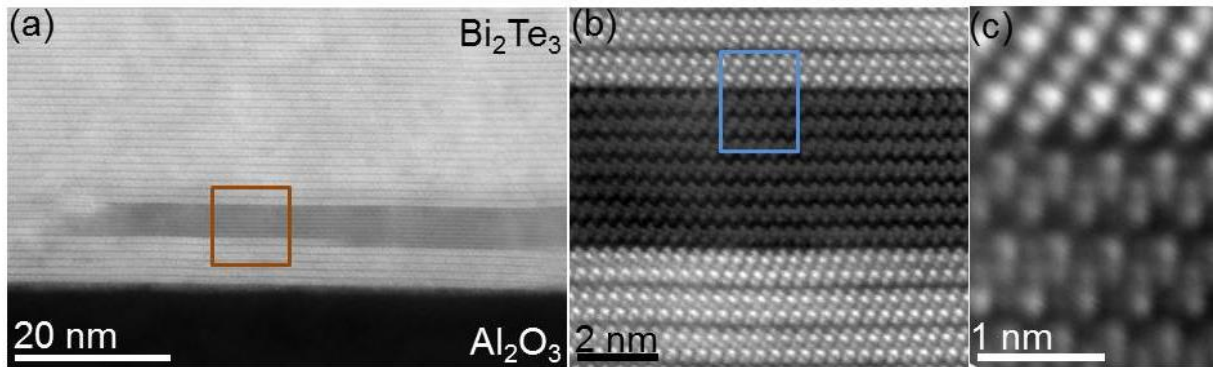
Figure 6.2: (a) Overview image of the $Fe_xCu_{1-x}Se$ inclusion close to the Bi_2Te_3/Al_2O_3 interface. (b) Magnified HAADF-STEM image from the region of interest outlined in (a). Both the film and the $Fe_xCu_{1-x}Se$ inclusion show good crystallinity. (c) High-magnification HAADF-STEM image from the interfacial region between the Bi_2Te_3 film and the $Fe_xCu_{1-x}Se$ outlined in (b).

Next the chemical structure analysis of the inclusions and the interface between $Fe_xCu_{1-x}Se/Bi_2Te_3$ by EELS elemental mapping is presented. **Figure 6.3a** shows a HAADF-STEM survey image from the $Fe_xCu_{1-x}Se/Bi_2Te_3$ interfacial area selected for chemical mapping. **Figure 6.3b** shows the HAADF-STEM image from the region of interest outlined in **Figure 6.3a** which is simultaneously acquired with the EELS elemental maps for Te, Fe, Cu and Se (**Figures 6.3c to 6.3f**). The $L_{2,3}$ edges were used to map Fe, Cu and Se, and $M_{4,5}$ for mapping Te. The chemical maps confirm the suggestion from HAADF imaging that the inclusion consists of Fe, Cu and Se (see **Figures 6.3d to 6.3f**). Since both FeSe and CuSe share the same structure, and Cu and Fe have similar size, Cu can easily substitute Fe within the tetragonal inclusion structure, as indicated in the **Figures 6.3d and 6.3e**.
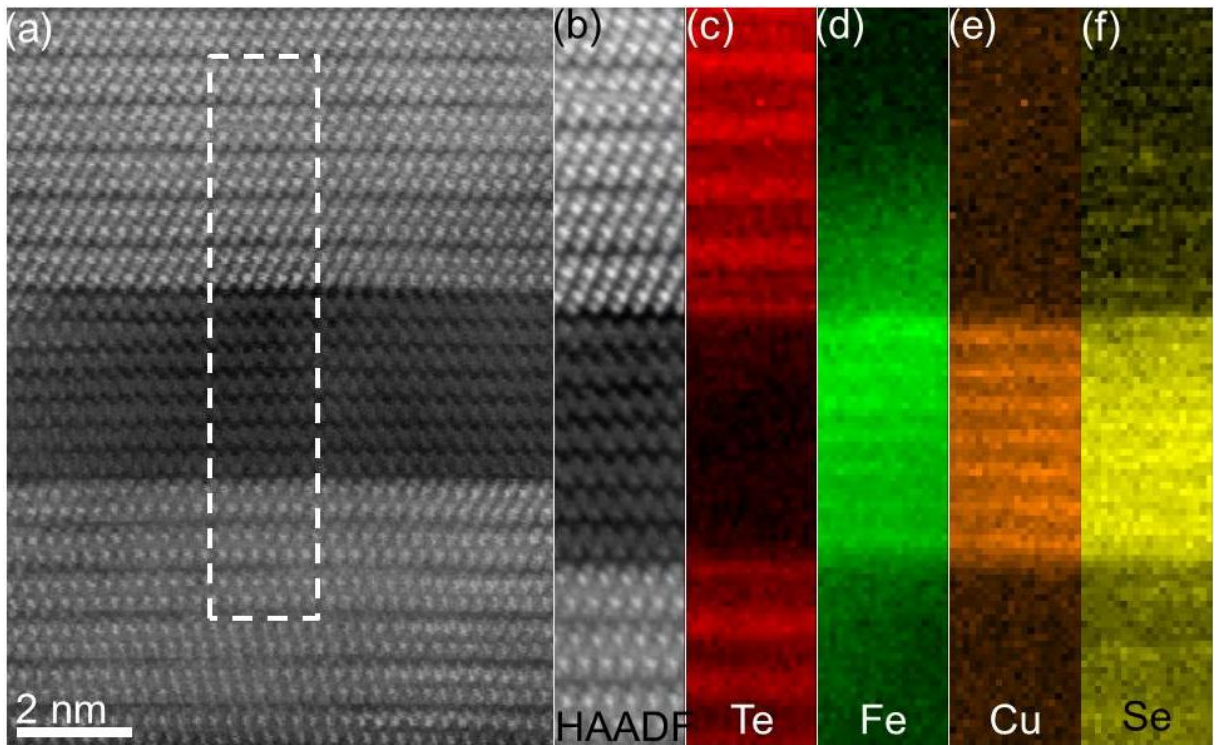
Figure 6.3: (a) HAADF-STEM survey image from the Bi_2Te_3 film and the $Fe_xCu_{1-x}Se$ inclusion. (b) HAADF-STEM signal from the region outlined by a dashed rectangle in (a), obtained simultaneously with the EELS data. (c-f) show Te $M_{4,5}$, Fe $L_{2,3}$, Cu $L_{2,3}$, and Se $L_{2,3}$ EELS signals at the $Fe_xCu_{1-x}Se/Bi_2Te_3$ interface, respectively.

The relative amount of Cu within FeSe inclusions is within 25±10% range, varying spatially among the inclusions. We note that Fe is continuously evaporated during the Bi_2Te_3 growth, hence outside the inclusion acts as a dopant for Bi_2Te_3 film [136]. The Se-Te atomic structure of the inclusion film interface is further supported by the EELS mapping from interface region shown in **Figure 6.4**.

Further HAADF and BF-STEM overview and high magnification images are taken using the JEOL 2200 microscope in York and are presented in **Figure A5** in appendix.
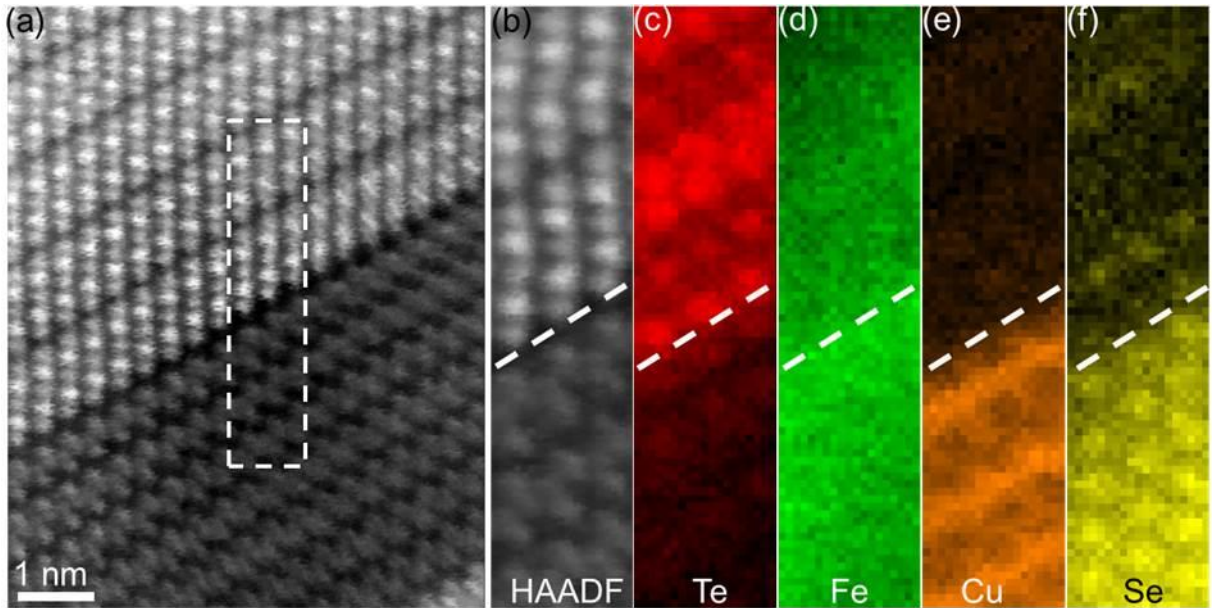
Figure 6.4: (a) HAADF-STEM survey image from the interface between the Bi_2Te_3 film and the $Fe_xCu_{1-x}Se$ inclusion. (b) HAADF-STEM signal from the interface region outlined by the dashed rectangle in (a), obtained simultaneously with the EELS data. (c-f) show Te $M_{4,5}$, Fe $L_{2,3}$, Cu $L_{2,3}$, and Se $L_{2,3}$ EELS signals at the $Fe_xCu_{1-x}Se/Bi_2Te_3$ interface, respectively.

We also note that the tetragonal phase of the inclusions is due to FeSe since the CuSe lowest structural phase is the hexagonal phase in comparison to tetragonal and orthorhombic phases [176, 177].

Figures 6.5a to 6.5c show ball-and-stick models of the tetragonal, hexagonal, and orthorhombic phases of Fe(Cu)Se, respectively. In order to infer the structure from the atomic resolution HAADF images (**Figure 6.5d**) STEM image simulations have been performed in order to correlate the experimental with simulated atomic stacking/positions and intensities. **Figures 6.5d to 6.5g** show the experimental HAADF image, constructed model in [100] zone axis of Fe(Cu)Se, and the image simulations of the Fe(Cu)Se inclusion in [100] and [110] zone axis, respectively. By comparing the HAADF-STEM and simulated images, it can be seen that the observed inclusion is the tetragonal phase of Fe(Cu)Se along the [100] zone axis. HAADF-STEM image simulations were performed using the multislice method as implemented in the QSTEM software

package [129]. For this purpose 6 layers of Fe(Cu)Se sandwiched in-between 2 QLs of Bi_2Te_3 from top and bottom.
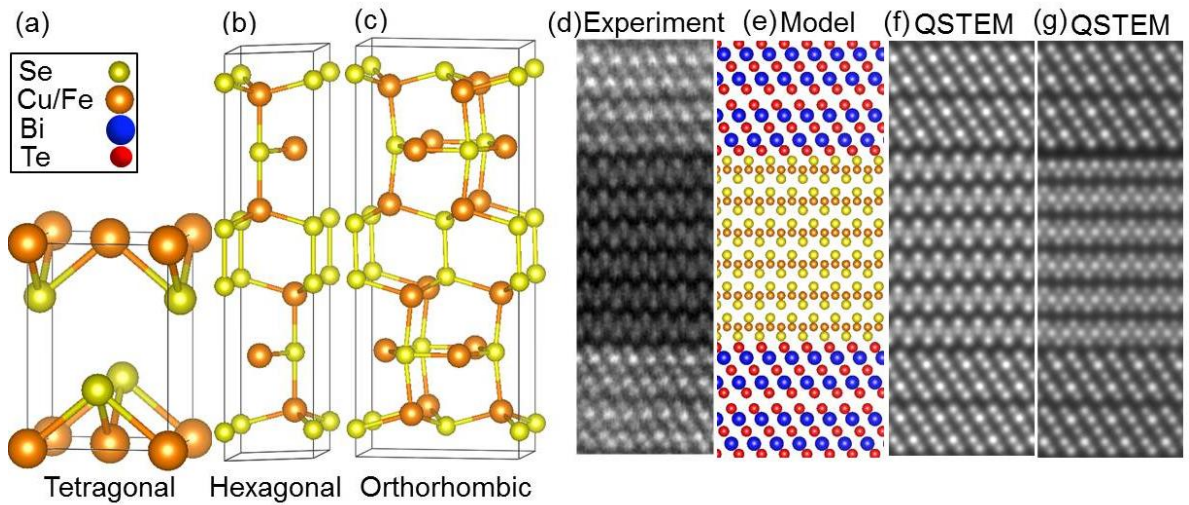
Figure 6.5: (a-c) Ball-and-stick models of tetragonal, hexagonal, and orthorhombic crystal structures of Fe(Cu)Se, respectively. The orange and yellow balls correspond to Fe(Cu) and Se atoms, respectively. (d) HAADF-STEM image from the Fe(Cu)Se inclusion inside the Bi_2Te_3 film. (e) Atomic model corresponding to the HAADF-STEM image in (d) using the tetragonal Fe(Cu)Se cell. The blue and red spheres correspond to Bi and Te atoms, respectively. (f) Image simulation using the model shown in (e). (f) and (g) show the two simulations of the Bi2Te3/ Fe(Cu)Se in [100] and [110] zone axis of Fe(Cu)Se, respectively. The comparison between (d), (f), and (g) reveals that the inclusion has the tetragonal crystal structure of Fe(Cu)Se in the [100] zone axis.

Furthermore DFT calculations prove that in an environment in which both Se and Te atoms are present, the formation of FeSe is more favourable than FeTe by ~ 0.78 eV/formula unit.

The atomic resolution images of the interface further help identify the crystallographic orientation between $Fe_xCu_{1-x}Se$ and Bi_2Te_3 as: $Fe_xCu_{1-x}Se(100)||Bi_2Te_3(11\bar{2}0)$ and $Fe_xCu_{1-x}Se(001)||Bi_2Te_3(0001)$.

Bearing in mind the different crystallographic structures of $Fe_xCu_{1-x}Se$ and Bi_2Te_3, as well as their lattice mismatch of 19%, one should expect a significant strain to develop at the $Fe_xCu_{1-x}Se/Bi_2Te_3$ interface. However, as shown next, no misfit dislocation are found at the interface indicating that the bonding between tetragonal $Fe_xCu_{1-x}Se$ and trigonal Bi_2Te_3 is rather weak, i.e., vdW-like.

Figure 6.6a shows a top view model of the interfacial Te and Se atomic planes. The positions of the first Se layer are shown with blue triangles on top of the red Te atoms. For clarity, the cross-sectional view of these two layers is also shown. The geometrical matching between the two lattices, e.g., along the $[10\bar{1}0]$ direction, shows that the coincidental lattice spots appear for every 5th Te atom, i.e., every 6th Se atom, which gives $\sim 19\%$ mismatch of the lattices. The realisation of such a structure is strongly unfavourable due to very large strain at the interface. Hence the formation of misfit dislocations is generally the mechanism that governs either covalently or ionically bonded heterostructures. However, a misfit dislocation network is not observed in our HAADF images.

By using the atomic resolution images of the interface, the atomic column displacement of the Se and Te interface columns with respect to the columns away from the interface region ('bulk' columns) is calculated. **Figure 6.6b** shows the variation of the interfacial atomic column positions with respect to the bulk for both Se and Te. The data shows the absence of the periodic interface atomic displacement (present when dislocation network forms), and arbitrary (random-like) variation with respect to the average bulk Se/Te atomic columns distances, with Se atomic columns having slightly larger displacements compared to Te. This implies that the bonding between the CuSe and Bi_2Te_3 is rather weak.
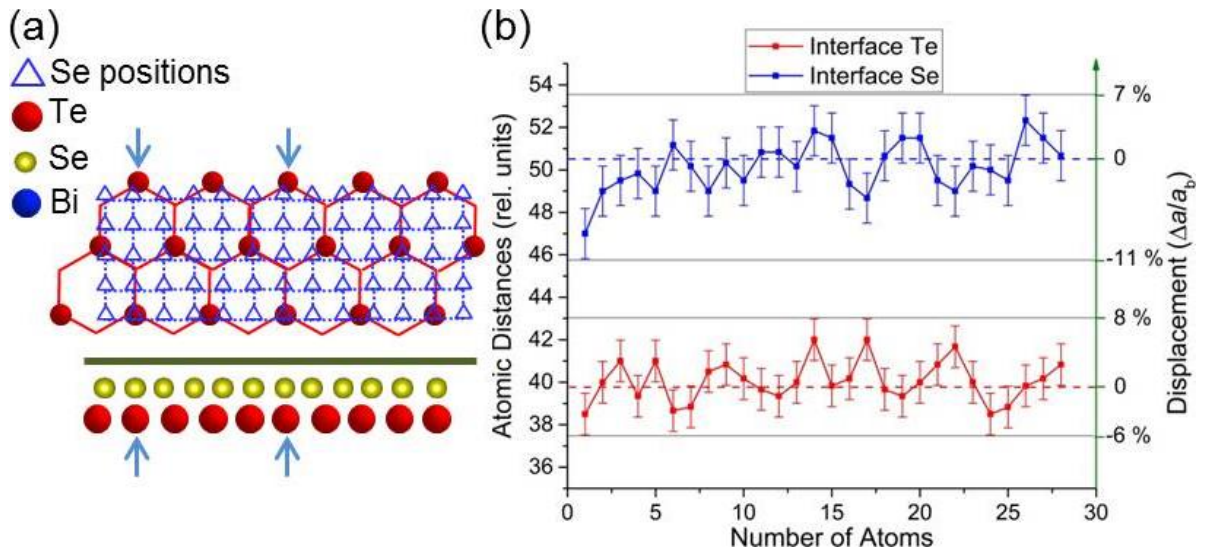
Figure 6.6: (a) Top view model of the Bi_2Te_3 lattice shows the trigonal crystal structure of the film with its top Te atoms (red spheres). The blue rectangles show the positions of the Se atoms on top of the Bi_2Te_3 film at the interface region with the $Fe_xCu_{1-x}Se$. The blue arrows show the positions in which the yellow Se atoms are located on top of the red Te atoms. (b) Variation of the interfacial atomic column positions with respect to bulk Se and Te. The blue and red graphs correspond to the Se and Te atomic columns at the interface, respectively. The Se (blue) graph has been shifted up vertically for clarity. The values on the second y-axis correspond to the minimum and maximum displacement percentages with respect to the bulk average (a_b), respectively.

In order to gain insight into the nature of the bonding between the $Fe_xCu_{1-x}Se$ and Bi_2Te_3 layers, first-principle calculations are performed. Since the interface bonding is mostly determined by the bonding between the first neighbouring atomic planes, the analysis is focused on calculating the bonding energy of the Se atom with respect to high symmetric points of the Bi_2Te_3 unit cell, i.e., the so-called top, bridge, and hollow sites, respectively. In addition to these high symmetric points the bonding energy at positions in-between them along the main paths within the unit cell, e.g., $[10\overline{1}0]$, $[11\overline{2}0]$ and $[01\overline{1}0]$ (**Figure 6.7a**) is also calculated. In total 32 distinct configurations for energy calculations is considered, in which Se is displaced by ~0.1 Å along the calculated paths.
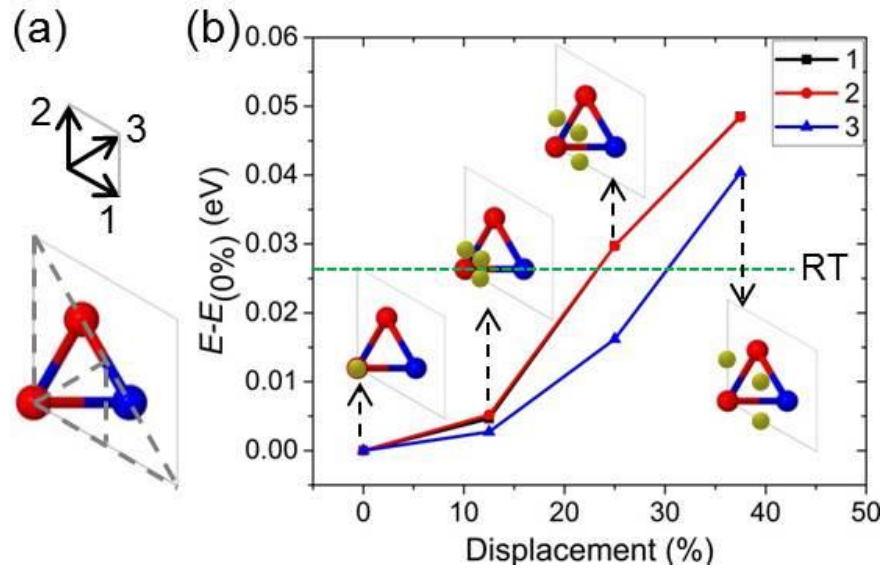
Figure 6.7: (a) Top view image of the Bi_2Te_3 unit-cell. The grey dashed lines show the positions of which 32 different sampling has been done for the Se bonding energy calculations. (b) Relative energy variations along the three main crystallographic paths outlined in (a). The green dashed line shows the corresponding energy at room temperature (0.0257 eV).

Figure 6.7b gives a summary of the results, where representative configurations of the Se-Bi_2Te_3 unit cell are shown. First, it is worth noting that the energy only changes by a small amount as the position of the Se atoms change. Even up to 19% displacement of the Se with respect to the top Te positions only changes the bond energy by less than 20 meV. This is less than the corresponding energy for room temperature (k_BT = 25.7 meV). These results demonstrate that the bonding between $Fe_xCu_{1-x}Se$ and Bi_2Te_3 has to be vdW-like, hence the experimentally observed 'insensitivity' of the atomic stacking registry at the interface.

6.4.   Conclusion

In summary, a structural study of single-crystalline $Fe_xCu_{1-x}Se$ inclusions embedded in a Bi_2Te_3 film was presented. $Fe_xCu_{1-x}Se$ and Bi_2Te_3 are fully epitaxial despite different lattice symmetries and a lattice mismatch of 19%. Atomic level structural and spectroscopic studies carried out using aberration-corrected TEM revealed atomically-sharp interfaces between the tetragonal phase of $Fe_xCu_{1-x}Se$ and the Bi_2Te_3 thin film. The very large lattice mismatch at the $Fe_xCu_{1-x}Se/Bi_2Te_3$ interface does not lead to the formation of any network of misfit dislocations. First-principles energy calculations show that the formation of an abrupt and chemically ordered interface is realised through vdW -like bonding between the Se and Te atomic planes at the interface. This study shows that epitaxial heterostructures of materials with significant differences in lattice symmetry with corresponding large lattice mismatch can be realised through vdW bonding across the interface. This study is of importance for the realisation of epitaxially-stacked chalcogenide superconductor materials, i.e., CuSe, FeSe, $Fe_xCu_{1-x}Se$ and 3D TIs.

7   Modification of the van der Waals interaction between Bi$_2$Te$_3$ and Ge(111)

This chapter is based on the work submitted to the applied physics letter journal for publication and forms a natural comparison with the works performed in the previous chapter.

In this chapter, a structural and DFT study of the interface of a Bi$_2$Te$_3$ 3D TI thin film grown on Ge(111) is demonstrated. Aberration-corrected STEM and EELS reveal the presence of an additional Te monolayer at the Bi$_2$Te$_3$/Ge interface.

First-principles calculations show that this Te monolayer overcomes the usually weak bonding between the Bi$_2$Te$_3$ QL and Ge due to the enhanced atomic hybridization. The formation energy of the additional Te layer is shown to be energetically favourable by 0.92 eV per Te atom.

In this work the film was produced by Prof. T. Hesjedal in the Physics department of University of Oxford, Oxford. Furthermore, the atomically resolved STEM-EELS have been performed by Dr. D. Kepaptsoglou and Prof. Q. Ramasse in the SuperSTEM national laboratory, Daresbury. Mr. K. Nawa and Prof. K. Nakamura (Mie University, Japan) have performed the all electron DFT calculations.

7.1.   Introduction

Bi$_2$Se$_3$, Bi$_2$Te$_3$, and Sb$_2$Te$_3$ are 3D TIs [25, 27] that have been attracting great attention in the recent years due to their topologically protected, fully spin-polarized surfaces states. These spin-momentum-locked surface states, protected by TRS, were the focus of numerous studies owing to their potential spintronics application [10-12, 69, 178]. In addition, a variety of interesting physical phenomena have been observed and predicted to occur in these materials, including the quantum anomalous Hall effect [55], the topological magneto-electric effect [73], image magnetic monopoles [74], and Majorana fermions [179].

The incorporation of TIs in device structures requires the fabrication of these materials as thin films. Thin film TIs have already been successfully used in spintronics applications, e.g., based on spin accumulation and spin-transfer torque [69, 180]. High-quality, single-crystalline films are usually grown by MBE. From a technological point of view, the integration of TIs with existing CMOS (complementary metal-oxide-semiconductor) technology requires the growth of TIs on semiconductor substrates. Consequently, MBE growth studies of Bi$_2$Se$_3$ and Bi$_2$Te$_3$ thin films have been carried out on a variety of substrates, e.g., Si(001) and (111) [181], GaN(001) [182], GaAs(001) and (111) [180, 183], CdTe(111) [184], SiC(001) [142], as well as on lattice-matched InP(111) [185].

One of the challenges for monolithic device integration of TIs is their weak bonding to most substrates, originating from the vdW-type interaction between film and substrate. While vdW bonding (inherent to the layered nature of the (Sb,Bi)$_2$(Se,Te)$_3$ TIs family) can be exploited for overcoming lattice mismatch in TI-based heterostructures [119], weak bonding between TI film and substrate renders the heterostructures unstable due to delamination issues.

In this work it is demonstrated that the Bi$_2$Te$_3$ bonding strength to a Ge(111) substrate can be significantly increased by changing the atomic structure at the interface. In particular, it is shown that the deposition of an additional monolayer of Te between the Bi$_2$Te$_3$ film and Ge(111) during the fabrication process overcomes the inherently weak bonding between the Te-terminated Te-Bi-Te-Bi-Te QLs and Ge. The stability of this

additional interface monolayer of Te was confirmed by DFT calculations which also show that it enables interface atomic hybridization.

7.2.   Methods

The Bi$_2$Te$_3$ thin films were grown in a Createc MBE system with a base pressure of 1×10^{-10} Torr. Bi and Te (99.9999% pure elemental source material) were co-evaporated out of standard effusion cells with a Te:Bi flux ratio of 10:1, as calibrated using an *in-situ* beam flux monitor. This overpressure of the chalcogenide has been shown to be necessary to reduce the Te vacancy defects in the film [186]. The deposition rate of the Bi$_2$Te$_3$ films was typically ~0.5 nm/min. The Bi$_2$Te$_3$ films were grown in a two-step growth process. First, a 15-nm-thick nucleation layer was deposited at a lower temperature of 200 °C. Subsequently, this layer was annealed at 300 °C for 30 minutes (with the Bi shutter closed), before continuing the growth at 300 °C up to the desired film thickness.

The film quality was evaluated using an *in-situ* RHEED system and an *ex-situ* XRD. Cross-sectional TEM specimen preparation was carried out by FIB milling using a FEI Helios NanoLab 600 instrument [119].

STEM imaging and EELS measurements were performed in a Nion UltraSTEM100 equipped with a Gatan Enfina spectrometer. The microscope was operated at 100 kV, with a beam convergence angle of 30 mrad; at these optical conditions the electron probe size is determined to be 0.8 Å. The inner detector angle for HAADF-STEM imaging was 76 mrad. The native energy spread of the electron beam for EELS measurements was 0.3 eV, with the spectrometer dispersion set at 1 eV/channel, yielding effective an energy resolution 3eV limited by the detector point spread function. The EELS collection angle was 33 mrad. In order to reduce noise in the EELS data, PCA (using the temDM plugin for Gatan's Digital Micrograph 2.3 software suite) [123] was applied prior to integrating the signal above the relevant ionisation edge onset over a 35 eV window, after subtraction of the decaying background using a power-law model. The image used in **Figure 7.2c** is

obtained by rigid registration of a stack of images recorded in quick succession (resulting in high signal-to-noise and precision in the image).

DFT calculations were performed to investigate the stability of the interfacial atomic structure. The calculations were carried out by the all-electron, full-potential linearized augmented plane wave (FLAPW) method with a single slab geometry [187-189], based on the local density approximation (LDA) [190] for the exchange-correlation functional. The LAPW basis functions are expanded within a cut-off of $|k + G| \leq 3.9$ a.u.$^{-1}$ and muffin-tin (MT) sphere radii of 2.7, 2.5, and 2.1 a.u. for Bi, Te, and Ge atoms, respectively. The angular momentum expansions inside the MT spheres are truncated at ℓ=8 for the wave functions, charge density, and potential. Two models of Bi_2Te_3/Te/Ge and Bi_2Te_3/Ge is considered, as shown in **Figures 7.4a and 7.5a**, respectively, where 3QLs of Bi_2Te_3 and three Ge layers of the Ge(111) substrate were taken into account. For Bi_2Te_3/Te/Ge, a monolayer of Te (ML-Te) is inserted at the interface between Bi_2Te_3 and the Ge substrate. For the distances between the ML-Te, the 3QLs Bi_2Te_3, and the Ge substrate experimentally observed values of 3.43 Å and 2.45 Å, respectively, were used. For Bi_2Te_3/Ge, the distance between 3QLs Bi_2Te_3 and the Ge substrate is assumed to have the same value of 2.45 Å. In order to suppress energy uncertainties in the numerical calculations (binding energy calculations), a convergence of E_B with respect to the number of k-points in BZ, up to 81 k-points, was confirmed.

7.3.   Results

Figures 7.1a and 7.1b show the RHEED patterns of the Ge substrate and the Bi_2Te_3 film, respectively. The sharp streaks indicate a flat surface for both the Ge(111) substrate and the grown Bi_2Te_3 film. The structural order of the films was examined by XRD. **Figure 7.1c** shows that the films are single-crystalline and free from secondary phases. The labelled (00l) peaks are consistent with the $R\overline{3}m$ space group of the c-axis oriented (growth direction along [001]) rhombohedral Bi_2Te_3 film. The c-axis lattice constant is found to be (30.47 ± 0.01) Å, which is comparable to the value of 30.48 Å obtained for Bi_2Te_3 bulk crystals.
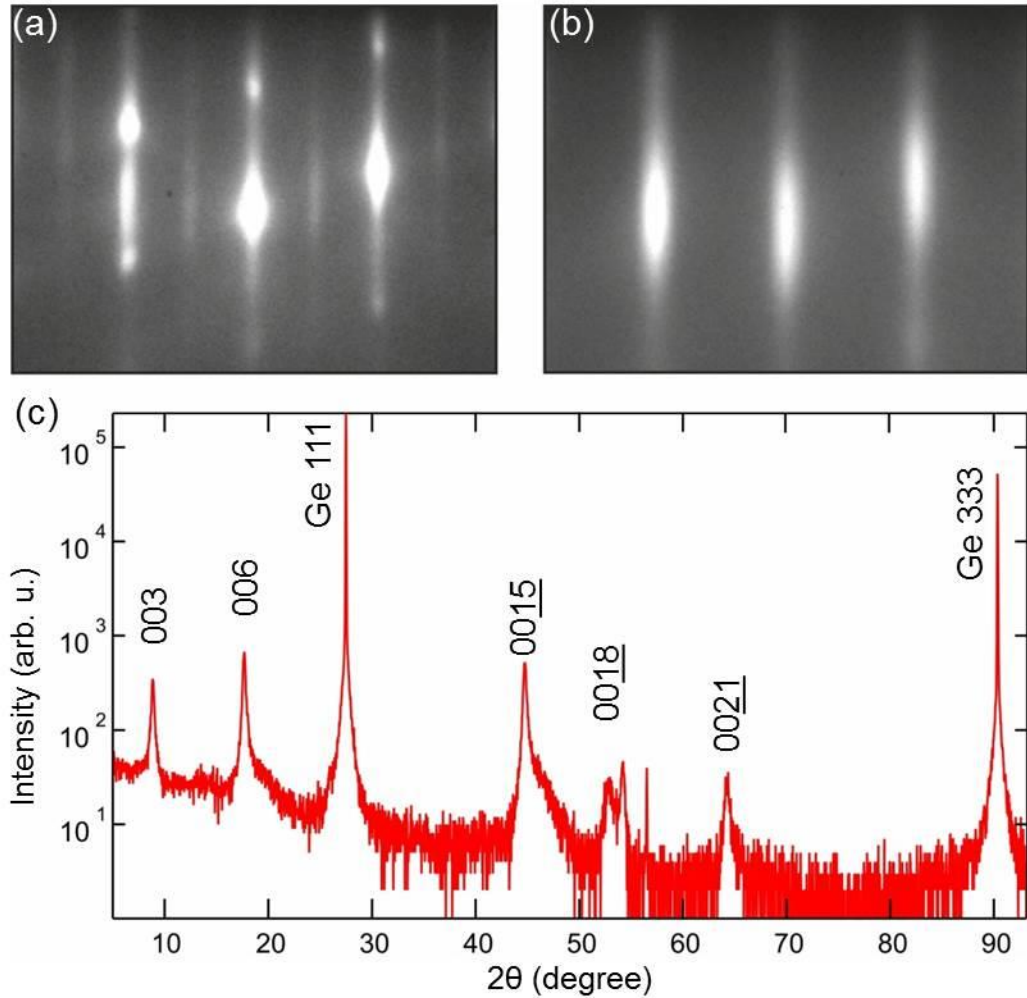
Figure 7.1: (a) and (b) show RHEED patterns obtained from the Ge and the Bi_2Te_3 surfaces, respectively. (c) XRD spectrum showing both film and substrate peaks as labelled.

Next, the structural ordering of the Bi_2Te_3 film at the atomic scale with a specific focus on the interface is investigated. A HAADF-STEM overview of the Bi_2Te_3 film on the Ge substrate is shown in **Figure 7.2a**, confirming the uniform film growth. **Figure 7.2b** gives a closer view of the interfacial region between Ge and Bi_2Te_3. The white fringes in **Figure 7.2b** show the continuous QL structure of the film, the ordered growth of the Bi_2Te_3 film, and the distinct crystallographic discontinuity between the Ge substrate and the film.
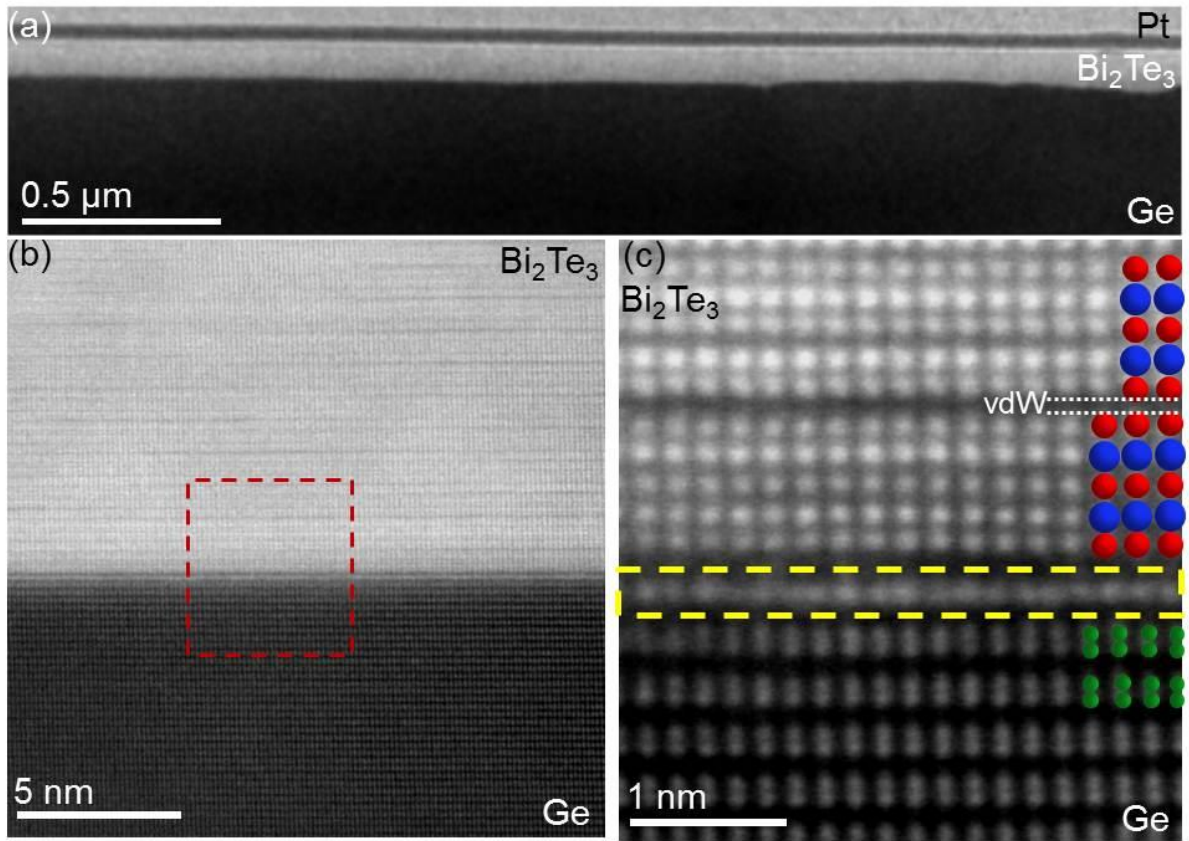
Figure 7.2: (a) Overview HAADF-STEM image of the Bi$_2$Te$_3$ film on Ge(111). (b) Magnified HAADF-STEM image from the interface region. (c) High-magnification HAADF-STEM image from the interfacial region between the Bi$_2$Te$_3$ film and the Ge outlined in (b). The overlaid structural model and the dashed rectangle show the Bi$_2$Te$_3$/Ge atomic positions as well as the extra layer at the interface; Bi (blue), Te (red), and Ge (green) atomic columns.

The close-up view of the selected region (outlined by the red rectangle in **Figure 7.2b**) shows the atomic structure of the interface, the QL structure of Bi$_2$Te$_3$, as well as the distinct dumbbell structure of Ge along the [11$\bar{2}$0] and [11$\bar{2}$] zone axis, respectively **Figure 7.2c**. Due to the atomic number dependence of image contrast in HAADF, a clear distinction between Ge, Bi and Te atomic columns is possible, as illustrated by the different atomic column colour coding shown in **Figure 7.2c**. In addition to the expected Bi$_2$Te$_3$ QLs and the Ge substrate, a continuous extra layer is present at the

interface (**Figure 7.2b**). This layer can also be seen in the high magnification image in **Figure 7.2c** as outlined by yellow rectangle.

In order to determine the chemical nature of the interfacial monolayer (ML), spatially resolved EELS mapping is performed, by rastering the electron probe across a defined region and collecting an EELS spectrum at each point. **Figure 7.3a** shows a HAADF-STEM survey image in which the region selected for EELS measurements of the Te $M_{4,5}$ and Ge $L_{2,3}$ edges is outlined (**Figure 7.3b**). The maps of the Te $M_{4,5}$ and Ge $L_{2,3}$ signals are shown in **Figures 7.3c and 7.3d**. Comparing the HAADF signal with the Te and Ge elemental maps of the layer under investigation reveals that the observed ML in fact consists dominantly of Te, with a small presence of Ge.
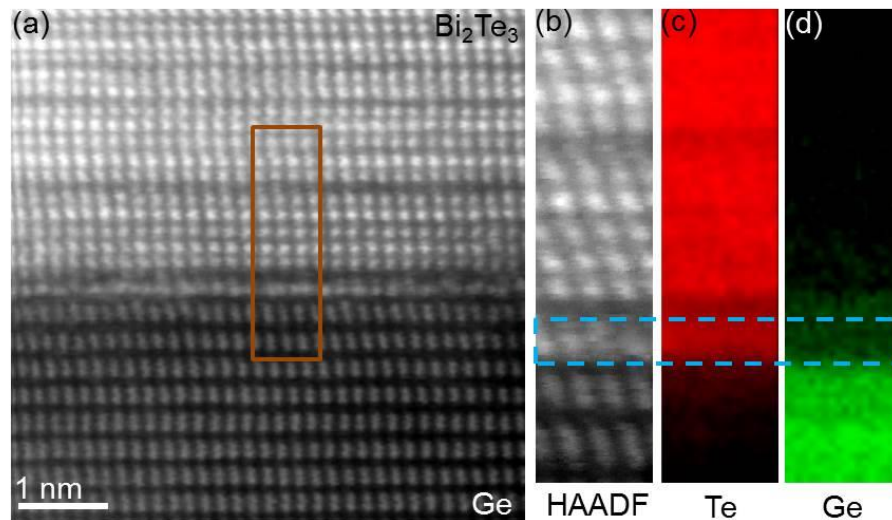
Figure 7.3: (a) HAADF-STEM survey image. (b) HAADF-STEM signal from the region of interest outlined in (a) produced simultaneously with the EELS acquisition. (c) and (d) Te $M_{4,5}$ and Ge $L_{2,3}$ EELS signals showing the presence of Te in the observed extra layer (outlined by a dashed blue rectangle).

These findings are consistent with the contrast of the ML which is between the first Bi_2Te_3 QL of the film and the last and Ge dumbbells of the substrate.

Furthermore, the Te $M_{4,5}$ and Ge $L_{2,3}$ EELS signals have been plotted in **Figure 7.4**. **Figure 7.4a** shows the overlapped Te and Ge EELS map from the area outlined in

Figure 7.3a. The Ge and Te intensity signals have been normalised to 1 and plotted with respect to the length of the EELS map (**Figure 7.4a**). In the ML region (outlined with the black rectangle) the Te intensity only decreases by 22% with respect to the Te intensity in the QL region; while the Ge intensity drops by 61% with respect to the intensity in the Ge substrate. This further demonstrates that the observed ML mostly consists of Te atoms.
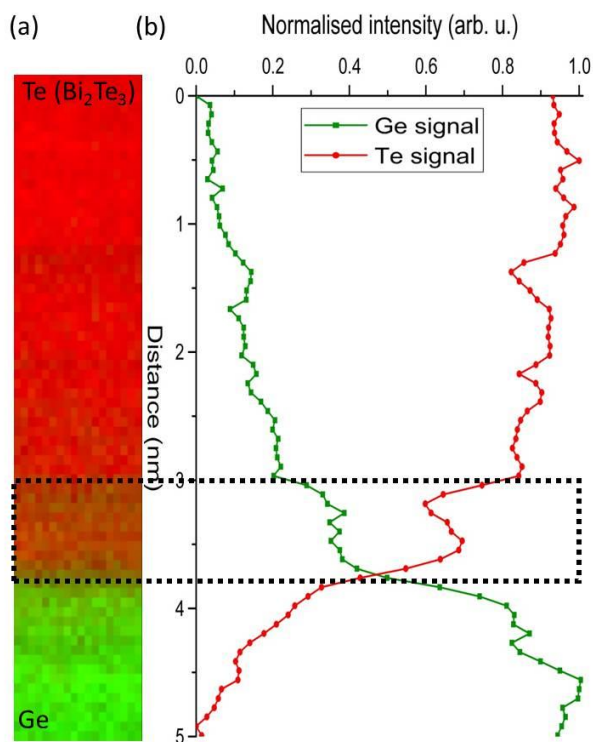
Figure 7.4: (a) and (b) show the overlaid maps of Te and Ge as well as their signal intensity profile across the area outlined in **Figure 7.3a**. Red and Green correspond to Te and Ge, respectively.

Further overview and high magnification TEM and STEM images are also taken using the JEOL 2011 and 2200 microscopes in York and are presented in **Figures A6 and A7** in appendix. We note that a series of misfit dislocations are observed at the interface which are presented in **Figure A7** in the appendix section.

To understand why it is energetically favorable for the system to form a ML of Te at the interface total energy DFT calculations is carried out. The binding energy, E_B, is given by

$$E_B = E_{\text{Bi}_2\text{Te}_3/\text{Te}/\text{Ge}} - \left[E_{\text{Bi}_2\text{Te}_3/\text{Ge}} + E_{\text{Te}} \right] \qquad (7.1)$$

The first term in Eq. (7.1) is the total energy of Bi$_2$Te$_3$/Te/Ge and the second term the sum for Bi$_2$Te$_3$/Ge and a free-standing Te monolayer. The calculated E_B is −0.92 eV per Te atom of the interface ML. This indicates that Te prefers to form a ML at the interface, in contrast to a 'clean' interface governed by Te-terminated QL/Ge bonds.

Finally, the band structure of this interface reconstruction is calculated, and the electronic properties of Bi$_2$Te$_3$/Ge with (**Figure 7.5**) and without (**Figure 7.6**) a Te ML at the interface is compared. Since the electronic origin of the strong binding energy is of interest, the band structure of each interfacial atomic plane, determined by Te from the QL (**Figure 7.5b**), ML-Te (**Figure 7.5c**), and the top-Ge layer (**Figure 7.5d**) is presented. We note that the layers' band structures consist of p orbitals. **Figure 7.5a** shows the atomic model of the Bi$_2$Te$_3$/Ge interface with a ML of Te. By comparing **Figure 7.5c and 7.5d** around the Γ-point and the Fermi energy (E=0), one can see that the p orbitals of the ML-Te strongly hybridize with that of the top-Ge layer. Hybridization between QL-Te and ML-Te is also present.
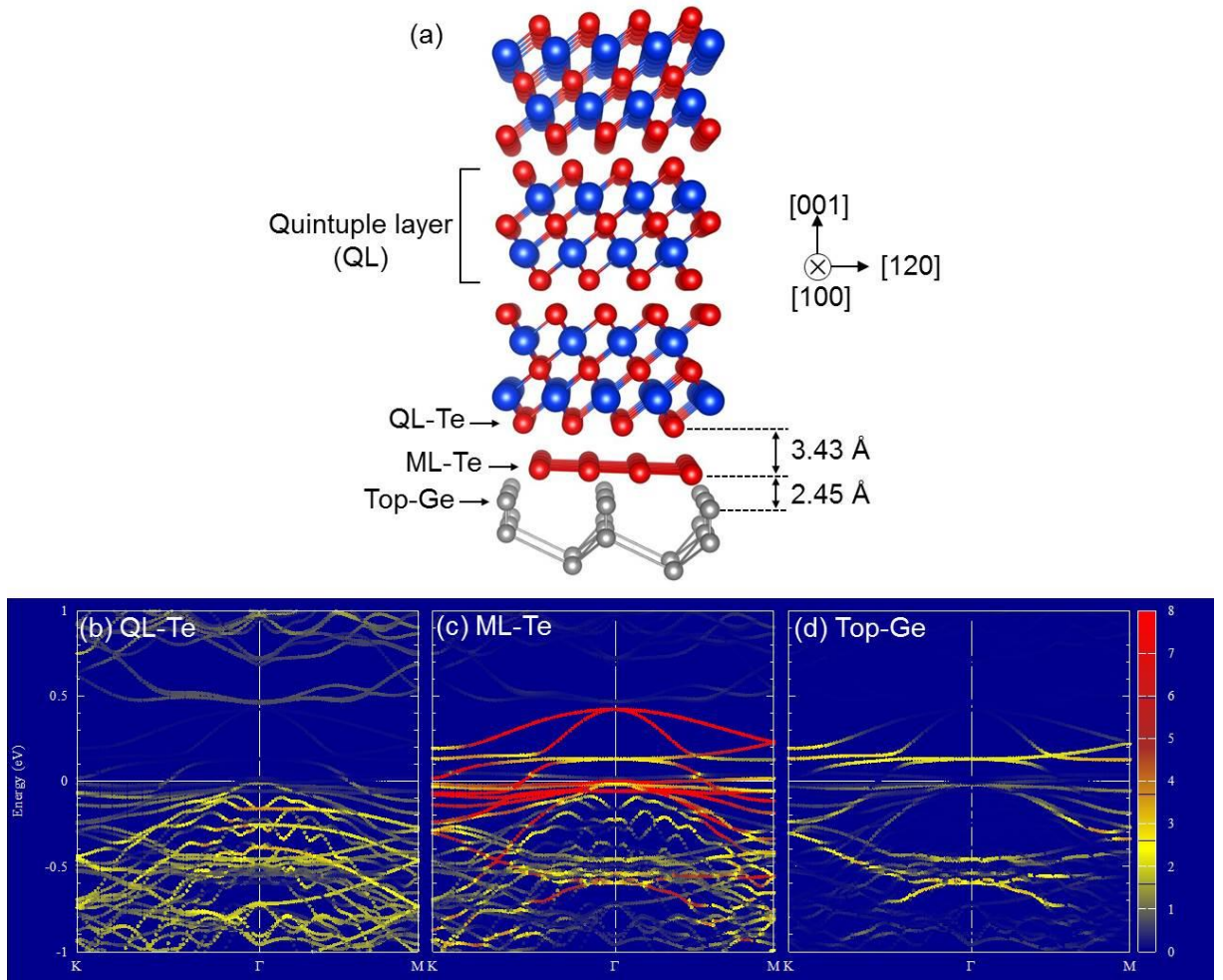
Figure 7.5: (a) The structure of 3QL-Bi$_2$Te$_3$/Te/Ge(111). Blue, red, and gray circles indicate Bi, Te, and Ge atoms, respectively. (b)-(d) Calculated band structures with weights of p orbitals along the $K \rightarrow \Gamma \rightarrow M$ direction in the BZ for Te at the bottom of the QL-Bi$_2$Te$_3$ (QL-Te), Te in the inserted monolayer (ML-Te), and Ge at top of Ge substrate (top-Ge), respectively.

In contrast to the ML-Te terminated interface, the Bi$_2$Te$_3$/Ge interface (**Figure 7.6**) shows almost no hybridization between the p orbitals of the QL-Te and the top-Ge, see **Figures 7.6b and 7.6c**. These electronic band calculations clearly demonstrate that the additional Te ML significantly enhances the chemical bonding between the Bi$_2$Te$_3$ layer and the Ge substrate.
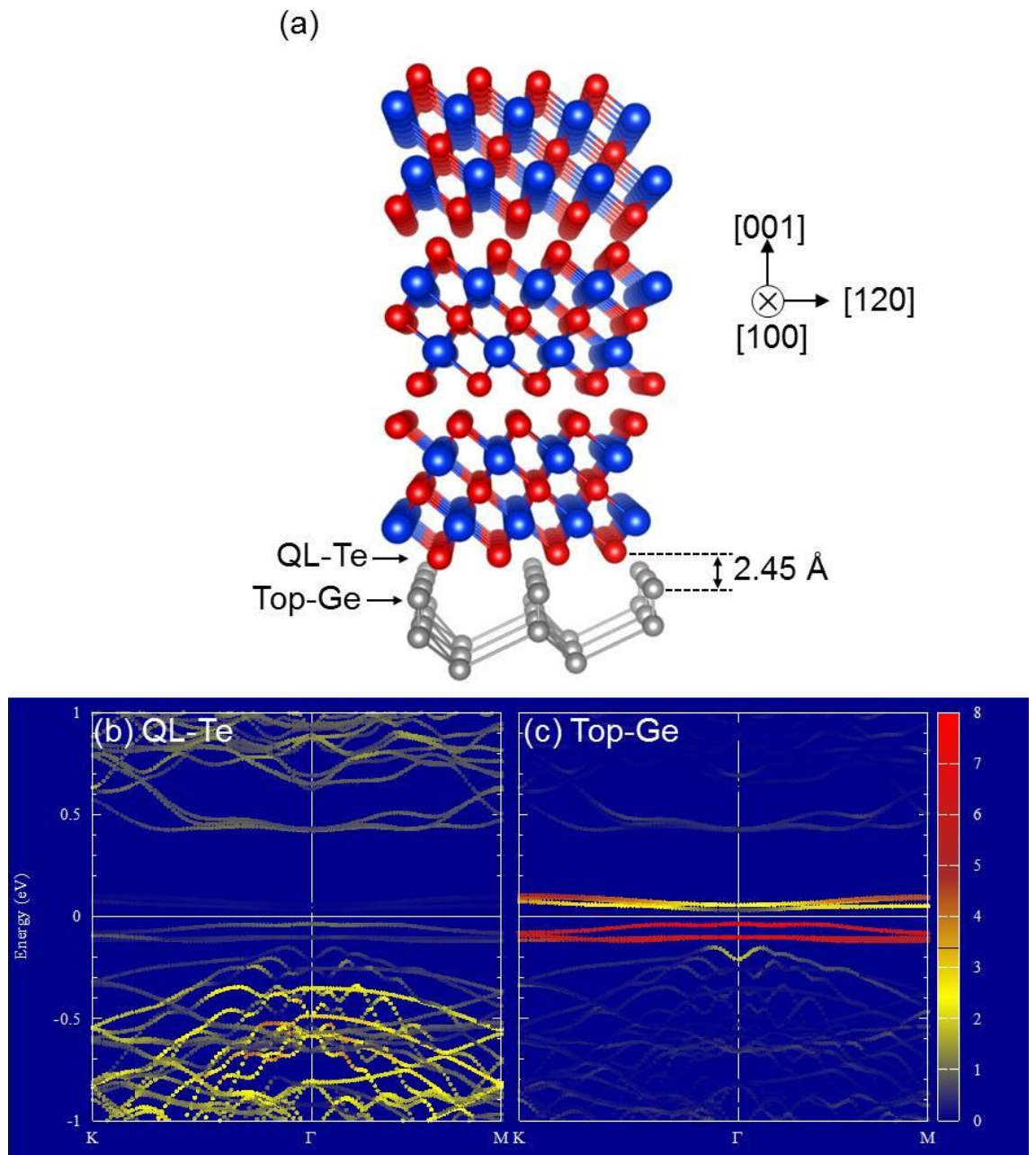
Figure 7.6: (a) Structure of 3QL-Bi_2Te_3/Ge(111) and band structures for (b) QL-Te and (c) top-Ge. The notations are the same as in **Figure 7.5**.

7.4.   Conclusion

In summary, the successful MBE growth of Bi$_2$Te$_3$ on Ge(111) was shown. By using aberration corrected STEM and EELS, it is found that a monolayer of Te has formed at the interface of Bi$_2$Te$_3$ and Ge(111). The presence of the Te monolayer at the interface drastically changes the electronic structure and bonding nature at the interface. DFT total energy calculations revealed that the formation of the Te monolayer is favourable by 0.92 eV per Te atom. Moreover, electronic band structure calculations revealed that the stronger atomic *p*-type orbital hybridization at the interface overcomes the inherent weak bonding between Bi$_2$Te$_3$ and Ge. Finally, our results demonstrate that in contrast to other Bi$_2$Te$_3$-substrate systems, which are governed by vdW epitaxy, the growth on Ge(111), due to the formation of the Te monolayer, is governed by an intimate interaction between film and substrate. Our work illustrates that weak bonding in TI heterostructures can be overcome by suitable atomic interface engineering, which is of great importance for fabricating monolithic device structures.

8   Conclusion

In this work it was shown that by carefully preparing cross-sectional specimens using FIB instrument, state-of-the-art electron microscopy imaging and spectroscopy can be performed on TI thin films.

It was shown that for the investigated Cr concentration (4.6 at-%) the dopant does not disturb the Bi_2Se_3 crystal structure and the Cr incorporation in Bi_2Se_3 film proceeds via substitution of Bi atoms. Furthermore, it was shown that the grain boundaries act like sinks for the Cr dopants. Therefore, by controlling the density of defects Cr segregation at the boundaries can be minimized and a uniform substitution of Bi can be achieved.

It was also demonstrated that Mn dopants in Bi_2Te_3 film tend to accumulate in the vdW gap as well as entering the lattice substitutionally on Bi sites. Moreover, Mn dopants can also substitute Te in regions of very high concentration. Furthermore, the DFT calculations predicted ferromagnetic coupling of Mn atoms inside the Bi_2Te_3 films which explains the previously observed overall magnetization in this system. This study shows that at low concentrations (*e.g.* ~ 2.5 at-%) Mn can be readily incorporate as a dopant in Bi_2Te_3 thin films, hence presents a system with promising properties as a magnetic 3D TI.

It was also demonstrated that $Fe_xCu_{1-x}Se$ and Bi_2Te_3 can be grown fully epitaxial with atomically-sharp interfaces despite their different lattice symmetries and extremely large lattice mismatch of 19%. Furthermore, it was shown that the very large lattice mismatch at the $Fe_xCu_{1-x}Se/Bi_2Te_3$ interface does not lead to the formation of any network of misfit dislocations. DFT calculations showed that epitaxial heterostructure of $Fe_xCu_{1-x}Se/Bi_2Te_3$ with different lattice symmetry and large lattice mismatch can be realised through vdW-like bonding across the interface.

The study of the interface between Bi_2Te_3 and Ge(111) showed that the formation of monolayer of Te drastically changes the electronic structure and bonding nature at the interface. Moreover, electronic band structure calculations of Bi_2Te_3/Te/Ge revealed that the weak vdW bonding at the interface can be overcome by the stronger atomic *p*-type

orbital hybridization at the interface. It was also illustrated that weak bonding in TI heterostructures can be overcome by suitable atomic interface engineering, which is of great importance for fabricating monolithic device structures.

There are many possibilities for further research into this subject. Since it was shown that the dopants positions can change the nature of the overall magnetisation in these materials, more fundamental study on different dopants can be carried out. Now that the growth of TIs on materials with high lattice mismatch is achievable, certainly there are plenty of potential interfaces that the vdW bonding can be also studied for. Another potential study is to explore the proximity effect between TIs and ferromagnets for spin-orbit torque magnetic random access memory devices.

Appendix

Here additional information about the samples under investigation in this thesis is given. First, we show overview and high magnification HAADF and BF-STEM images of Cr doped Bi_2Se_3 and Mn doped Bi_2Te_3. Additionally results of energy-dispersive X-ray spectroscopy of Mn doped Bi_2Te_3 specimen are given. Furthermore, HAADF and BF-STEM images and analysis of $Fe_xCu_{1-x}Se/Bi_2Te_3$ and Bi_2Te_3/Ge is presented.

1. HAADF and BF-STEM imaging of Cr doped Bi_2Se_3

Figure A1 presents the HAADF and BF-STEM images of Cr doped Bi_2Se_3 studied in **chapter 4**. **Figures A1c and A1d** clearly show the QL structure of Bi_2Se_3 using both HAADF and BF imaging.
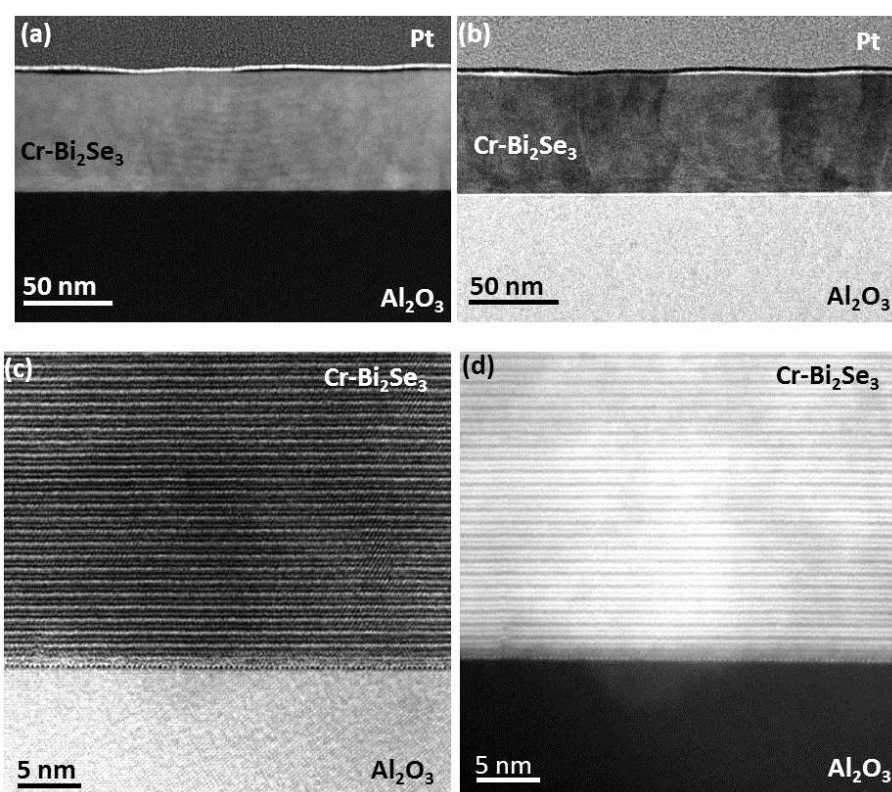
Figure A1: (a) and (b) show HAADF and BF-STEM images of the Cr doped Bi_2Se_3. (c) and (d) show high magnification HAADF and BF-STEM images of the Cr doped Bi_2Se_3 sample. QL structure of Bi_2Se_3 can be seen in (c) and (d).

2. HAADF and BF-STEM imaging of Mn doped Bi$_2$Te$_3$

Figure A2 shows the uniform presence of dark patches inside the Mn doped Bi$_2$Te$_3$ thin film investigated in **chapter 5**.
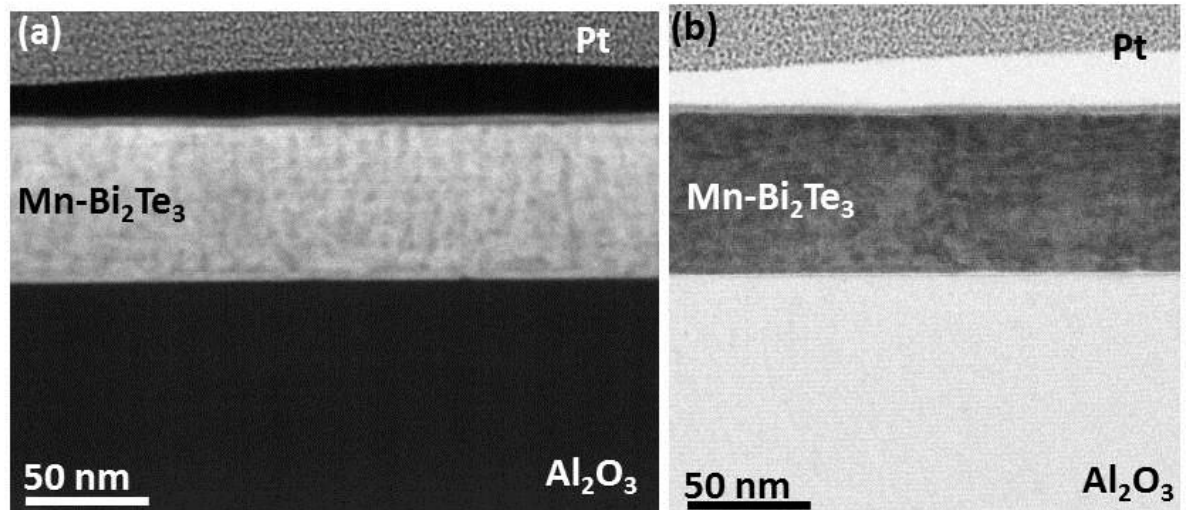
Figure A2: (a) and (b) show low magnification HAADF and BF-STEM images of the Mn doped Bi$_2$Te$_3$.

3. Energy-dispersive X-ray spectroscopy of Mn doped Bi$_2$Te$_3$

Figure A3a is a HAADF-STEM image of Mn doped Bi$_2$Te$_3$ sample investigated in **chapter 5**. The red circle on **Figure A3a** outlines the position of the dark patch inside the TI film. By comparing the HAADF-STEM image (**Figure A3a**) with the energy-dispersive X-ray maps of Al, Bi, Mn, and Te we can confirm that the dark patches are indeed Mn rich. This observation confirms the results of the EELS analysis presented in **chapter 5**.
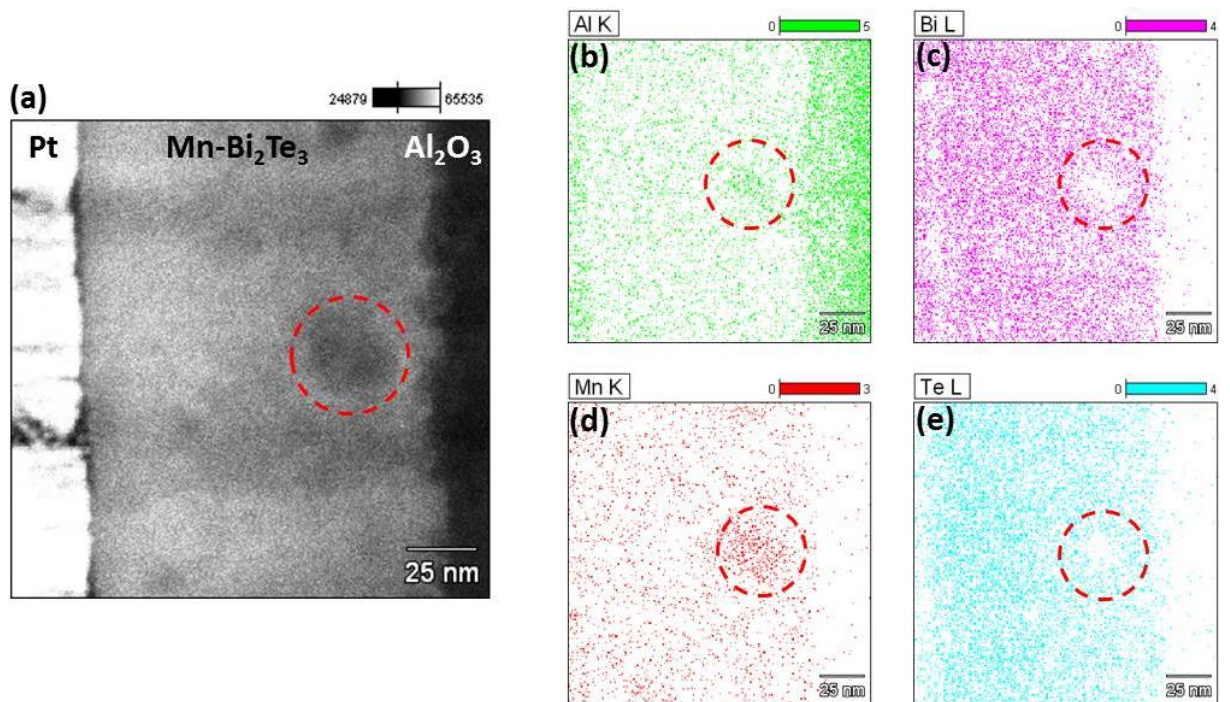
Figure A3: (a) Shows HAADF-STEM image of a dark patch inside the Mn doped Bi_2Te_3 sample. (b), (c), (d), and (e) show the energy-dispersive X-ray spectroscopy maps of Al, Bi, Mn, and Te, respectively.

Figure A4 and its corresponding table (**Table A1**) show the energy-dispersive X-ray spectrum and the number of Mn and Te counts in two different area of the Mn doped Bi_2Te_3 sample. Circles 1 and 2 show the area of sample from which the energy-dispersive X-ray spectrum are taken and are regions with and without dark patch, respectively. The increase of Te peak and decrease of Mn peak outside of the dark patch (point 2) indicates that Mn dopants substitute Te atoms which further confirm the presented EELS data in **chapter 5**.
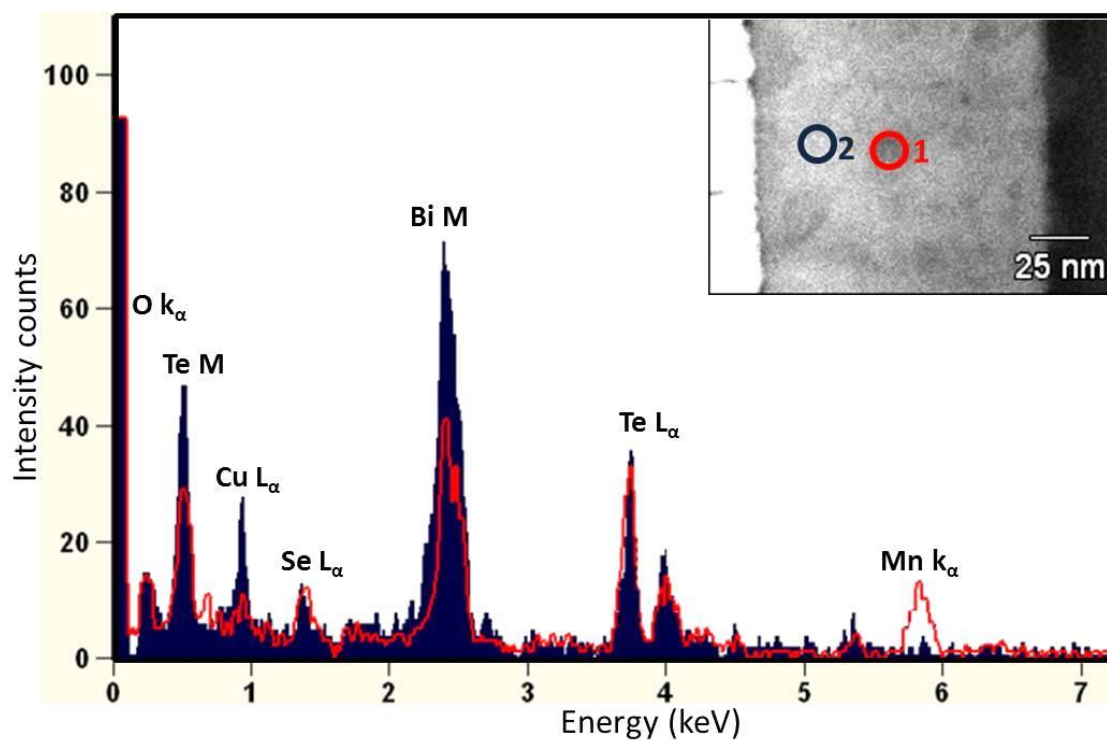
Figure A4: Shows the energy-dispersive X-ray spectrums of two positions inside the Mn doped Bi_2Te_3 sample. The red line and filled blue spectrums correspond to points 1 and 2 in the HAADF-STEM image shown as an inset, respectively. From the peak intensities, it is clear that the dark patch (point 1) is higher in Mn and lower in Te and Bi, comparing to the second sampling area (point 2).

Table A1: Shows the number of Mn and Te counts of the two points shown in **Figure A4**.

Total number of counts	Mn-K	Te-L
Point 1	160	597
Point 2	6	491

4. HAADF and BF-STEM imaging of $Fe_xCu_{1-x}Se$ inclusions inside Bi_2Te_3

Figure A5 shows the overview and high magnification HAADF and BF-STEM images of FexCu1-xSe inclusions inside Bi_2Te_3 film. Using the high magnification HAADF-STEM image in **Figure A5c** we generated the QSTEM image simulations shown in **chapter 6**.
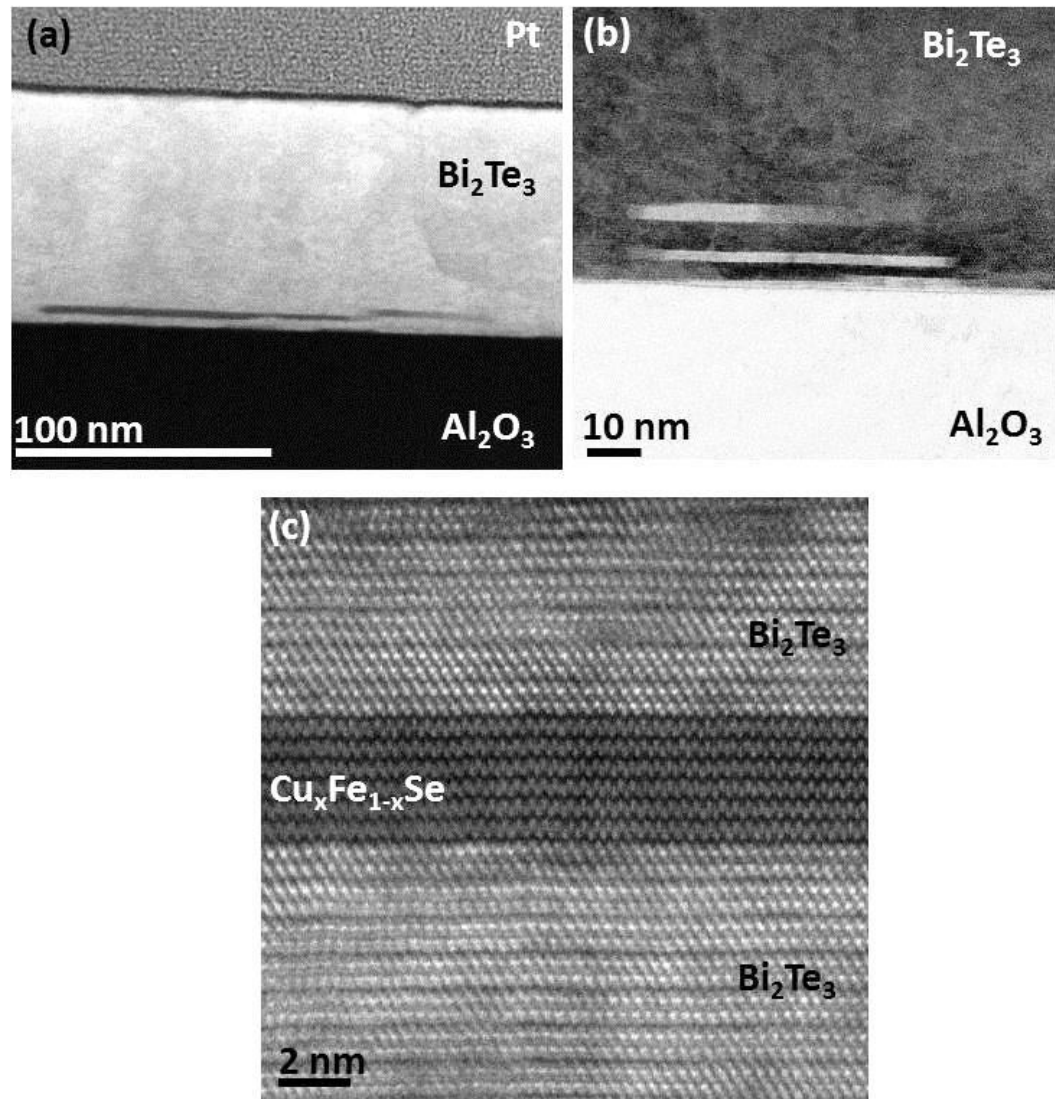
Figure A5: (a) and (b) show the HAADF and BF-STEM images of $Fe_xCu_{1-x}Se$ within the Bi_2Te_3 TI. The dark and bright areas inside the Bi_2Te_3 film in (a) and (b) show the $Fe_xCu_{1-x}Se$ inclusions, respectively.

5. TEM imaging of Bi$_2$Te$_3$ TI on Ge(111) substrate

Figure 6 shows the overview and high magnification TEM image of Bi$_2$Te$_3$ thin film on Ge(111) substrate. High magnification TEM image (**Figure A6b**) clearly shows the atomic column fringes of Bi$_2$Te$_3$ films.
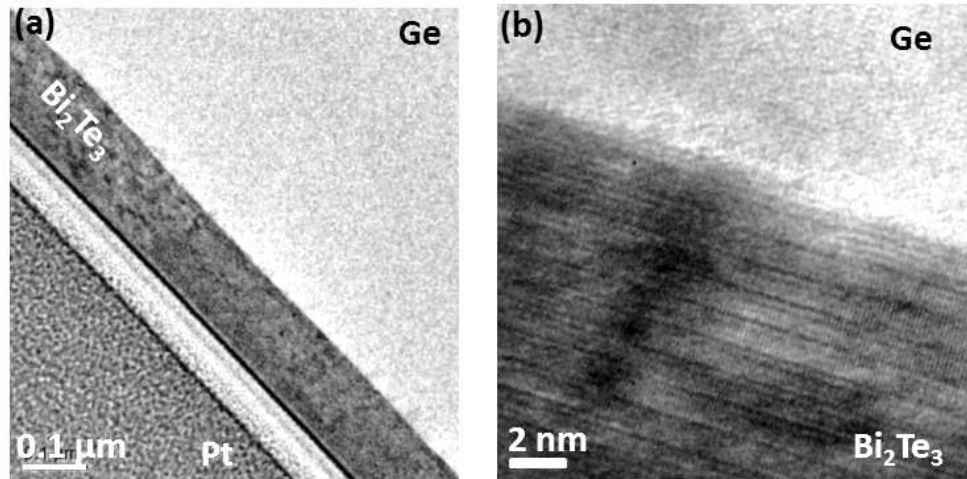
Figure A6: (a) and (b) show the overview and high magnification TEM images of the Bi$_2$Te$_3$ on the Ge substrate.

6. HAADF-STEM imaging and analysis of Bi$_2$Te$_3$/Ge(111) interface

Figure A7a shows the HAADF-STEM image of the Bi$_2$Te$_3$ /Ge(111) interface with the investigated Te ML. A set of misfit dislocations can be seen after masking the HAADF-STEM image to only see planes in (0001) direction (**Figure A7c**). It is demonstrated that after few atomic planes (numbers in **Figure A7b**) at the interface a misfit dislocation is present (red lines).
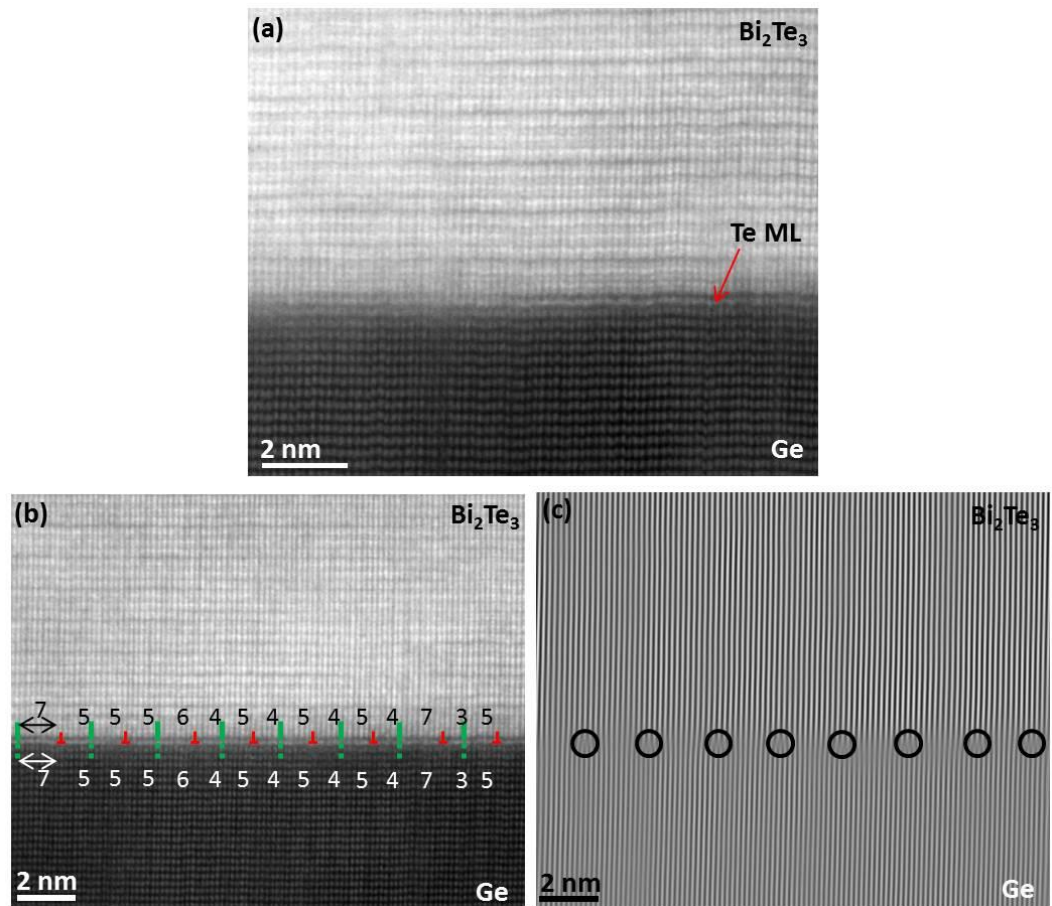
Figure A7: (a) and (b) show the HAADF-STEM images of the Bi_2Te_3 film on the Ge substrate with the ML of Te at the interface. (c) HAADF-STEM image masked to only show the vertical planes reveals the misfit dislocations at the interface. The green and red features on (b) show the position of not stressed and stressed atomic planes with their corresponding number of atomic planes in-between them, respectively.

Abbreviations

2D/3D	Two dimensions/three dimensions
2DEG	2D electron gas
AFM	Atomic force microscope
AHE	Anomalous Hall effect
BF	Bright field
BZ	Brillouin zone
DF	Dark field
DFT	Density functional theory
DOS	Density of states
EELS	Electron energy loss spectroscopy
EXAFS	Extended X-ray absorption fine structure
FIB	Focused ion beam
HAADF	High angle annular dark field
IQHE	Integer quantum Hall effect
ISHE	Inverse spin Hall effect
MAADF	middle angle annular dark field
MBE	Molecular beam epitaxy
PCA	Principal component analysis
QHE	Quantum Hall effect
QL	Quintuple layer

Abbreviations

QSHE	Quantum spin Hall effect
RHEED	Reflection high energy electron diffraction
SAED	Selected area electron diffraction
SHE	Spin Hall effect
SOC	Spin orbit coupling
STEM	Scanning transmission electron microscopy
STI	Strong topological insulator
TI	Topological insulator
TRS	Time reversal symmetry
vdW	Van der Waals
WTI	Weak topological insulator
XANES	X-ray absorption near edge structure
XAS	X-ray absorption spectroscopy
XRD	X-ray diffraction

Symbols

°	Degree
Å	Angstrom
$\boldsymbol{A}$	Magnetic potential
$\mathcal{A}_n$	Berry connection
at-%	Atomic percentage
(a,b,c)	Lattice constants
$\boldsymbol{B}$	Magnetic field
e	Electron
$\boldsymbol{E}$	Electric field
E_n	Energy function
$\boldsymbol{F}$	Force
$\boldsymbol{\phi}$	Electric potential
g	Genus number
G_E	Electrons splitting energy
G_H	Holes splitting energy
Γ	Gamma point
Ω_n	Berry Curvature
γ_n	Phase
H	Hamiltonian
h	Plank's constant

Symbols

I	Current
J	Quantum number
$\boldsymbol{K}$	Momentum
k	Wave vector
$L_{2,3}$	EELS edge
l	Angular momentum
λ_{mfp}	Mean free path
M	Magnetisation
m	Mass
$M_{4,5}$	EELS edge
μ_B	Bohr magneton
$\mu_{1,2,3}$	Invariants
n	Quantum number
P	Pressure
$P\ 4/nmm$	Space group
π	Pi
Ψ	Wave function
q	Charge of the particle
R_H	Hall resistivity
R_n	Radius of cyclotron motion
$R\bar{3}m$	Space group
ρ_e	Density of charged carriers

Symbols

ρ^{xy}	Resistivity in xy directions
S	Spin
$\boldsymbol{\sigma}$	Pauli matrices
σ^{xy}	Resistivity in xy directions
ς	Exchange field
$\boldsymbol{T}$	Gaussian curvature
T_c	Transition temperature
$u(x)$	Wave function
$u_k^\mu(r)$	Bloch function
V_H	Hall voltage
v	Velocity of particles/ Landau levels
$v_{0,1,2,3}$	Invariants
W	Sample width
ω_c	Angular frequency
X	X point in BZ
x,y,z	Directions
Z	Atomic number
ξ	Arbitrary smooth function

References

1. Williams, D.B.B.C., C. , *Transmission Electron Microscopy: A Textbook for Materials Science*.

2. Moore, J.E. and L. Balents, *Topological invariants of time-reversal-invariant band structures.* Physical Review B, 2007. **75**(12): p. 121306.

3. Kane, C.L. and E.J. Mele, *Quantum Spin Hall Effect in Graphene.* Physical Review Letters, 2005. **95**(22): p. 226801.

4. Kane, C.L. and E.J. Mele, *Z_2 Topological Order and the Quantum Spin Hall Effect.* Physical Review Letters, 2005. **95**(14): p. 146802.

5. Fu, L., C.L. Kane, and E.J. Mele, *Topological Insulators in Three Dimensions.* Physical Review Letters, 2007. **98**(10): p. 106803.

6. Roy, R., *Topological phases and the quantum spin Hall effect in three dimensions.* Physical Review B, 2009. **79**(19): p. 195322.

7. Moore, J.E., *The birth of topological insulators.* Nature, 2010. **464**(7286): p. 194-198.

8. König, M., et al., *Quantum Spin Hall Insulator State in HgTe Quantum Wells.* Science, 2007. **318**(5851): p. 766-770.

9. Hsieh, D., et al., *A topological Dirac insulator in a quantum spin Hall phase.* Nature, 2008. **452**(7190): p. 970-974.

10. Xia, Y., et al., *Observation of a large-gap topological-insulator class with a single Dirac cone on the surface.* Nat Phys, 2009. **5**(6): p. 398-402.

11. Chen, Y.L., et al., *Experimental Realization of a Three-Dimensional Topological Insulator, Bi_2Te_3.* Science, 2009. **325**(5937): p. 178-181.

12. Zhang, H., et al., *Topological insulators in Bi_2Se_3, Bi_2Te_3 and Sb_2Te_3 with a single Dirac cone on the surface.* Nature Physics, 2009. **5**(6): p. 438-442.

13. Anderson, P.W., *Absence of Diffusion in Certain Random Lattices.* Physical Review, 1958. **109**(5): p. 1492-1505.

14. Abrahams, E., et al., *Scaling Theory of Localization: Absence of Quantum Diffusion in Two Dimensions.* Physical Review Letters, 1979. **42**(10): p. 673-676.

15. Lee, P.A. and T.V. Ramakrishnan, *Disordered electronic systems.* Reviews of Modern Physics, 1985. **57**(2): p. 287-337.

16. Hall, E.H., *On a New Action of the Magnet on Electric Currents.* American Journal of Mathematics, 1879. **2**(3): p. 287-292.

References

17. Klitzing, K.v., G. Dorda, and M. Pepper, *New Method for High-Accuracy Determination of the Fine-Structure Constant Based on Quantized Hall Resistance.* Physical Review Letters, 1980. **45**(6): p. 494-497.

18. Tsui, D.C., H.L. Stormer, and A.C. Gossard, *Two-Dimensional Magnetotransport in the Extreme Quantum Limit.* Physical Review Letters, 1982. **48**(22): p. 1559-1562.

19. Halperin, B.I., *Quantized Hall conductance, current-carrying edge states, and the existence of extended states in a two-dimensional disordered potential.* Physical Review B, 1982. **25**(4): p. 2185-2190.

20. Thouless, D.J., et al., *Quantized Hall Conductance in a Two-Dimensional Periodic Potential.* Physical Review Letters, 1982. **49**(6): p. 405-408.

21. Simon, B., *Holonomy, the Quantum Adiabatic Theorem, and Berry's Phase.* Physical Review Letters, 1983. **51**(24): p. 2167-2170.

22. Berry, M.V., *Quantal phase-factors accompanying adiabatic changes.* Proc. Roy. Soc. Lond. A 1984. **392**: p. 45-57.

23. Wen, X.-G., *Topological orders and edge excitations in fractional quantum Hall states.* Advances in Physics, 1995. **44**(5): p. 405-473.

24. Fu, L. and C.L. Kane, *Time reversal polarization and a Z_2 adiabatic spin pump.* Physical Review B, 2006. **74**(19): p. 195312.

25. Hasan, M.Z. and C.L. Kane, *Colloquium: Topological insulators.* Reviews of Modern Physics, 2010. **82**(4): p. 3045-3067.

26. Moore, J., *Topological insulators: The next generation.* Nat Phys, 2009. **5**(6): p. 378-380.

27. Qi, X.L.Z., S.-C. , *The quantum spin Hall effect and feature topological insulators.* Phys. Today, 2010.

28. Qi, X.-L. and S.-C. Zhang, *Topological insulators and superconductors.* Reviews of Modern Physics, 2011. **83**(4): p. 1057-1110.

29. Kittel, C., *Introduction to Solid State Physics*. 8th ed. 2004: Wiley, John & Sons, Incorporated.

30. von Klitzing, K., *Developments in the quantum Hall effect.* Philosophical Transactions of the Royal Society A: Mathematical, Physical and Engineering Sciences, 2005. **363**(1834): p. 2203-2219.

31. Avron, J.E., R. Seiler, and B. Simon, *Homotopy and Quantization in Condensed Matter Physics.* Physical Review Letters, 1983. **51**(1): p. 51-53.

32. Born, M. and V. Fock, *Beweis des Adiabatensatzes.* Zeitschrift für Physik, 1928. **51**(3): p. 165-180.

References

33. Kato, T., *On the Adiabatic Theorem of Quantum Mechanics.* Journal of the Physical Society of Japan, 1950. **5**(6): p. 435-439.

34. Fock, V., *Über die Beziehung zwischen den Integralen der quantenmechanischen Bewegungsgleichungen und der Schrödingerschen Wellengleichung.* Zeitschrift für Physik, 1928. **49**(5): p. 323-338.

35. Niu, G.S.a.Q., *Wave-packet dynamics in slowly perturbed crystals: Gradient corrections and Berry-phase effects.* Phys. Rev. B 1999. **59**: p. 14915-14925.

36. Dirac, P.A.M., *Quantised Singularities in the Electromagnetic Field* Proc. Roy. Soc. Lond. A 1931. **133**: p. 60-72.

37. Nakahara, M., *Geometry, Topology And Physics*, ed. P.D.F. Brewer. 2003: Institute of Physics Publishing.

38. Kane, C.M., J. , *Topological Insulators.* Physics World, 2011. **24**(32): p. 32-36.

39. Qi, X.-L., Y.-S. Wu, and S.-C. Zhang, *General theorem relating the bulk topological number to edge states in two-dimensional insulators.* Physical Review B, 2006. **74**(4): p. 045125.

40. Laughlin, R.B., *Quantized Hall conductivity in two dimensions.* Physical Review B, 1981. **23**(10): p. 5632-5633.

41. Hall, E.H., *On the "Rotational Coefficient" in nickel and cobalt.* Philosophical Magazine, 1881. **12**: p. 157-172.

42. Karplus, R. and J.M. Luttinger, *Hall Effect in Ferromagnetics.* Physical Review, 1954. **95**(5): p. 1154-1160.

43. Nagaosa, N., et al., *Anomalous Hall effect.* Reviews of Modern Physics, 2010. **82**(2): p. 1539-1592.

44. Chang, M.-C. and Q. Niu, *Berry phase, hyperorbits, and the Hofstadter spectrum: Semiclassical dynamics in magnetic Bloch bands.* Physical Review B, 1996. **53**(11): p. 7010-7023.

45. Sinova, J., et al., *Spin Hall effects.* Reviews of Modern Physics, 2015. **87**(4): p. 1213-1260.

46. Haldane, F.D.M., *Model for a Quantum Hall Effect without Landau Levels: Condensed-Matter Realization of the "Parity Anomaly".* Physical Review Letters, 1988. **61**(18): p. 2015-2018.

47. Fu, L. and C.L. Kane, *Topological insulators with inversion symmetry.* Physical Review B, 2007. **76**(4): p. 045302.

48. Ando, T. and H. Suzuura, *Presence of Perfectly Conducting Channel in Metallic Carbon Nanotubes.* Journal of the Physical Society of Japan, 2002. **71**(11): p. 2753-2760.

References

49.   Xu, C. and J.E. Moore, *Stability of the quantum spin Hall effect: Effects of interactions, disorder, and Z_2 topology.* Physical Review B, 2006. **73**(4): p. 045322.

50.   Bernevig, B.A., T.L. Hughes, and S.-C. Zhang, *Quantum Spin Hall Effect and Topological Phase Transition in HgTe Quantum Wells.* Science, 2006. **314**(5806): p. 1757-1761.

51.   Liu, C.-X., S.-C. Zhang, and X.-L. Qi, *The quantum anomalous Hall effect.* arXiv preprint arXiv:1508.07106, 2015.

52.   Liu, C.-X., et al., *Quantum Anomalous Hall Effect in $Hg_{1-y}Mn_yTe$ Quantum Wells.* Physical Review Letters, 2008. **101**(14): p. 146802.

53.   Qi, X.-L., Y.-S. Wu, and S.-C. Zhang, *Topological quantization of the spin Hall effect in two-dimensional paramagnetic semiconductors.* Physical Review B, 2006. **74**(8): p. 085308.

54.   Yu, R., et al., *Quantized Anomalous Hall Effect in Magnetic Topological Insulators.* Science, 2010. **329**(5987): p. 61-64.

55.   Chang, C.-Z., et al., *Experimental Observation of the Quantum Anomalous Hall Effect in a Magnetic Topological Insulator.* Science, 2013. **340**(6129): p. 167-170.

56.   Chang, C.-Z., et al., *Thin Films of Magnetically Doped Topological Insulator with Carrier-Independent Long-Range Ferromagnetic Order.* Advanced Materials, 2013. **25**(7): p. 1065-1070.

57.   Hor, Y.S., et al., *Development of ferromagnetism in the doped topological insulator $Bi_{2-x}Mn_xTe_3$.* Physical Review B, 2010. **81**(19): p. 195203.

58.   Kou, X., et al., *Interplay between Different Magnetisms in Cr-Doped Topological Insulators.* ACS Nano, 2013. **7**(10): p. 9205-9212.

59.   Kou, X., et al., *Manipulating Surface-Related Ferromagnetism in Modulation-Doped Topological Insulators.* Nano Letters, 2013. **13**(10): p. 4587-4593.

60.   Li, M., et al., *Experimental Verification of the Van Vleck Nature of Long-Range Ferromagnetic Order in the Vanadium-Doped Three-Dimensional Topological Insulator Sb_2Te_3.* Physical Review Letters, 2015. **114**(14): p. 146802.

61.   Dyck, J.S., et al., *Low-temperature ferromagnetic properties of the diluted magnetic semiconductor $Sb_{2-x}Cr_xTe_3$.* Physical Review B, 2005. **71**(11): p. 115214.

62.   Bestwick, A.J., et al., *Precise Quantization of the Anomalous Hall Effect near Zero Magnetic Field.* Physical Review Letters, 2015. **114**(18): p. 187201.

63.   Watson, M.D., et al., *Study of the structural, electric and magnetic properties of Mn-doped Bi_2Te_3 single crystals.* New Journal of Physics, 2013. **15**(10): p. 103016.

64.   Collins-McIntyre, L.J., et al., *Magnetic ordering in Cr-doped Bi_2Se_3 thin films.* EPL (Europhysics Letters), 2014. **107**(5): p. 57009.

References

65. Figueroa, A.I., et al., *Local Structure and Bonding of Transition Metal Dopants in Bi$_2$Se$_3$ Topological Insulator Thin Films.* The Journal of Physical Chemistry C, 2015. **119**(30): p. 17344-17351.

66. Kim, N.S., et al., *Leakage current: Moore's law meets static power.* Computer, 2003. **36**(12): p. 68-75.

67. Pesin, D. and A.H. MacDonald, *Spintronics and pseudospintronics in graphene and topological insulators.* Nat Mater, 2012. **11**(5): p. 409-416.

68. Vobornik, I., et al., *Magnetic Proximity Effect as a Pathway to Spintronic Applications of Topological Insulators.* Nano Letters, 2011. **11**(10): p. 4079-4082.

69. Mellnik, A.R., et al., *Spin-transfer torque generated by a topological insulator.* Nature, 2014. **511**(7510): p. 449-451.

70. Fan, Y., et al., *Electric-field control of spin–orbit torque in a magnetically doped topological insulator.* Nat Nano, 2016. **11**(4): p. 352-359.

71. Hsieh, D., et al., *A tunable topological insulator in the spin helical Dirac transport regime.* Nature, 2009. **460**(7259): p. 1101-1105.

72. Shiomi, Y., et al., *Spin-Electricity Conversion Induced by Spin Injection into Topological Insulators.* Physical Review Letters, 2014. **113**(19): p. 196601.

73. Qi, X.-L., T.L. Hughes, and S.-C. Zhang, *Topological field theory of time-reversal invariant insulators.* Physical Review B, 2008. **78**(19): p. 195424.

74. Qi, X.-L., et al., *Inducing a Magnetic Monopole with Topological Surface States.* Science, 2009. **323**(5918): p. 1184-1187.

75. Maciejko, J., et al., *Fractional Topological Insulators in Three Dimensions.* Physical Review Letters, 2010. **105**(24): p. 246809.

76. Ohring, M., *Materials science of thin films deposition & structure*. Second ed. 1991. 794.

77. Shozo, I., *Some New Techniques in Reflection High Energy Electron Diffraction (RHEED) Application to Surface Structure Studies.* Japanese Journal of Applied Physics, 1977. **16**(6): p. 891.

78. Maksym, P.A. and J.L. Beeby, *A theory of RHEED.* Surface Science, 1981. **110**(2): p. 423-438.

79. Dobson, P.J., et al., *Current understanding and applications of the RHEED intensity oscillation technique.* Journal of Crystal Growth, 1987. **81**(1): p. 1-8.

80. MacRae, A.U., *Low-Energy Electron Diffraction.* Improved experimental methods provide new information on the structure of surfaces of solids, 1963. **139**(3553): p. 379-388.

References

81.   Mitchell, K.A.R., *Low-energy electron diffraction.* Contemporary Physics, 1973. **14**(3): p. 251-271.

82.   Davisson, C. and L.H. Germer, *Diffraction of Electrons by a Crystal of Nickel.* Physical Review, 1927. **30**(6): p. 705-740.

83.   Nishikawa, S. and S. Kikuchi, *The Diffraction of Cathode Rays by Calcite.* Proceedings of the Imperial Academy, 1928. **4**(8): p. 475-477.

84.   Nishikawa, S. and S. Kikuchi, *Diffraction of Cathode Rays by Mica.* Nature, 1928. **121**(3061): p. 1019-1020.

85.   Binnig, G., C.F. Quate, and C. Gerber, *Atomic Force Microscope.* Physical Review Letters, 1986. **56**(9): p. 930-933.

86.   Meyer, E., *Atomic force microscopy.* Progress in Surface Science, 1992. **41**(1): p. 3-49.

87.   Zachariasen, W., *A general theory of X-ray diffraction in crystals.* Acta Crystallographica, 1967. **23**(4): p. 558-564.

88.   Bragg, W.H. and W.L. Bragg, *The Reflection of X-rays by Crystals.* Proceedings of the Royal Society of London. Series A, 1913. **88**(605): p. 428-438.

89.   Holý, V., et al., *High-resolution x-ray diffraction of epitaxial bismuth chalcogenide topological insulator layers.* Advances in Natural Sciences: Nanoscience and Nanotechnology, 2017. **8**(1): p. 015006.

90.   Bunker, G., *Introduction to XAFS: A paractical guid to X-ray absorption fine structure spectroscopy.* 2010: Cambridge University Press.

91.   Nelsen, J. and D. McMorrow, *Elements of modern X-ray physics.* 2001: Wiley New York.

92.   Rehr, J.J. and R.C. Albers, *Theoretical approaches to x-ray absorption fine structure.* Reviews of Modern Physics, 2000. **72**(3): p. 621-654.

93.   Cox, D.C., *Introduction to Focused Ion Beam Nanometrology.* 2015, Morgan & Claypool Publishers.

94.   Taylor, G., *Disintegration of Water Drops in an Electric Field.* Proceedings of the Royal Society of London. Series A. Mathematical and Physical Sciences, 1964. **280**(1382): p. 383.

95.   Wien, W., *Untersuchungen über die electrische Entladung in verdünnten Gasen.* Annalen der Physik, 1898. **301**(6): p. 440-452.

96.   De Broglie, L., *Recherches sur la Theorie des Quanta (Researches on the Quantum Theory).* Ann. Phys., 1925. **3**: p. 22-128.

97.   Nedelkoski, Z., et al., *Realisation of magnetically and atomically abrupt half-metal/semiconductor interface: $Co_2FeSi_{0.5}Al_{0.5}$/Ge(111).* Scientific Reports, 2016. **6**: p. 37282.

References

98.   Kuerbanjiang, B., et al., *The role of chemical structure on the magnetic and electronic properties of Co2FeAl0.5Si0.5/Si(111) interface.* Applied Physics Letters, 2016. **108**(17): p. 172412.

99.   Gilks, D., et al., *Structural study of $Fe_3O_4(111)$ thin films with bulk like magnetic and magnetotransport behaviour.* Journal of Applied Physics, 2014. **115**(17): p. -.

100.   Liu, Y., et al., *Charging Dirac States at Antiphase Domain Boundaries in the Three-Dimensional Topological Insulator Bi_2Se_3.* Physical Review Letters, 2013. **110**(18): p. 186804.

101.   Gilks, D., et al., *Origin of anomalous magnetite properties in crystallographic matched heterostructures: $Fe_3O_4(111)/MgAl_2O_4(111)$.* Journal of Physics: Condensed Matter, 2013. **25**(48): p. 485004.

102.   Zlatko, N., et al., *Controlling the half-metallicity of Heusler/Si(1 1 1) interfaces by a monolayer of Si–Co–Si.* Journal of Physics: Condensed Matter, 2016. **28**(39): p. 395003.

103.   Nedelkoski, Z., et al., *The antiphase boundary in half-metallic Heusler alloy $Co_2Fe(Al,Si)$: atomic structure, spin polarization reversal, and domain wall effects.* Applied Physics Letters, 2016. **109**(22): p. 222405.

104.   Novoselov, K.S., et al., *2D materials and van der Waals heterostructures.* Science, 2016. **353**(6298): p. 461-472.

105.   van Benthem, K. and S.J. Pennycook, *Imaging and spectroscopy of defects in semiconductors using aberration-corrected STEM.* Applied Physics A, 2009. **96**(1): p. 161-169.

106.   Fangsen, L., et al., *Atomically resolved $FeSe/SrTiO_3$ (001) interface structure by scanning transmission electron microscopy.* 2D Materials, 2016. **3**(2): p. 024002.

107.   Harrison, S.E., et al., *Massive Dirac Fermion Observed in Lanthanide-Doped Topological Insulator Thin Films.* Scientific Reports, 2015. **5**: p. 15767.

108.   Pratt, A., et al., *Enhanced oxidation of nanoparticles through strain-mediated ionic transport.* Nat Mater, 2014. **13**(1): p. 26-30.

109.   He, Q.L., et al., *Two-dimensional superconductivity at the interface of a Bi_2Te_3/FeTe heterostructure.* Nat Commun, 2014. **5**.

110.   Hirohata, A., et al., *Heusler-alloy films for spintronic devices.* Applied Physics a-Materials Science & Processing, 2013. **111**(2): p. 423.

111.   Gilks, D., et al., *Magnetism and magnetotransport in symmetry matched spinels: $Fe_3O_4/MgAl_2O_4$.* Journal of Applied Physics, 2013. **113**(17): p. 17B107-3.

References

112.	Shi, Y., et al., *van der Waals Epitaxy of MoS$_2$ Layers Using Graphene As Growth Templates.* Nano Letters, 2012. **12**(6): p. 2784-2791.

113.	LeBeau, J.M., et al., *Standardless Atom Counting in Scanning Transmission Electron Microscopy.* Nano Letters, 2010. **10**(11): p. 4405-4408.

114.	Findlay, S.D., et al., *Dynamics of annular bright field imaging in scanning transmission electron microscopy.* Ultramicroscopy, 2010. **110**(7): p. 903-923.

115.	LeBeau, J.M., et al., *Quantitative Atomic Resolution Scanning Transmission Electron Microscopy.* Physical Review Letters, 2008. **100**(20): p. 206101.

116.	Krivanek, O.L., et al., *An electron microscope for the aberration-corrected era.* Ultramicroscopy, 2008. **108**(3): p. 179-195.

117.	Ghasemi, A., et al., *Atomic-level structural and chemical analysis of Cr-doped Bi$_2$Se$_3$ thin films.* Scientific Reports, 2016. **6**: p. 26549.

118.	Ghasemi, A., et al., *Experimental and density functional study of Mn doped Bi$_2$Te$_3$ topological insulator.* APL Materials, 2016. **4**(12): p. 126103.

119.	Ghasemi, A., et al., *Van der Waals epitaxy between the highly lattice mismatched Cu-doped FeSe and Bi$_2$Te$_3$.* NPG Asia Mater, 2017. **9**: p. e402.

120.	Mitchell, D. *Dave Mitchell's DigitalMicrograph™ Scripting Website*. 15-Jul-2017; Available from: http://www.dmscripting.com/.

121.	Schaffer, B., W. Grogger, and G. Kothleitner, *Automated spatial drift correction for EFTEM image series.* Ultramicroscopy, 2004. **102**(1): p. 27-36.

122.	Cueva, P., et al., *Data Processing for Atomic Resolution Electron Energy Loss Spectroscopy.* Microscopy and Microanalysis, 2012. **18**(4): p. 667-675.

123.	Potapov, P. *temDM*. Available from: http://temdm.com/.

124.	Lucas, G., et al., *Multivariate statistical analysis as a tool for the segmentation of 3D spectral data.* Micron, 2013. **52–53**: p. 49-56.

125.	Momma, K. and F. Izumi, *VESTA 3 for three-dimensional visualization of crystal, volumetric and morphology data.* Journal of Applied Crystallography, 2011. **44**(6).

126.	*JEMS*. Available from: http://www.jems-saas.ch/Home/jemsWebSite/jems.html.

127.	*CrystalKit*. Available from: http://www.totalresolution.com/CrystalKit.html.

128.	*ICSD* Available from: http://icsd.cds.rsc.org/search/basic.xhtml;jsessionid=5C12531922DD285E3F7C5AC3A031 BD05?cdsrdr=3.

129.	Koch, C., *Determination of Core Structure Periodicity and Point Defect Density along Dislocations*. 2002, Arizona State University.

References

130. Hohenberg, P. and W. Kohn, *Inhomogeneous Electron Gas.* Physical Review, 1964. **136**(3B): p. B864-B871.

131. Martin, R., *Electronic Structure: Basic Theory and Practical Methods*. Cambridge University Press.

132. Kohn, W. and L.J. Sham, *Self-Consistent Equations Including Exchange and Correlation Effects.* Physical Review, 1965. **140**(4A): p. A1133-A1138.

133. Clark, S.J., et al., *First principles methods using CASTEP.* Crystalline Materials, 2005. **220**(5-6): p. 567.

134. Zhang, J.M., et al., *Tailoring Magnetic Doping in the Topological Insulator Bi_2Se_3.* Physical Review Letters, 2012. **109**(26): p. 266405.

135. Kou, X.F., et al., *Magnetically doped semiconducting topological insulators.* Journal of Applied Physics, 2012. **112**(6): p. 063912.

136. Zhang, J.M., et al., *Stability, electronic, and magnetic properties of the magnetically doped topological insulators Bi_2Se_3, Bi_2Te_3 ,and Sb_2Te_3.* Physical Review B, 2013. **88**(23): p. 235131.

137. Haazen, P.P.J., et al., *Ferromagnetism in thin-film Cr-doped topological insulator Bi_2Se_3.* Applied Physics Letters, 2012. **100**(8): p. 2404.

138. Collins-McIntyre, L.J., et al., *Magnetic ordering in Cr-doped Bi_2Se_3 thin films.* EPL (Europhysics Letters), 2014. **107**(5): p. 57009.

139. Chen, T., et al., *High-Mobility Sm-Doped Bi2Se3 Ferromagnetic Topological Insulators and Robust Exchange Coupling.* Advanced Materials, 2015. **27**(33): p. 4823-4829.

140. Collins-McIntyre, L.J., et al., *X-ray magnetic spectroscopy of MBE-grown Mn-doped Bi_2Se_3 thin films.* AIP Advances, 2014. **4**(12): p. 127136.

141. Figueroa, A.I., et al., *Magnetic Cr doping of Bi_2Se_3: Evidence for divalent Cr from x-ray spectroscopy.* Physical Review B, 2014. **90**(13): p. 134402.

142. Liu, Y., et al., *Tuning Dirac states by strain in the topological insulator Bi_2Se_3.* Nat Phys, 2014. **10**(4): p. 294-299.

143. Chang, C.-Z., et al., *Chemical-Potential-Dependent Gap Opening at the Dirac Surface States of Bi_2Se_3 Induced by Aggregated Substitutional Cr Atoms.* Physical Review Letters, 2014. **112**(5): p. 056801.

144. Trebbia, P. and N. Bonnet, *EELS elemental mapping with unconventional methods I. Theoretical basis: Image analysis with multivariate statistics and entropy concepts.* Ultramicroscopy, 1990. **34**(3): p. 165-178.

145. Zhang, J.L., et al., *Pressure-induced superconductivity in topological parent compound Bi_2Te_3.* Proceedings of the National Academy of Sciences, 2011. **108**(1): p. 24-28.

146. Collins-McIntyre, L.J., et al., *Magnetic ordering in Cr-doped Bi_2Se_3 thin films.* EPL (Europhysics Letters), 2014. **107**(5): p. 57009.

147. Choi, J., et al., *Magnetic properties of Mn-doped Bi_2Te_3 and Sb_2Te_3.* physica status solidi (b), 2004. **241**(7): p. 1541-1544.

148. Niu, C., et al., *Mn induced ferromagnetism and modulated topological surface states in Bi_2Te_3.* Applied Physics Letters, 2011. **98**(25): p. 252502.

149. Růžička, J., et al., *Structural and electronic properties of manganese-doped Bi_2Te_3 epitaxial layers.* New Journal of Physics, 2015. **17**(1): p. 013028.

150. Egerton, R.F., *Electron Energy-Loss Spectroscopy in the Electron Microscope*. third ed. 2011: Springer. 490.

151. Ravel, B. and M. Newville, *ATHENA, ARTEMIS, HEPHAESTUS: data analysis for X-ray absorption spectroscopy using IFEFFIT.* Journal of Synchrotron Radiation, 2005. **12**(4): p. 537-541.

152. Ravel, B., *ATOMS: crystallography for the X-ray absorption spectroscopist.* Journal of Synchrotron Radiation, 2001. **8**(2): p. 314-316.

153. Perdew, J.P., K. Burke, and M. Ernzerhof, *Generalized Gradient Approximation Made Simple.* Physical Review Letters, 1996. **77**(18): p. 3865-3868.

154. Monkhorst, H.J. and J.D. Pack, *Special points for Brillouin-zone integrations.* Physical Review B, 1976. **13**(12): p. 5188-5192.

155. McNellis, E.R., J. Meyer, and K. Reuter, *Azobenzene at coinage metal surfaces: Role of dispersive van der Waals interactions.* Physical Review B, 2009. **80**(20): p. 205414.

156. Figueroa, A.I., et al., *Oxidation Effects in Rare Earth Doped Topological Insulator Thin Films.* Scientific Reports, 2016. **6**: p. 22935.

157. Hor, Y.S., et al., *Development of ferromagnetism in the doped topological insulator $Bi_2Mn_xTe_3$.* Physical Review B, 2010. **81**(19): p. 195203.

158. Frank, F.C. and J.H. van der Merwe, *One-Dimensional Dislocations. I. Static Theory.* Proceedings of the Royal Society of London. Series A. Mathematical and Physical Sciences, 1949. **198**(1053): p. 205.

159. Frank, F.C. and J.H. van der Merwe, *One-Dimensional Dislocations. II. Misfitting Monolayers and Oriented Overgrowth.* Proceedings of the Royal Society of London. Series A. Mathematical and Physical Sciences, 1949. **198**(1053): p. 216.

References

160. Merwe, J.H.v.d., *Equilibrium Structure of a Thin Epitaxial Film.* Journal of Applied Physics, 1970. **41**(11): p. 4725-4731.

161. Gourley, P.L. and R.M. Biefeld, *Ga(As,P) strained-layer superlattices: A ternary semiconductor with independently adjustable band gap and lattice constant.* Journal of Vacuum Science & Technology B: Microelectronics Processing and Phenomena, 1983. **1**(2): p. 383-386.

162. Koma, A., *Van der Waals epitaxy—a new epitaxial growth method for a highly lattice-mismatched system.* Thin Solid Films, 1992. **216**(1): p. 72-76.

163. Geim, A.K. and I.V. Grigorieva, *Van der Waals heterostructures.* Nature, 2013. **499**(7459): p. 419-425.

164. Liu, X., et al., *Structural properties of Bi_2Te_3 and Bi_2Se_3 topological insulators grown by molecular beam epitaxy on GaAs(001) substrates.* Applied Physics Letters, 2011. **99**(17): p. 171903.

165. Liu, H.-C., et al., *Robust two-dimensional superconductivity and vortex system in Bi_2Te_3/FeTe heterostructures.* Scientific Reports, 2016. **6**: p. 26168.

166. Xu, J.-P., et al., *Experimental Detection of a Majorana Mode in the core of a Magnetic Vortex inside a Topological Insulator-Superconductor Bi_2Te_3\$NbSe_2$ Heterostructure.* Physical Review Letters, 2015. **114**(1): p. 017001.

167. Qing Lin, H., et al., *Anisotropic magnetic responses of a 2D-superconducting Bi_2Te_3/FeTe heterostructure.* Journal of Physics: Condensed Matter, 2015. **27**(34): p. 345701.

168. Sochnikov, I., et al., *Direct Measurement of Current-Phase Relations in Superconductor/Topological Insulator/Superconductor Junctions.* Nano Letters, 2013. **13**(7): p. 3086-3092.

169. Wang, M.-X., et al., *The Coexistence of Superconductivity and Topological Order in the Bi_2Se_3 Thin Films.* Science, 2012.

170. Leijnse, M. and K. Flensberg, *Introduction to topological superconductivity and Majorana fermions.* Semiconductor science and technology, 2012. **27**(12): p. 124003.

171. Nadj-Perge, S., et al., *Observation of Majorana fermions in ferromagnetic atomic chains on a superconductor.* Science, 2014. **346**(6209): p. 602-607.

172. Zareapour, P., et al., *Proximity-induced high-temperature superconductivity in the topological insulators Bi_2Se_3 and Bi_2Te_3.* Nature Communications, 2012. **3**: p. 1056.

173. Mizukami, Y., et al., *Extremely strong-coupling superconductivity in artificial two-dimensional Kondo lattices.* Nat Phys, 2011. **7**(11): p. 849-853.

References

174. Raveau, B. and T. Sarkar, *Superconducting-like behaviour of the layered Chalcogenides CuS and CuSe below 40 K.* Solid State Sciences, 2011. **13**(10): p. 1874-1878.

175. Harrison, S.E., et al., *Two-step growth of high quality Bi2Te3 thin films on Al2O3 (0001) by molecular beam epitaxy.* Applied Physics Letters, 2013. **102**(17): p. 171906.

176. Shojaei, A.R., et al., *First-principles study of optical properties of α-CuSe/klockmannite: Bulk and nano-layers.* Thin Solid Films, 2014. **556**: p. 425-433.

177. Shojaei, A.R., *Electrical conductivity plus probability of superconductivity in α-CuSe/klockmannite; bulk and nano-layers.* Journal of Alloys and Compounds, 2015. **632**: p. 568-574.

178. Hsieh, D., et al., *Observation of Time-Reversal-Protected Single-Dirac-Cone Topological-Insulator States in Bi_2Te_3 and Sb_2Te_3.* Physical Review Letters, 2009. **103**(14): p. 146401.

179. Fu, L. and C.L. Kane, *Probing Neutral Majorana Fermion Edge Modes with Charge Transport.* Physical Review Letters, 2009. **102**(21): p. 216403.

180. Mahmoud, E., et al., *Low-temperature Raman fingerprints for few-quintuple layer topological insulator Bi_2Se_3 films epitaxied on GaAs.* Nanotechnology, 2014. **25**(24): p. 245701.

181. Zhang, T., et al., *Experimental Demonstration of Topological Surface States Protected by Time-Reversal Symmetry.* Physical Review Letters, 2009. **103**(26): p. 266803.

182. Pang, M.Y., et al., *Characterizations of bismuth telluride/gallium nitride heterojunction photovoltaic detector for MWIR detection under room temperature.* Journal of Physics: Conference Series, 2009. **152**(1): p. 012046.

183. Chen, Z., et al., *Molecular Beam Epitaxial Growth and Properties of Bi_2Se_3 Topological Insulator Layers on Different Substrate Surfaces.* Journal of Electronic Materials, 2014. **43**(4): p. 909-913.

184. Cho, S., et al., *Antisite defects of Bi_2Te_3 thin films.* Applied Physics Letters, 1999. **75**(10): p. 1401-1403.

185. Schreyeck, S., et al., *Molecular beam epitaxy of high structural quality Bi_2Se_3 on lattice matched InP(111) substrates.* Applied Physics Letters, 2013. **102**(4): p. 041914.

186. Chan, L.H., E.I. Altman, and Y. Liang, *Development of procedures for obtaining clean, low-defect-density Ge(100) surfaces.* Journal of Vacuum Science & Technology A: Vacuum, Surfaces, and Films, 2001. **19**(3): p. 976-981.

187. Wimmer, E., et al., *Full-potential self-consistent linearized-augmented-plane-wave method for calculating the electronic structure of molecules and surfaces: O_2 molecule.* Physical Review B, 1981. **24**(2): p. 864-875.

References

188. Weinert, M., E. Wimmer, and A.J. Freeman, *Total-energy all-electron density functional method for bulk solids and surfaces.* Physical Review B, 1982. **26**(8): p. 4571-4578.

189. Nakamura, K., et al., *Enhancement of magnetocrystalline anisotropy in ferromagnetic Fe films by intra-atomic noncollinear magnetism.* Physical Review B, 2003. **67**(1): p. 014420.

190. Barth, U.v. and L. Hedin, *A local exchange-correlation potential for the spin polarized case: I.* J. Phys. C: Solid State Phys., 1972. **5**: p. 1629-1642.